LR 24122

CR 114290

RESEARCH PROGRAM TO DETERMINE ROTOR RESPONSE CHARACTERISTICS AT HIGH ADVANCE RATIOS

FINAL REPORT

FEBRUARY 1971

by

W.A. Kuczynski

G.J. Sissingh

for

U.S. ARMY AERONAUTICAL RESEARCH LABORATORY
MOFFETT FIELD, CALIFORNIA

Contract NAS 2-5419

LOCKHEED-CALIFORNIA COMPANY • BURBANK, CALIFORNIA
A DIVISION OF LOCKHEED AIRCRAFT CORPORATION

RESEARCH PROGRAM TO DETERMINE ROTOR RESPONSE CHARACTERISTICS AT HIGH ADVANCE RATIOS

FINAL REPORT

FEBRUARY 1971

by

W.A. Kuczynski

G.J. Sissingh

for

U.S. ARMY AERONAUTICAL RESEARCH LABORATORY
MOFFETT FIELD, CALIFORNIA

Contract NAS 2-5419

LOCKHEED-CALIFORNIA COMPANY • BURBANK, CALIFORNIA
A DIVISION OF LOCKHEED AIRCRAFT CORPORATION

FOREWORD

The report was prepared for the U.S. Army Aeronautical Research Laboratory in fulfillment of Phase 1 of the Lockheed/ AARL High Advance Ratio Research Program (Contract NAS 2-5419). The program period of performance extended from June 1969 to December 1970. AARL program direction was provided by D. L. Sharpe. Technical advice was supplied by Dr. G. J. Sissingh of Lockheed.

SUMMARY

The Lockheed-California Company and the U.S. Army Aeronautical Research Laboratory (AARL) are currently conducting a research program to determine the dynamic characteristics of hingeless rotor systems at high advance ratios. The research is being conducted in two phases; Phase 1 considers rotors which are directly controlled and Phase 2 rotor systems which are equipped with moment feedback controls. Phase 1 has recently been completed and the results are discussed herein. Phase 2 is presently being executed and will be reported at a later date.

The initial effort involved the fabrication and testing of a small scale rotor model in the AARL 7 x 10 ft wind tunnel at Moffett Field, California. The specific objectives were to (1) experimentally determine the stability and response characteristics of directly controlled rigid rotors at high advance ratios and (2) evaluate the applicability of an existing mathematical model by correlation with the test results. Provisions were made in the design of the rotor to vary the blade Lock number (γ) and the first flapping mode frequency ($P\Omega$). γ was changed by adding weight at the tip of each blade. The flapping frequency was varied in two ways; by changing the stiffness of an inboard section of the blade (flapping flexure) and by changing the rotor speed. For each blade, one tip weight and two flexures were available which yielded four basic rotor configurations. Each basic configuration was tested at various rotational speeds. Eighteen discreet combinations of γ and P were investigated. Nominal γ values were 5.0 and 3.0 and P ranged from 1.14 to 2.39. Response data were taken at advance ratios up to 1.75 (including hover).

Rotor derivatives with respect to four excitations were obtained:

- Collective pitch, θ_o
- Longitudinal cyclic pitch, θ_s
- Lateral cyclic pitch, ϑ_c
- Rotor shaft angle of attack, α

The response included rotor pitching and rolling moments and lift. Rotor coning was also obtained from the Fourier analysis of the flapping moment of a single blade.

The test data indicate that at a fixed forward speed and rotational frequency the rotor response to the four excitations is linear. (Moderate angles were applied to avoid blade stall.) The derivatives, however, are not linear functions of advance ratio. In general they increase with increasing advance ratio. Derivatives with respect to θ_o, θ_s and α generally exhibit the same characteristics. The magnitudes are different but the gradients of change with μ are similar. The rotor responds somewhat differently to lateral cyclic pitch. The resulting rotor moment increases only slightly with advance ratio. In fact the rolling moment derivative remains constant or decreases with increased μ. Rotor lift was found to be independent of θ_c at all advance ratios.

The stability of several rotor configurations (defined by γ and P) was examined at advance ratios as high as 2.15. No classical indications of an approaching flapping instability were observed. This is attributed to the high apparent stiffness (P) of the rotor at the rotational speeds where the high μ-values were achieved. A splitting of the tip path plane was observed at a rotor speed of 800 RPM with $\mu > 0.80$. The phenomenon was not caused by a half-per-rev oscillation nor can it be attributed to unstable pitching moments caused by transonic blade tip Mach numbers.

The acquisition of good test data facilitated the evaluation of an existing mathematical model. The theoretical approach is documented in two prior American Helicopter Society Journal papers (References 1 and 2) and summarized in Appendix A. The rotor blade is assumed to be rigid in flapping and elastic in torsion. Hypothetical flapping and torsional restraints are selected to simulate the first flapping and first torsion mode natural frequencies. With the exception of the damping of blade torsion, steady state aerodynamic theory is used. Compressibility and stall effects are ignored. The reversed flow region is totally accounted for and the theory is valid for all advance ratios.

The predicted rotor response generally correlates satisfactorily with the test results. The agreement is particularly good for the tested rotors having the softer of the two flapping flexures. For these configurations most of the blade flap bending occurs close to the center of rotation and the assumed linear mode shape approximates the elastic bending adequately. For the stiffer flexure, bending occurs farther outboard and the correlation deteriorates somewhat. The implication is that the mathematical model may be improved by replacing rigid flapping by the first flap bending elastic mode shape.

The good agreement between theory and test results allows several additional conclusions to be drawn concerning rotor response. An increase in the flapping frequency parameter P reduces both the magnitude of flapping motion and the phase angle of response to an excitation. Likewise, a decrease in the Lock number γ produces a corresponding reduction in the amplitude of response. Finally both theory and test data confirm that high blade torsional stiffness reduces the involvement of torsion in the flapping motion at high advance ratios.

Theoretical rotor stability is calculated by matrix Floquet theory. The results do not disagree with the test data. That is, no indications of an approaching instability were observed or predicted within the tested advance ratio range.

TABLE OF CONTENTS

LIST OF FIGURES

LIST OF FIGURES (CONTINUED)

LIST OF FIGURES (CONTINUED)

LIST OF FIGURES (CONTINUED)

LIST OF FIGURES (CONTINUED)

LIST OF FIGURES (CONTINUED)

LIST OF FIGURES (CONTINUED)

LIST OF FIGURES (CONTINUED)

LIST OF FIGURES (CONTINUED)

SECTION 1

INTRODUCTION

The Lockheed-California Company is currently engaged in a research program with the U.S. Army Aeronautical Research Laboratory (USAARL) to determine the dynamic characteristics of hingeless rotors operating at high advance ratios (Contract NAS 2-5819). The research is applicable for several modes of flight. In recent years compound helicopters have been flown at steadily increasing advance ratios. For example, Lockheed's high speed research compound, XH-51A, has achieved an advance ratio of $\mu \sim 0.70$ at 95% of normal RPM. Slowed and stopped rotor aircraft will also operate at high advance ratios. An analytical study to expand the speed capability of the XH-51A by slowing the rotor is reported in Reference 3. Advance ratios up to $\mu \sim 1.5$ are anticipated at high forward speed-reduced rotor speed flight conditions. Advance ratios from 0 to ∞ would be traversed during normal stopped rotor operation. Lockheed has conducted several test programs to evaluate stopped rotor configurations during the past decade. This research is also continuing under USAARL sponsorship. The current effort involves the testing of a 33 ft diameter stopped rotor model in the 40 x 80 ft NASA Wind Tunnel at Moffett Field, California.

The research program which will be discussed in this report complements the several programs mentioned above. By design the program is comprehensive and is applicable in principle to high speed rotor flight and slowed and stopped rotor vehicles.

The Lockheed/AARL High Advance Ratio Research Program is presently being conducted in two phases. Phase 1, Research Program to Determine Rotor Response Characteristics at High Advance Ratios, involves the fabrication and testing of a small scale rotor model which is controlled by means of a conventional swashplate. The specific objectives of the initial program are to:

- Determine, by experiment, the dynamic characteristics of restrained rotors at high advance ratios
- Evaluate the applicability of a simple mathematical model by comparing the test data with theoretical predictions.

Both stability and steady state rotor response to external and control excitations are of interest. Provisions for changing the blade Lock number (γ) and first flap bending natural frequency ($P\,\Omega$) are supplied so that an array of rotor systems characterized by γ and P can be examined.

The results of the Phase 1 program are discussed in this report. The details of the design, fabrication and testing the model are described. The test data are nondimensionalized and compared with theoretical predictions. The mathematical model is fully described in Appendix A.

The second phase of the program, Theoretical and Experimental Investigation of Rotors with Moment Feedback Controls, is currently being executed. The objectives of Phase 2 are to

- Examine a first order lag moment feedback control system theoretically and determine its practical operating limits
- Conduct wind tunnel tests to collaborate the theory

The mathematical description of blade flapping in Appendix A will be coupled with appropriate control system equations of motion to perform the theoretical analysis. The Phase 1 rotor model will be equipped with an electronic feedback control system and tested at Moffett Field. Tunnel entry is scheduled for March 1971.

SECTION 2

SYMBOLS

a	lift curve slope for normal flow
a'	lift curve slope for reversed flow
a_o	rotor coning angle, rad
a_1	fore-aft rotor tilt, rad
b_1	lateral rotor tilt, rad
c	blade chord, ft
$f\Omega$	blade torsional frequency, sec^{-1}
$\Sigma f(\psi)$	nondimensional forcing functions for blade flapping see eq A14, A15
i_f	polar mass moment of inertia about elastic axis for unit length of blade, $lb\text{-}sec^2$
$\ell_r(\psi)$	nondimensional lift of reversed flow region, see eq A28, A29 and Table 8 $\ell_r(\psi) = \dfrac{\text{lift}}{R^3\Omega^2\frac{\rho}{2}a'c}$
$m(\psi)$	nondimensional aerodynamic flapping moment, $m(\psi) = \dfrac{\text{flapping moment}}{R^4\Omega^2\frac{\rho ac}{2}}$
x	distance of rotor blade element from center of rotation, $x = r/R$
B	tip loss factor, assumed to be 0.97
$\frac{C_T}{\sigma}$	blade loading coefficient; $\frac{C_T}{\sigma} = \dfrac{\text{rotor lift}}{\pi R^2\rho(\Omega R)^2\sigma}$

$C(\psi)$ nondimensional damping coefficient for flapping, see eq A15

$C_\delta(\psi)$ nondimensional aerodynamic damping of blade torsion, see eq A23

$C_\theta(\psi)$ nondimensional aerodynamic damping of blade feathering (excluding torsion)

F nondimensional quantity characterizing the aerodynamic damping of the blade torsional degree of freedom, see eq A33

I_1 flapping mass moment of inertia of one blade about the rotor center, lb-ft-sec^2

I_f feathering mass moment of inertia of blade, lb-ft-sec^2

K_β blade flapping stiffness, ft-lb/rad

$K_\delta(\psi)$ nondimensional aerodynamic spring effect of blade torsion, see eq A26

K_θ rotor stiffness, $K_\theta = 2\ K_\beta$, ft-lb/rad

$K(\psi)$ nondimensional aerodynamic spring effect for flapping, see eq A15

L_R(r in.) rotor rolling moment at blade station r, in.-lb

M_R(r in.) rotor pitching moment at blade station r, in.-lb

M_{β_o}(r in.) steady rotating blade flapping moment at blade station r, in.-lb

$P\Omega$ blade flapping frequency, sec^{-1}

Q nondimensional quantity describing the excitation of blade torsion by the lift of the reversed flow region, see eq A34

R rotor radius, ft

U_P, U_T nondimensional components of relative velocity at blade element, see eq A4, A5

$\{X\}$ matrix of state variables $X_1 = \beta$, $X_2 = \frac{d\beta}{d\psi}$

α rotor shaft angle of attack, rad

β flapping angle $\beta = a_o - a_1 \cos \psi - b_1 \sin \psi$, rad

γ blade Lock number, $\gamma = \frac{R^4 \rho a c}{I_1}$

δ torsional deflection of blade tip, rad

ε angle defining mixed flow region of blade, rad (see Figure 66) and eq A1

θ pitch setting of a blade element without consideration of torsion, rad,

$$\theta = \theta_o + x\,\theta_t + \theta_s \sin \psi + \theta_c \cos \psi$$

θ_o collective pitch, rad

θ_t built-in blade twist, rad

θ_c lateral cyclic pitch control input, rad

θ_s longitudinal cyclic pitch control input, rad

$\Delta\theta$ pitch change due to blade torsion, rad, $\Delta\theta = \phi\delta$

κc distance between elastic axis and center of pressure in reversed flow, ft, $\kappa \sim 0.5$

λ inflow ratio

λ_ϕ eigenvalues of the state transition matrix

μ advance ratio

ρ density of air, slugs/ft^3

σ rotor solidity

ϕ normalized mode shape for torsion

$\underline{\phi}$ state transition matrix

ψ blade azimuth angle, rad

Ω rotor angular velocity, sec^{-1}

GENERAL COMMENTS:

- The flow regions 1, 2, 3 identify normal, mixed and reversed flow, respectively. The mixed flow region 2 is further broken down into 2_n and 2_r where the subscripts refer to normal and reversed flow.
- Barred quantities refer to the virtual work done for the mode shape ϕ investigated.

SECTION 3

DESIGN AND FABRICATION

DESCRIPTION OF MODEL

The Lockheed/AARL High Advance Ratio Rotor System is a four-bladed, 7 1/2-ft-diameter model designed for testing in the U.S. Army Aeronautical Research Laboratory's 7 x 10 ft wind tunnel at Moffett Field, California. The rotor is driven by two 37 horsepower variable frequency induction motors. Rotor control is direct with cyclic and collective pitch applied by means of a conventional swashplate which is positioned by electrically controlled hydraulic actuators.

The rotor blades are of aluminum skin, aluminum honeycomb construction with one spar located at the 25% chord position. The center of gravity is maintained at the quarter-chord by means of a spanwise ballast weight affixed to the inside of the leading edge skin. The blades are an untwisted, NACA 0012 airfoil section and have a 4 1/2 inch chord. They are attached to the rotor hub through the use of "flexible flapping restraints" (flexures) at a zero precone angle. Two sets of flexures (soft and stiff) are furnished to allow a variation of the rotor blade nonrotating flapping frequency. The blade Lock number may also be changed by adding a tip weight. A nominal value of $\gamma = 5.0$ is calculated assuming a lift curve slope of 2π. One set of tip weights is furnished which reduces γ to 3.0. Consequently, four basic rotor configurations are available for testing, which will be referred to in this report as configurations 1, 2, 3 and 4. They are defined as:

- Configuration 1 - soft flexure without tip weight ($\gamma = 5.0$)
- Configuration 2 - soft flexure with tip weight ($\gamma = 3.0$)
- Configuration 3 - stiff flexure without tip weight ($\gamma = 5.0$)
- Configuration 4 - stiff flexure with tip weight ($\gamma = 3.0$)

DESIGN CONCEPT

The Lockheed/AARL High Advance Ratio Rotor Model was designed to be consistent with the fundamental objectives of the program; to experimentally determine the basic dynamic characteristics of restrained rotors at high advance ratios and to compare the test results with a documented theory. A simple rotor blade design was selected to best fulfill these objectives. The rotor diameter of 7 1/2 ft was dictated by the 10 ft width of the AARL wind tunnel. A blade aspect ratio of 10 was chosen as representative resulting in a four-bladed rotor solidity of 0.127. A NACA 0012 airfoil section was selected for the constant chord blade. Refinements such as twist, camber and taper which would have improved rotor lifting performance were not considered. Since moderate lift levels were anticipated the need for blade precone to relieve steady blade stresses did not exist. Rotor precone generates appreciable cyclic moments at high advance ratios which would complicate the operation of the rotor as well as the reduction of the data.

The formulation of the program required that the characteristics of several restrained rotors be examined. For the purposes of this study, a rotor configuration is described by its Lock number (γ), its first flapping mode frequency ($P\Omega$). Lock number is the ratio of aerodynamic forces and inertia forces and a change is effected by changing the flapping inertia of the blade. This is conventionally accomplished by adding weight at the tip of the blade. The flapping frequency parameter P may be changed in two ways; by changing rotor rotational speed, Ω , and by changing the flapping frequency of the nonrotating blade. The latter was achieved by varying the flexibility of a flapping restraint located between the actual blade and the hub.

Because of the nature of the aerodynamic forces acting on a rotor blade as it passes through the region of reversed airflow, a requirement that the blade be very stiff torsionally developed. This constraint tends to minimize the involvement of torsion in the flapping response of the rotor. Such involvement not only affects the steady state flapping response of the rotor to various excitations but also increases the possibility of high frequency blade flutter.

FABRICATION

In order to achieve the highest possible Lock number (i.e. minimum rotor blade flapping moment of inertia), the blade outboard of the flexure was constructed almost entirely of aluminum. The exception is the spanwise brass balance weight required to locate the section cg at the quarter-chord. Torsional stiffness was provided by a single main spar located at the quarter-chord and an aluminum honeycomb core construction. Spanwise aluminum doublers provided flapping strength. The NACA 0012 airfoil section is modified at the trailing edge to accommodate a flat bonding strip between the upper and lower skins for additional structural strength. The cross-section of the blade at a typical radial position is sketched below:

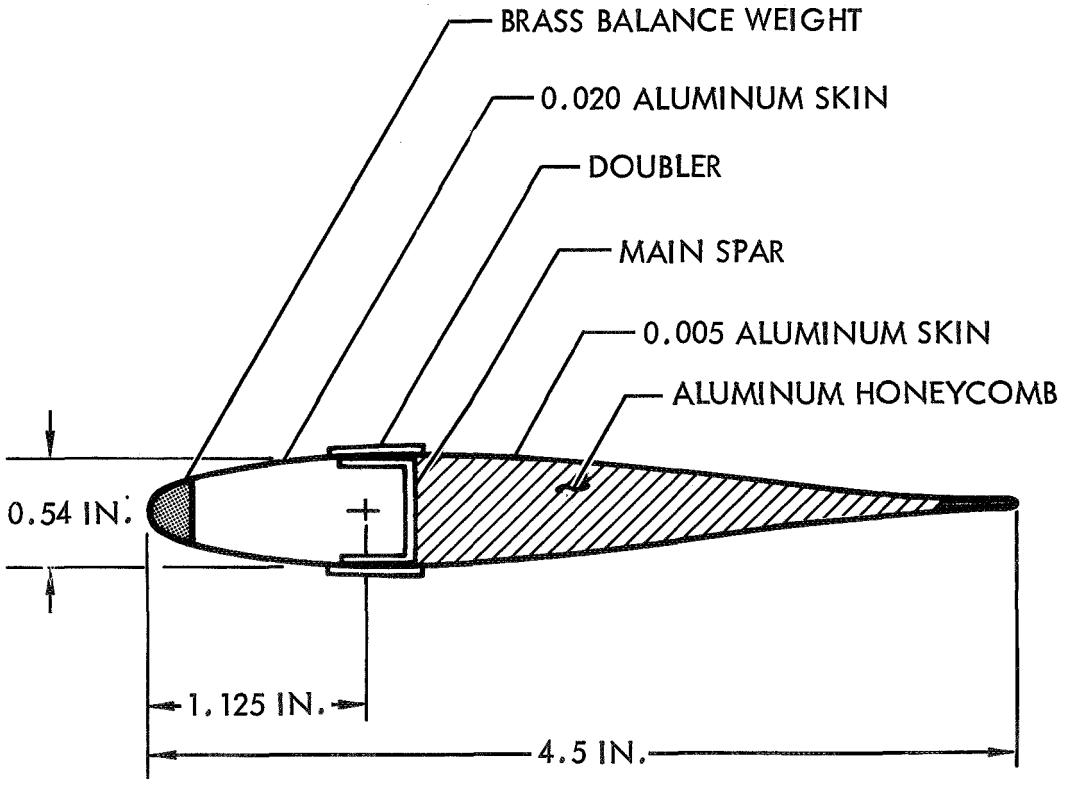

Two sets of flapping restraints (flexures) were fabricated which provided a maximum variation in the nonrotating blade first mode flapping frequency consistent with the anticipated loading spectrum. The flexures are made of titanium and form the attachment between the blades and the steel rotor hub. Centrifugal forces are resisted by a ball thrust bearing which also acts as the feathering bearing. The bearing housing and pitch horn are aluminum.

One set of tip weights were machined from titanium which reduce the blade Lock number from a nominal value of 5.0 to 3.0. The pitch links through which control inputs are transferred to the rotor are equipped with teflon bearings at both ends to minimize control system deadband (slop). Figure 1 is a photograph of the various components which constitute the rotor.

A description of the rotor blade in terms of its radially distributed mass and stiffness properties is presented in the next three figures. The weight distribution is plotted as a function of radial position (measured from the center of rotation) in Figure 2. The variations in the distribution due to tip weight and flexure are noted on the curve. Also plotted in the same figure are the locations of the shear center, neutral axis and mass centroid relative to the feathering axis (25% chord). The blade flapping, inplane and torsional stiffness distributions are plotted in Figures 3 and 4. The effect of the two flexures is noted on the flapping and inplane curves. The flexure has no effect on torsional stiffness because it is located inboard of the feathering bearing. It is clear that the tip weight cannot influence stiffness.

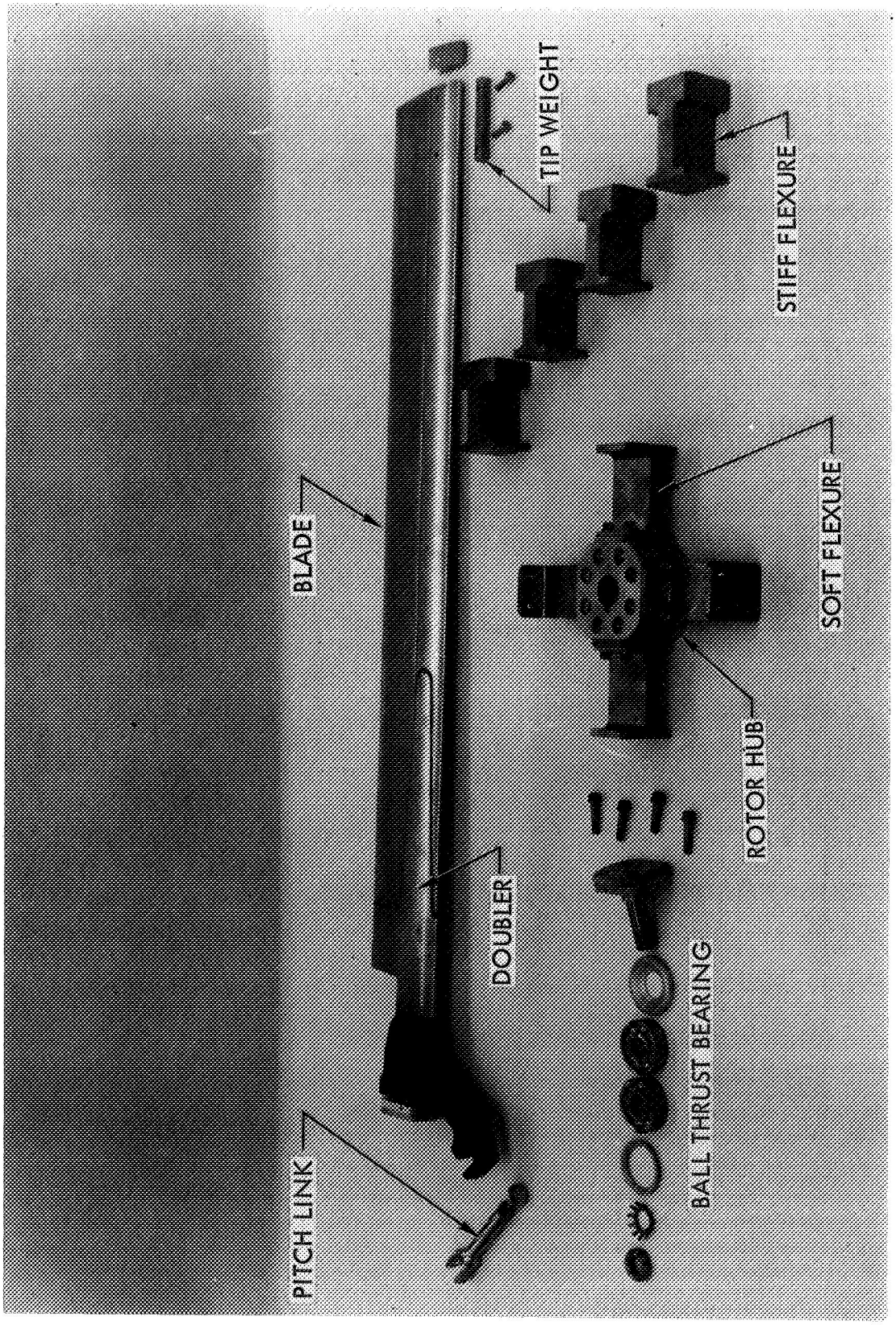

Figure 1. Model Rotor Components

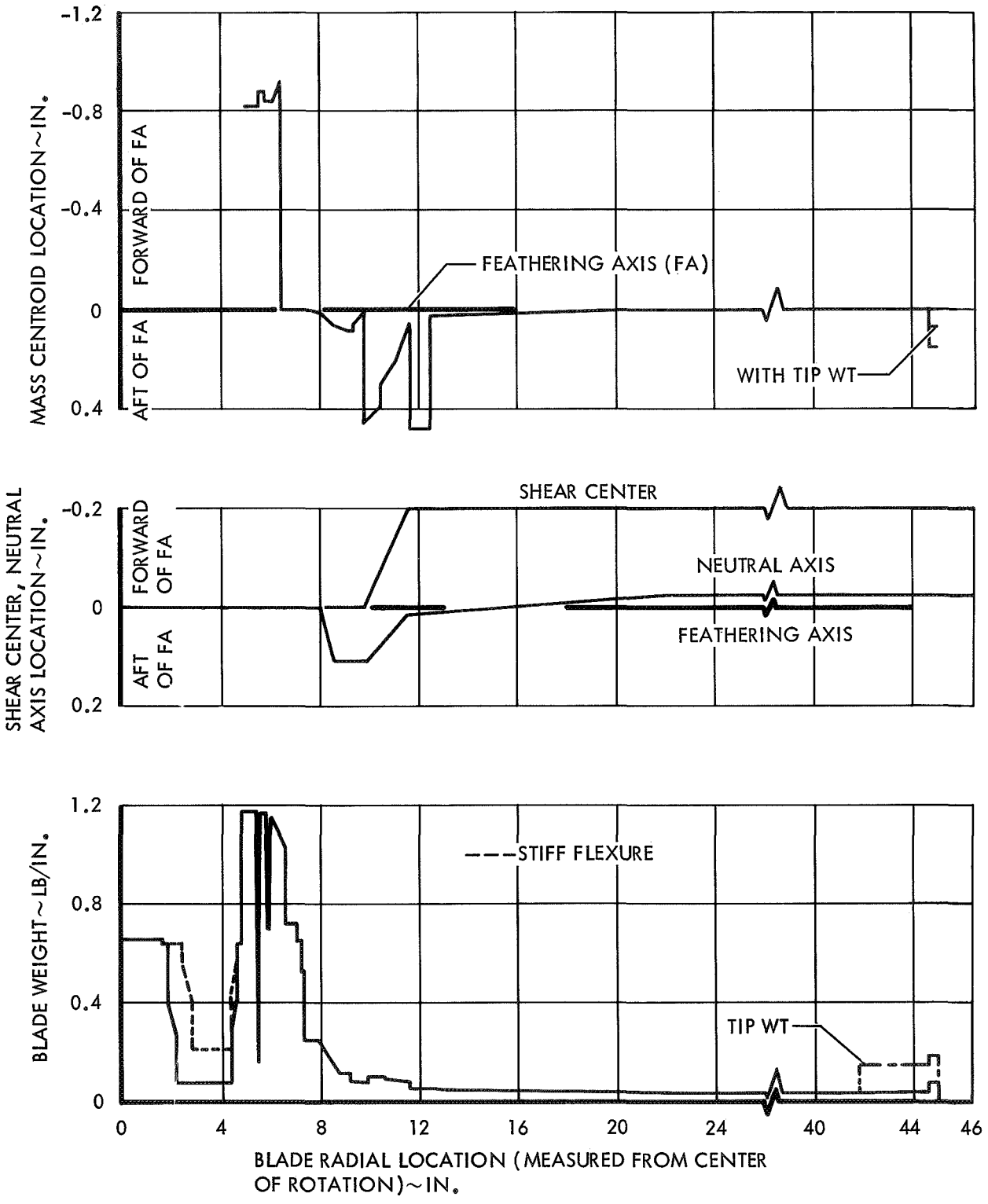

Figure 2. Rotor Blade Mass Characteristics

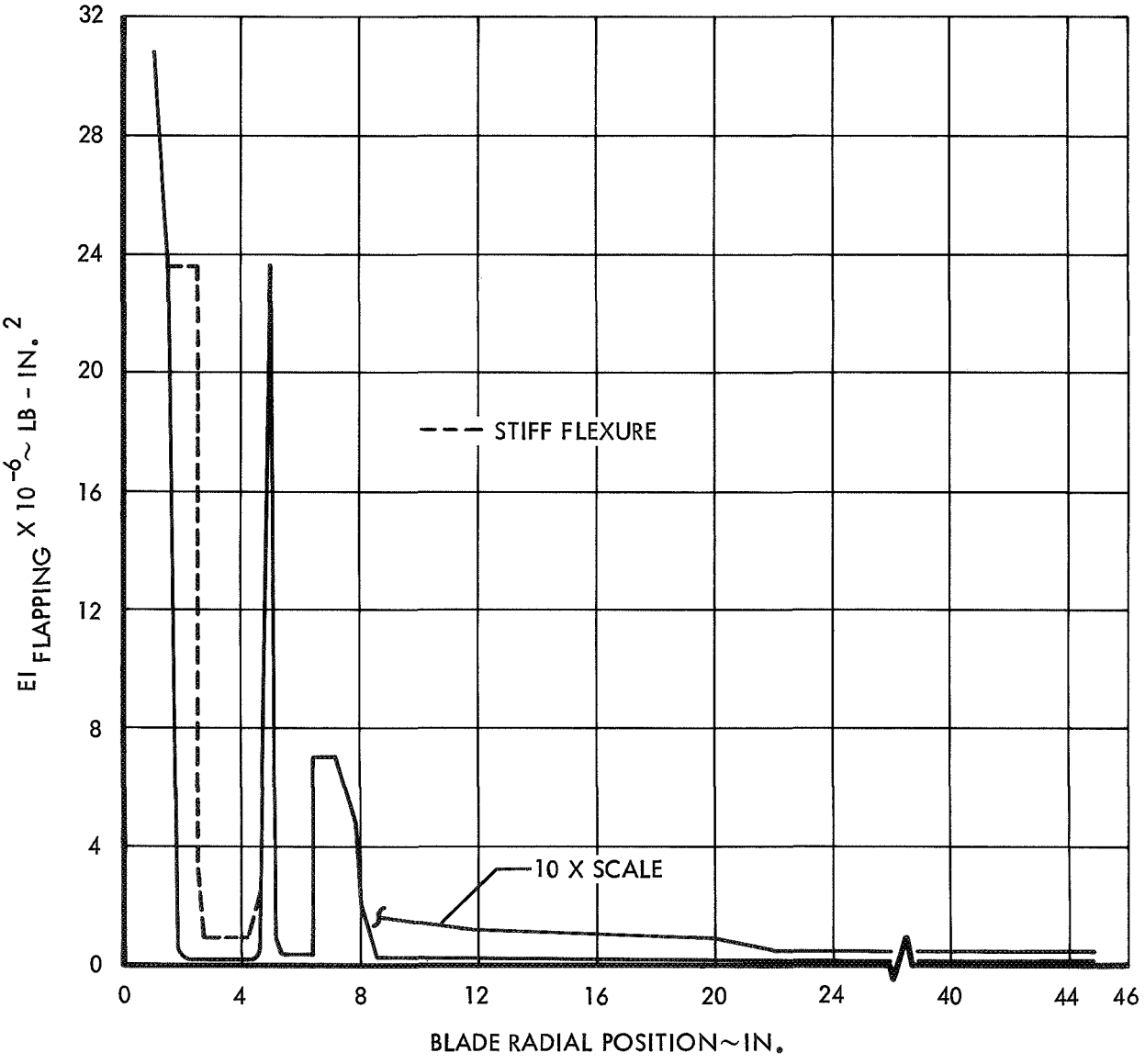

Figure 3. Rotor Blade Flapping Stiffness

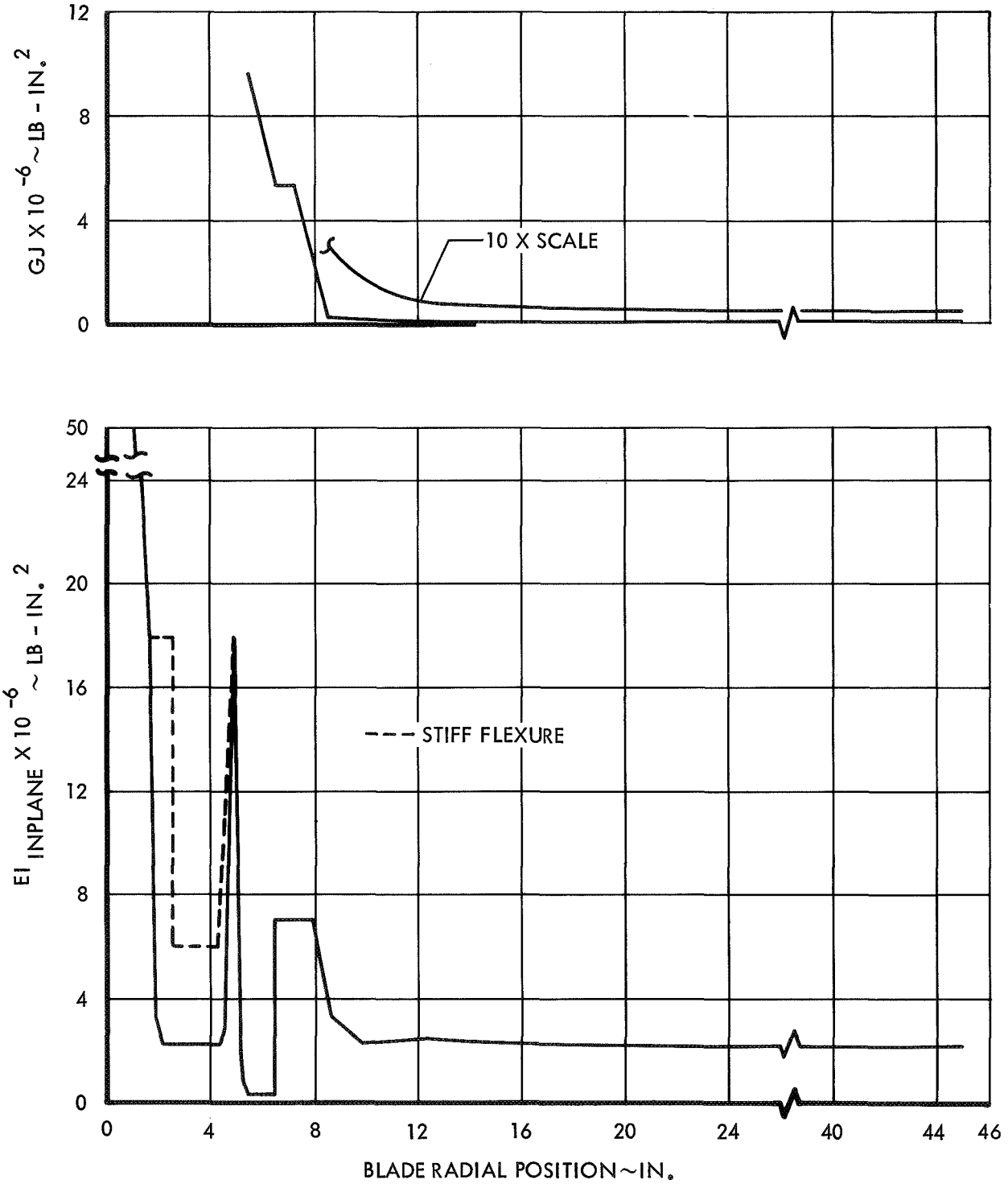

Figure 4. Blade Inplane and Torsional Stiffness

SECTION 4

INSTRUMENTATION AND DATA ACQUISITION

INSTRUMENTATION

The instrumentation was an integral part of the model. The various devices can be conveniently categorized according to their location in the rotating or nonrotating systems. The rotating instrumentation consisted of blade bending strain gages, a tension-compression pitch link gage and a linear position potentiometer which measured instantaneous blade angle. The signals from the gages and the pot were transferred to the stationary coordinate system by means of a slipring assembly which also served to supply power to the gages. The strain gages on the blades served a two-fold purpose. First, they were the means by which dynamic rotor data were sensed to be recorded on an analog tape. Second, their outputs were displayed on oscilloscopes which were continuously monitored to insure that critical blade stresses were not exceeded.

The rotor mounted instrumentation consisted specifically of three flap bending strain gages bridges, two chord bending bridges, one torsion bridge and a feathering position potentiometer on one blade. The pitch link of the same blade was equipped with the tension-compression gage.

The rotor was also equipped with a system of four strain gage bridges and a sine-cosine potentiometer for the purpose of resolving rotating blade moments into stationary rotor pitching and rolling moments. (These moments will constitute the feedback to the electrical control system in the next phase of the program.) They were visually displayed during the test and were the principal indicator of rotor trim. The bridges are located at the same radial position on each of the four blades. The difference between the moments of opposite blades are formed electrically and passed through the sine-cosine pot. The pot is attached to the rotor shaft and continuously generates the sine and cosine of the rotor azimuth position, ψ. The

rotor pitching and rolling moments (in stationary coordinates) are formed by properly combining the rotating blade moments after they have been multiplied by sin ψ and cos ψ,. i.e.,

$$\text{Rotor pitching moment} = (M_{\beta_3} - M_{\beta_1})\cos\psi + (M_{\beta_2} - M_{\beta_4})\sin\psi \quad (1)$$

$$\text{Rotor rolling moment} = (M_{\beta_3} - M_{\beta_1})\sin\psi + (M_{\beta_4} - M_{\beta_2})\cos\psi \quad (2)$$

M_{β_1} through M_{β_4} represent the rotating blade moments of blades 1 through 4.

Linear position potentiometers which indicate the travel of the collective and cyclic pitch actuators are located in the nonrotating coordinate system. They were used to measure the applied control inputs (θ_o, θ_s, θ_c). A magnetic pickup which was triggered at the zero rotor azimuth position provided a measure of the rotor speed. A six-component strain gage balance was an integral part of the model support strut and measured body moments and forces.

Other instrumentation included a pitot-static tube and a temperature probe which were used to measure the tunnel speed. The model was mounted directly on the wind tunnel scales which remained operative during the test as a backup for the strain gage balance measurements.

DATA ACQUISITION

Data were recorded with three devices:

- AARL DATEX System
- Honeywell Medium Band Magnetic Tape System
- Honeywell Visicorder

The DATEX is a data sampling system composed of analog to digital converters having a 1 to 2 cps bandwidth. During the test it was used only to record steady data such as actuator positions and body and rotor moments and forces. The Honeywell Magnetic Tape System was used as an analog tape recorder. High frequency data such as rotating blade bending moments were recorded on the tape. The Honeywell Visicorder is an oscillograph which records time history data on photo-sensitive paper. It was used to record all steady and dynamic data which would indicate the proper and safe operation of the model. Table 1

summarizes all of the model instrumentation, the datum measured by each and the equipment used to record each datum. Also included are the radial locations of the blade bending strain gages, measured in inches from the center of rotation.

TABLE 1

SUMMARY OF INSTRUMENTATION AND DATA ACQUISITION

Instrumentation	Datum	Data Acquisition Equipment**
Flap Bending Strain Gage at Sta 22.3	Flap Bending Moment at Sta 22.3	T, V
Flap Bending Strain Gage at Sta 13.15	Flap Bending Moment at Sta 13.15	T, V
Flap Bending Strain Gage at Sta 2.3(3.0*)	Flap Bending Moment at Sta 2.3(3.0*)	T, V
4 Flap Bending Strain Gages at Sta 3.3(3.9*)	Rotor Pitching and Rolling Moments at Sta 3.3(3.9*)	T, V, D
Chord Bending Strain Gage at Sta 13.15	Chord Bending Moment at Sta 13.15	T, V
Chord Bending Strain Gage at Sta 2.3(3.0*)	Chord Bending Moment at Sta 2.3(3.0*)	T, V
Torsion Gage at Sta 9.28	Blade Torsion Moment at Sta 9.28	T, V
Pitch Link Tension/Compression Strain Gage	Pitch Link Tension Compression Load	T, V
Blade Feathering Position Potentiometer	Instantaneous Pitch Angle of Blade No. 1	T, V
Body Mounted Strain Gage Balance	Body Moments and Forces	D, T(Lift)
Longitudinal Cyclic Pitch Actuator Position Potentiometer	Applied Longitudinal Cyclic Pitch (θ_s)	V, D
Lateral Cyclic Pitch Actuator Position Potentiometer	Applied Lateral Cyclic Pitch (θ_c)	V, D
Collective Pitch Actuator Position Potentiometer	Applied Collective Pitch (θ_o)	V, D
One-per-Rev Magnetic Pickup	Rotor Rotational Speed	T, V, D
Wind Tunnel Balance	Body Moments and Forces	D
Wind Tunnel Pitot Static Probe	Tunnel Dynamic Pressure	D
Wind Tunnel Temperature Probe	Tunnel Temperature	D

* Stiff flexure

** T = analog tape; V = Visicorder; D = Datex

SECTION 5

CHECKOUT AND WHIRL

Prior to the shipment of the model to Moffett Field, static and functional whirl tests were conducted at Lockheed. The objectives of these tests were to experimentally verify the analytical description of the rotor system and to insure that the model and instrumentation were totally operational. The activities included:

- Control system stiffness test
- Rotor blade inertia test
- Nonrotating and rotating rotor blade natural frequency tests
- Whirl tests

STATIC TESTS

Control System Stiffness

The stiffness of the control system is important in high advance ratio testing because increased feathering moments are generated as a rotor blade passes through the reversed flow region. If the control system stiffness is not sufficiently high, the possibility of a first mode flapping-feathering instability exists. Collective and cyclic control system stiffnesses, respectively, of K_{coll} = 1100 in.-lb/deg/blade and K_{cyclic} = 123 in.-lb/deg/blade were determined by static loading. K_{coll} is very high and can be ignored compared to the K_{cyclic}. In terms of frequency, 123 in.-lb/deg represents an undamped natural feathering frequency of 5.2 Ω at a rotor speed of 1500 RPM, i.e.,

$$\omega_{feathering} \sim \sqrt{\frac{K_{cyclic}}{I_o \Omega^2} + 1} \qquad (3)$$

where I_o is the effective feather inertia of one rotor blade.

A simplified flapping-feathering stability analysis was conducted which incorporated the experimental control system stiffness. Rigid flapping and feathering each restrained by a hypothetical spring constituted the mathematical

model. The aerodynamic environment was the same as that described in Appendix A. Matrix Floquet Theory was used to determine stability. The results of the analysis indicated that a first mode flapping-feathering instability could not occur within the anticipated rotor speed and advance ratio ranges.

Rotor Blade Inertia

The flapping inertia of a rotor blade (without tip weight) was determined experimentally by suspending it as a torsional pendulum and measuring its period of oscillation. An inertia of 455 lb-in.^{2} was measured about the blade cg which converts to 1035 lb-in.^{2} about the center of rotation. This compares favorably with the analytical value of 1020 lb-in.^{2}.

Rotor Blade Natural Frequencies

Nonrotating rotor blade natural frequencies were determined experimentally by a shake test of the cantilevered blade isolated from the model. Accoustic and mechanical shakers were used over a frequency range of 0 to 200 cps. The frequencies of three flap bending modes, one chord bending mode and one torsion mode were measured. They are compared with frequencies calculated using a classical mass and stiffness distribution analysis in Figures 5 and 6. Some experimental rotating blade natural frequencies are also spotted on the curves. They were indicated during the whirl tests by increased flapping and chord motion at rotor rotational frequencies which were in resonance with the blade frequencies. With the exception of the first inplane frequency, the analytical and experimental results agree to within approximately 8%. The predicted first flapping mode frequency agrees extremely well with the test data with the deviation less than 2%.

WHIRL TESTS

The rotor was tracked and balanced at the beginning of the functional whirl tests. Rotor track was easily obtained by simply adjusting the nominal pitch settings of the four blades. The blades were manufactured to very high tolerances making balancing almost unnecessary. Two and four grams of weight were required at the tips of two blades to balance the rotor.

Additional whirls tests were conducted to fully check out the model. All instrumentation was activated (except the strain gage balance) and recorded on an oscillograph. All four rotor configurations were tested at

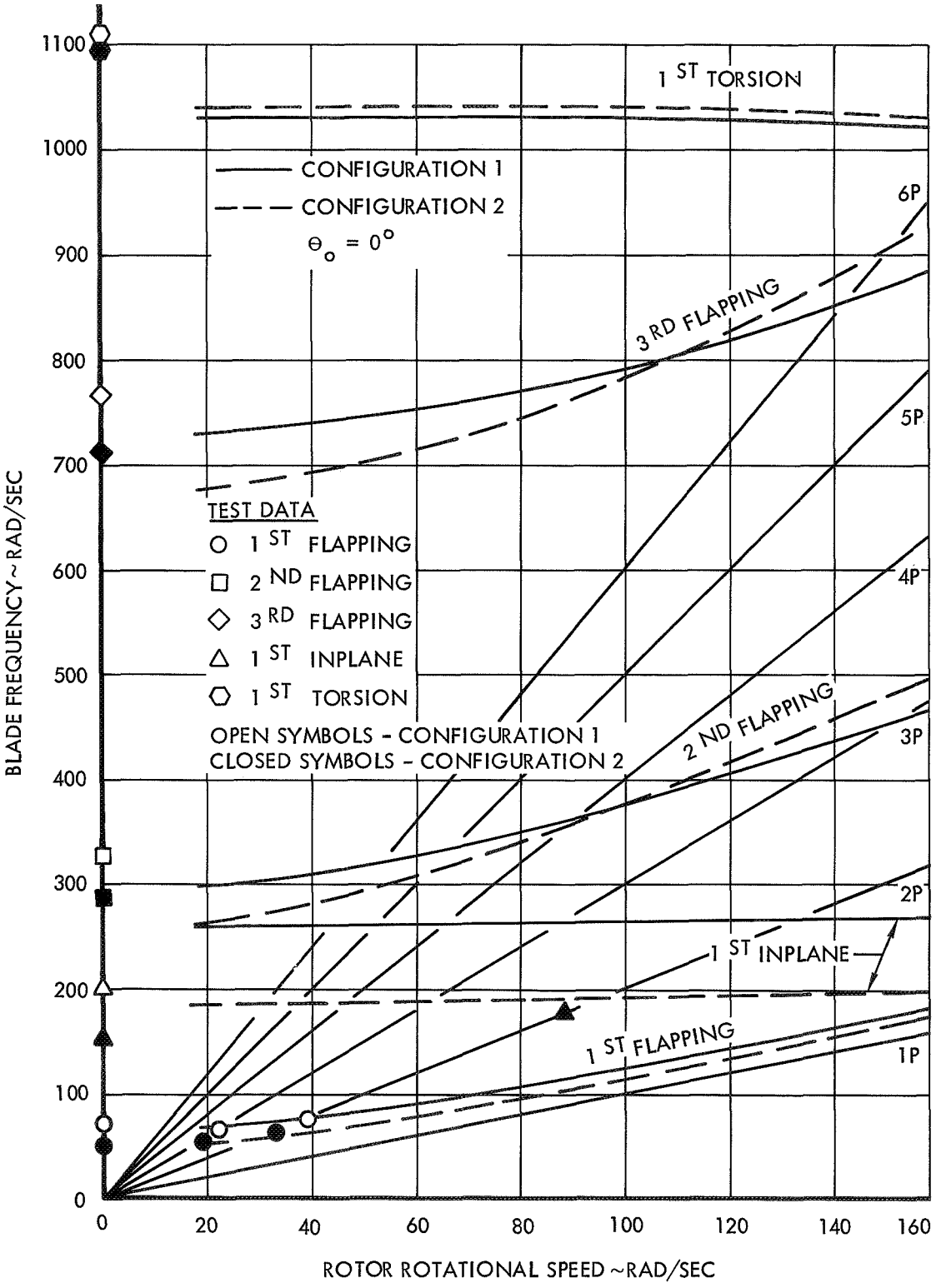

Figure 5. Coupled Blade Natural Frequencies, Configurations 1 and 2

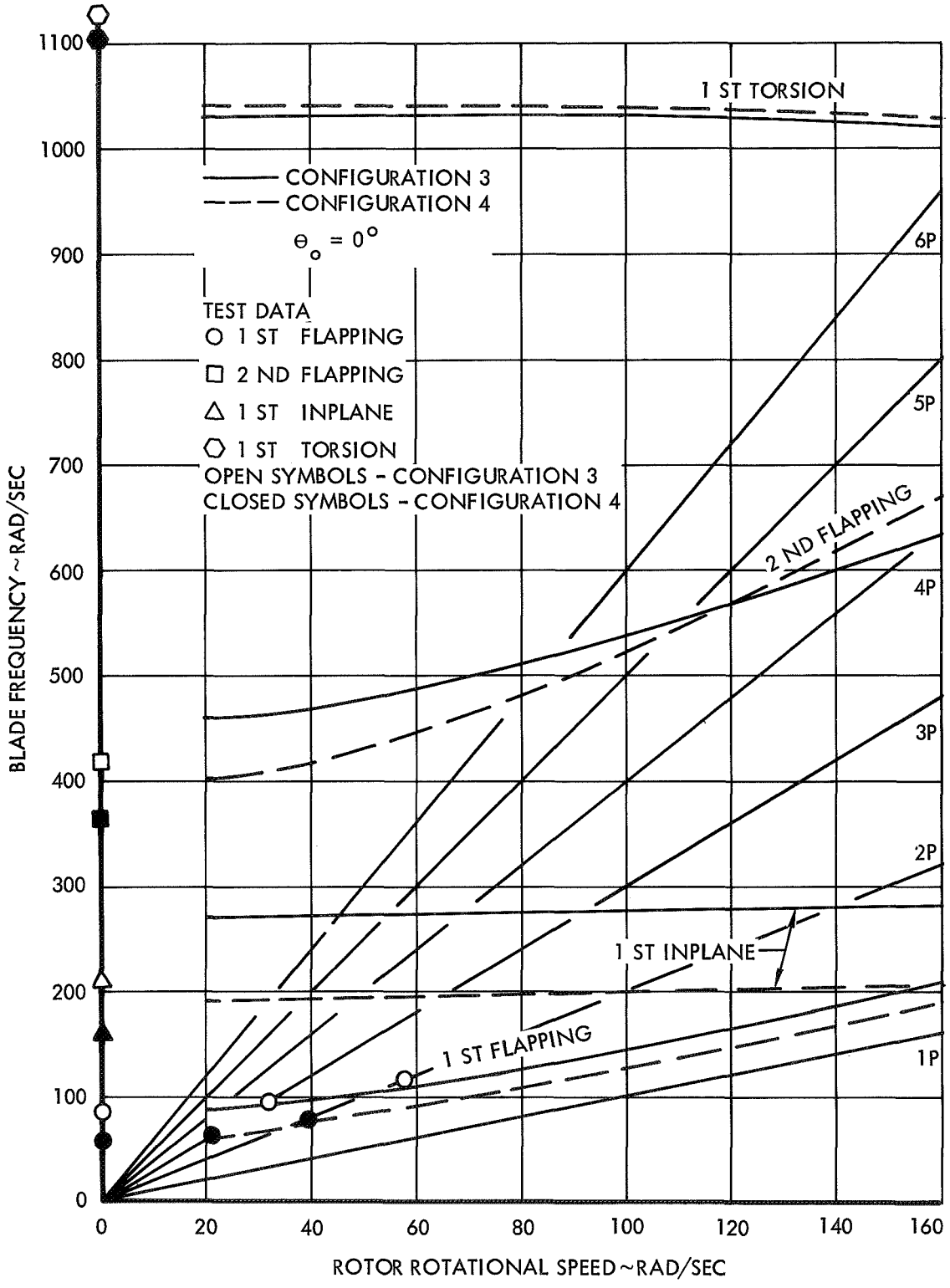

Figure 6. Coupled Blade Natural Frequencies, Configurations 3 and 4

various rotor speeds up to 1000 RPM. Collective and cyclic blade angles in excess of the planned wind tunnel test values were applied to the rotor. Model support stand natural frequencies and blade natural frequencies were noted. Generally the functional performance of the system was found to be excellent.

Following the successful completion of the whirl tests at Lockheed, the model was shipped to the USAARL at Moffett Field. Several weeks of additional model preparation were conducted there, including the checkout of the complete data acquisition system and hover tests.

Discussion of Hover Test Data

Hover tests were conducted as a part of model checkout in the AARL model preparation area. The tests served as the final checkout of the model, its instrumentation and the data acquisition equipment prior to wind tunnel installation. The scope of the testing was limited to the experimental determination of rotor lift and moment derivatives with respect to collective and cyclic pitch. For each of the four basic rotor configurations, modest ranges of collective pitch (θ_o) and longitudinal cyclic pitch (θ_s) were applied to the rotor while maintaining a constant rotor speed. Three tip speeds were tested.

The results of the collective pitch perturbations are shown in Figures 7 and 8. Rotor lift is represented by a nondimensional blade loading coefficient, C_T/σ. The derivative $\partial C_T/\sigma/\partial\theta_o$ is approximately the same for all four configurations. This is to be expected since the blade and disc areas are identical for the four rotors. The nonlinear characteristic of the curves at low collective pitch values is due to a pronounced reduction in the effective blade angle of attack caused by induced downwash. At higher blade angles this effect is stabilized. It is noted that no rotor moments were detected during the collective pitch excursions confirming that cyclic and collective pitch were not mechanically coupled.

The slight scatter which is evident in the lift data can be attributed to the single sampling characteristic of the data acquisition equipment used

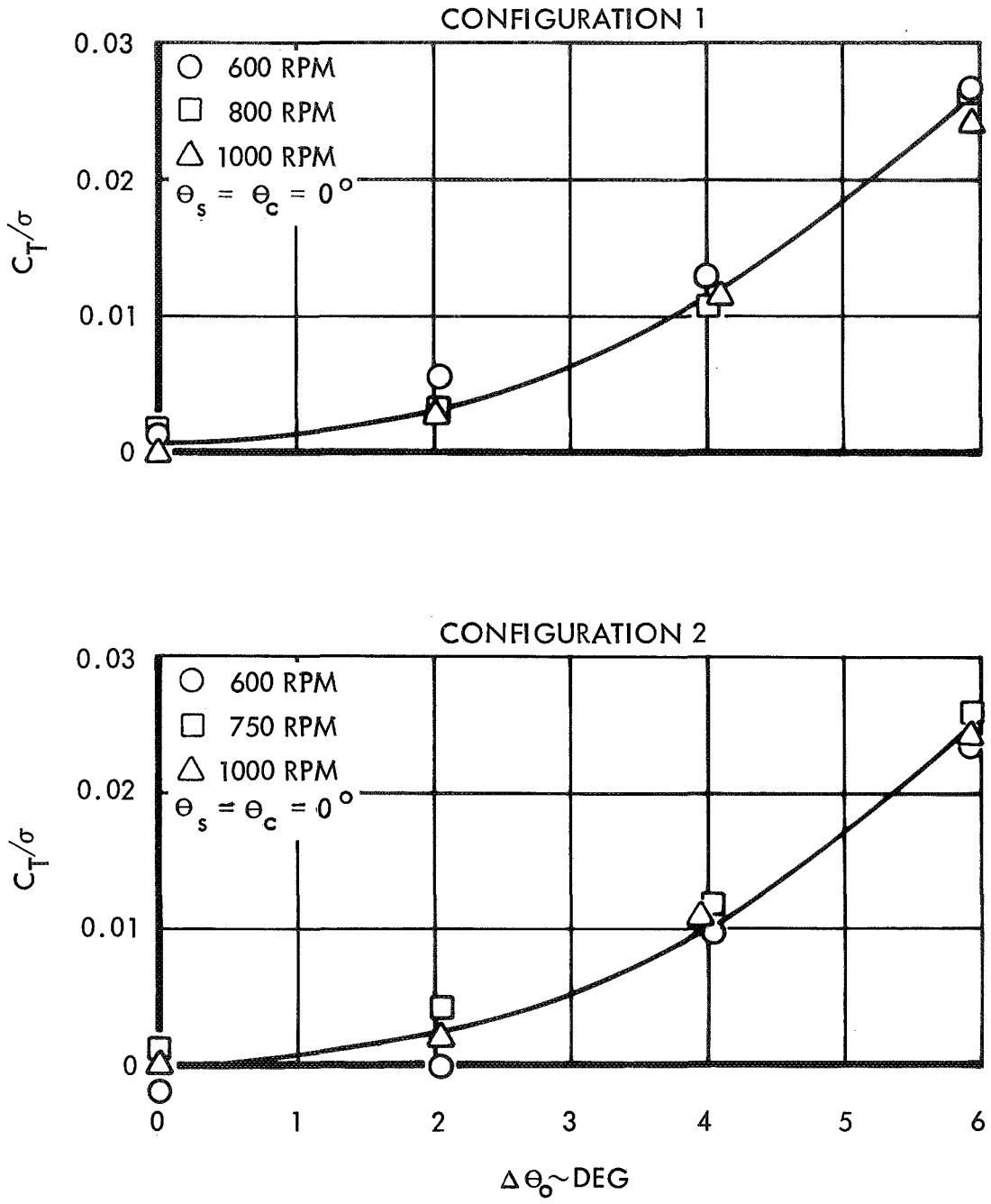

Figure 7. Rotor Lift in Hover, Configurations 1 and 2

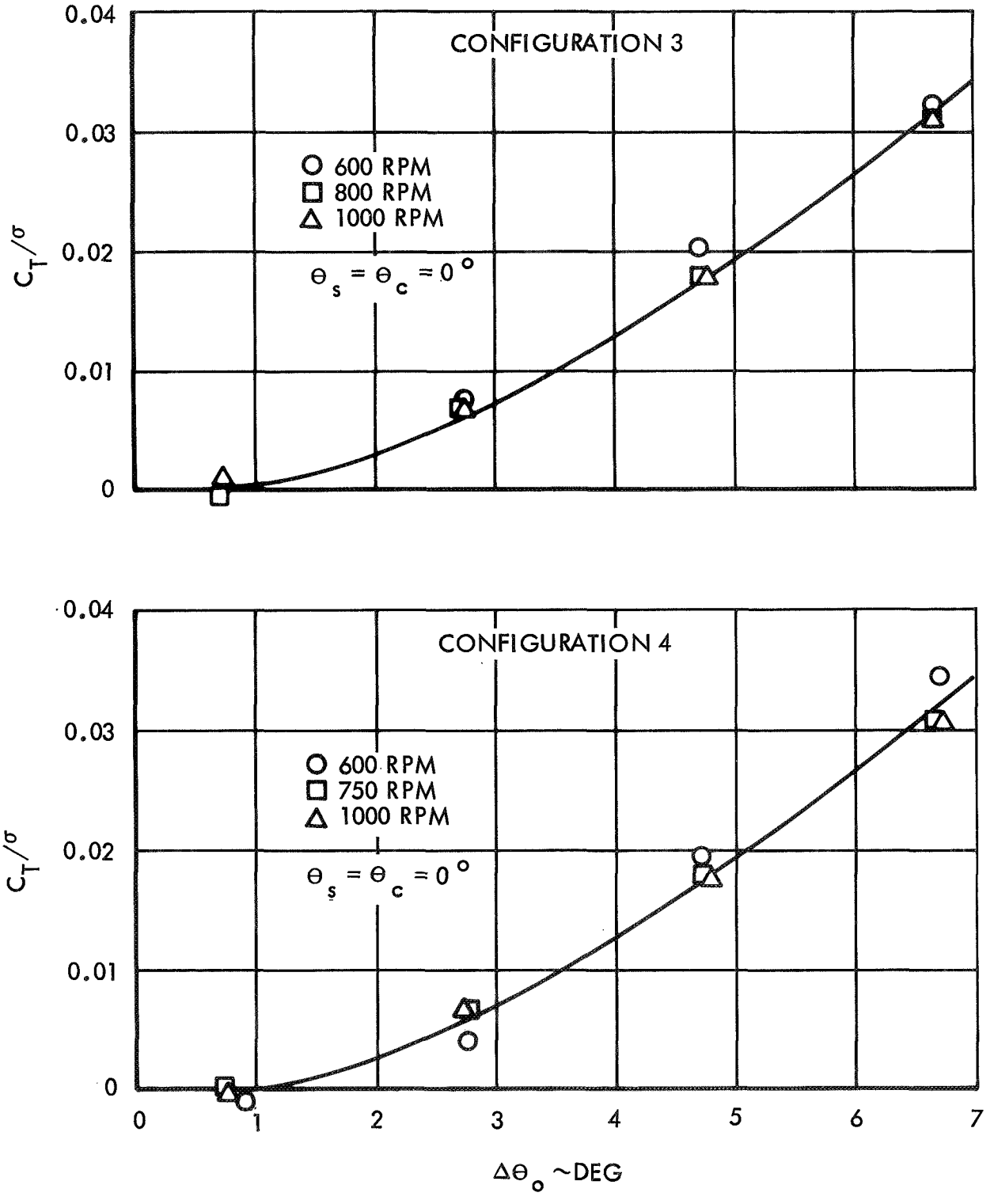

Figure 8. Rotor Lift in Hover, Configurations 3 and 4

to record steady data during the hover tests. The data are recorded at one instant in time and errors could be introduced if a datum is not constant with time. In the case of rotor lift, vibration is seen as time varying lift. The maximum error (scatter) which is possible, depends upon the level of vibration. The condition is shown graphically below.

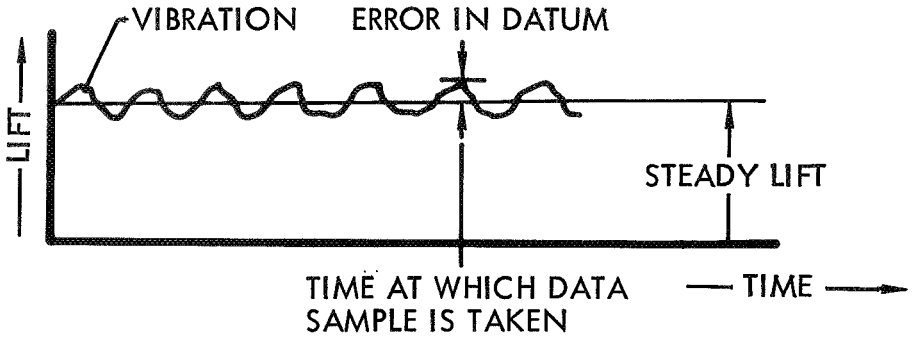

Obviously, the magnitude of the error is left totally to change. Such data acquisition errors were minimized during the wind tunnel tests by averaging 10 data samples at each test point.

The rotor pitching and rolling moments resulting from the application of longitudinal cyclic pitch (θ_s) are shown in Figures 9 through 12. It is clear that no additional information would be obtained by exciting the system with lateral cyclic pitch also. Measurements were recorded at three rotational speeds for each basic rotor configuration. The values of the nondimensional flapping frequency P associated with each rotor speed are indicated on the figures. They were deduced from Figures 5 and 6 and are tabulated in the next Section of this report. The moments have been resolved from rotating to stationary coordinates through the strain gage/sine-cosine pot arrangement described in Section 4. Consequently they are not values at the rotor shaft. Rather they are moments at the radial position of the strain gage bridges on the blades. The rotor blade bending moment distributions required to ascertain shaft moments based upon radially offset values will be presented in Section 7.

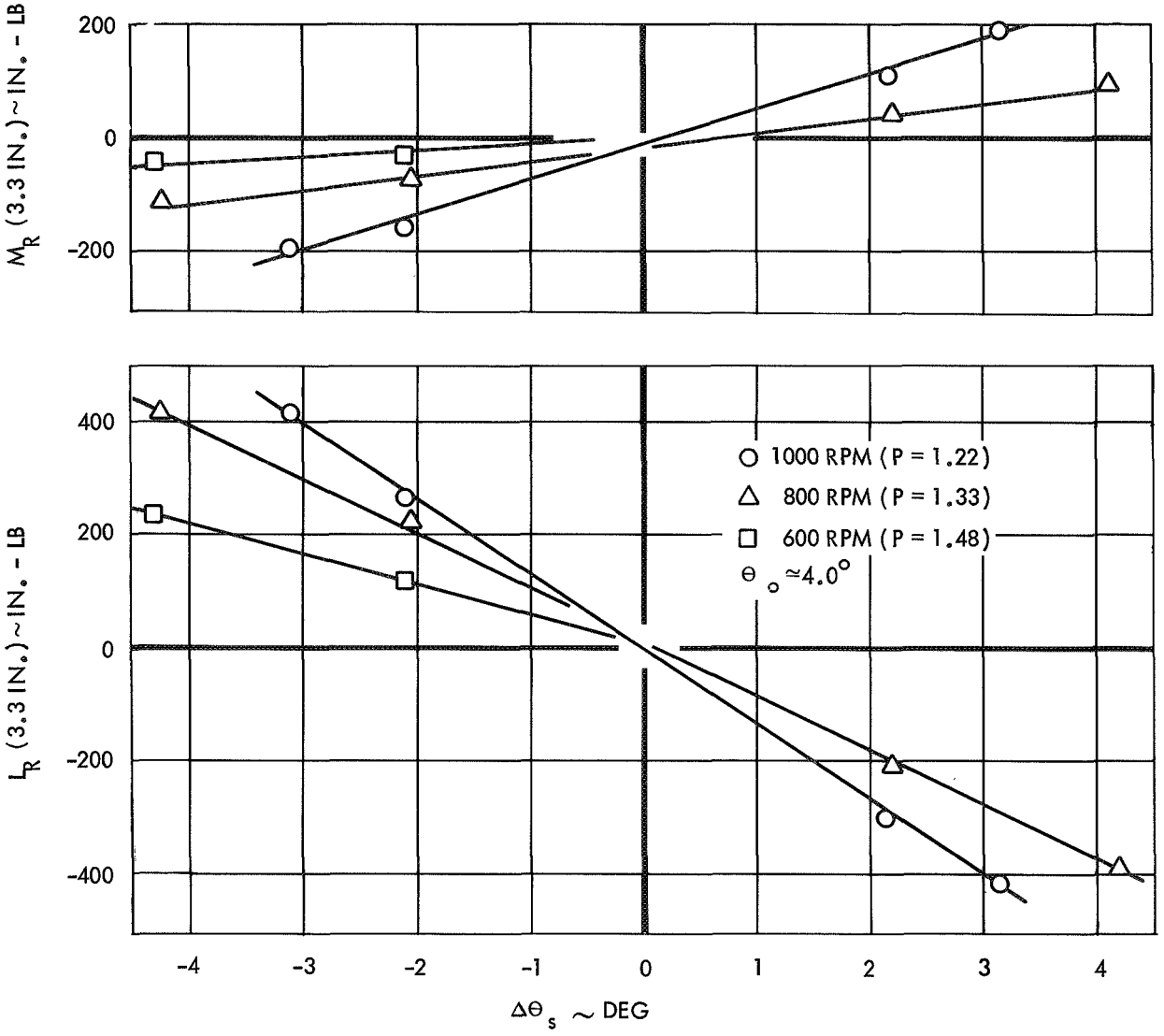

Figure 9. Rotor Pitch and Roll Response to Longitudinal Cyclic Pitch in Hover, Configuration 1

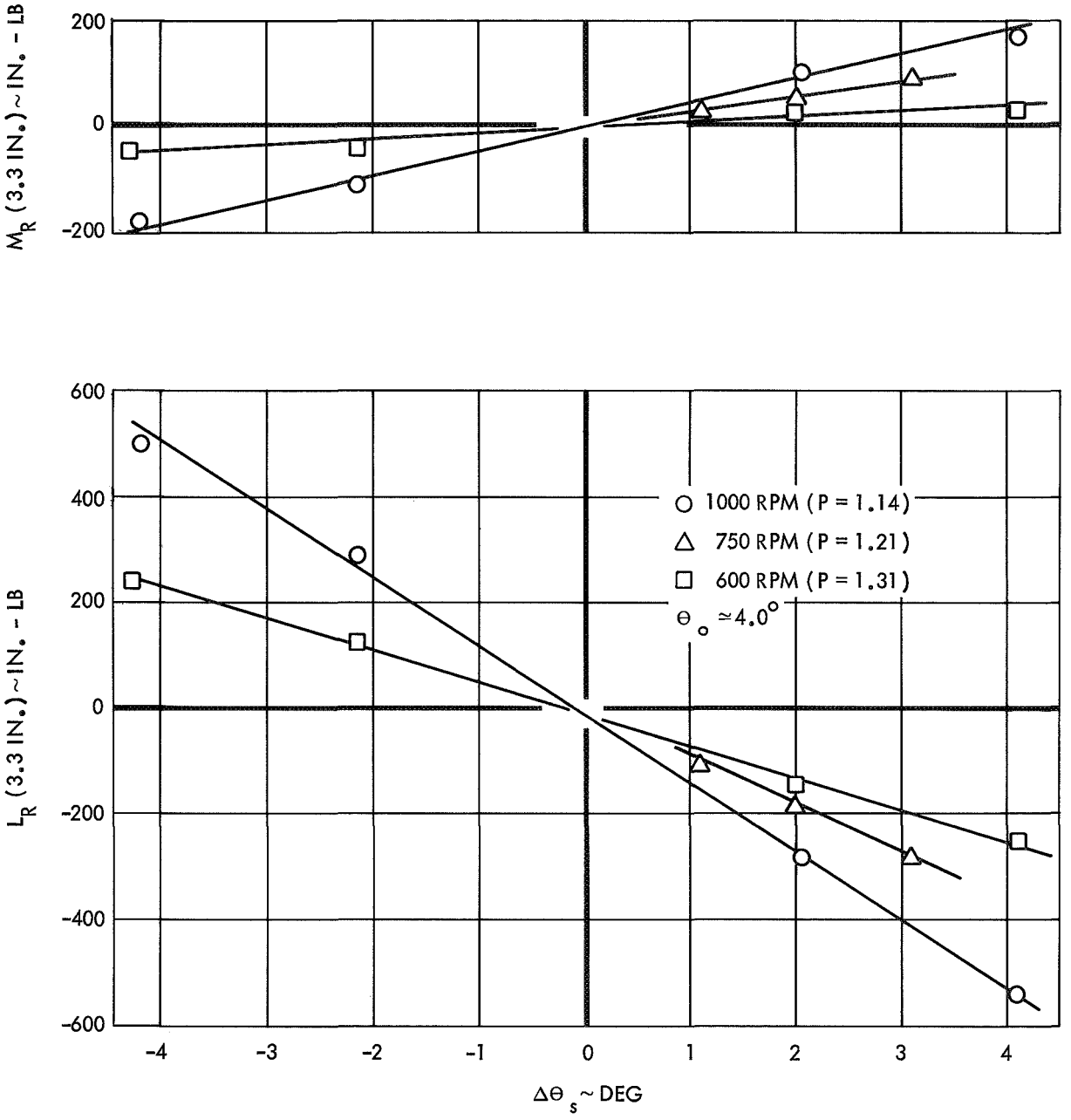

Figure 10. Rotor Pitch and Roll Response to Longitudinal Cyclic Pitch in Hover, Configuration 2

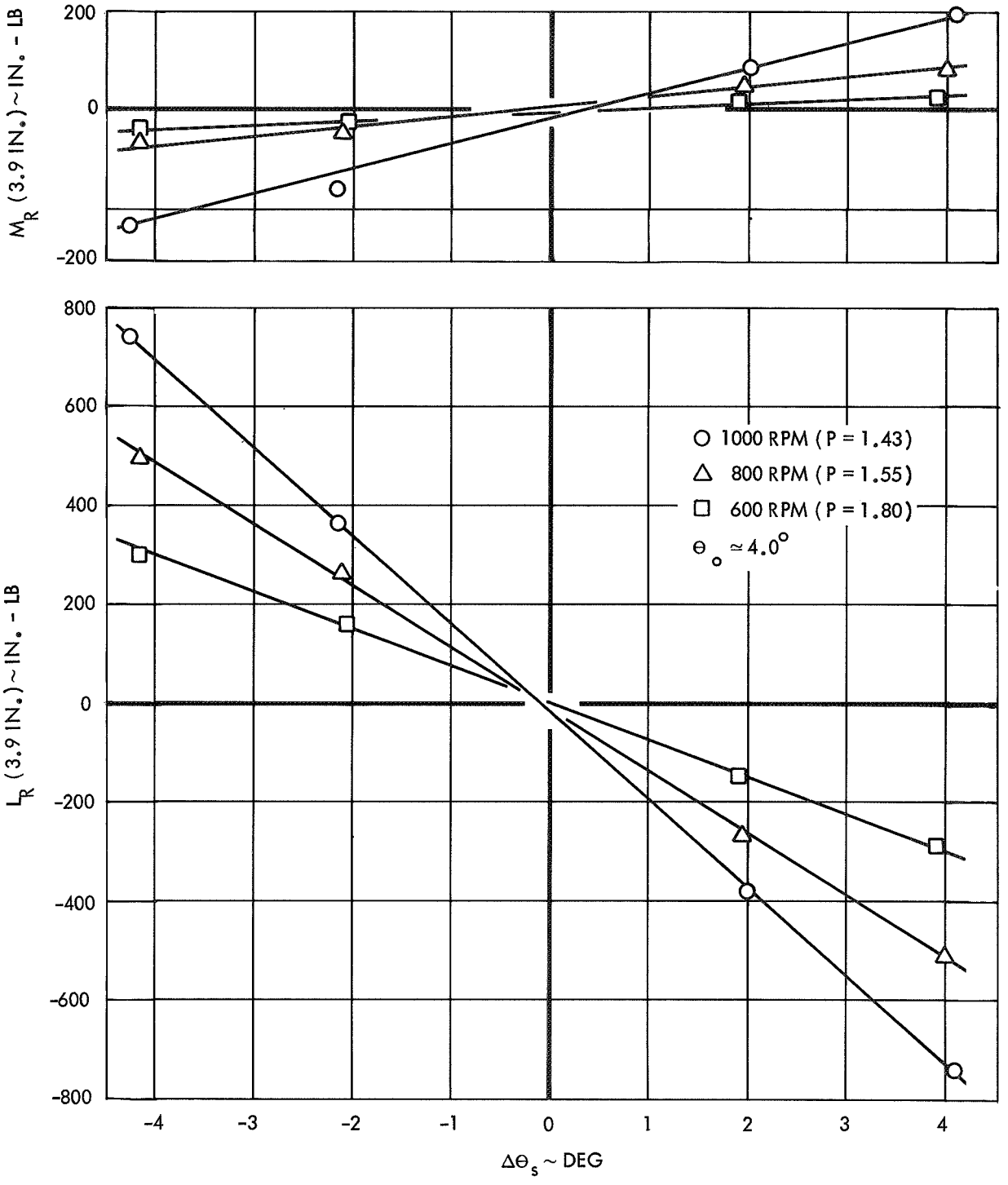

Figure 11. Rotor Pitch and Roll Response to Longitudinal Cyclic Pitch in Hover, Configuration 3

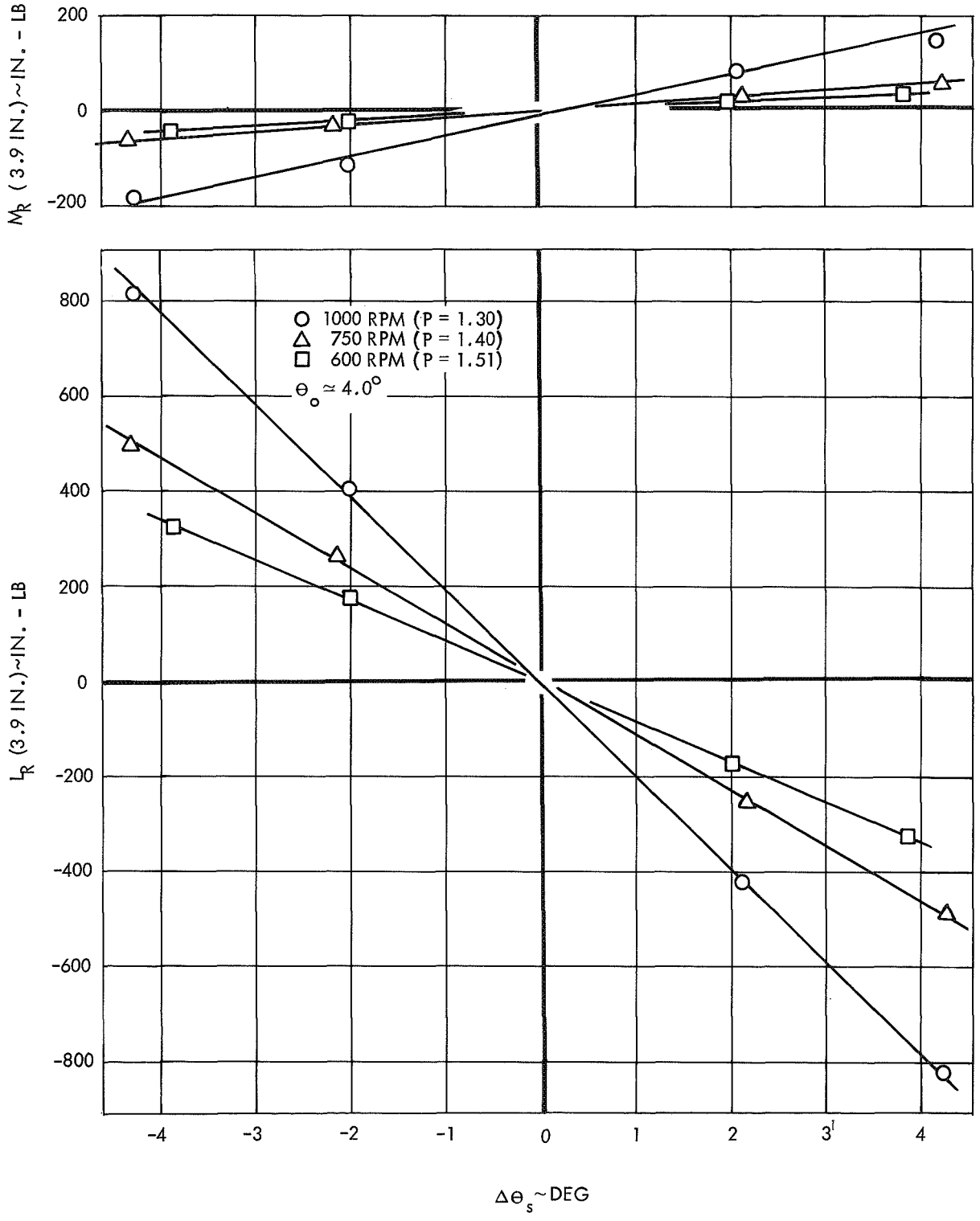

Figure 12. Rotor Pitch and Roll Response to Longitudinal Cyclic Pitch in Hover, Configuration 4

The moments of Figures 9 through 12 are average values extracted from time history recordings and as such are not affected by the data sampling error previously discussed. A nominal collective pitch of approximately 4 deg was maintained for all cyclic pitch excursions. This was done to avoid a nonlinear rotor response at small cyclic pitch angles due to induced downwash, similar to that experienced during the collective pitch tests. The test results indicate that the rotor pitch and roll response to a cyclic pitch input is quite linear. Very little scatter can be seen in the data.

A collective comparison of all the hover moments in terms of the rotor phase angle of response, i.e.

$$\text{PHASE ANGLE} = \text{ARCTAN}\left(-M_{R_{\theta_s}} / L_{R_{\theta_s}}\right) \tag{4}$$

to longitudinal cyclic pitch indicates good consistency among the four configurations. The data are presented in this form in Figure 13 where the phase angle is plotted versus γ and P^2-1. From rudimentary theory it can be shown that the rotor phase angle of response is directly proportional to the flap damping and inversely proportional to the blade flapping restraint. The Lock number is a measure of the damping and P^2-1 a measure of the restraint.

$$\text{PHASE ANGLE} = \text{ARCTAN}\left(\frac{\gamma B^4/8}{P^2-1}\right) \tag{4a}$$

The trends of the test data conform well to this simple expression. The magnitudes of the measured phase angles, however, are significantly less than those calculated by eq 4a. Possible causes for the discrepancy include the rigid flapping mode shape and the uniform inflow ratio which are implicity assumed in eq 4a.

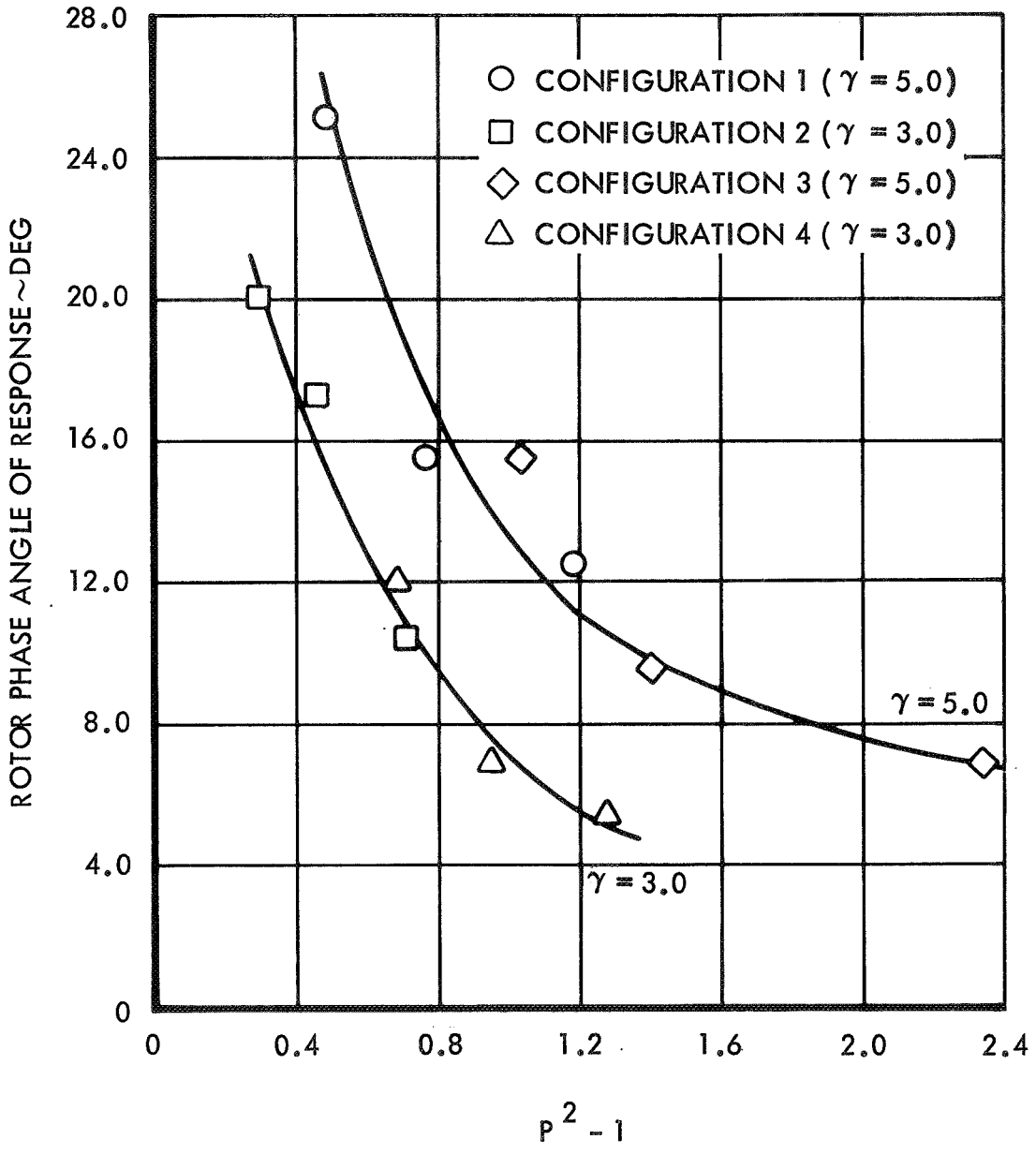

Figure 13. Rotor Phase Angle of Response to Longitudinal Cyclic Pitch in Hover, All Configurations

SECTION 6

WIND TUNNEL TESTS

DESCRIPTION OF WIND TUNNEL

Wind tunnel testing was conducted in the USAARL 7 x 10 ft wind tunnel at Moffett Field. The tunnel is a single return closed jet facility. It has a 14:1 contraction ratio, a maximum speed of 380 ft/sec or 225 knots (q = 170 lb/ft^2), and a maximum air exchange of 29.2%. The 15 ft long test section operates at ambient stagnation pressure; hence the static pressure is reduced by test dynamic pressure. The tunnel drive system employs a 1,600 horsepower variable speed direct current motor driving a fixed pitch propeller at 0 to 310 RPM. The wind tunnel is shown schematically in Figure 14.

The Wind Tunnel Data Acquisition System processes a total of up to 576 channels of analog data at one time which are selected from the following:

680 channels of analog data
12 channels of scanivalve data
50 channels of thermocouple data
24 channels of strain gage data

The signals are converted to digital data which are displayed on lamp banks. In addition, eight channels of digital data and 28 digits of parameter data are available from Toledo Scale equipment, and four channels are available for electronic counter measurements. All channels of data are recorded on an IBM 523 card punch and/or an IBM Selectric printer. An additional output is available to permit the digital signals to be fed directly to a customer-supplied computer. Frame and cycle numbers are also recorded and displayed.

WIND TUNNEL INSTALLATION

The model was mounted directly upon the wind tunnel scales with the six component strain gage balance serving as the interface between the model support strut and the scales. All of electrical wiring and hydraulic lines required to power the model and its control system were routed through the

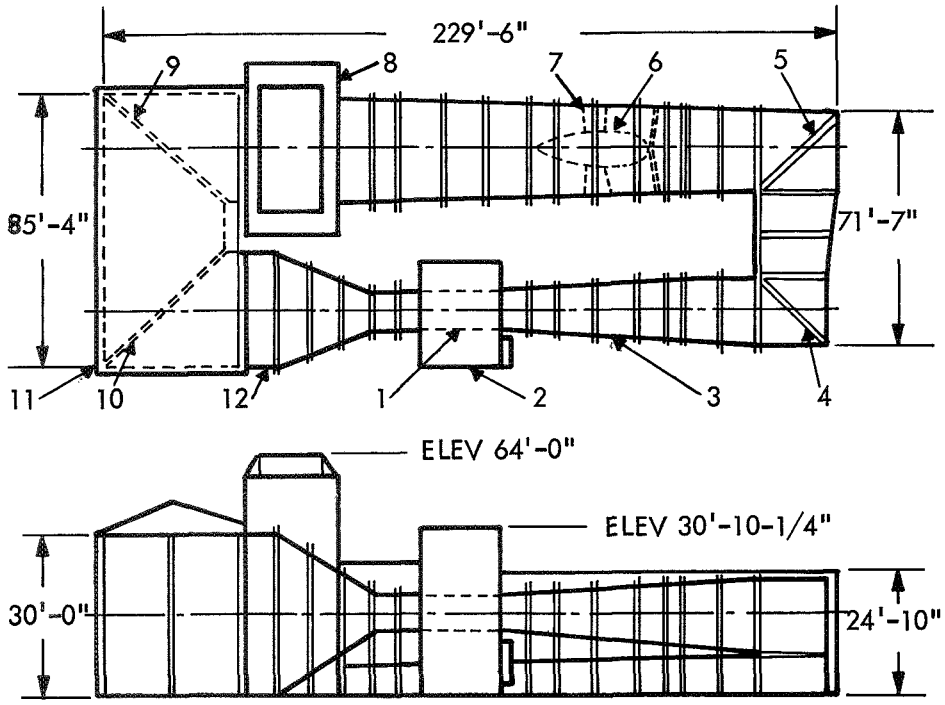

LEGEND

1. TEST SECTION
2. LABORATORY AND WORKSHOP
3. DIFFUSER
4. NO. 1 CORNER VANES
5. NO. 2 CORNER VANES
6. PROPELLER AND MOTOR NACELLE
7. FLOW STRAIGHTENING VANES
8. AIR EXCHANGE TOWER
9. NO. 3 CORNER VANES
10. NO. 4 CORNER VANES
11. SETTLING CHAMBER
12. ENTRANCE CONE

DESIGN DATA

SINGLE RETURN-CLOSED JET

CONTRACTION RATIO 14:1

MAXIMUM SPEED, 380 ft/sec (225 Kt)

TEST SECTION (q = 170 lb/ft^2)

HEIGHT 7 ft WIDTH 10 ft LENGTH 15 ft

STAGNATION PRESSURE IN TEST SECTION, AMBIENT

MAXIMUM AIR EXCHANGE, 29.3%

TUNNEL DRIVE SYSTEM, 1600 HP D.C. MOTOR

FIXED PITCH PROPELLER

VARIABLE PROPELLER RPM 0-310

Figure 14. U.S. Army Aeronautical Research Laboratory 7 x 10 Foot Wind Tunnel Characteristics

floor of the tunnel. The instrumentation cables were routed similarly to a patchboard under the tunnel and from there to the various data acquisition devices. A photograph of the model installed in the tunnel constitutes Figure 15. Control of the model, the data acquisition equipment and the wind tunnel was centrally located in a room adjacent to the test section which provided excellent visibility of the model.

DISCUSSION OF WIND TUNNEL TEST DATA

Following a complete checkout of the model and the data acquisition system installed in the wind tunnel, a comprehensive test program to determine the dynamic characteristics of the four basic rotor configurations at high advance ratios was embarked upon. Forty hours of actual test time were logged and approximately 1500 data points were recorded. The testing was separated into steady state response tests and stability tests, with stability considered last because of its higher degree of risk. Rotor response characteristics were determined for the four configurations at rotor speeds ranging from 300 to 800 RPM and tunnel velocities from 50 to 120 knots. The stability of the soft flexure configurations was examined at several rotor speeds up to a tunnel velocity of 175 knots. A summary of the rotor speeds and forward velocities which were examined during the test are shown graphically in Figure 16.

The most serious difficulty encountered in obtaining steady rotor lift and moment data was caused by turbulence in the wind tunnel. The turbulence appeared as a rapid change in the free stream velocity to which the rotor responded. The frequency of the turbulence was very erratic and its effect on the steady rotor response became more pronounced at higher tunnel dynamic pressures. The gross effect of the turbulence was to generate time varying rotor lift and moments at approximately the same frequency as the occurance of turbulence. The problem of minimizing the effect of the turbulence from the steady data was effectively solved by averaging many samples of data at each test condition.

The only other significant difficulty occurred late in the test program and was caused by a deterioration of the strain gage bridges used to resolve the rotating rotor moments into stationary coordinates. The failure of any

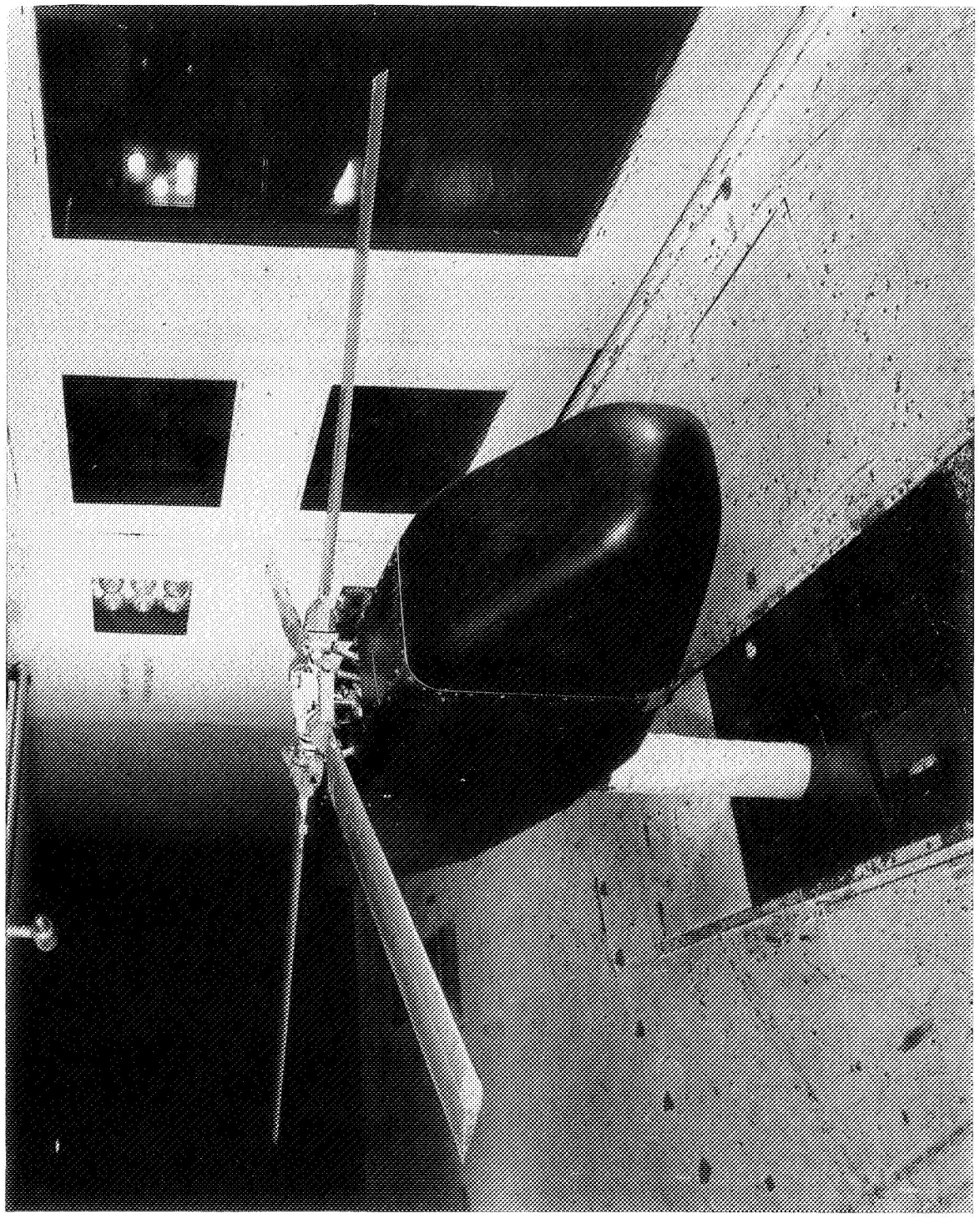

Figure 15. Lockheed/AARL High Advance Ratio Rotor Model

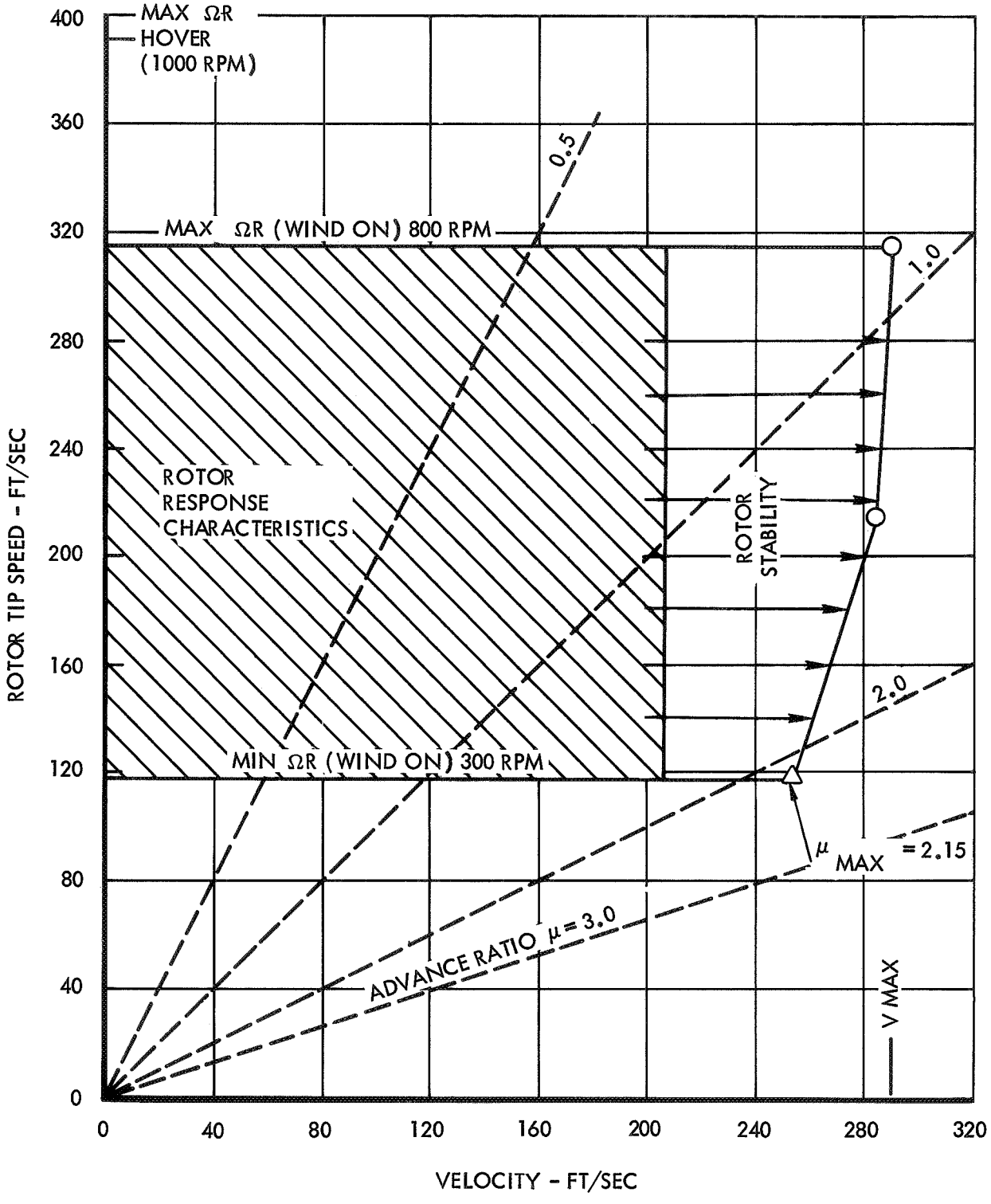

Figure 16. Test Conditions

one of the four bridges which made up the circuit would destroy the moment signals. The moment resolution circuit was temporarily corrected by converting the full strain gage bridges on the blades to half bridges. However, after only a very short period of operation, the half bridges failed also and the circuit was rendered unusable and unrepairable without the installation of new strain gages. With the demise of the moment resolution went the moment data and the visual capability of trimming the rotor. This problem occurred during the last RPM of the response tests of the last configuration. The steady state data for these test conditions are available from the harmonic analysis of the output of the flexure flap bending strain gage.

ROTOR RESPONSE TEST DATA

The steady state response of each basic rotor configuration was determined for four separate excitations:

- Collective pitch, θ_o
- Longitudinal cyclic pitch, θ_s
- Lateral cyclic pitch, θ_c
- Rotor shaft angle of attack, α

Sufficient test conditions were examined so that derivatives of rotor pitching moment, rolling moment and lift with respect to the several excitations could be accurately defined as a function of advance ratio. A wide range of advance ratios was obtained by varying both tunnel velocity and rotor speed. A change in rotor speed also effected a change in the rotor blade nondimensional flapping frequency, P. Table 2 summarizes the advance ratios and rotor speeds examined for each basic rotor configuration. Listed also are the values of P corresponding to each RPM. The reader is reminded that configurations 1 and 3 are characterized by a Lock number of 5.0. For rotors 2 and 4, $\gamma = 3.0$.

TABLE 2

ROTOR RESPONSE TEST CONDITIONS

CONFIGURATION	RPM	P	μ
1 (γ = 5.0)	1000	1.22	0
	800	1.33	0, 0.29, 0.40, 0.54, 0.66
	600	1.48	0
	550	1.56	0.43, 0.58, 0.79, 0.96
	300	2.32	0.78, 1.07, 1.44, 1.75
2 (γ = 3.0)	1000	1.14	0
	750	1.21	0, 0.32, 0.43, 0.58, 0.71
	600	1.31	0
	375	1.59	0.62, 0.85, 1.15, 1.39
3 (γ = 5.0)	1000	1.43	0
	800	1.55	0, 0.29, 0.40, 0.54, 0.66
	650	1.73	0.36, 0.49, 0.66, 0.80
	600	1.80	0
	400	2.32	0.59, 0.80, 1.08, 1.31
4 (γ = 3.0)	1000	1.30	0
	750	1.40	0, 0.32, 0.43, 0.58, 0.71
	600	1.51	0, 0.38, 0.53, 0.73, 0.87

The test schedule was formulated to minimize fluctuations in advance ratio while the several disturbances were imposed upon the rotor. This was accomplished by maintaining constant both the rotor and tunnel speeds while the various control inputs were applied to the blades. The rotor shaft angle of attack variations had to be handled differently. The angle of attack was changed by hand which necessitated shutting down the rotor and tunnel. Therefore, for these cases constant shaft angle and rotor speed were maintained while the tunnel velocity was varied.

The principal objective of the response tests was to experimentally determine the rotor pitching and rolling moment and lift derivatives with respect to the four excitations (θ_o, θ_s, θ_c, α) as a function of advance ratio and rotor RPM. A nondimensional description of the rotors and their response characteristics can be extracted from these data to facilitate a comparison of test results with nondimensional theory. In order to accurately define the derivatives of rotor response with respect to a selected excitation,

many magnitudes of the exciting parameters were considered. At a fixed flight condition (V and ΩR), the rotor was disturbed from a trimmed condition with increasing magnitudes of an excitation. The maximum allowable input was defined when the blade bending moments reached a fatigue limit.

Data were recorded at a large number of discreet test conditions. They represent a valuable data bank which may be correlated with appropriate mathematical theories. To graphically present all of the data in the main body of this report, however, would not serve the purposes of the current study. Consequently only a summary of the rotor derivatives plotted versus advance ratio and rotor speed will be presented. An example of the data leading to the derivatives will be shown. All of the data from which the rotor lift and moment derivatives were ascertained are plotted in Appendix B. Steady blade moments obtained from a Fourier analysis of the flapping of a single blade are documented in Appendix C.

Examples of the data from which the rotor moment response derivatives were extracted are shown in Figures 17 through 19. They present the rotor pitching and rolling moments resulting from the application of collective pitch. The data on each figure were obtained at one rotor speed and four tunnel velocities. The moments have been resolved from rotating to fixed coordinates. The plotted values are moments which are radially offset 3.3 in. from the center of rotation. Data taken at $\Delta\theta_o = 0$ deg have been omitted where they detract from the clarity of the presentation.

These three figures are typical of the rotor response data obtained during the test. Each datum is the average of ten samplings which were recorded at each test condition. The figures indicate that this data averaging method effectively minimizes scatter due to the various sources of noise. The small band of scatter which is detectable is due primarily to wind tunnel turbulence. Had time permitted a longer sampling period, virtually all scatter would have been eliminated. The curves indicate that the rotor response to collective pitch is very linear. This is to be expected since the rotor operated in a linear two dimensional aerodynamic environment. Blade tip Mach numbers were always low and blade angles were well below stall values. The effect of increasing advance ratio is seen as

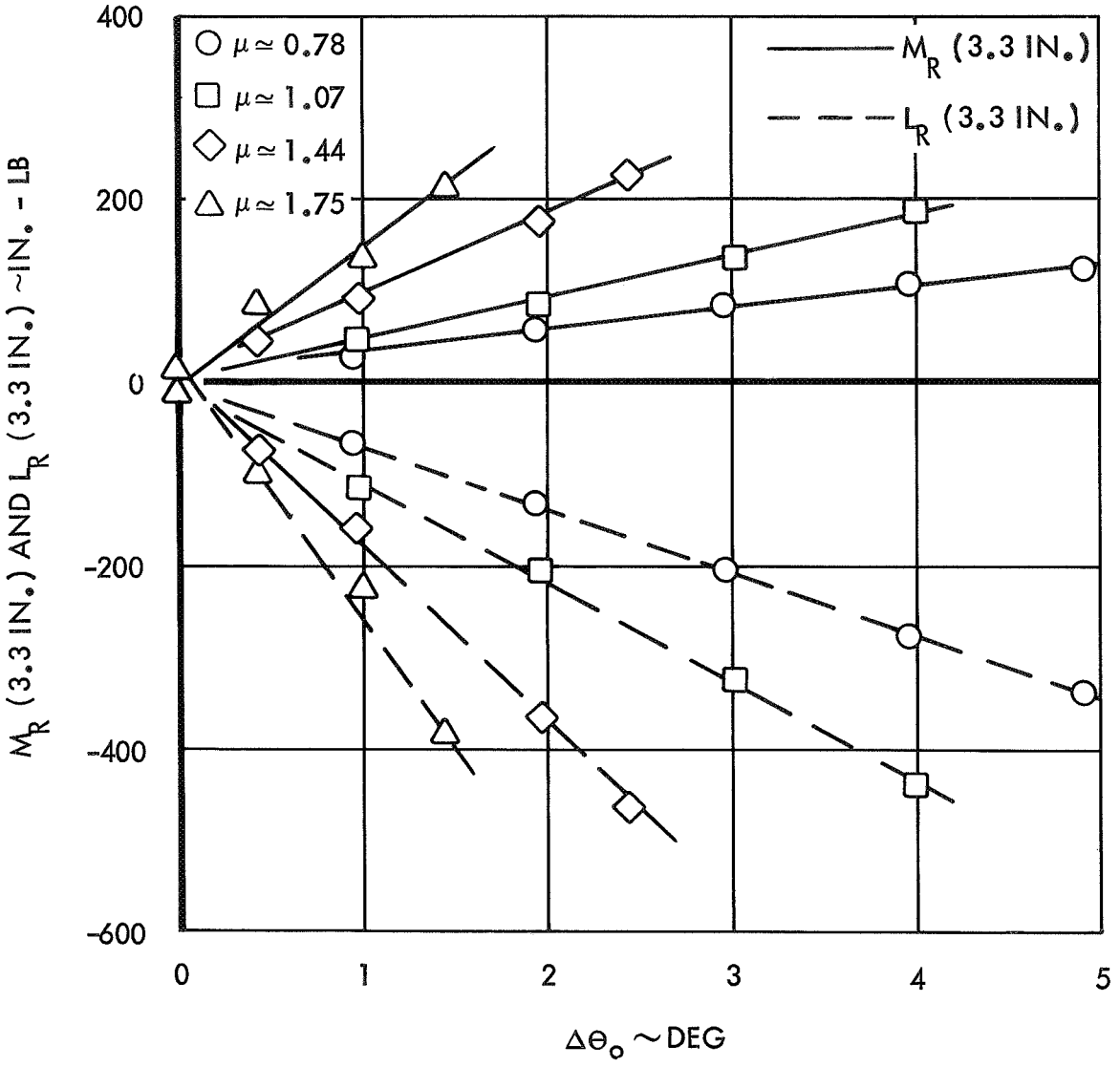

Figure 17. Rotor Pitch and Roll Response to Collective Pitch, Configuration 1, 300 RPM (γ=5.0, P=2.32)

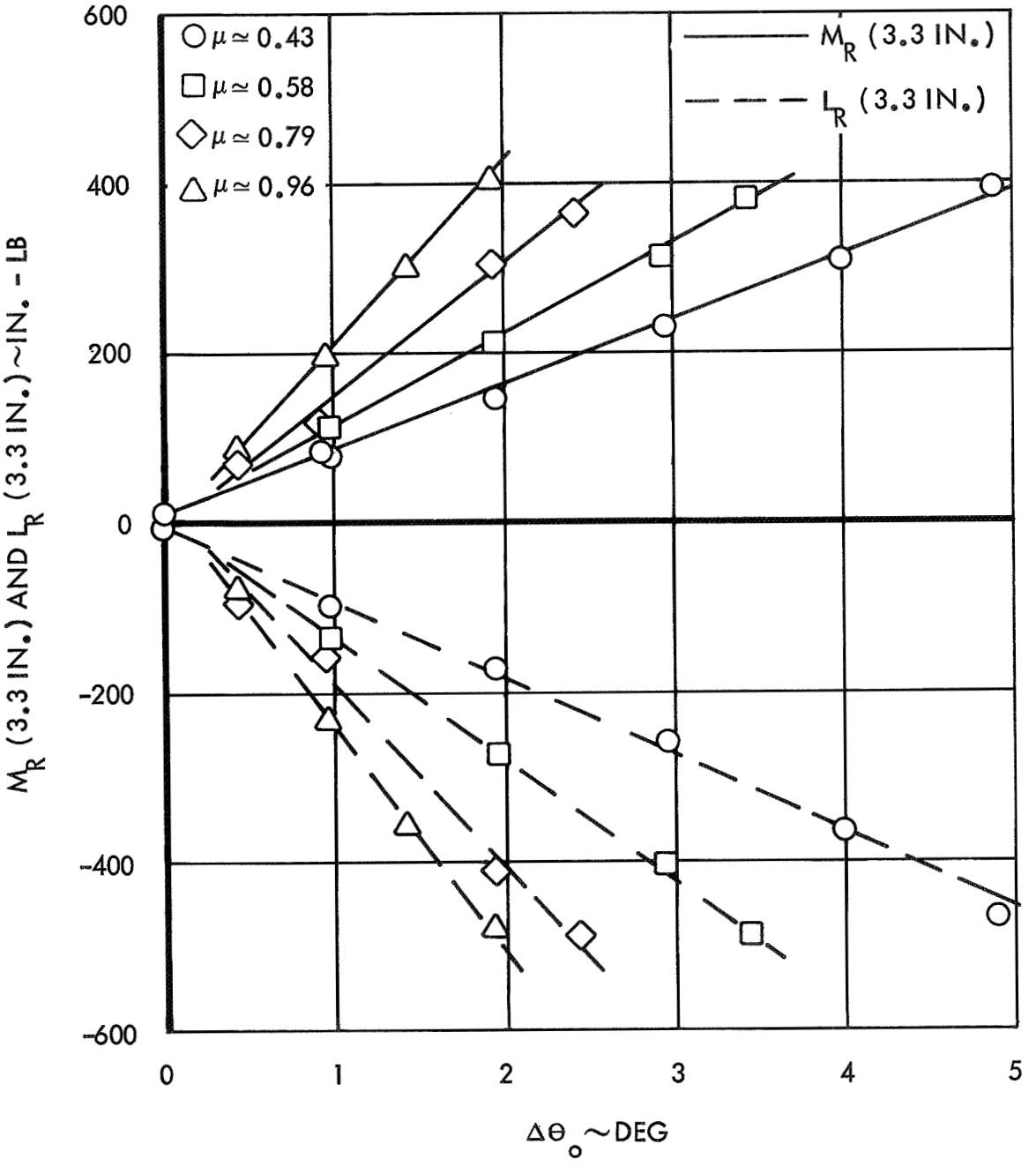

Figure 18. Rotor Pitch and Roll Response to Collective Pitch, Configuration 1, 550 RPM (γ=5.0, P=1.56)

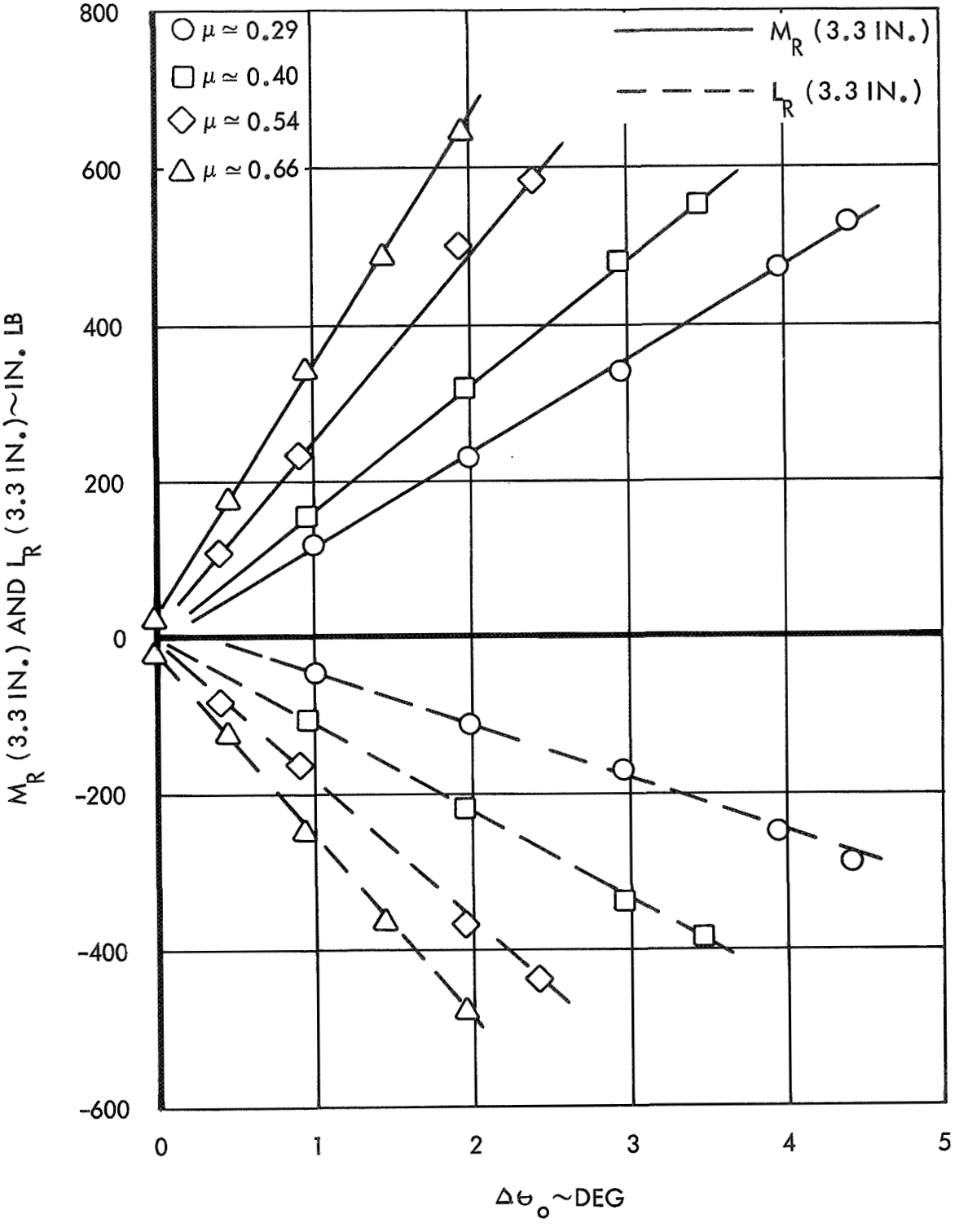

Figure 19. Rotor Pitch and Roll Response to Collective Pitch, Configuration 1, 800 RPM (γ=5.0, P=1.33)

an increase in the rate of change of response with collective pitch. At a constant rotor speed an increase in advance ratio produces a corresponding increase in the strength of the aerodynamic forces.

All of data shown in Figures 17 through 19 may be conveniently summarized by considering the moment derivatives with respect to collective pitch. These are simply the slopes of the $M_R - \theta_o$ and $L_R - \theta_o$ curves. They are plotted versus advance ratio for the tested rotor speeds in Figure 20. Several characteristics of the rotor response to a collective pitch excitation are apparent from the plot. The derivatives are not linear functions of advance ratio; the rotor phase angle of response is not constant with advance ratio; and the response decreases with rotor rotational speed. The first two characteristics may be explained by examining the periodic aerodynamic forces acting on a rotor blade as it rotates through its azimuth range. Table 6 of Appendix A contains expressions for the nondimensional aerodynamic flapping moments in terms of advance ratio (μ). Idealized two-dimensional theory is assumed. It can be seen that the various moments are functions of μ^2, μ^3 and μ^4. The aerodynamic damping and spring restraint of the flapping also vary with higher orders of μ which will affect the rotor phase angle of response. The decrease in rotor moments at reduced rotor speeds reflects a decrease in the aerodynamic forces acting on the blades.

Figures 21 and 22 present a summary of the rotor moment response derivatives with respect to longitudinal and lateral cyclic pitch. These curves were generated in exactly the same manner as the collective pitch summary data. The ranges of cyclic pitch tested were approximately -4° to $+4^\circ$. A nominal collective pitch of $\sim 1^\circ$ or $\sim 0.5^\circ$ was maintained to effect a pre-load on the control system and rotor. The lower θ_o value was used at the two higher forward velocities. In most cases the rotor was initially disturbed from a trimmed condition. That is, the moments generated by the nominal collective pitch were trimmed before the cyclic pitch variations were made. All input cyclic pitch (i.e., $\Delta\theta_s$ and $\Delta\theta_c$) was measured relative to the values required for trim.

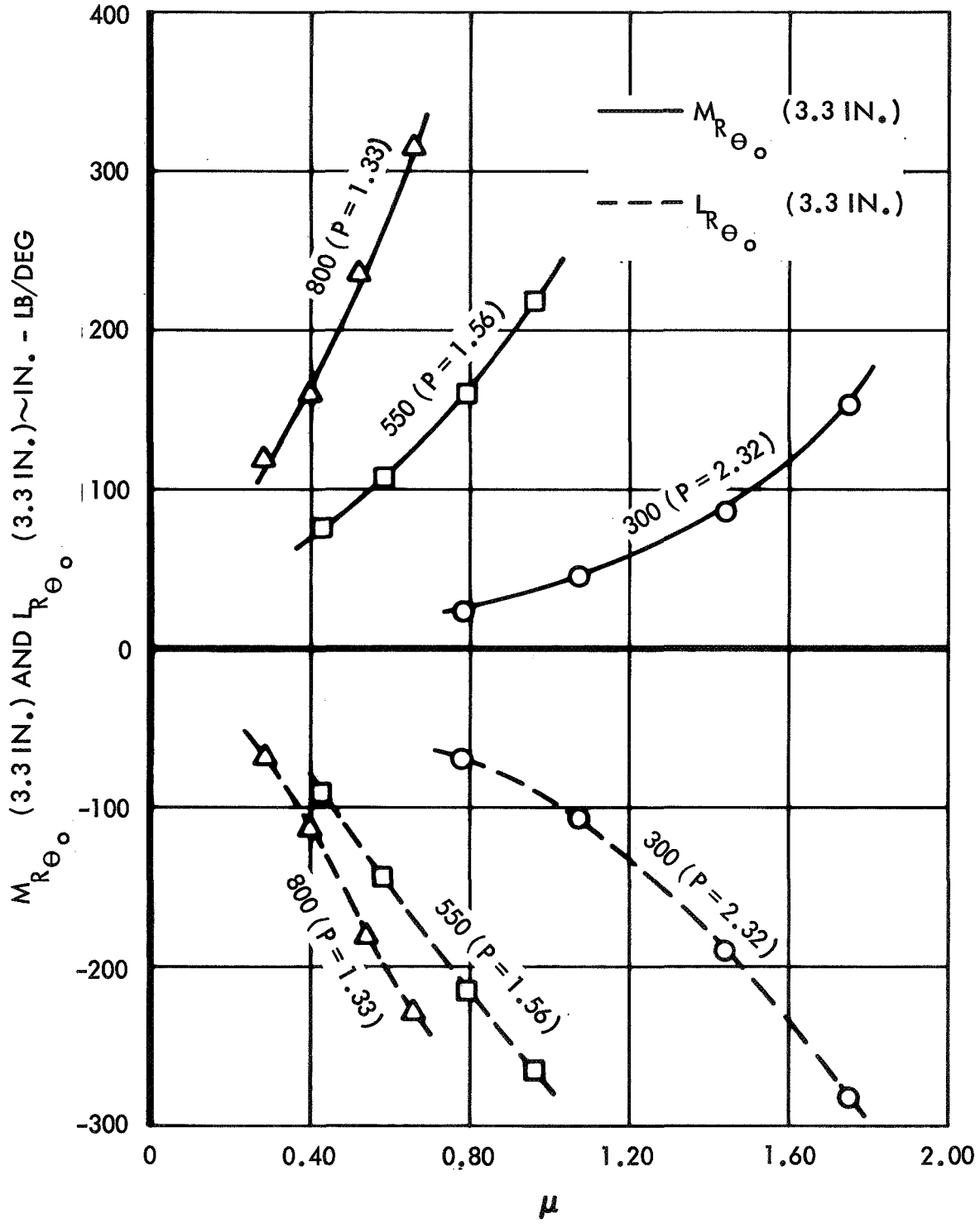

Figure 20. Rotor Pitching and Rolling Moment Derivatives with Respect to Collective Pitch, Configuration 1 (γ=5.0)

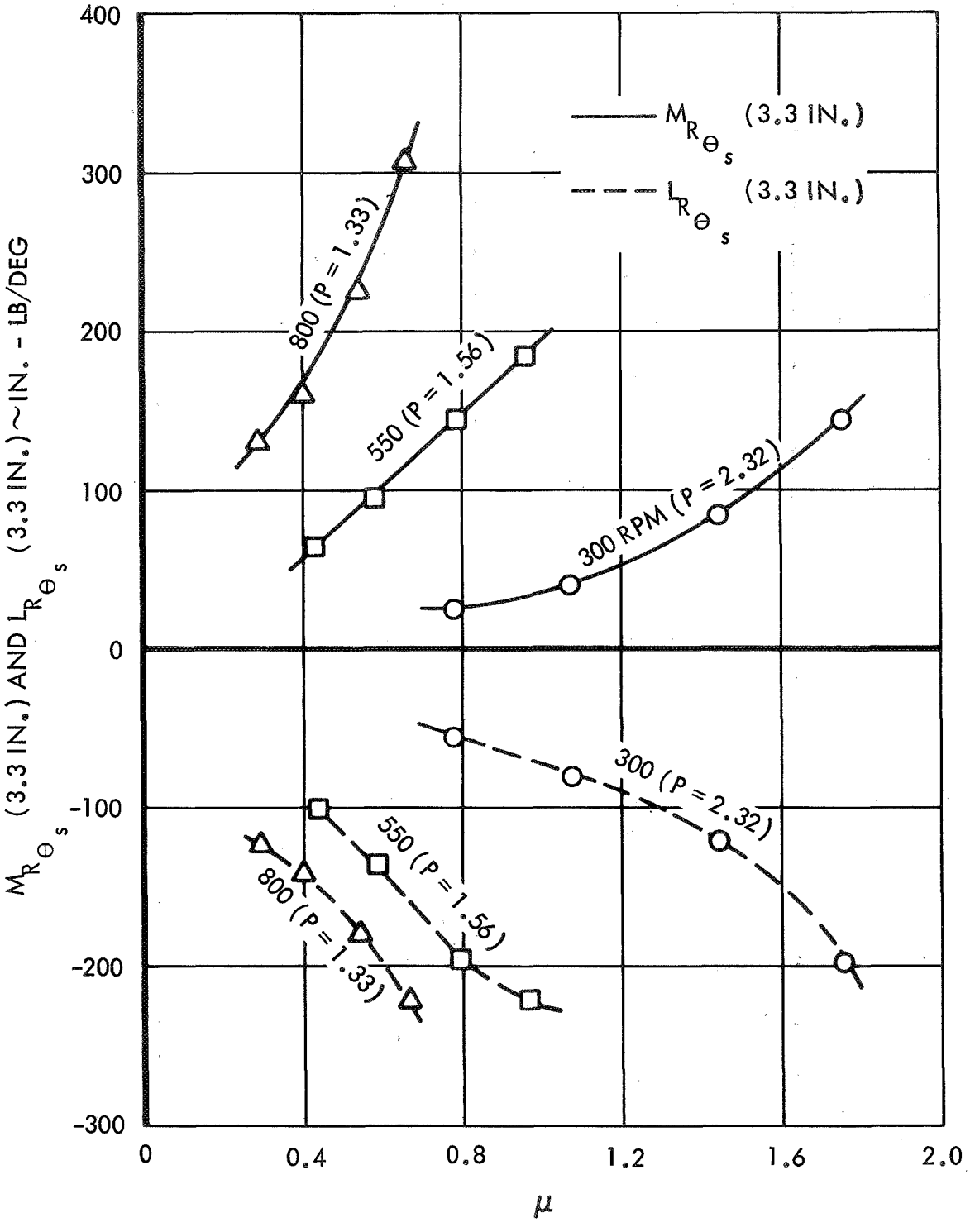

Figure 21. Rotor Pitching and Rolling Moment Derivatives with Respect to Longitudinal Cyclic Pitch, Configuration 1 (γ=5.0)

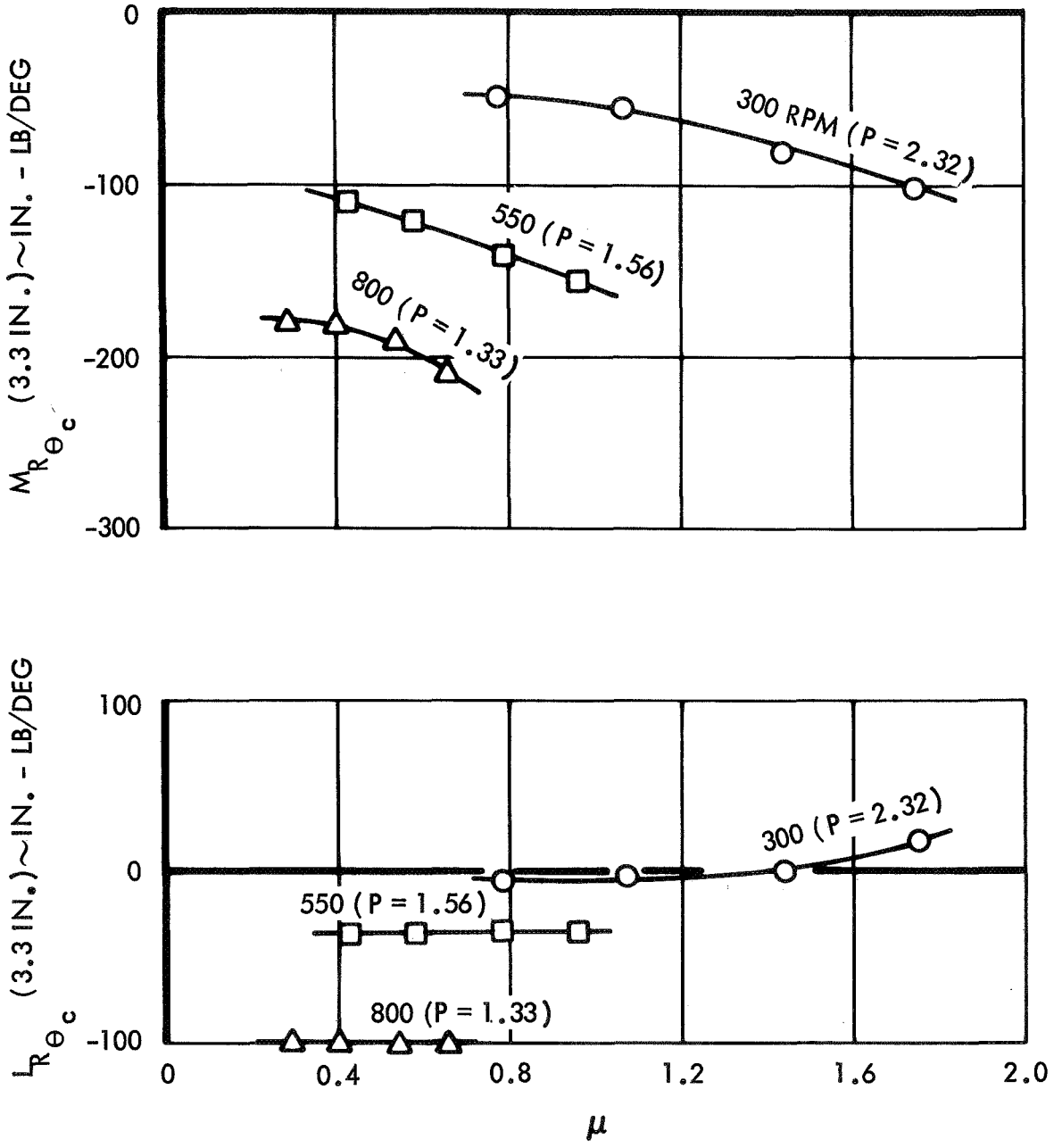

Figure 22. Rotor Pitching and Rolling Moment Derivatives with Respect to Lateral Cyclic Pitch, Configuration 1 (γ=5.0)

The rotor response to longitudinal cyclic pitch (θ_s) is similar to that generated by collective pitch. Both θ_o and θ_s disturbances produce identical maximum excitations when the rotor blade is in the 90 deg azimuth position. The rotor response to lateral cyclic pitch (θ_c) is shown in Figure 22. At a fixed rotor speed the response is not strongly affected by forward speed. This is the case because at the zero azimuth position, where a rotor blade experiences its maximum excitation, the blade tangential velocity is due totally to rotor rotation. The cause of the change in sign of the rolling moment derivative at 300 RPM is not obvious. It is, however, predictable by the theory of Appendix A as will be shown in Section 7.

The determination of the response derivatives with respect to rotor shaft angle of attack was not as precise as that for the cyclic and collective control inputs. The lack of a remote angle of attack capability limited the number of angular variations which could be tested. Three discrete shaft angles were considered; 0°, -1.5° and -3°. The three data points did not always form a straight line as illustrated in Figure 23. The pitching and rolling moments are plotted versus incremental geometric angle of attack at one rotor speed and four tunnel velocities. It is reasoned that the angle of attack which the rotor actually experiences is not the same as the geometric angle. The distortion is probably caused by the flow over the fuselage and appears also to be a function of the geometric angle. In most cases the nonlinearities were not severe and average slopes were used to define the rotor moment derivatives. All of the data leading to the angle of attack derivatives are plotted in Appendix B.

The rotor moments generated by an angle of attack disturbance are summarized for configuration 1 in Figure 24. The format of the figure is the same as that used to summarize the rotor response to collective and cyclic pitch. The derivatives are plotted showing the effect of both rotor speed and advance ratio. The angle of attack response of the rotor is similar to that caused by both collective pitch and longitudinal cyclic pitch. The magnitudes are generally lower, however.

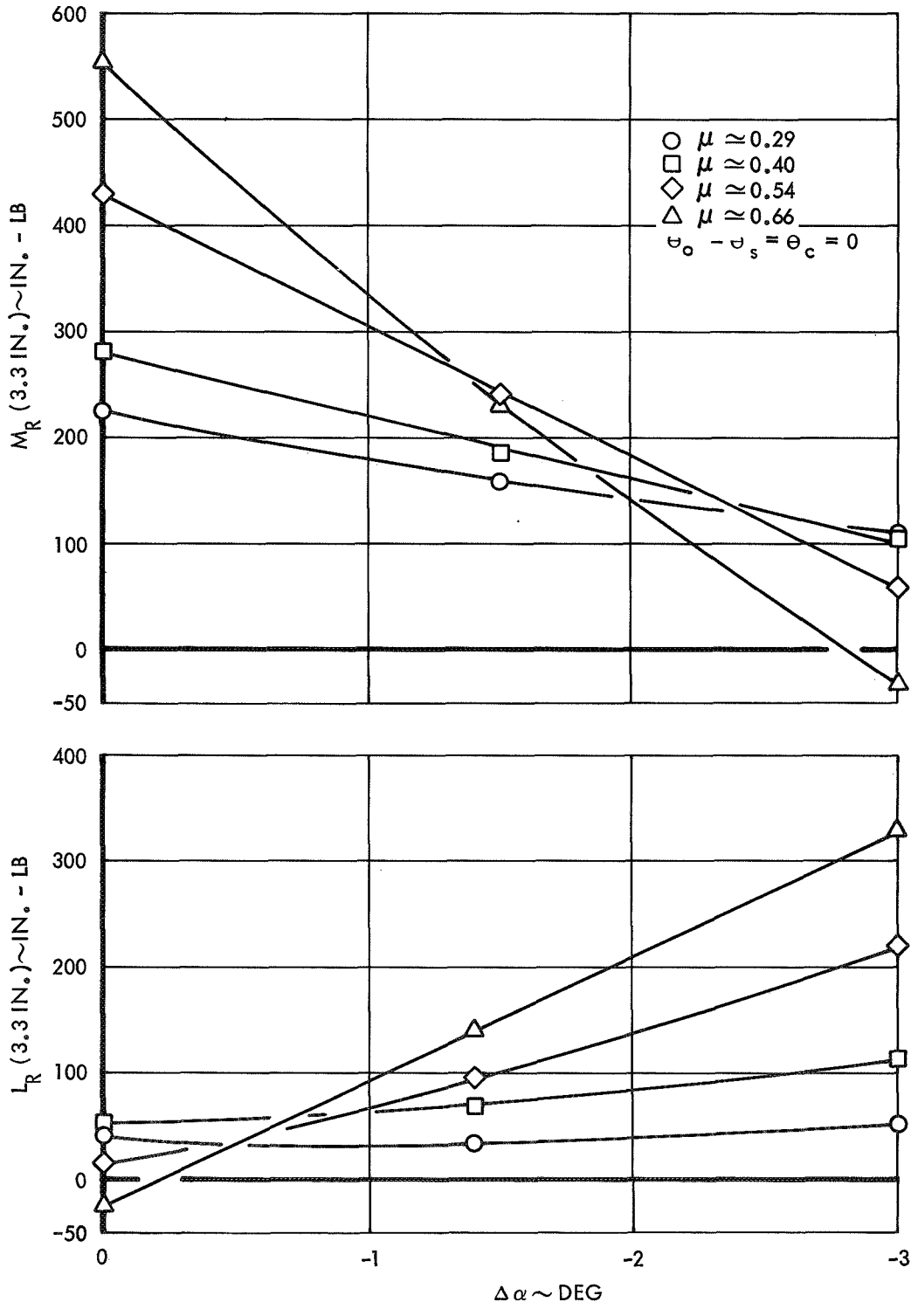

Figure 23. Rotor Pitch and Roll Response to a Rotor Shaft Angle of Attack Increment, Configuration 1, 800 RPM (γ=5.0, P=1.33)

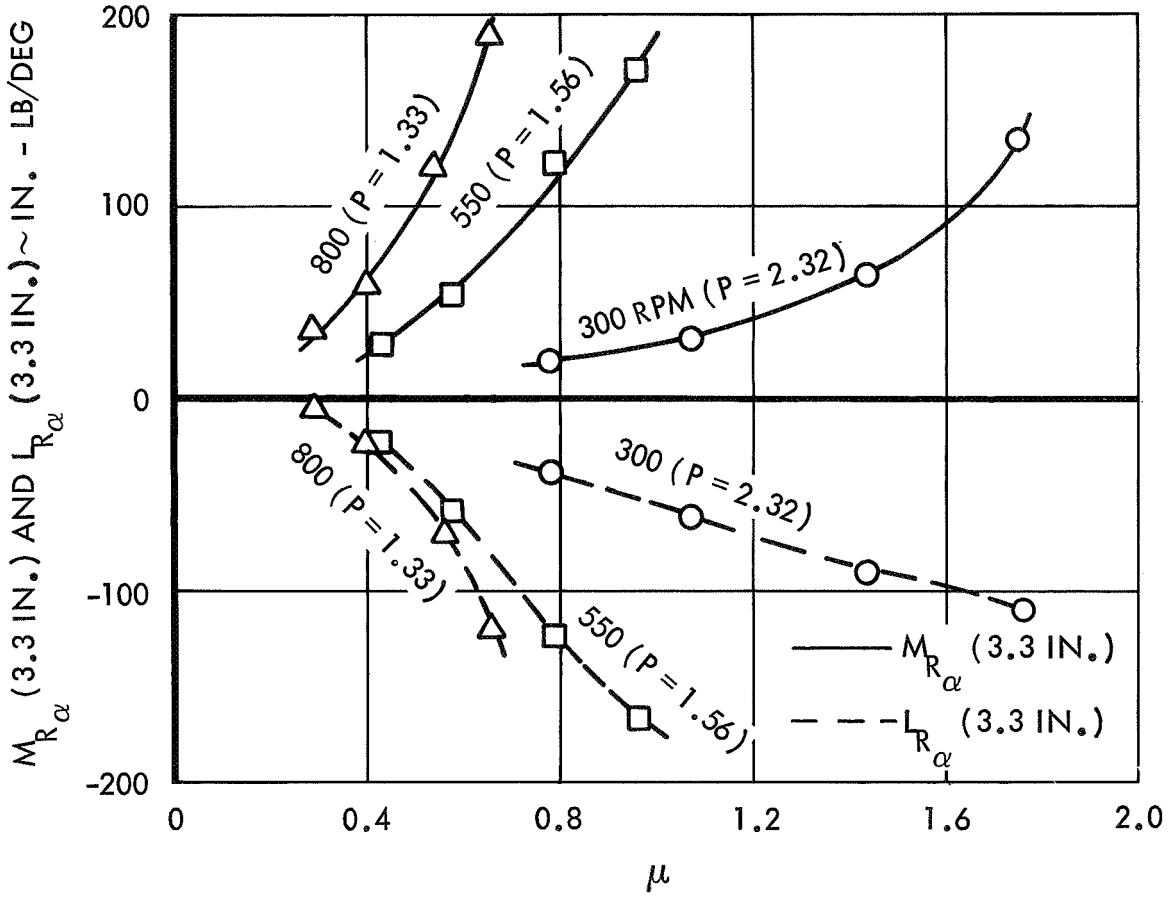

Figure 24. Rotor Pitching and Rolling Moment Derivatives with Respect to Rotor Shaft Angle of Attack, Configuration 1 (γ=5.0)

The lift of the rotor resulting from the various excitations is shown in nondimensional derivative form in Figure 25. These data were obtained at the same time as the rotor moment data were. The lift is represented by the blade loading coefficient $C_{T/\sigma}$. The derivatives are plotted versus advance ratio. The several tested rotor speeds are designated by different symbols. The curves indicate that the role of rotor RPM as an independent variable is compensate by $C_{T/\sigma}$. The lift due to lateral cyclic pitch is not shown because the rotor does not respond to the excitation (i.e., $\partial(C_T/\sigma)/\partial\theta_c = 0$).

When considering the curves of Figure 25 it is important to remember the conditions under which the data were obtained. The collective pitch variations were made at a constant angle of attack and constant cyclic pitch settings. Consequently the $\partial(C_T/\sigma)/\partial\theta_o$ vs μ curve does not represent a trimmed rotor. The moment derivatives of Figure 20 define the untrimmed state of the rotor. In a similar fashion the angle of attack variations were made with both collective and cyclic pitch held constant at approximately 0 deg, producing the untrimmed conditions described by Figure 24.

In the next section of this document the test results will be compared with theoretical predictions. One of the items to be correlated is the rotor coning angle. While coning can be deduced from the lift data it is more correctly obtained from a harmonic analysis of the flap bending moment of a single blade. Such an analysis produced the steady rotating blade moments for the four configurations plotted in Appendix C. A summary curve showing the derivatives as a function of advance ratio and rotor speed for configuration 1 constitutes Figure 26. The steady blade response to collective pitch, longitudinal cyclic pitch and rotor shaft angle of attack are shown. As indicated previously, rotor lift (and consequently steady blade moment) is independent of lateral cyclic pitch. The only significant difference between rotor data and blade data (beyond magnitude) is that dissimilar responses among the four blades are automatically averaged in the formation of the rotor moments.

After the tests designed to determine the fundamental response characteristics of a basic rotor configuration were completed, a series of test runs were made to check the results. The checking procedure consisted of "flying"

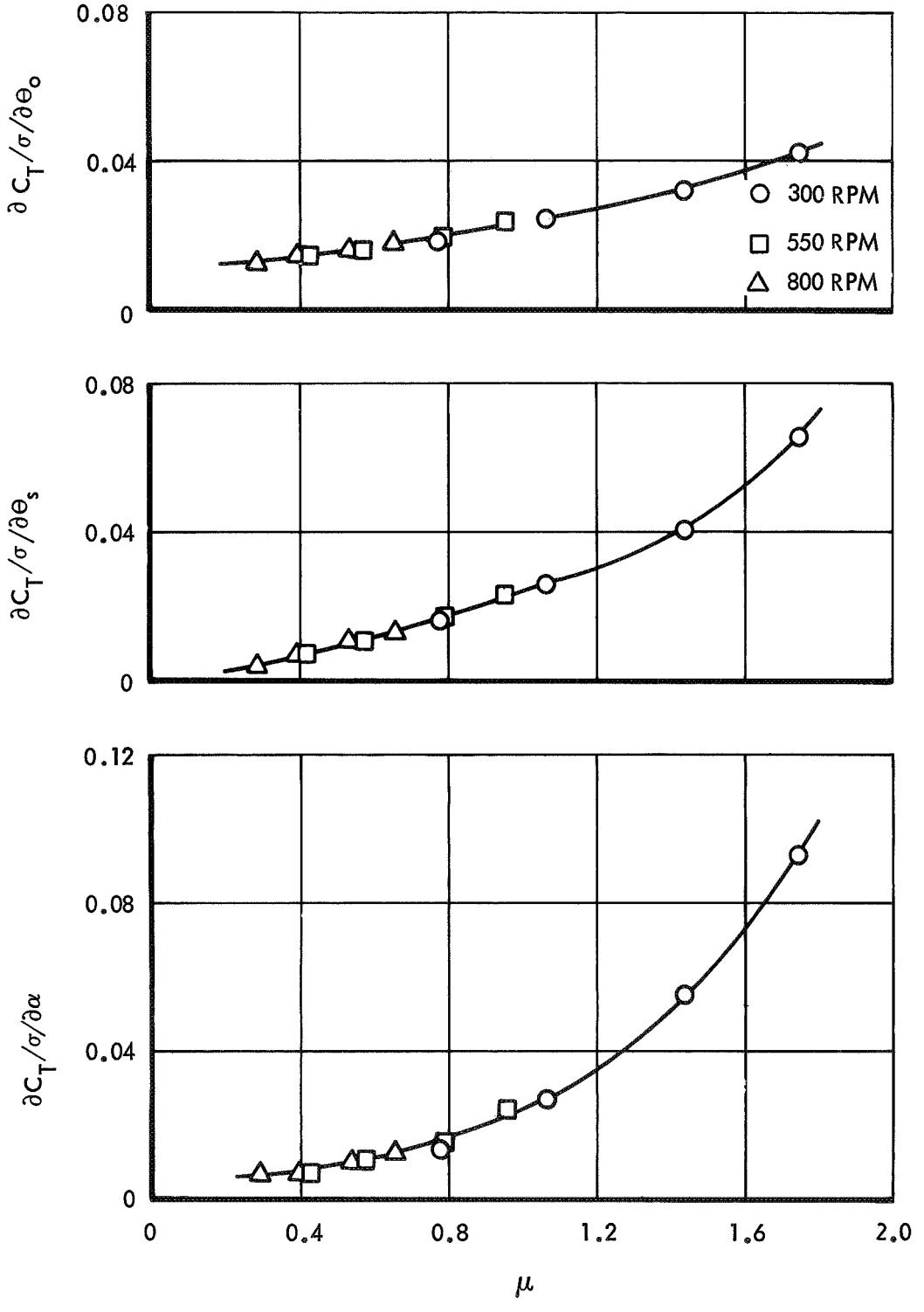

Figure 25. Rotor Lift Derivatives with Respect to Collective Pitch, Longitudinal Cyclic Pitch and Rotor Shaft Angle of Attack, Configuration 1 (γ=5.0)

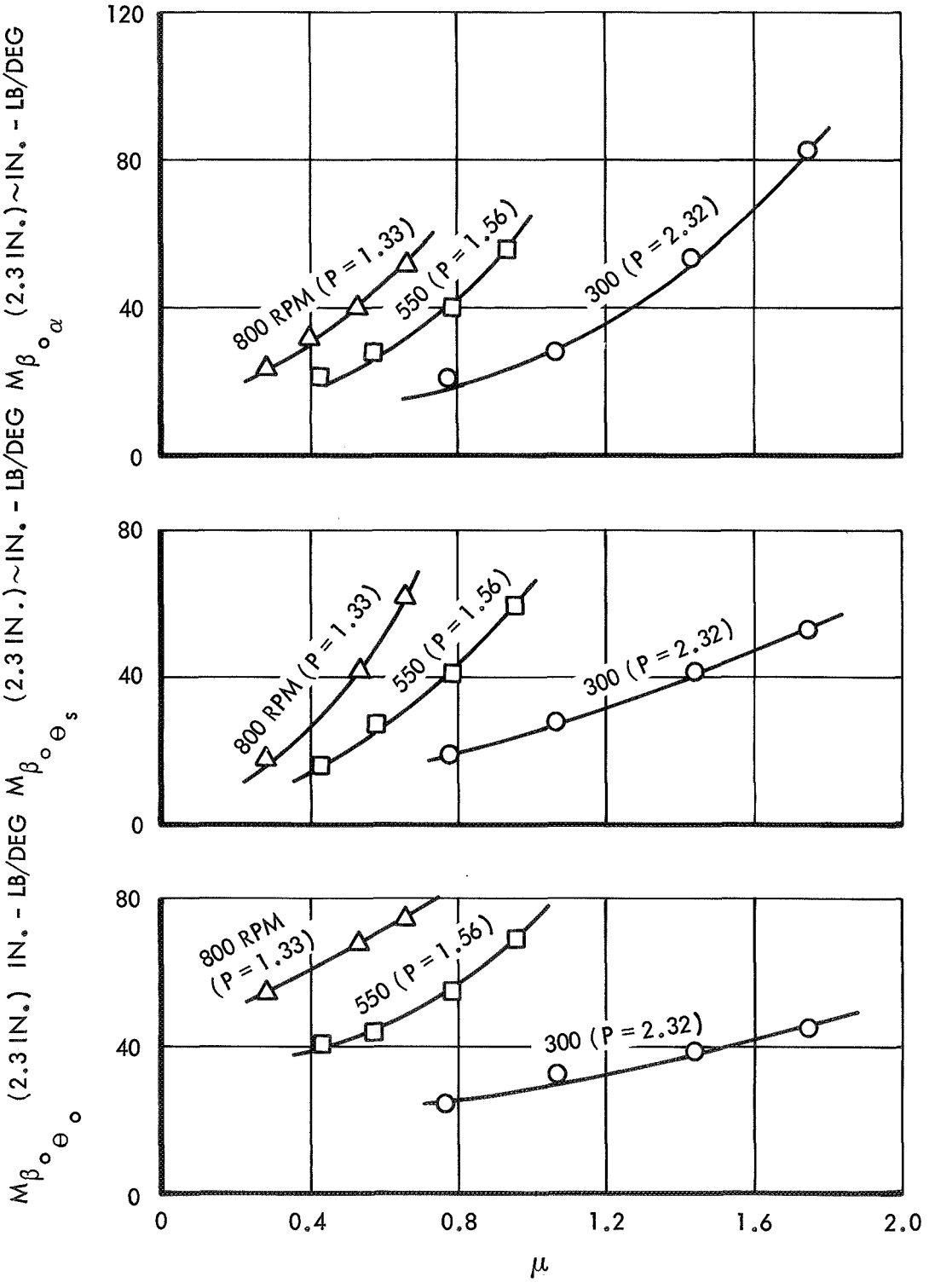

Figure 26. Steady Rotating Blade Moment Derivatives, Configuration 1 (γ=5.0)

the model. At a given shaft angle of attack and flight condition (V and ΩR), rotor lift was commanded by applying collective pitch. The resulting moments were then trimmed by applying appropriate cyclic pitch. Several flight conditions and rotor lift levels were tested. The results of these tests for configuration 1 are shown in Figure 27 where the collective pitch, longitudinal and lateral cyclic pitch combinations required to maintain rotor trim are plotted. Several advance ratios were tested at a constant rotor speed (550 RPM) and geometric rotor shaft angle of attack (-3°). The curves confirm the linearity of the rotor response to collective and cyclic pitch. A nonlinear variation of the derivatives with respect to advance ratio is also indicated.

The test data of Figure 27 may be used to verify the moment derivatives with respect to θ_o, θ_s, and θ_c, summarized in Figures 20, 21 and 22. At a fixed advance ratio and angle of attack the angular derivatives $\partial\theta_s/\partial\theta_o$ and $\partial\theta_c/\partial\theta_o$ can be determined by solving the following two linear equations simultaneously.

$$\left.\begin{aligned} M_R\Big/_{\alpha = -3^{\circ}} + \theta_o M_{R_{\theta_o}} &= -\theta_s M_{R_{\theta_s}} - \theta_c M_{R_{\theta_c}} \\ L_R\Big/_{\alpha = -3^{\circ}} + \theta_o L_{R_{\theta_o}} &= -\theta_s L_{R_{\theta_s}} - \theta_c L_{R_{\theta_c}} \end{aligned}\right\} \qquad (5)$$

The intercepts of the $\theta_o - \theta_s$ and $\theta_o - \theta_c$ curves correspond to the trim cyclic pitch values when $\theta_o = 0^{\circ}$. The rotor pitching and rolling moments at $\alpha = -3^{\circ}$ are required because the angle of attack is not defined absolutely. They may be found in Appendix B. A comparison of the trim cyclic pitch requirements determined by "flying" the model and by solving eqs 5 is shown in Figure 28. The coordinates and conditions of the figure are identical to those of Figure 27 except data at only two advance ratios are compared. The trim results deduced from the moment derivatives are indicated by dashed lines. Comparable results obtained directly by testing are represented by symbols. The comparison is good. Slight scatter is seen in the lateral cyclic pitch data. This can be attributed to wind tunnel turbulence which made rotor trim difficult to identify.

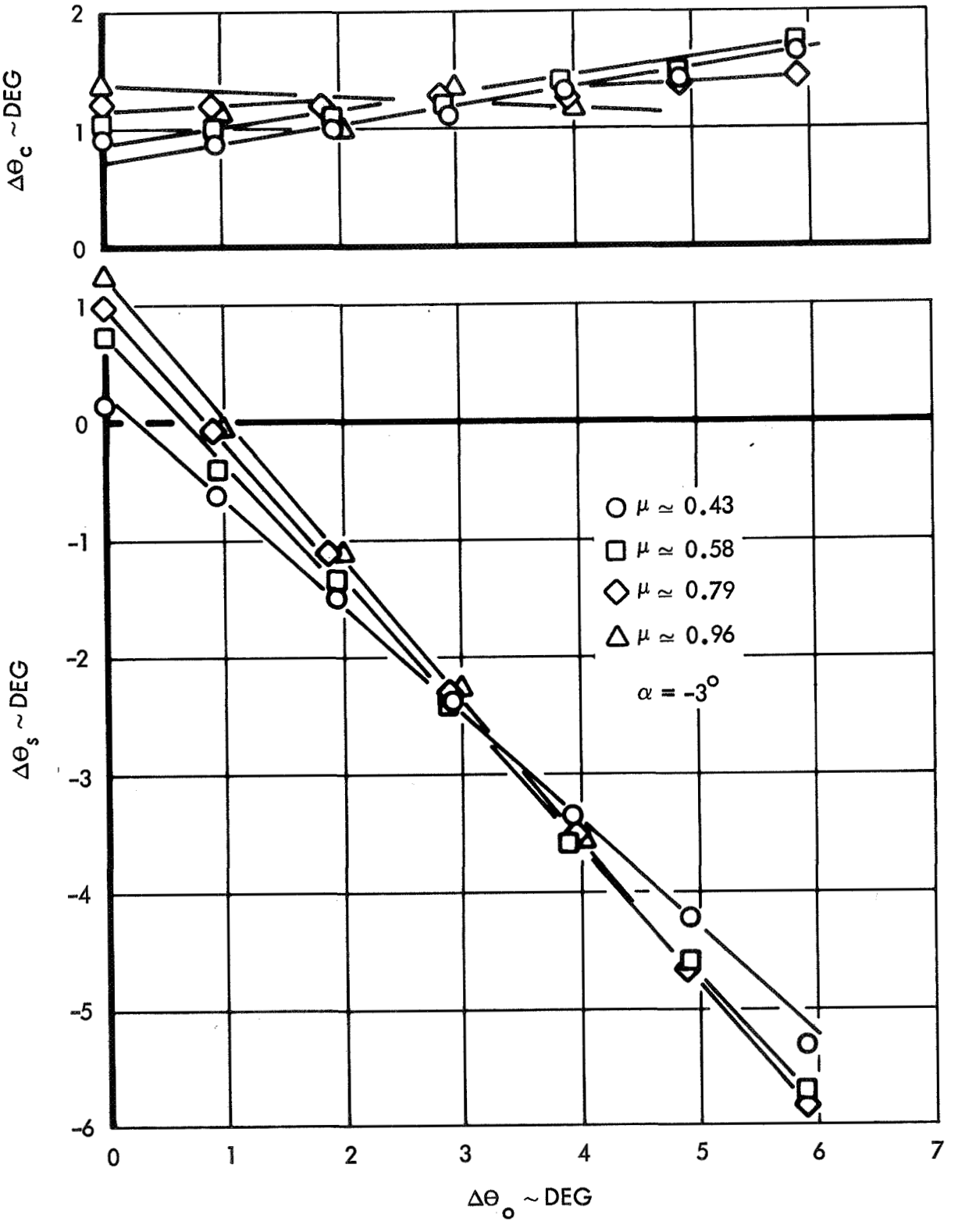

Figure 27. Cyclic Pitch Required for Rotor Trim, Configuration 1, 550 RPM, $\alpha = -3°$ (γ=5.0, P=1.56)

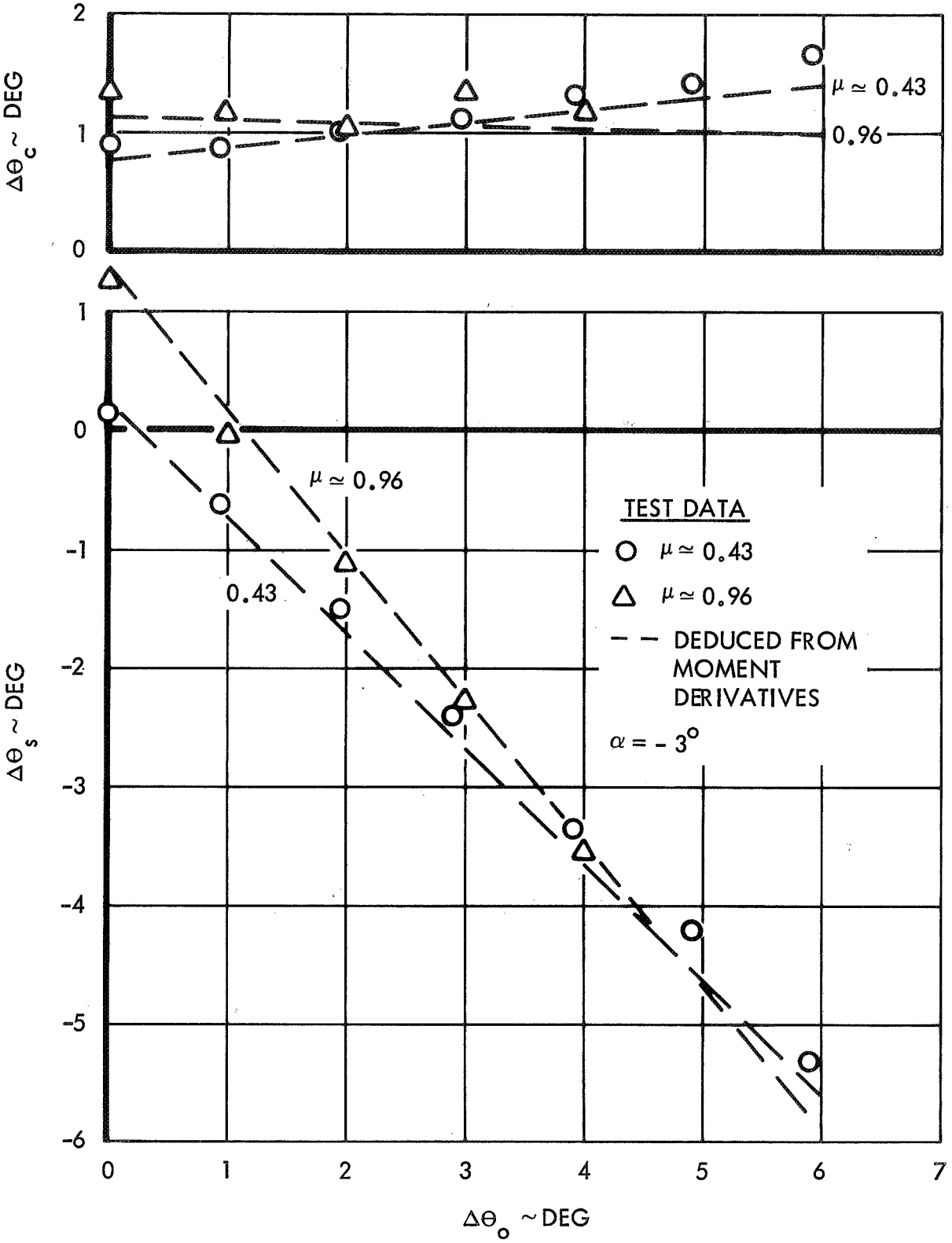

Figure 28. Comparison of Trim Cyclic Pitch Determined by Test and by Implementation of Rotor Response Derivatives, Configuration 1, 550 RPM

The good comparison of the data shown in Figure 28 greatly enhances the validity of the rotor response derivatives. It indicates that the several steps leading to their determination did not eliminate any real rotor response characteristics. That fact that the data comprised in the figure were recorded at different times during the test suggests good repeatability in the data.

The lift which was generated while the rotor was "flown" is presented in Figure 29 where C_T/σ is plotted versus θ_o for several advance ratios. The cyclic pitch required to trim the rotor at the various collective pitch values corresponds to that shown previously in Figure 27. The curves of Figure 29 indicate that the rotor lift capability at higher advance ratios is reduced when rotor trim is maintained. At the highest advance ratio ($\mu \simeq 0.96$) the reduction in rotor lift due to trim cyclic pitch is greater than that produced by collective pitch.

The data of Figure 29 provide a check of the lift response derivatives of Figure 25. The slopes of the C_T/σ vs. θ_o curves for the trimmed rotor may be calculated from the lift derivatives. The slope is simply

$$\left.\frac{\partial(C_T/\sigma)}{\partial\theta_o}\right/_{\substack{\text{rotor}\\\text{trimmed}}} = \frac{\partial(C_T/\sigma)}{\partial\theta_o} + \frac{\partial\theta_s}{\partial\theta_o}\,\frac{\partial(C_T/\sigma)}{\partial\theta_s} \qquad (6)$$

where the functional relationship between θ_o and θ_s is defined in Figure 27. The values of the trimmed $\partial(C_T/\sigma)/\partial\theta_o$ determined by test agree satisfactorily with those calculated using eq 6. The comparison is shown in Figure 29.

At this point in the discussion all of the fundamental response test data pertaining to basic rotor configuration 1 have been considered. The remaining three configurations were tested in an identical manner and summary curves showing their response characteristics are presented in Figures 30 - 48. For the most part the curves are very similar to those representing configuration 1. The number of conditions tested for each configuration varied but the quality of the data remained unchanged. The failure of the strain gages used to resolve rotating rotor moments into stationary coordinates occurred during the testing of configuration 2.

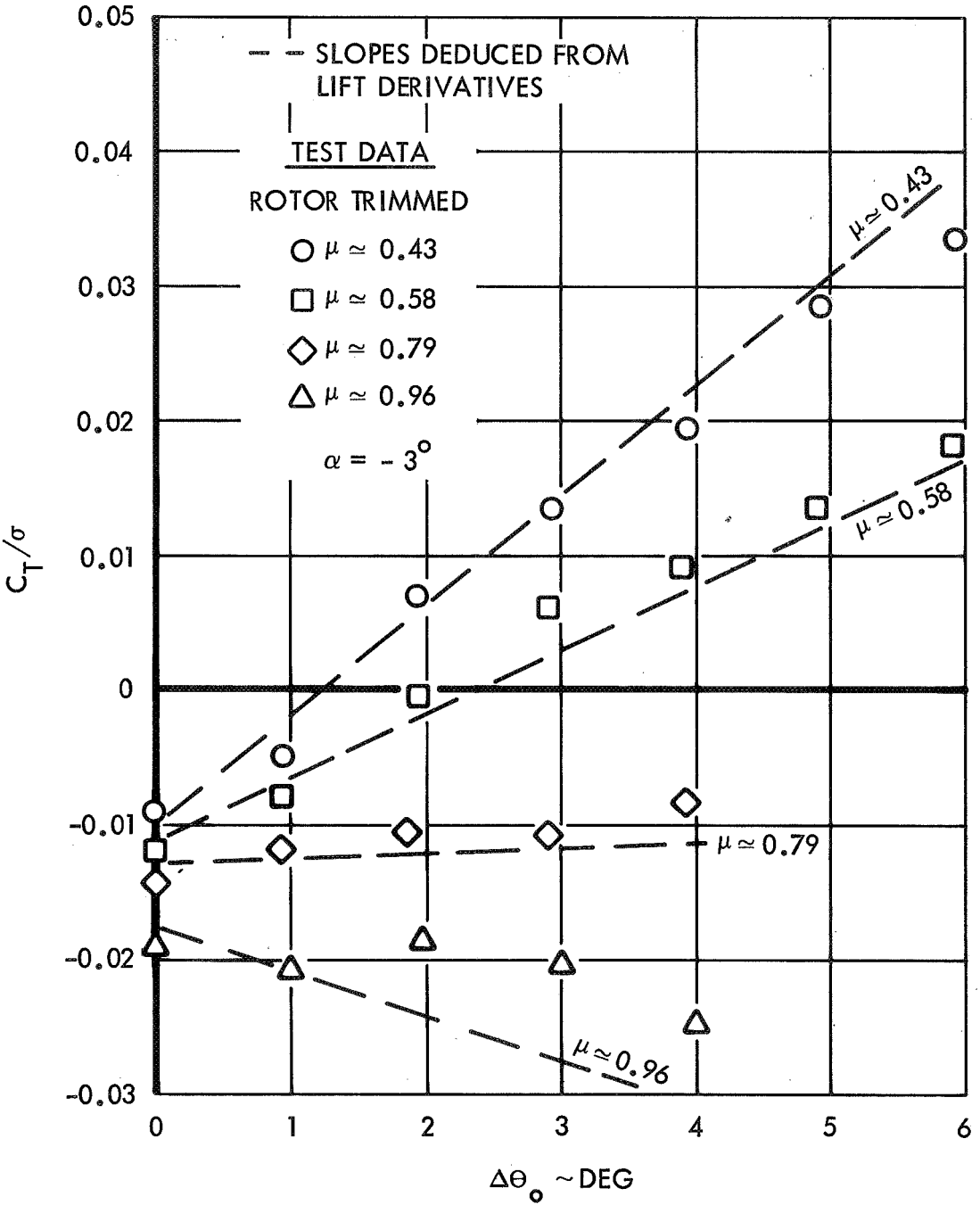

Figure 29. Lift vs Collective Pitch for the Trimmed Rotor, Configuration 1, 550 RPM (γ=5.0, P=1.56)

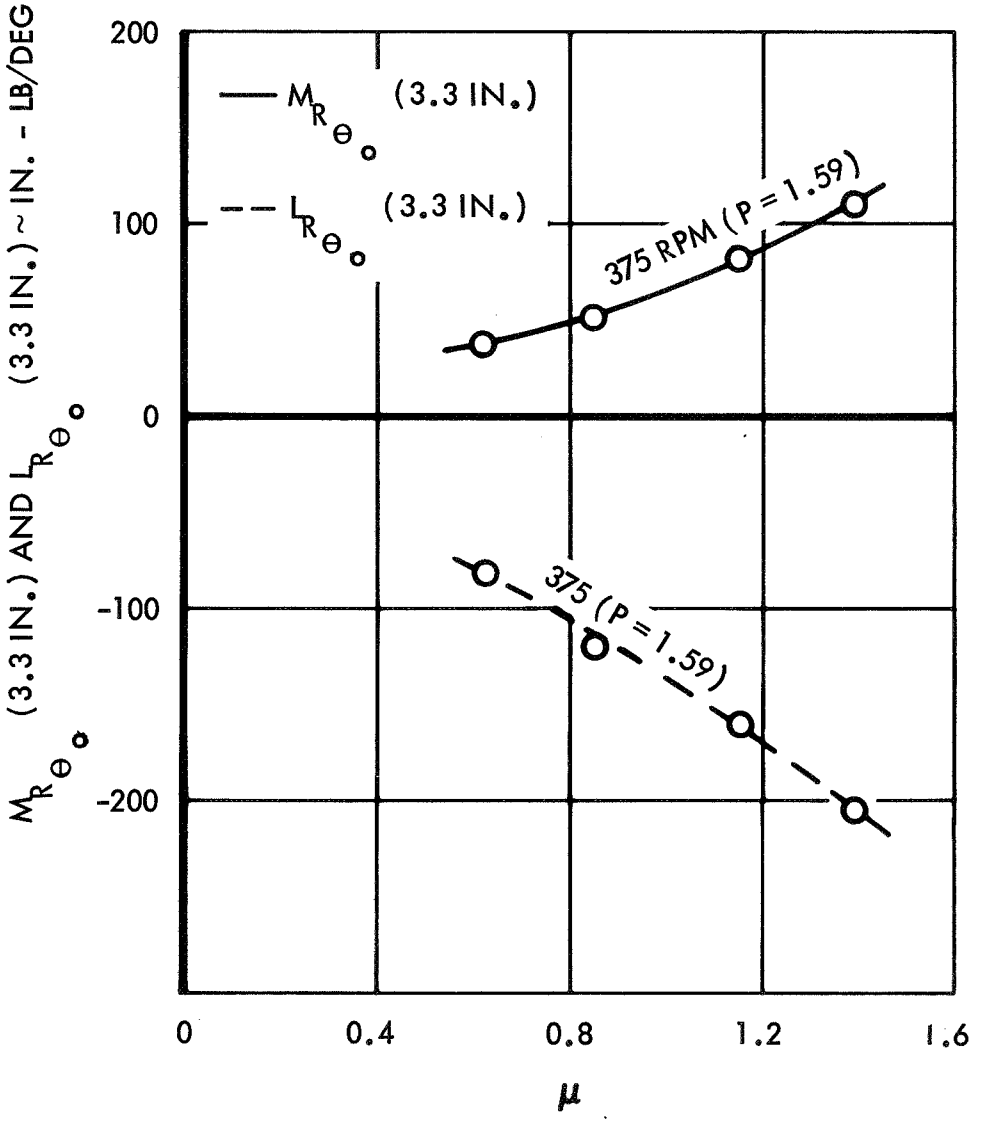

Figure 30. Rotor Pitching and Rolling Moment Derivatives with Respect to Collective Pitch, Configuration 2 (γ=3.0)

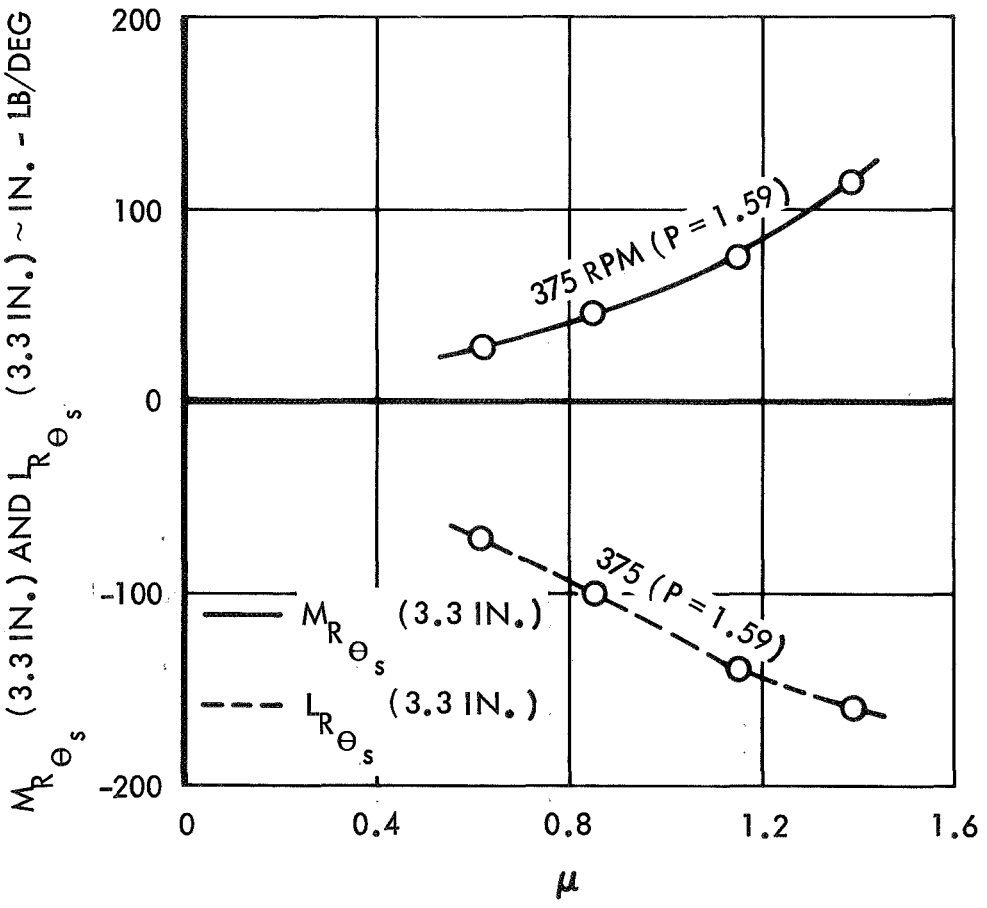

Figure 31. Rotor Pitching and Rolling Moment Derivatives with Respect to Longitudinal Cyclic Pitch, Configuration 2 (γ=3.0)

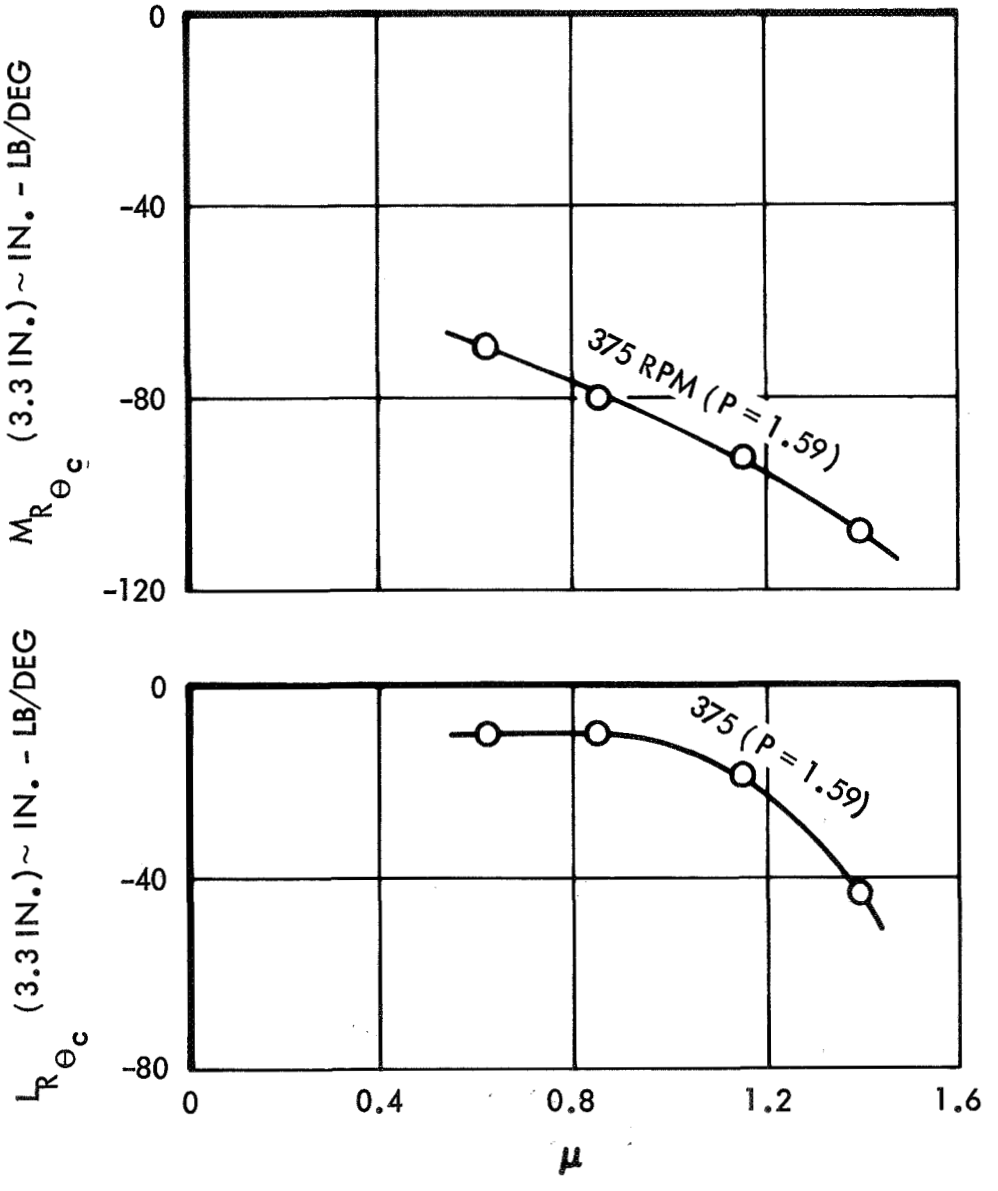

Figure 32. Rotor Pitching and Rolling Moment Derivatives with Respect to Lateral Cyclic Pitch, Configuration 2 (γ=3.0)

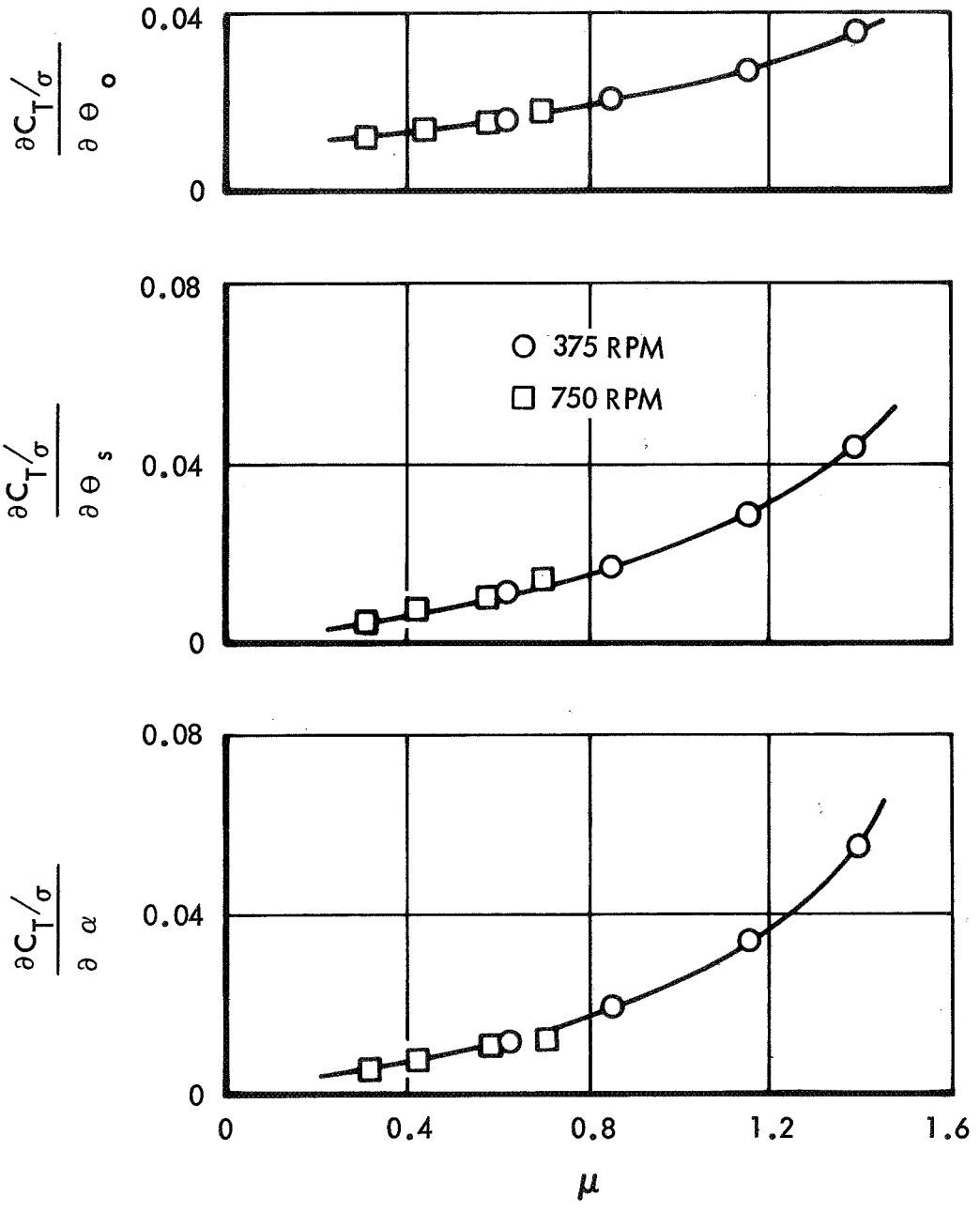

Figure 33. Rotor Lift Derivatives with Respect to Collective Pitch, Longitudinal Cyclic Pitch and Rotor Shaft Angle of Attack, Configuration 2 (γ=3.0)

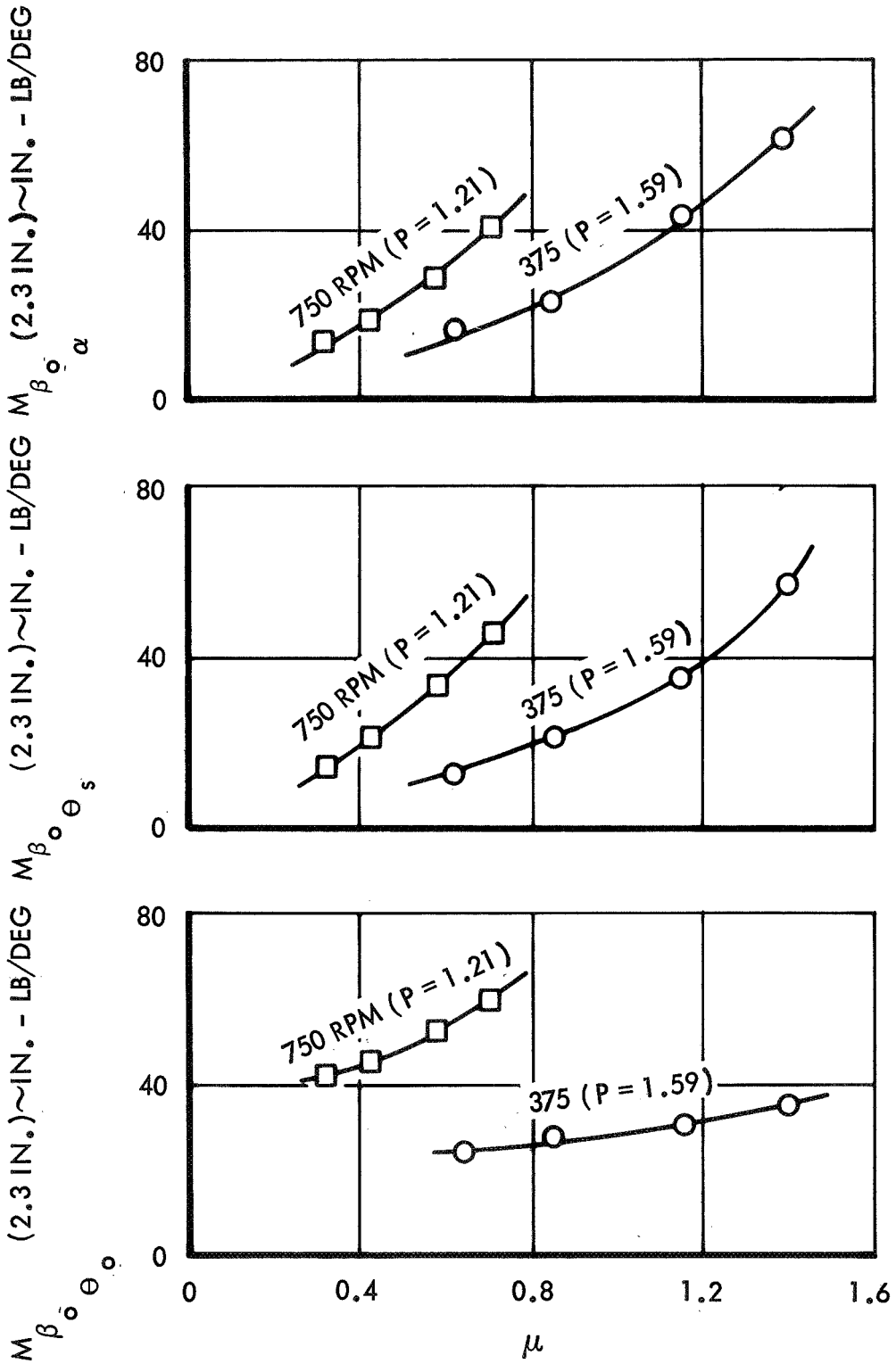

Figure 34. Steady Rotating Blade Moment Derivatives, Configuration 2 (γ=3.0)

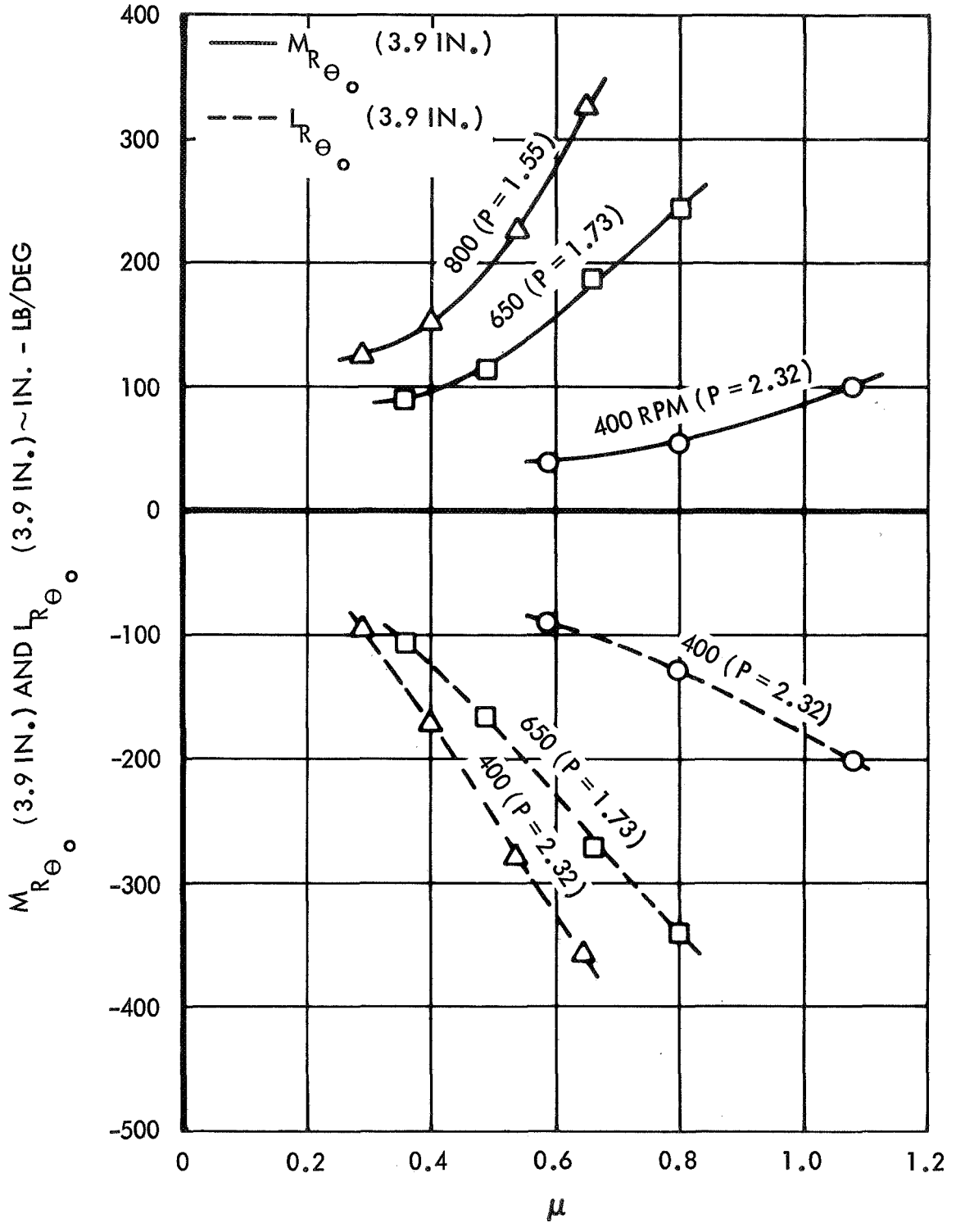

Figure 35. Rotor Pitching and Rolling Moment Derivatives with Respect to Collective Pitch, Configuration 3 (γ=5.0)

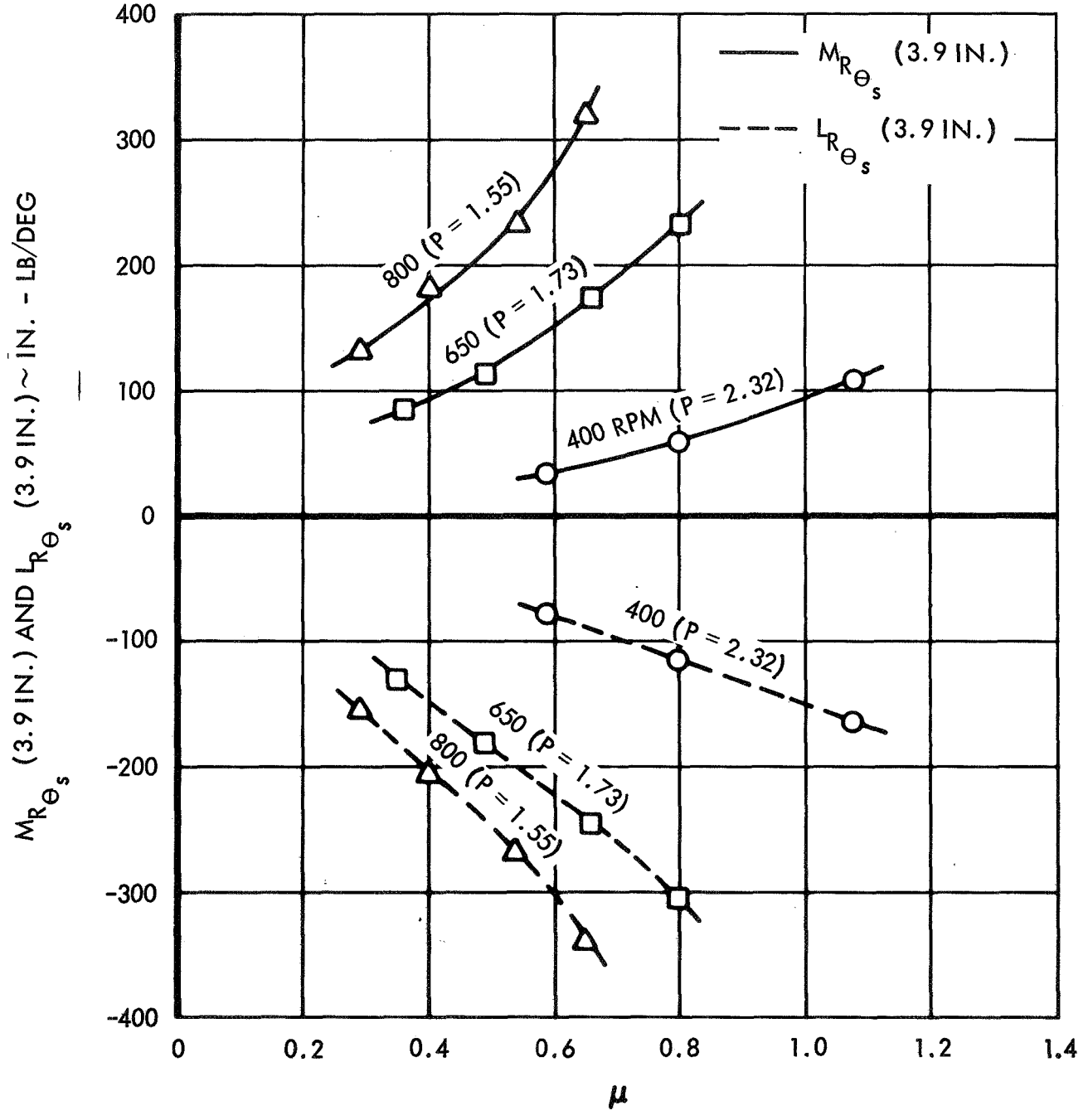

Figure 36. Rotor Pitching and Rolling Moment Derivatives with Respect to Longitudinal Cyclic Pitch, Configuration 3 (γ=5.0)

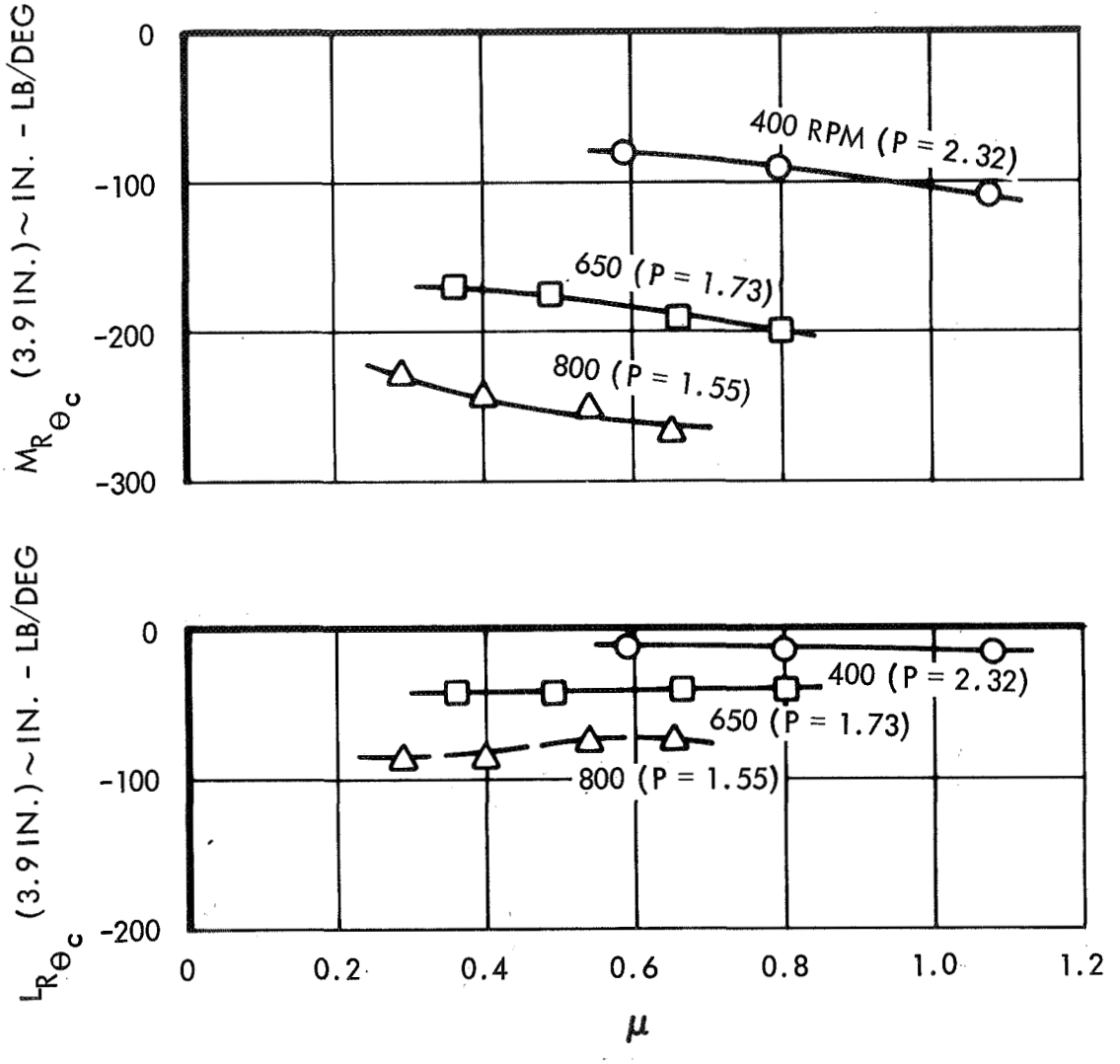

Figure 37. Rotor Pitching and Rolling Moment Derivatives with Respect to Lateral Cyclic Pitch, Configuration 3 (γ=5.0)

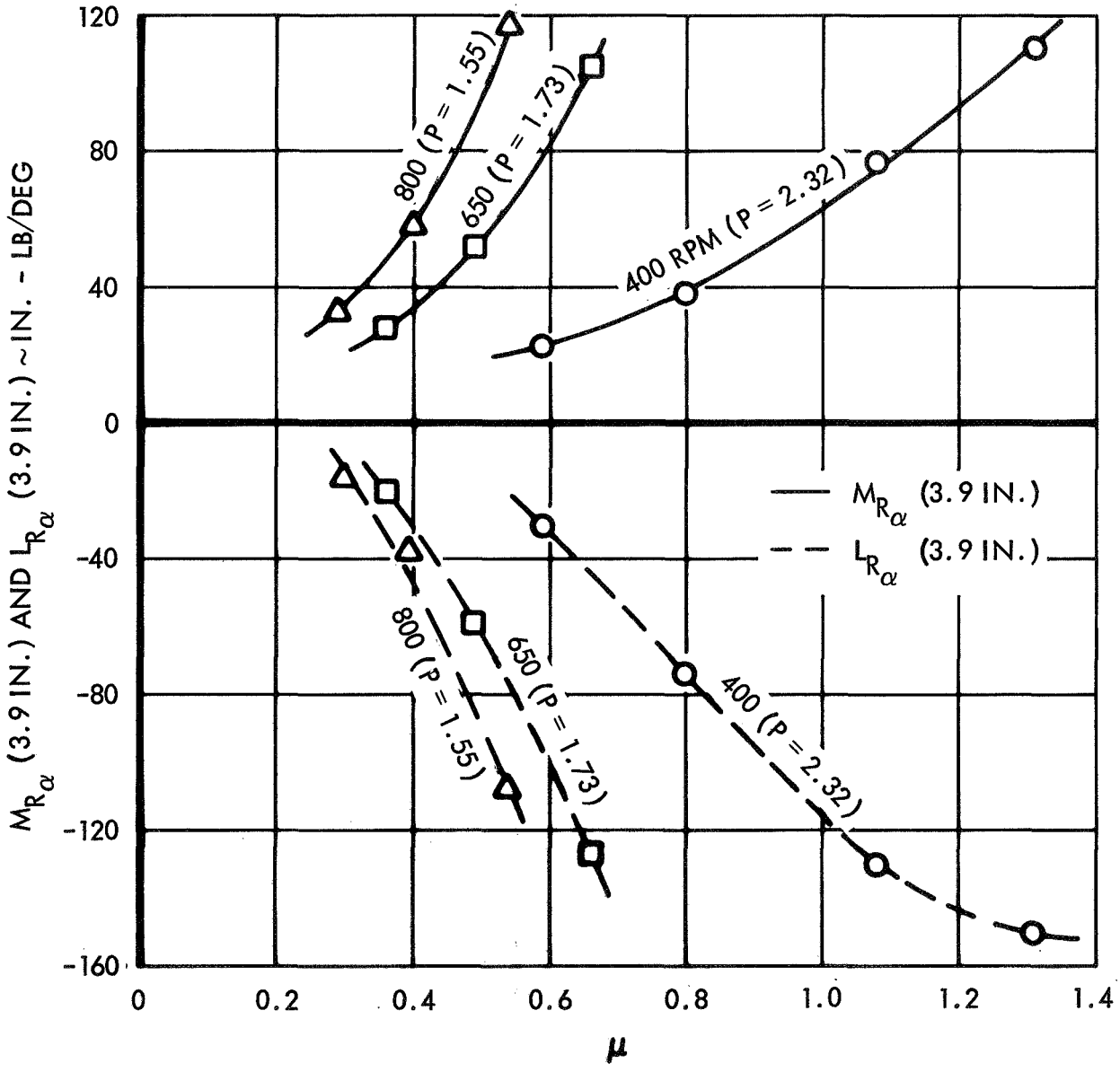

Figure 38. Rotor Pitching and Rolling Moment Derivatives with Respect to Angle of Attack, Configuration 3 (γ=5.0)

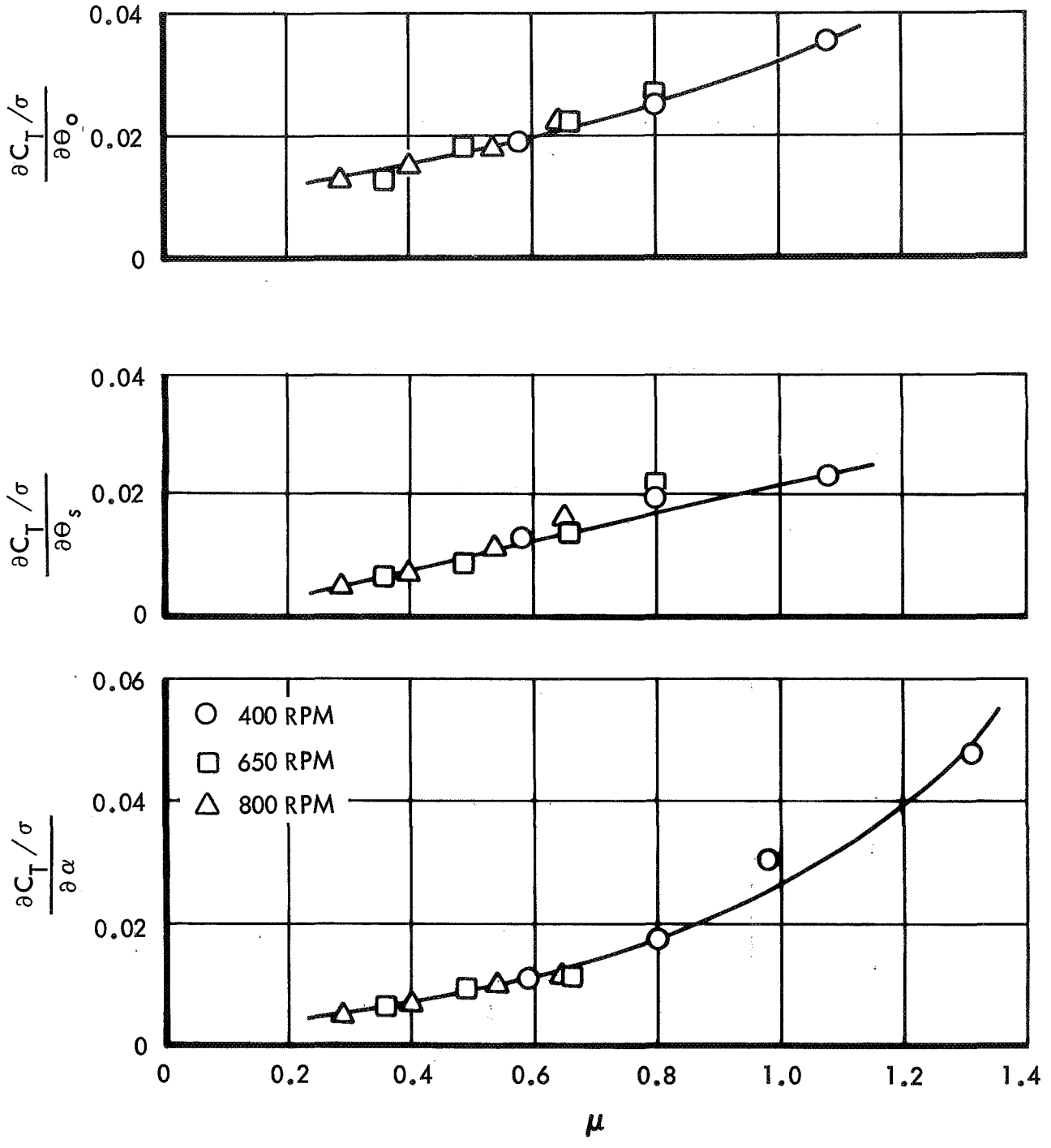

Figure 39. Rotor Lift Derivatives with Respect to Collective Pitch, Longitudinal Cyclic Pitch and Rotor Shaft Angle of Attack, Configuration 3 (γ=5.0)

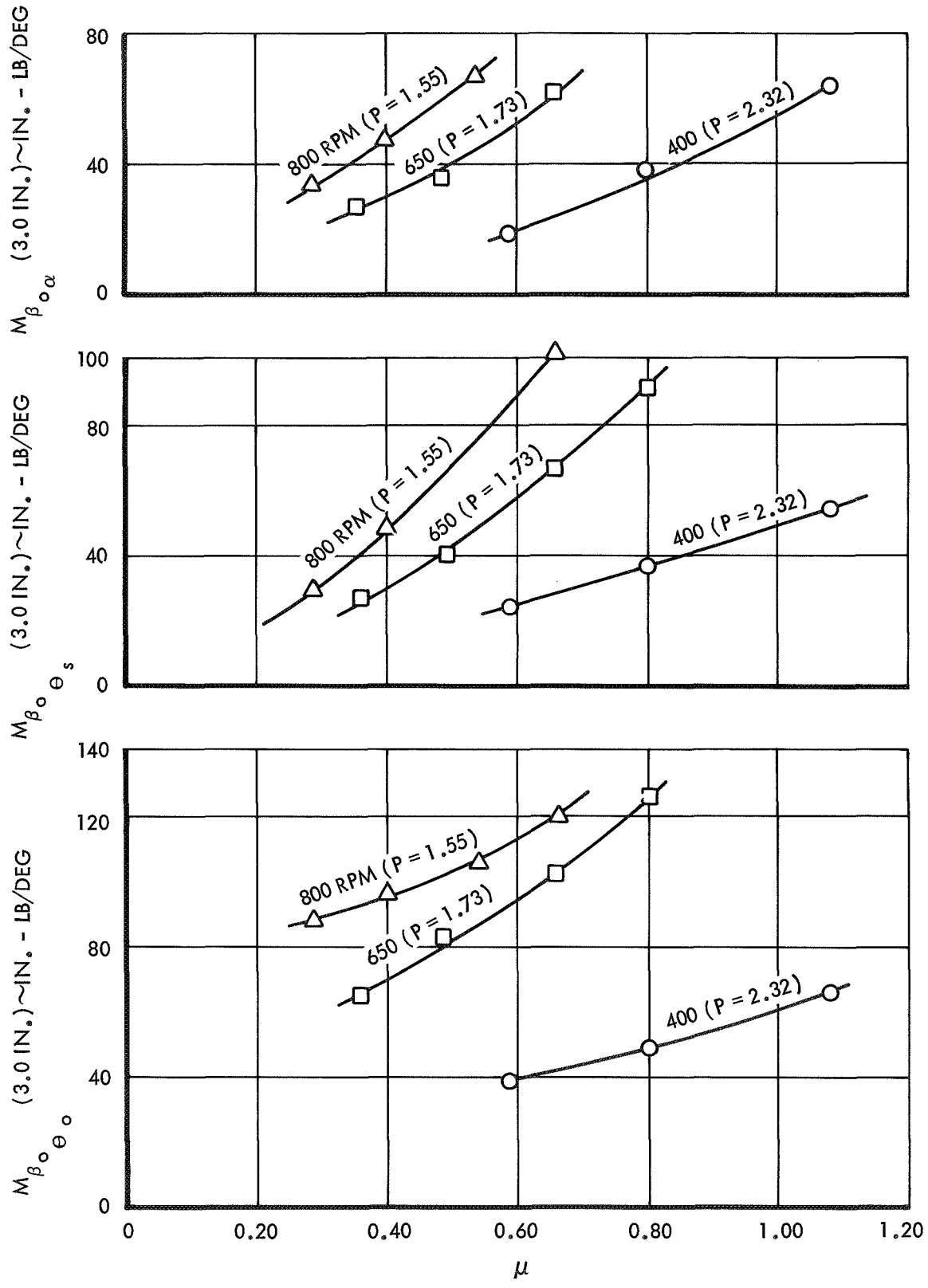

Figure 40. Steady Rotating Blade Moment Derivatives, Configuration 3 (γ=5.0)

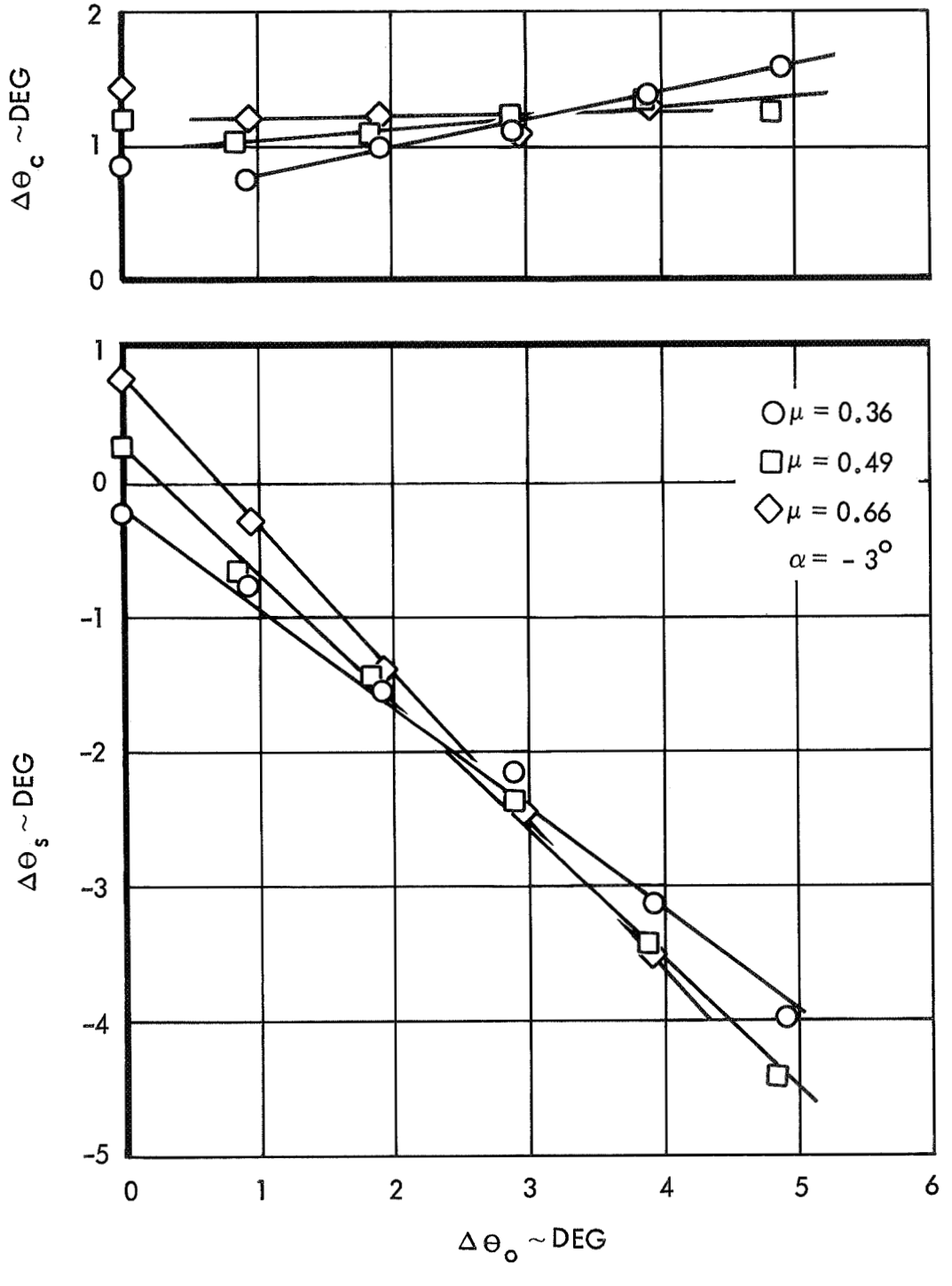

Figure 41. Cyclic Pitch Required for Rotor Trim, Configuration 3, 650 RPM, α=-3° (γ=5.0, P=1.73)

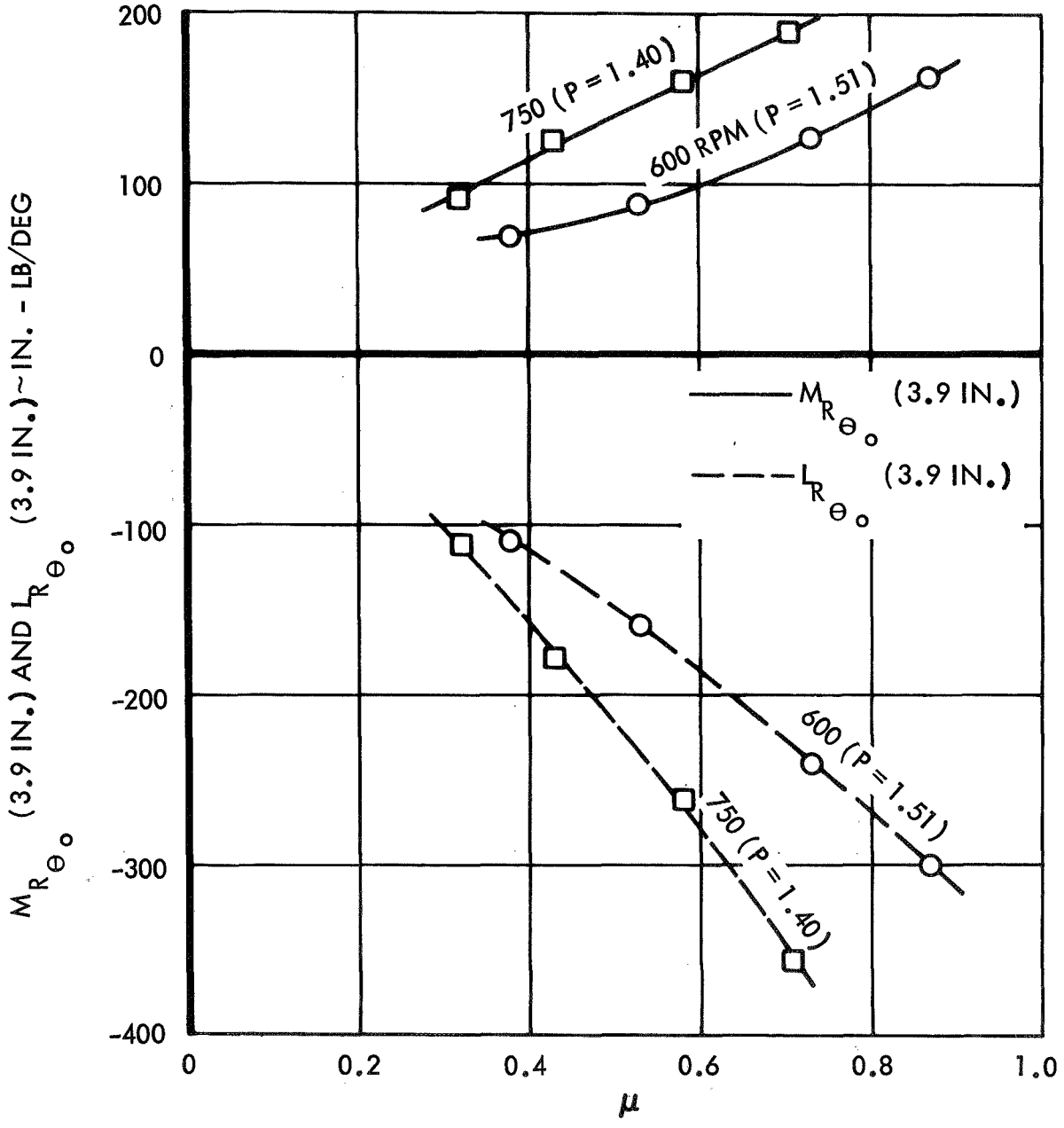

Figure 42. Rotor Pitching and Rolling Moment Derivatives with Respect to Collective Pitch, Configuration 4 (γ=3.0)

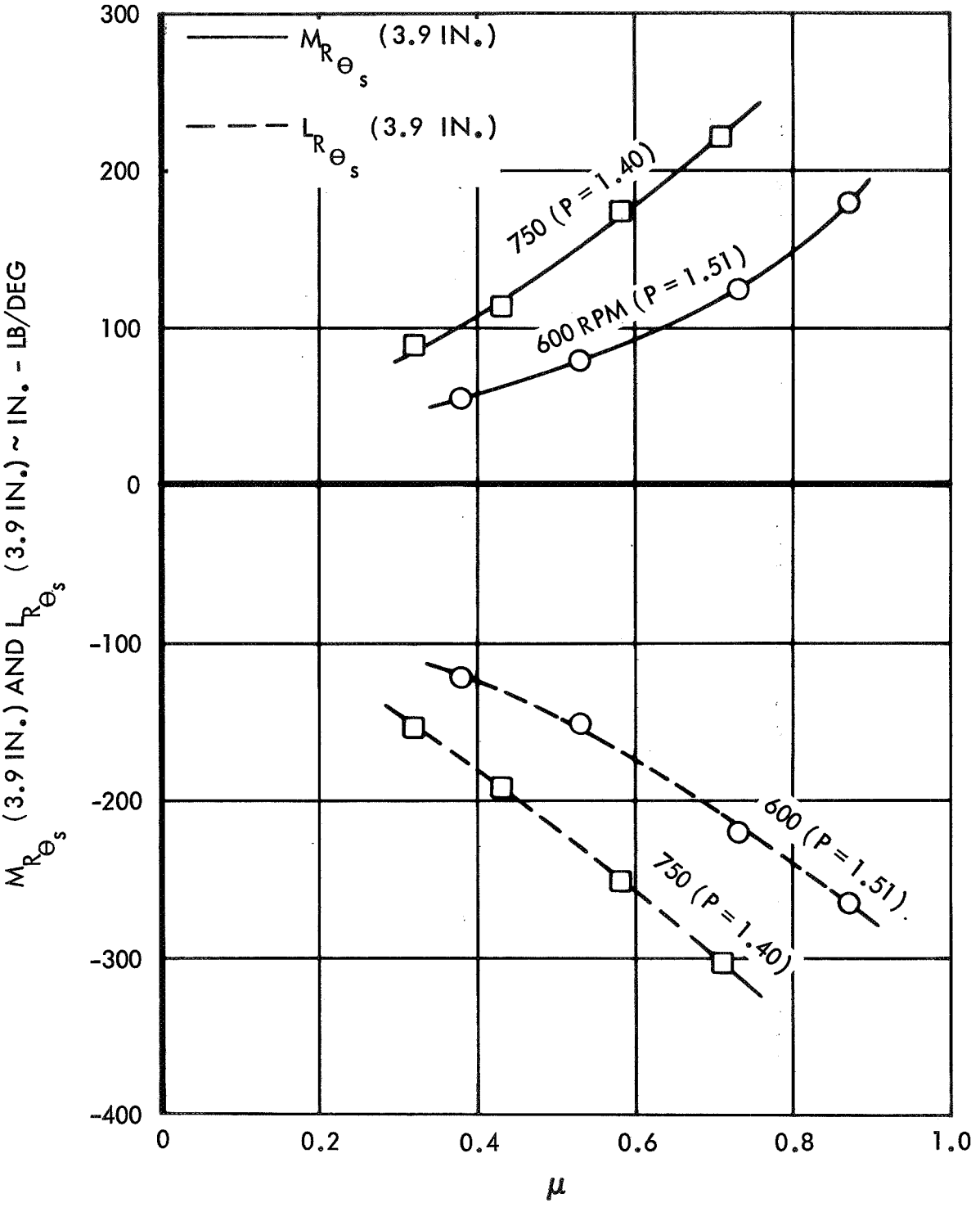

Figure 43. Rotor Pitching and Rolling Moment Derivatives with Respect to Longitudinal Cyclic Pitch, Configuration 4 (γ=3.0)

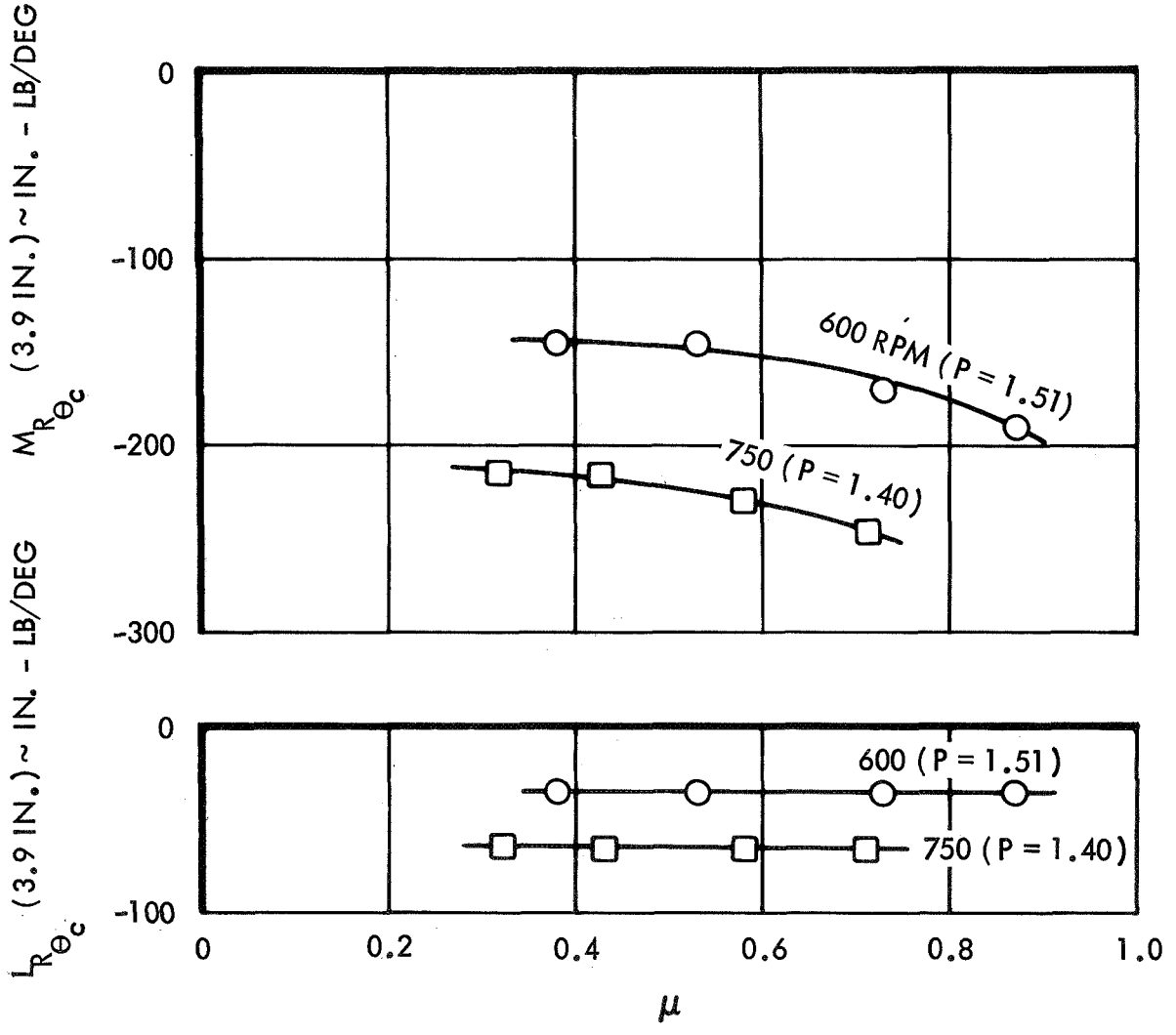

Figure 44. Rotor Pitching and Rolling Moment Derivatives with Respect to Lateral Cyclic Pitch, Configuration 4 (γ=3.0)

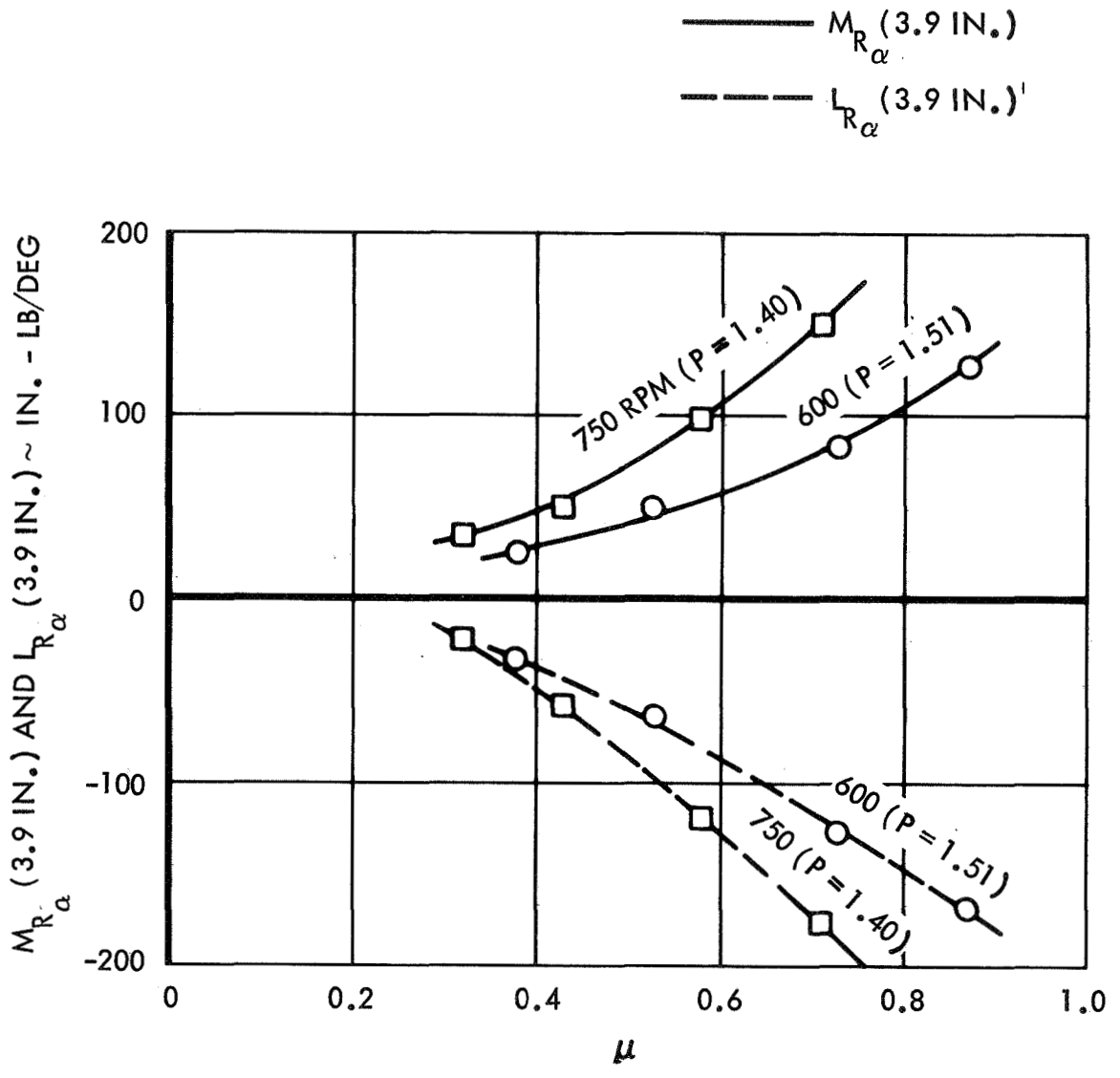

Figure 45. Rotor Pitching and Rolling Moment Derivatives with Respect to Angle of Attack, Configuration 4 (γ=3.0)

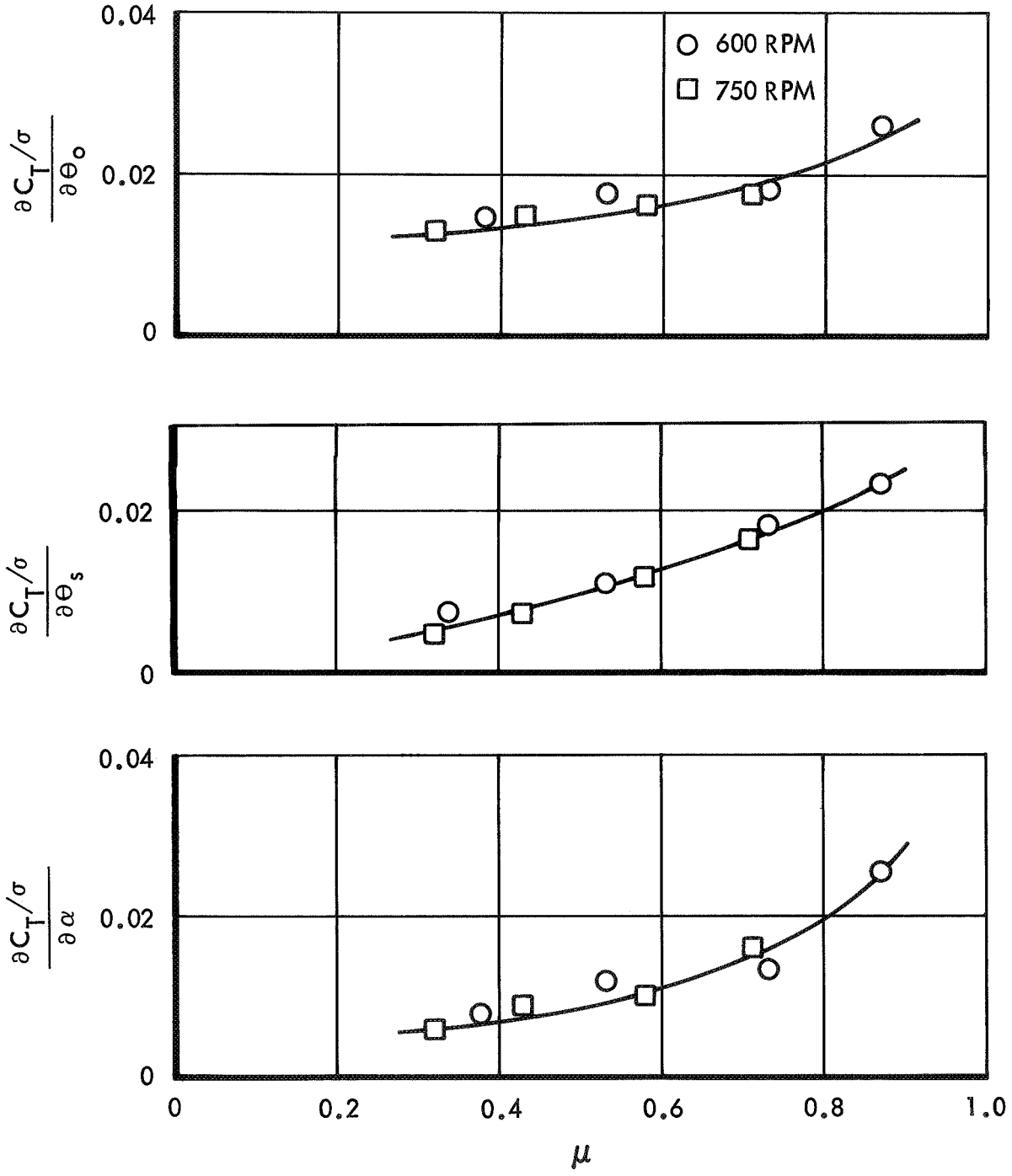

Figure 46. Rotor Lift Derivatives with Respect to Collective Pitch, Longitudinal Cyclic Pitch and Rotor Shaft Angle of Attack, Configuration 4 (γ=3.0)

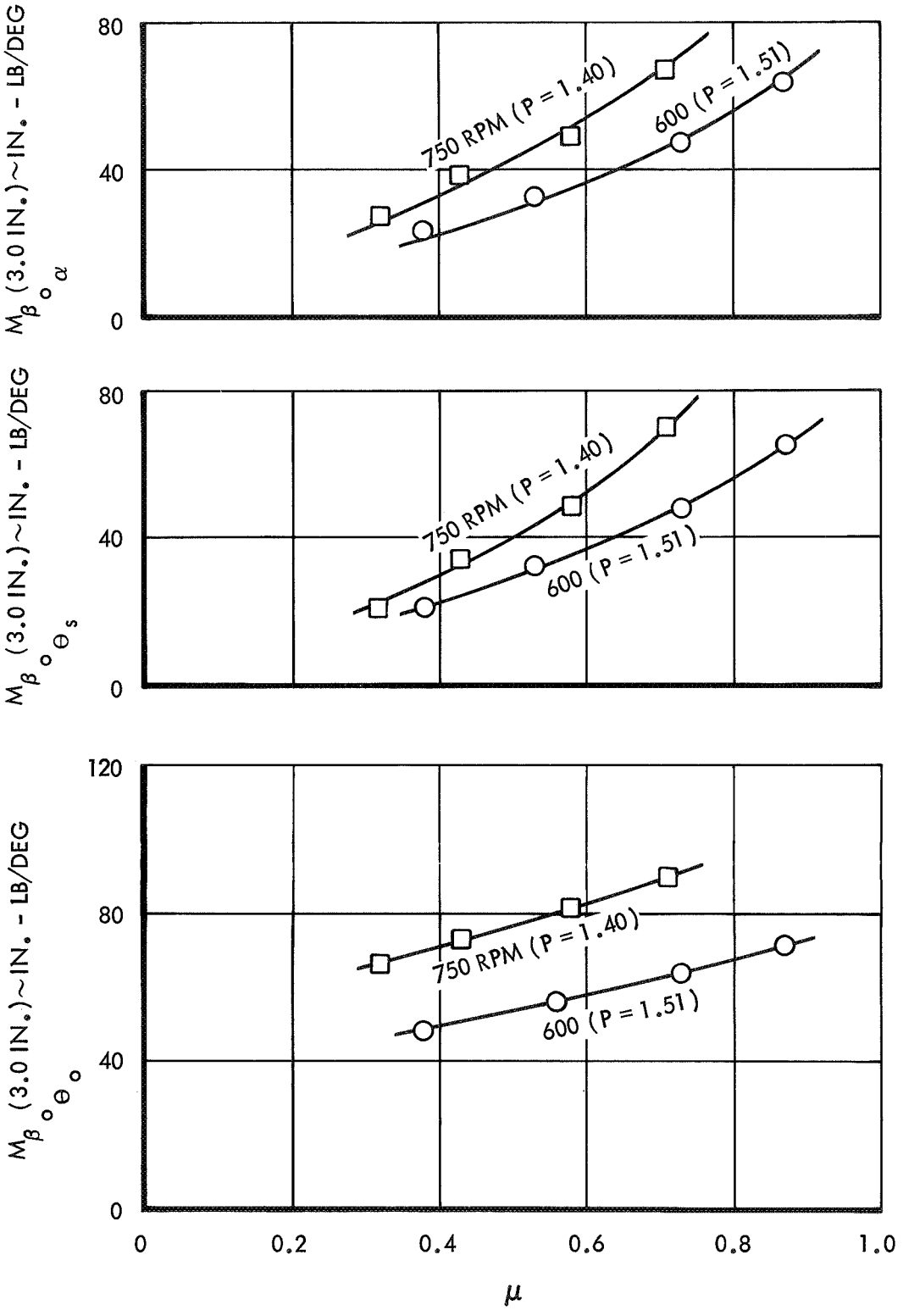

Figure 47. Steady Rotating Blade Moment Derivatives, Configuration 4 (γ=3.0)

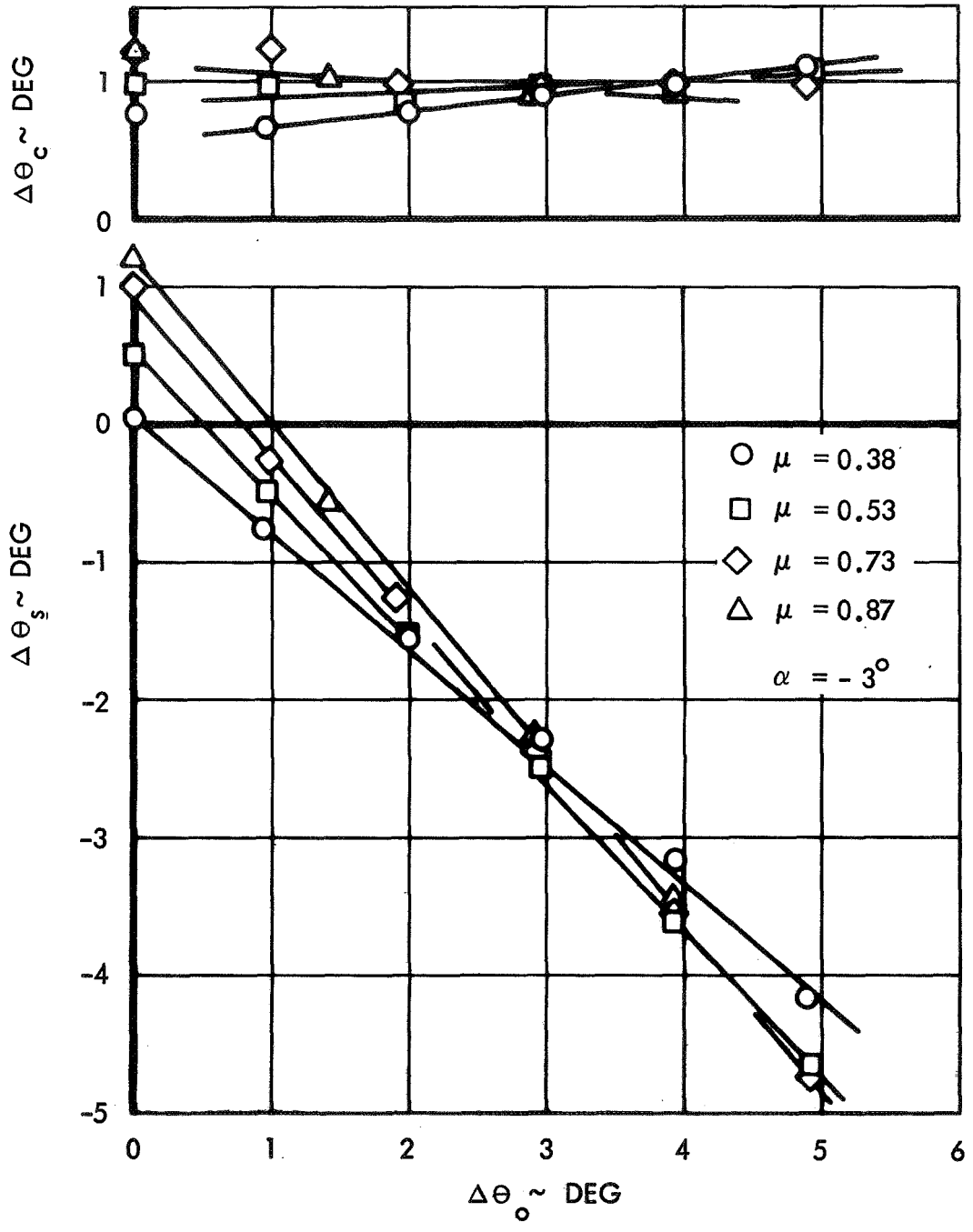

Figure 48. Cyclic Pitch Required for Rotor Trim, Configuration 4, 600 RPM, α=-3° (γ=3.0, P=1.51)

Consequently the reader will note that moment derivatives at only one rotor speed are presented and that similar derivatives with respect to shaft angle of attack are excluded. The acquisition of lift data was not affected by the strain gage failures and all such data are presented. It is noted that the missing response characteristics for configuration 2 can be obtained from the harmonic analysis of the rotating blade flapping moment.

ROTOR STABILITY TEST DATA

The stability of configurations 1 and 2 were examined at the conclusion of the response tests. Table 3 summarizes the flight conditions which were considered.

TABLE 3

ROTOR STABILITY TEST CONDITIONS

Configuration	RPM	P	μ Range
1 (γ = 5.0)	800	1.33	0→0.94
	550	1.56	0→1.35
	300	2.32	0→2.15
2 (γ = 3.0)	650	1.27	0→1.13

The test procedure consisted simply of increasing the tunnel velocity in small increments while maintaining a constant rotor rotational speed. A collective pitch setting of ~0.5 deg was maintained and the rotor was trimmed as required to reduce blade loads. The rotor blade flap bending and torsion moments were continuously monitored for signs of an instability.

For the conditions tested the rotor did not exhibit any classical signs of an approaching instability. The rotor response was almost always in a transient state because of the wind tunnel turbulence. Indications of one-half-per-rev flapping frequencies and integer multiples thereof could not be seen in the flap bending moment time histories. Large changes in flapping and torsion moments with moderate increases in advance ratio did not occur. However, the rotor did become sensitive to the tunnel turbulence. Large

transient flapping response (i.e., maximum allowable blade stresses) to the turbulence limited the testing to tunnel dynamic pressures of 100 psf or less.

An interesting phenomenon occurred during the stability testing of configuration 1 at 800 RPM. A splitting of the rotor tip-path plane was observed at the higher advance ratios. The occurence was first observed at $\mu \simeq 0.80$. The spread increased with increasing forward velocity and was approximately 2 in. at the rotor tip at $\mu \simeq 0.94$. An examination of the rotating blade flapping moment time history indicated that the split was not caused by a one-half-per-rev flapping oscillation. Also, since the blade tip Mach number was low it is unlikely that the Sikorsky experience (Ref. 4) with split tip path planes is applicable. The blade tips will be color coded for the Phase 2 test and a color movie of the phenomenon taken so that the nature of the rotor motion can be more explicity defined.

SECTION 7

COMPARISON OF THEORY AND TEST DATA

The mathematical model described in Appendix A has been used to predict the dynamic characteristics of the model rotor at high advance ratios. A comparison of the theoretical results with the test data will be shown in this section. Both rotor stability and constant and first order steady state response will be considered. Theoretical steady state rotor response was determined from a Fourier analysis of blade flapping. Stability was ascertained using the Floquet State Transition Matrix approach.

Before any comparison can be accomplished it is necessary to describe the rotor and the test data in nondimensional terms. For purposes of comparing with the stated theory, the rotor is described by its nondimensional flapping frequency, P, and its Lock number, γ. The values for these parameters for all basic rotor configurations at the tested rotor speeds have been listed previously in Tables 2 and 3.

The test data can be nondimensionalized by calculating the first order blade flapping angle from the rotor moments and rotor stiffness. The stiffness, K_θ, has been calculated analytically using the same coupled aerostructures response analysis used to calculate blade natural frequencies. K_θ has the dimensions in.-lb/deg and is calculated from the shaft moment and deflection at the 3/4 radial position associated with the first flap bending mode. Figure 49 presents the stiffness of the four rotor configurations as a function of rotor speed.

The rotor moments recorded during the test were sensed by strain gages which were radially offset from the center of rotation. Therefore the stiffness values of Figure 49 are not directly applicable. They must be reduced by the ratio of the blade bending moment at the location of the strain gages to the moment at the center of rotation. The blade radial bending moment distributions in hover for the four basic rotor configurations are shown in Figure 50 at three rotor speeds. By modifying the rotor stiffnesses shown in Figure 49 according to the distributions of Figure 50 radially offset rotor

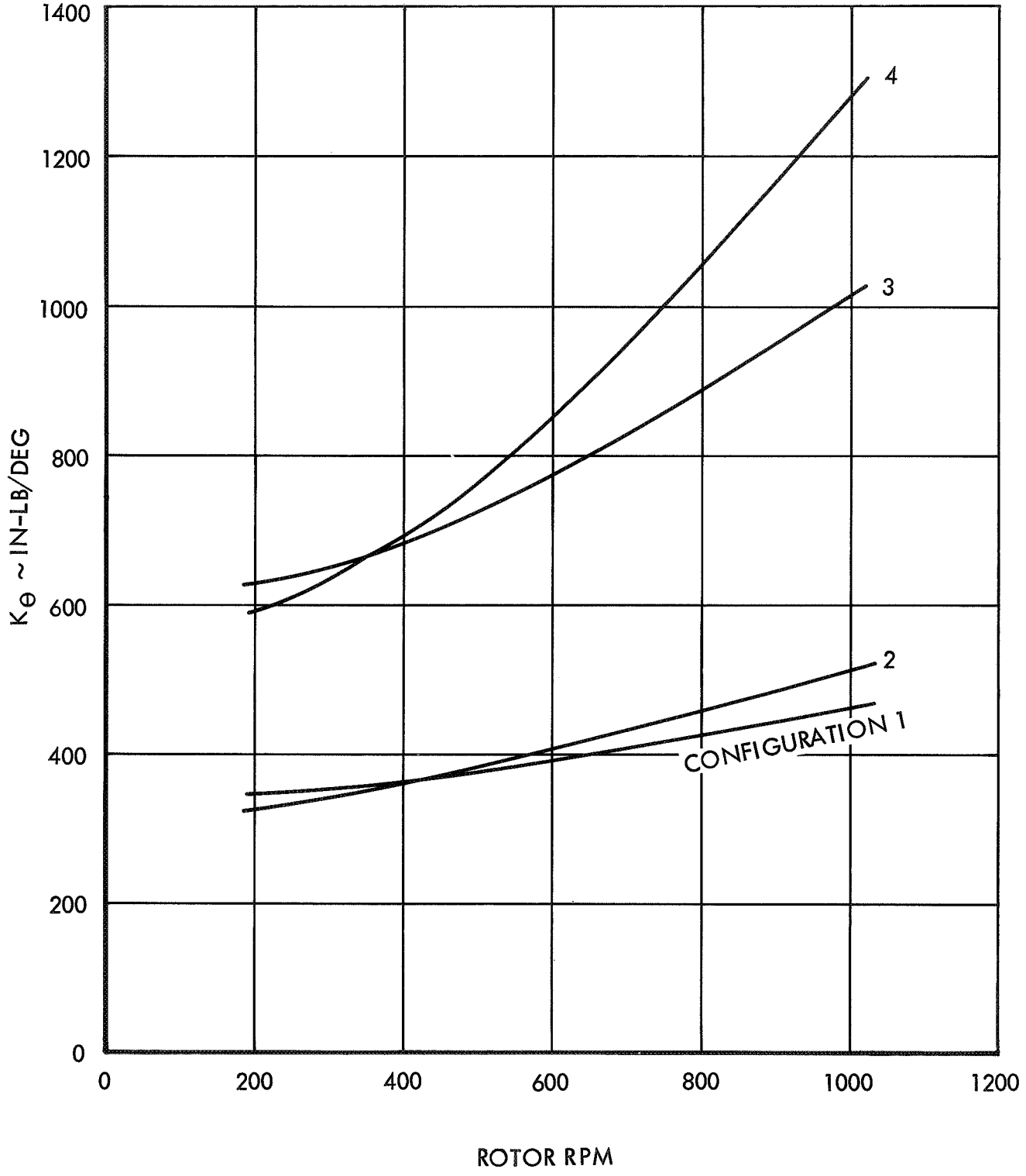

Figure 49. Rotor Stiffness

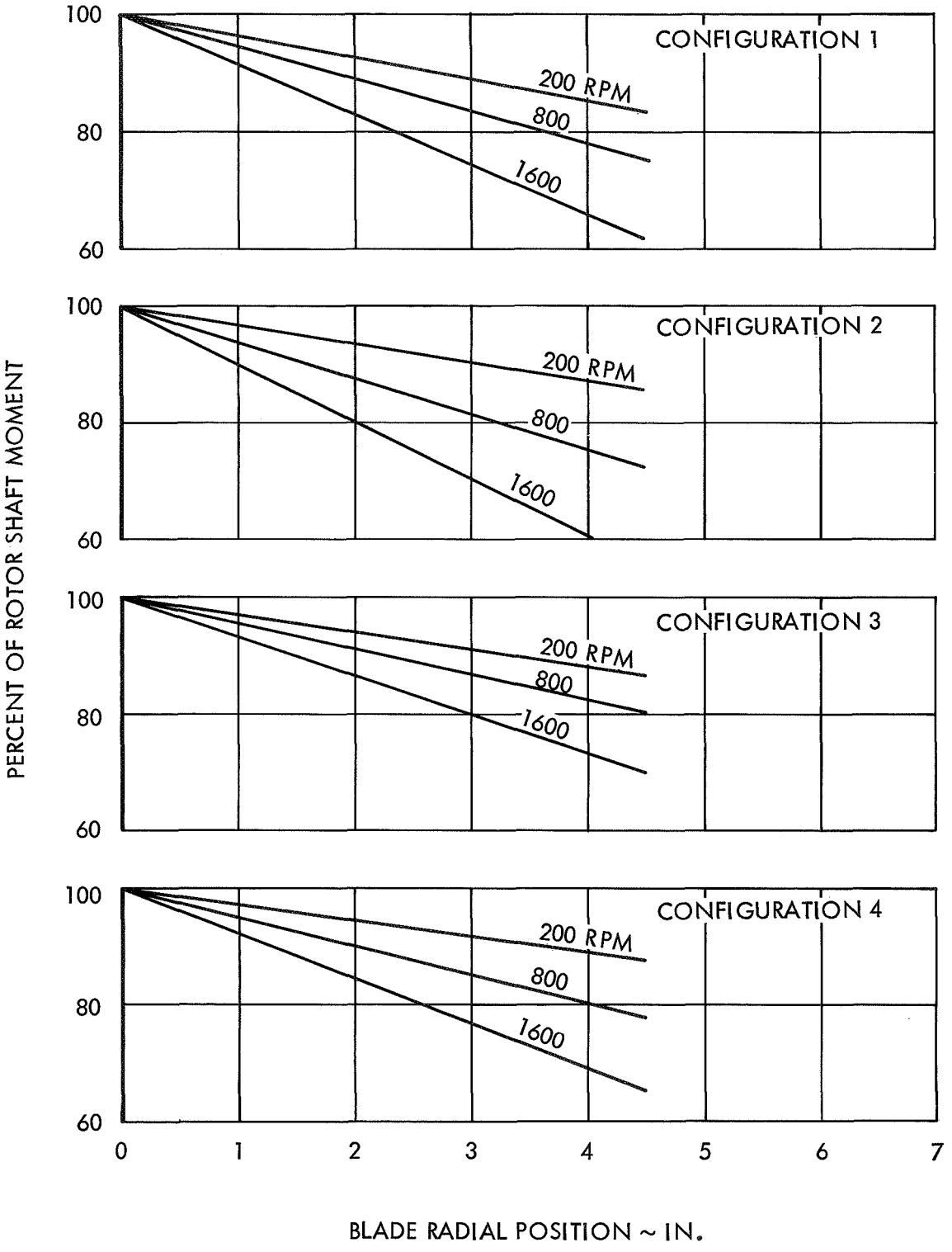

Figure 50. Radial Distribution of Rotor Flap Bending Moment

stiffnesses are available. The adjusted stiffnesses required to reduce all rotor moment test data to nondimensional form are listed in Table 4.

TABLE 4

RADIALLY OFFSET ROTOR AND BLADE STIFFNESS

Configuration	RPM	K_θ @ 3.3 In. or 3.9 In. (in.-lb/deg)	K_β @ 2.3 In. or 3.0 In. (in.-lb/deg)
1	1000	368	NA
K_θ gages at 3.3 in.	800	348	186
K_β gage at 2.3 in.	600	331	NA
	550	327	172
	300	309	161
2	1000	400	NA
K_θ gages at 3.3 in.	750	360	193
K_β gage at 2.3 in.	600	340	NA
	375	310	162
3	1000	830	NA
K_θ gages at 3.9 in.	800	736	386
K_β gage at 3.0 in.	650	672	350
	600	653	NA
	400	592	306
4	1000	990	NA
K_θ gages at 3.9 in.	750	802	425
K_β gage at 3.0 in.	600	716	375

With the flapping angle conventionally defined as

$$\beta = a_o - a_1 \cos \psi - b_1 \sin \psi - \ldots .$$

the fore-aft (a_1) and lateral (b_1) tilts of rotor are calculated from the test data.

$$a_1 = M_R \text{ (@sta r)}/K_\theta \text{ (@sta r)} \qquad (7)$$

$$b_1 = L_R \text{ (@sta r)}/K_\theta \text{ (@sta r)} \qquad (8)$$

where r is the radial position of the strain gages.

The stiffness data and bending moment distributions of Figures 49 and 50 can also be used to reduce rotating blade flap bending moments to nondimensional form. One must simply recognize that the blade stiffness, K_β, is one-half the rotor stiffness, K_θ. Consequently, blade coning (a_o) can be computed from the steady blade flapping moment.

$$a_o = M_{\beta_o} \text{ (@sta r)}/K_\beta \text{ (@sta r)} \qquad (9)$$

Required K_β - values are also tabulated in Table 4.

An alternate method of non-dimensionalizing the test data is to adjust the measured moment derivatives to the rotor shaft according to the distributions of Figure 50 and nondimensionalize by the rotor stiffnesses of Figure 49. As an aid to those preferring this latter method and analysis techniques which compute shaft moments the experimental response derivatives have been adjusted to the center of rotation. They are tabulated in Table 5.

The theoretical constant and first order rotor flapping response is compared with test data in the 12 figures that follow. The format of the curves is the same as that used for the presentation of the test data except angular derivatives with respect to the several excitations are shown instead of moment derivatives. As has been explained the conversion is simply

$$\left.\begin{aligned} a_{o_{\theta_o}} &= M_{\beta_{o_{\theta_o}}} \text{ (sta r)}/K_\beta \text{ (sta r)} \\ a_{1_{\theta_o}} &= M_{R_{\theta_o}} \text{ (sta r)}/K_\theta \text{ (sta r)} \\ b_{1_{\theta_o}} &= L_{R_{\theta_o}} \text{ (sta r)}/K_\theta \text{ (sta r)} \end{aligned}\right\} \qquad (10)$$

TABLE 5

ROTOR RESPONSE DERIVATIVES ADJUSTED TO THE CENTER OF ROTATION

Configuration	RPM	P	μ	$M_{\beta_o}{}_{\alpha}$ in.-lb/deg	M_{R_α} in.-lb/deg	L_{R_α} in.-lb/deg	$M_{\beta_o}{}_{\theta_o}$ in.-lb/deg	$M_{R_{\theta_o}}$ in.-lb/deg	$L_{R_{\theta_o}}$ in.-lb/deg	$M_{\beta_o}{}_{\theta_s}$ in.-lb/deg	$M_{R_{\theta_s}}$ in.-lb/deg	$L_{R_{\theta_s}}$ in.-lb/deg	$M_{R_{\theta_c}}$ in.-lb/deg	$L_{R_{\theta_c}}$ in.-lb/deg
1	1000	1.22	0	-	-	-	-	-	-	-	79	-169	-	-
	800	1.33	0	-	-	-	-	-	-	-	31	-117	-	-
			0.29	27	46	- 5	63	147	- 83	21	159	-149	-219	-121
			0.40	37	72	- 26	-	194	-138	-	198	-171	-219	-121
			0.54	46	149	- 84	78	290	-220	49	274	-220	-235	-121
			0.66	59	240	-144	86	385	-279	71	377	-270	-259	-121
	600	1.48	0	-	-	-	-	-	-	-	7	- 65	-	-
	550	1.56	0.43	28	33	- 26	46	90	-106	18	76	-119	-131	- 43
			0.58	31	65	- 69	49	128	-171	30	111	-158	-142	- 43
			0.79	45	144	-145	61	188	-255	45	171	-229	-165	- 43
			0.96	63	204	-194	77	257	-313	67	217	-261	-182	- 43
	300	2.32	0.78	23	23	- 43	28	28	- 78	21	28	- 63	- 55	- 6
			1.07	32	36	- 69	36	54	-123	31	47	- 93	- 62	- 6
			1.44	58	73	-103	43	100	-218	46	98	-140	- 91	0
			1.75	91	155	-109	50	177	-323	58	164	-232	-114	20
2	1000	1.14	0	-	-	-	-	-	-	-	60	-172	-	-
	750	1.21	0	-	-	-	-	-	-	-	35	-114	-	-
			0.32	17	-	-	49	-	-	16	-	-	-	-
			0.43	21	-	-	52	-	-	24	-	-	-	-
			0.58	34	-	-	60	-	-	38	-	-	-	-
			0.71	46	-	-	69	-	-	53	-	-	-	-
	600	1.31	0	-	-	-	-	-	-	-	13	- 74	-	-
	375	1.59	0.62	19	-	-	26	43	- 95	14	32	- 83	- 80	- 12
			0.85	25	-	-	31	59	-140	24	52	-114	- 92	- 12
			1.15	47	-	-	33	95	-185	39	88	-160	-107	- 22
			1.39	67	-	-	39	127	-238	63	130	-182	-125	- 50
3	1000	1.43	0	-	-	-	-	-	-	-	63	-221	-	-
	800	1.55	0	-	-	-	-	-	-	-	24	-151	-	-
			0.29	39	40	- 21	101	154	-116	33	159	-187	-280	-106
			0.40	54	70	- 45	121	185	-205	55	220	-246	-294	-106
			0.54	77	141	-130	111	275	-338	-	282	-324	-304	- 91
			0.66	-	-	-	138	395	-531	118	388	-444	-324	- 91
	650	1.73	0.36	32	33	- 24	74	105	-125	31	101	-154	-200	- 50
			0.49	40	61	- 69	92	136	-196	45	136	-214	-200	- 50
			0.66	-	124	-150	115	222	-320	76	207	-290	-224	- 47
			0.80	70	-	-	142	289	-402	105	278	-361	-234	- 49
	600	1.80	0	-	-	-	-	-	-	-	10	- 88	-	-
	400	2.32	0.59	20	26	- 35	43	46	-105	28	39	- 90	- 93	- 13
			0.80	42	44	- 85	55	64	-147	41	69	-132	-105	- 17
			1.08	71	89	-150	73	117	-230	61	125	-188	-124	- 17
			1.31	105	128	-173	-	-	-	-	-	-	-	-
4	1000	1.30	0	-	-	-	-	-	-	-	55	-254	-	-
	750	1.40	0	-	-	-	-	-	-	-	17	-144	-	-
			0.32	31	41	- 28	77	113	-134	24	110	-188	-262	- 78
			0.43	45	61	- 72	85	153	-218	39	139	-236	-262	- 78
			0.58	58	119	-147	95	196	-321	57	216	-307	-282	- 78
			0.71	79	184	-217	105	233	-436	82	273	-372	-300	- 78
	600	1.51	0	-	-	-	-	-	-	-	19	-102	-	-
			0.38	27	30	- 38	55	82	-132	24	65	-145	-174	- 42
			0.53	38	60	- 78	64	104	-191	37	95	-180	-174	- 42
			0.73	54	98	-151	73	151	-286	55	149	-263	-202	- 42
			0.87	73	152	-200	81	194	-358	75	215	-316	-227	- 42

where a collective pitch excitation is used as an example. Theoretical predictions are indicated by dashed lines and test data by symbols. The derivatives are plotted versus advance ratio for several values of P. Recall that P is the nondimensional flapping frequency and depends upon the rotor rotational speed and the flapping restraint. It is noted that the theoretical results indicate that within the tested advance ratio range, blade torsion has a negligible effect on flapping. Measured blade torsional moments confirm this conclusion.

The theory and the test data agree well for configuration 1. Figures 51 to 54 show both the theoretical and experimental rotor response derivatives with respect to collective pitch, rotor shaft angle of attack, longitudinal cyclic pitch and lateral cyclic pitch. Generally the quality of the correlation is consistent among the four figures. The agreement deteriorates slightly with reduced P particularily with regard to lateral rotor tilt (b_1). All trends, however, are predicted excellently.

The comparison of test data and theory for configuration 2 yielded approximately the same quality of correlation obtained for configuration 1. Because of the limited amount of test data describing the response characteristics of configuration 2 and in the interest of brevity, the comparison is not shown.

The correlation of theory and test data suffers somewhat when configuration 3 is considered. The coning, fore-aft and lateral response derivatives with respect to the several excitations are compared with theoretical predictions in Figures 55 to 58. The fore-aft rotor tilt compares well for θ_o, α and θ_s excitations. The lateral rotor response to these excitations, however, indicates that the test data tend to be more conservative than the theoretical predictions. For the rotor response to lateral cyclic pitch, θ_c, the opposite is true. The experimental and theoretical lateral tilt compare well and the fore-aft tilt does not. The deterioration in the correlation with reduced P which was observed for configuration 1 is also noted for configuration 3. Despite the disagreement in the magnitudes of the predicted and actual response, the trends with both advance ratio and flapping frequency agree very well.

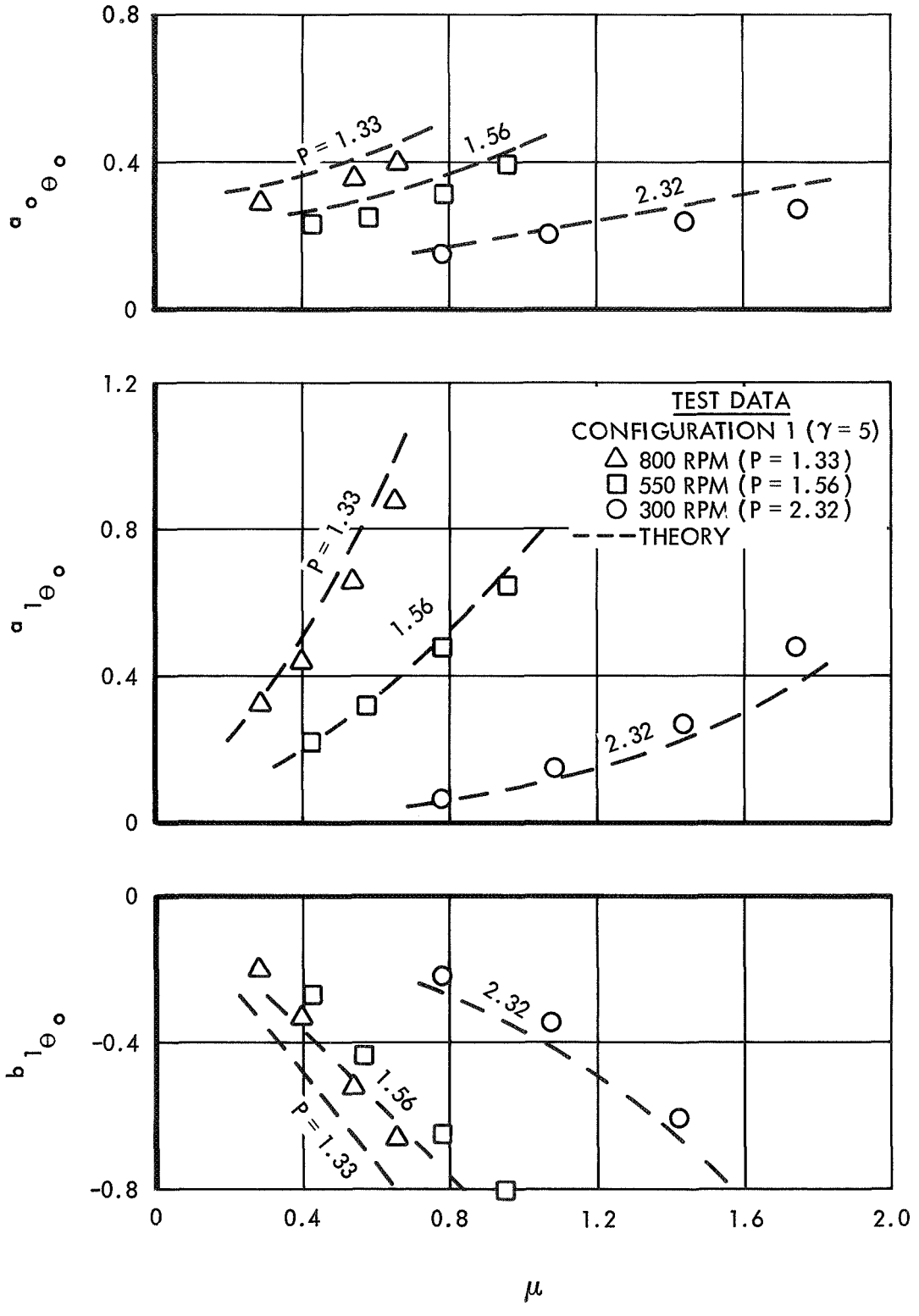

Figure 51. Comparison of Theoretical and Experimental Rotor Response Derivatives with Respect to Collective Pitch, Configuration 1

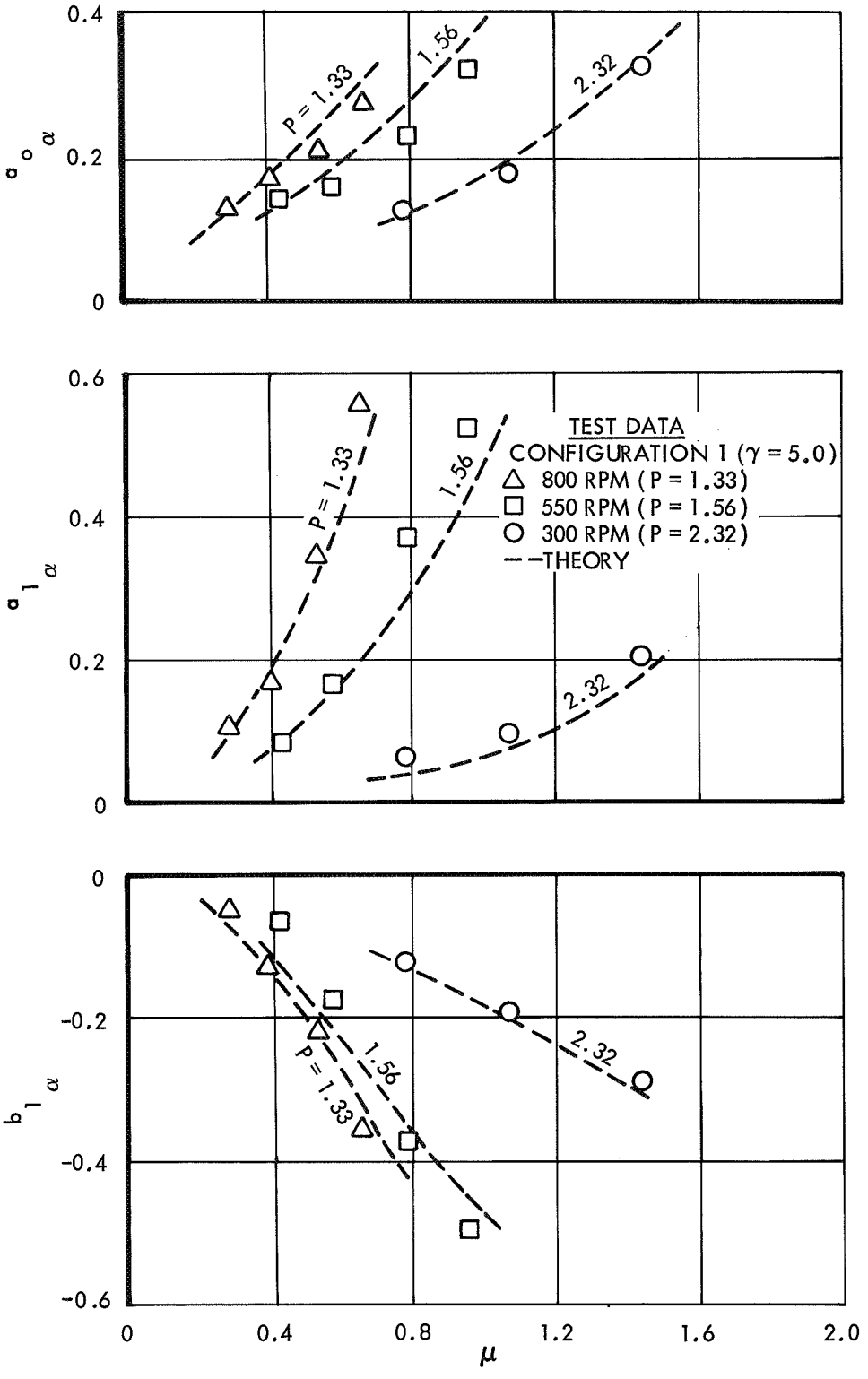

Figure 52. Comparison of Theoretical and Experimental Rotor Response Derivatives with Respect to Rotor Shaft Angle of Attack, Configuration 1

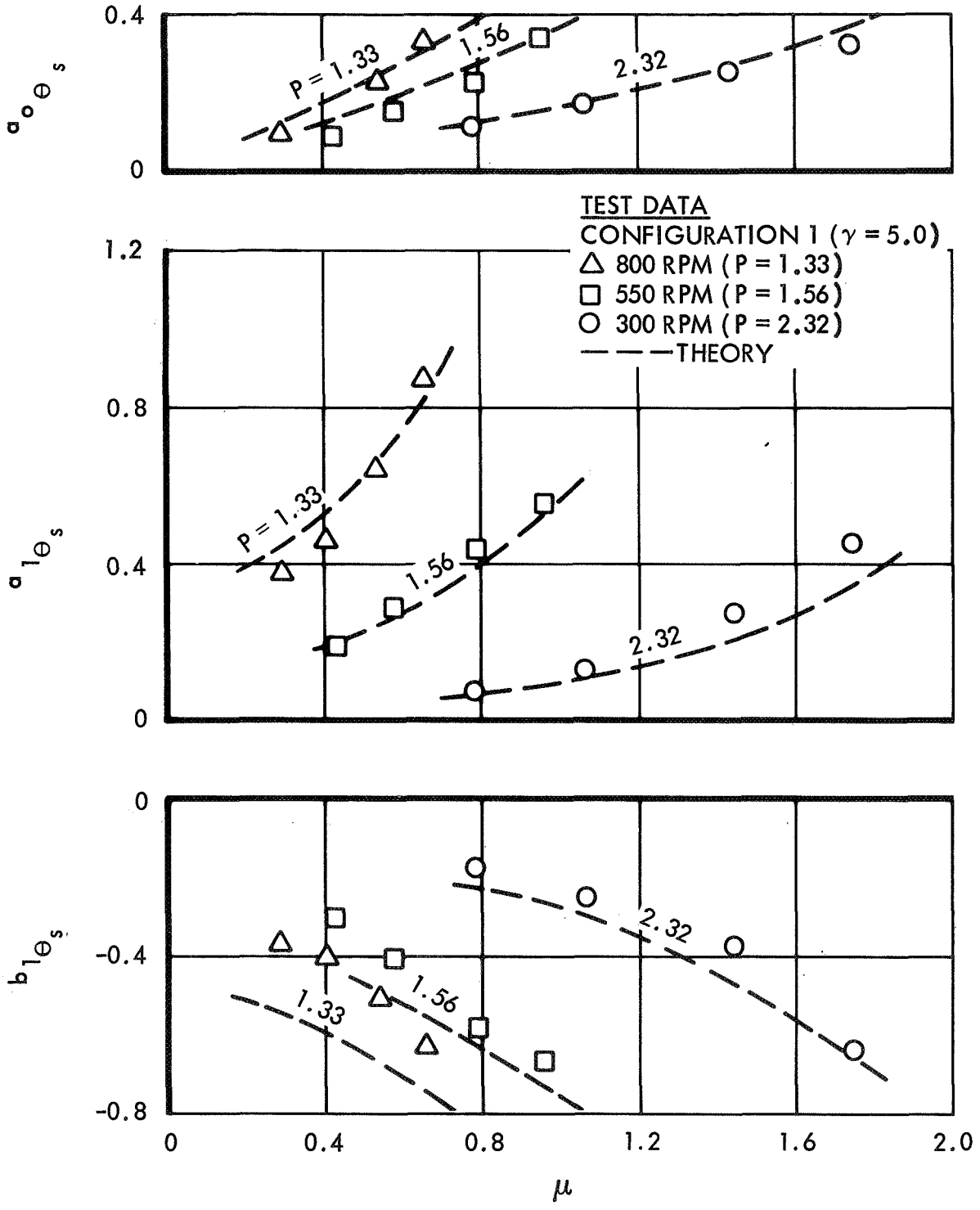

Figure 53. Comparison of Theoretical and Experimental Rotor Response Derivatives with Respect to Longitudinal Cyclic Pitch, Configuration 1

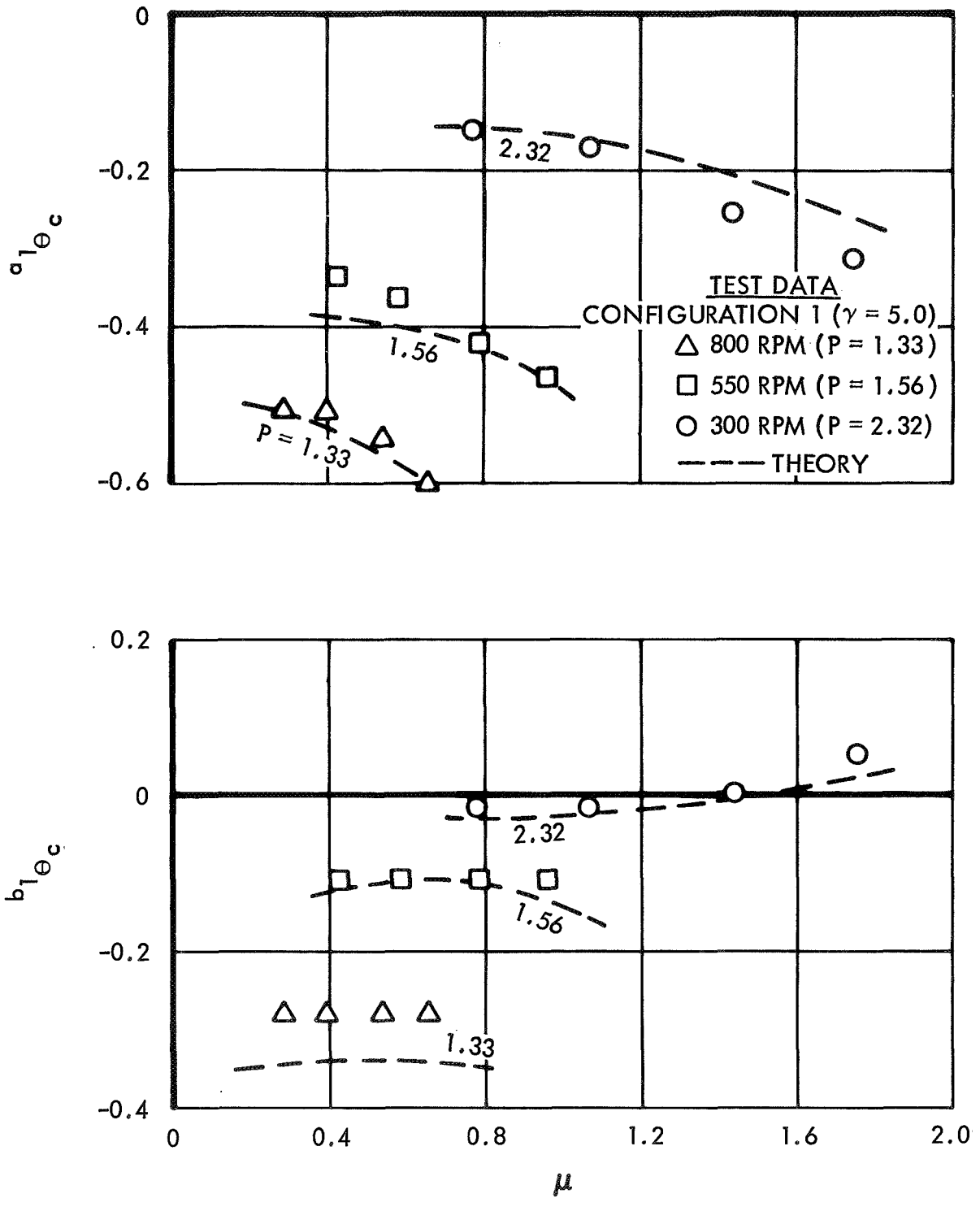

Figure 54. Comparison of Theoretical and Experimental Rotor Response Derivatives with Respect to Lateral Cyclic Pitch, Configuration 1

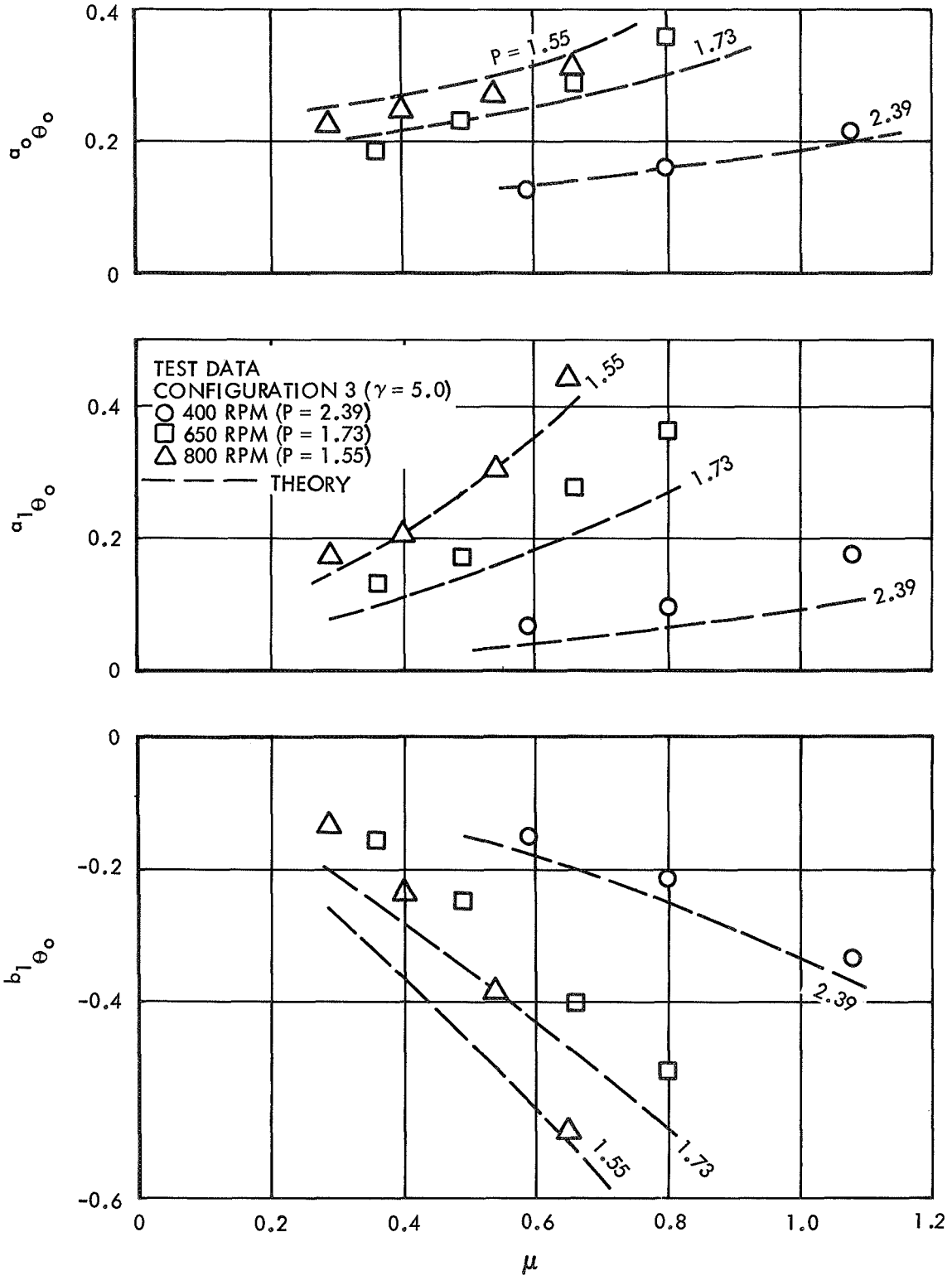

Figure 55. Comparison of Theoretical and Experimental Rotor Response Derivatives with Respect to Collective Pitch, Configuration 3

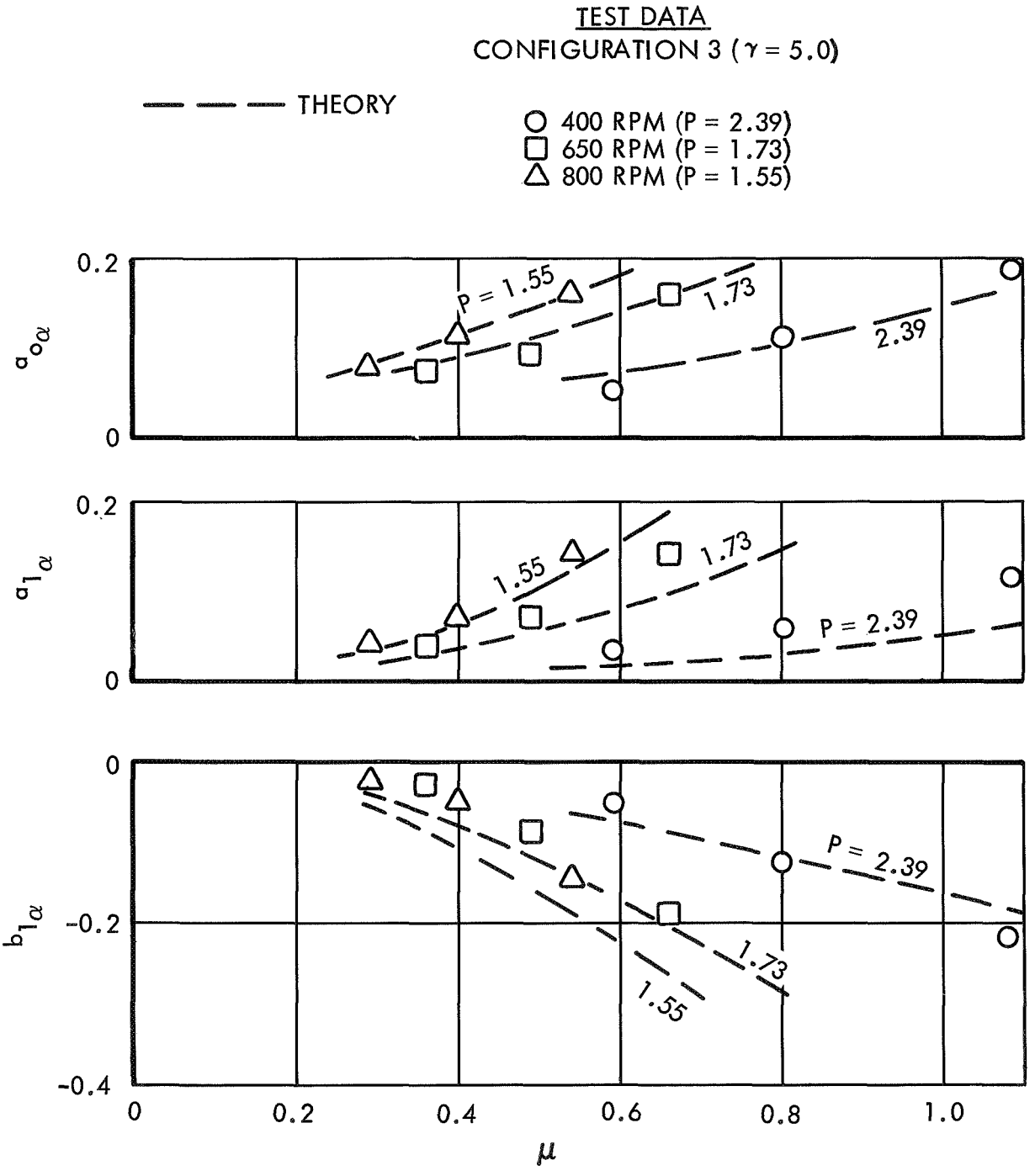

Figure 56. Comparison of Theoretical and Experimental Rotor Response Derivatives with Respect to Rotor Shaft Angle of Attack, Configuration 3

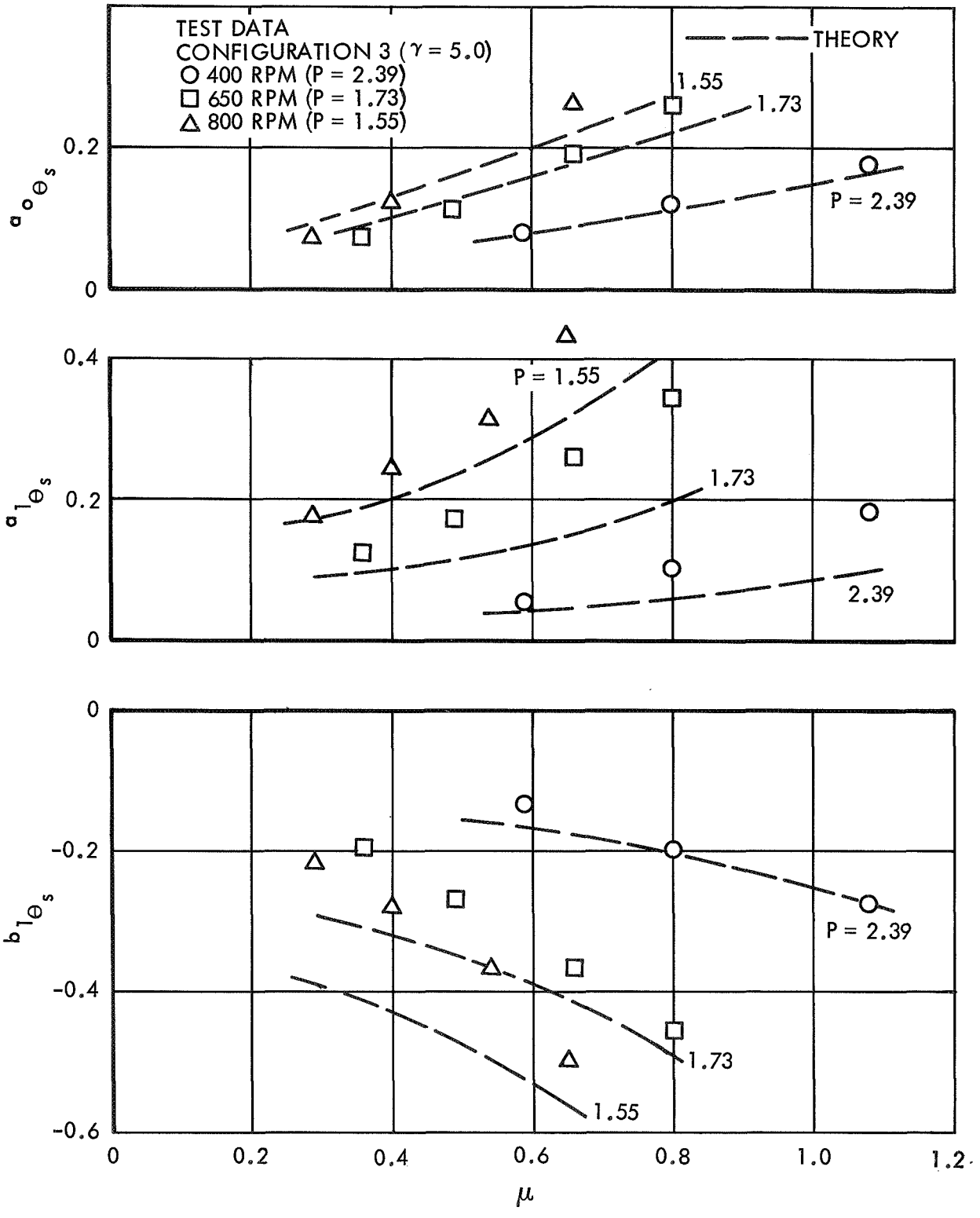

Figure 57. Comparison of Theoretical and Experimental Rotor Response Derivatives with Respect to Longitudinal Cyclic Pitch, Configuration 3

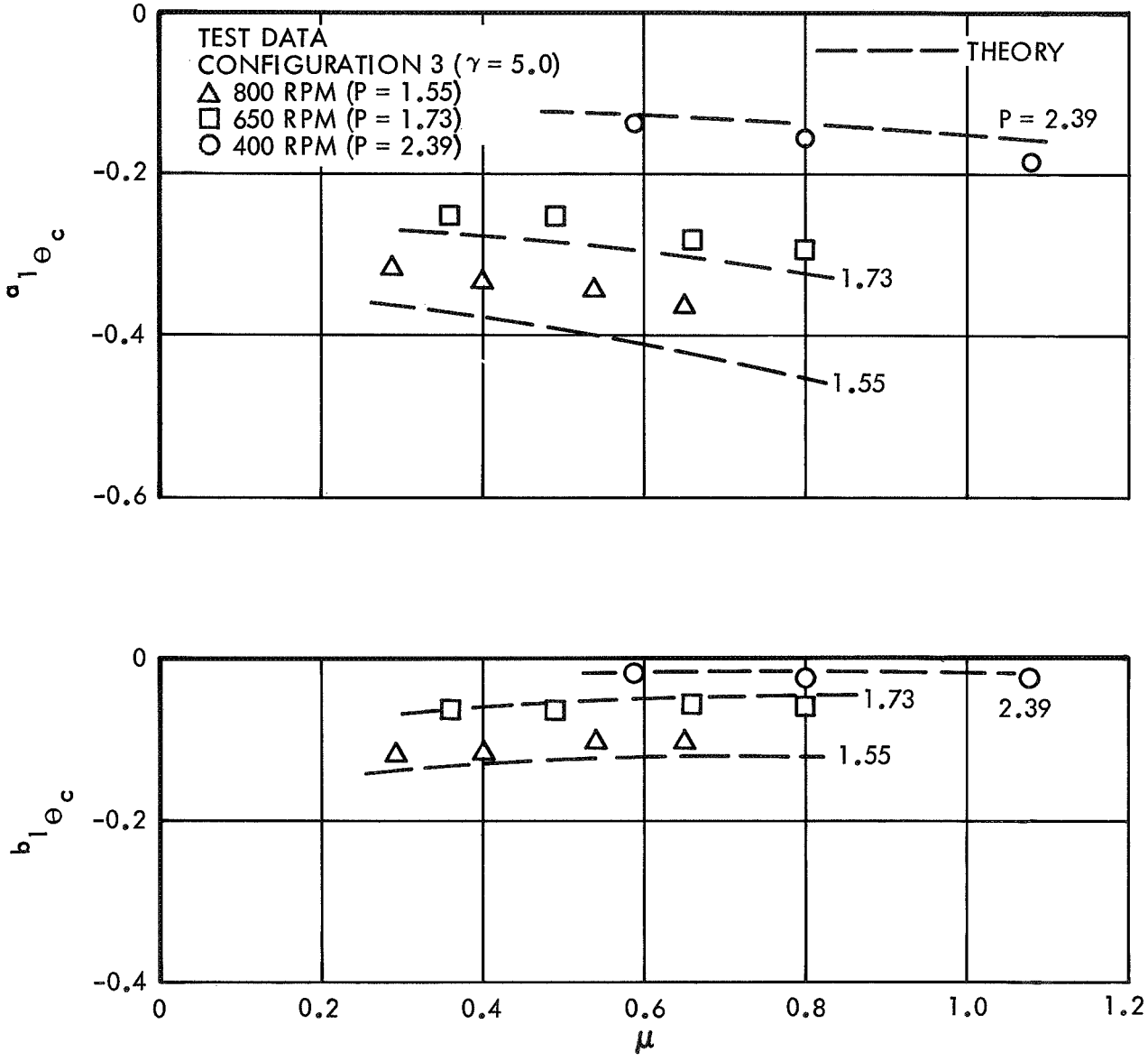

Figure 58. Comparison of Theoretical and Experimental Rotor Response Derivatives with Respect to Lateral Cyclic Pitch, Configuration 3

The comparison of theory and test data for configuration 4 is shown in Figures 59 to 62. The general agreement is the same as that obtained for configuration 3.

It has been shown that the theory and test data agree well for configurations 1 and 2 and "not so well" for configurations 3 and 4. This indicates that the nominal Lock number, γ, and the nondimensional flapping frequency, P, may not always suffice to describe the physical rotor. The fundamental difference between configurations 1 and 2 and configurations 3 and 4 is the stiffness of the root bending restraint. In the mathematical model this was reflected totally by a change in P. The stiffness of the restraint also has another effect which is not accounted for in the mathematical model. The shape of the first flap bending mode of an elastic blade is strongly influenced by its radial stiffness distribution. The change in the mode shape caused by interchanging soft and stiff flexures is shown in Figure 63. It is immediately obvious that the mathematical description of flapping (i.e., rigid blade which flaps about a centrally arranged hinge) represents the soft flexure better than the stiff flexure. The stiff flexure mode shape indicates that an adequate mathematical description may require an offset flapping hinge or the inclusion of the first flap bending mode shape itself. A change of this nature would be expected to modify the damping of the flapping motion and in turn the steady-state flapping response.

THEORETICAL STABILITY BY MATRIX FLOQUET THEORY

The stability of the Lockheed/AARL High Advance Ratio Rotor Model was examined theoretically using Matrix Floquet Theory. The advantage of Floquet Theory is that a quantitative measure of the stability of linear equations with periodic coefficients can be obtained. One can determine whether a system is stable or unstable from a time history solution but can obtain only a qualitative measure of the degree of stability. A brief description of the implementation of the method will be presented here. The reader is referred to References 5 and 6 for a more rigorous discussion of the theory.

For the initial investigations both the blade flapping and the blade torsion degrees of freedom were considered. It was immediately discovered

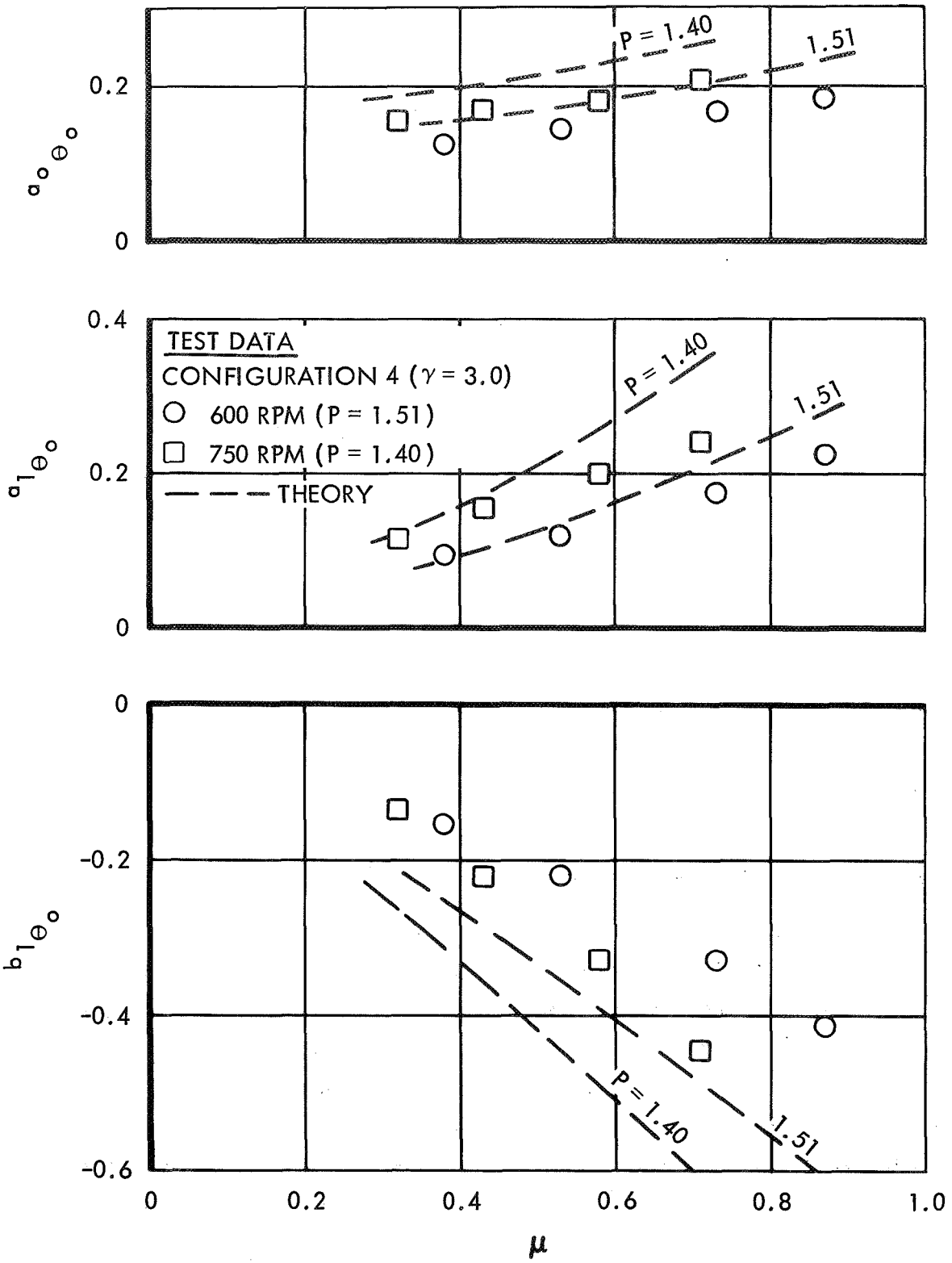

Figure 59. Comparison of Theoretical and Experimental Rotor Response Derivatives with Respect to Collective Pitch, Configuration 4

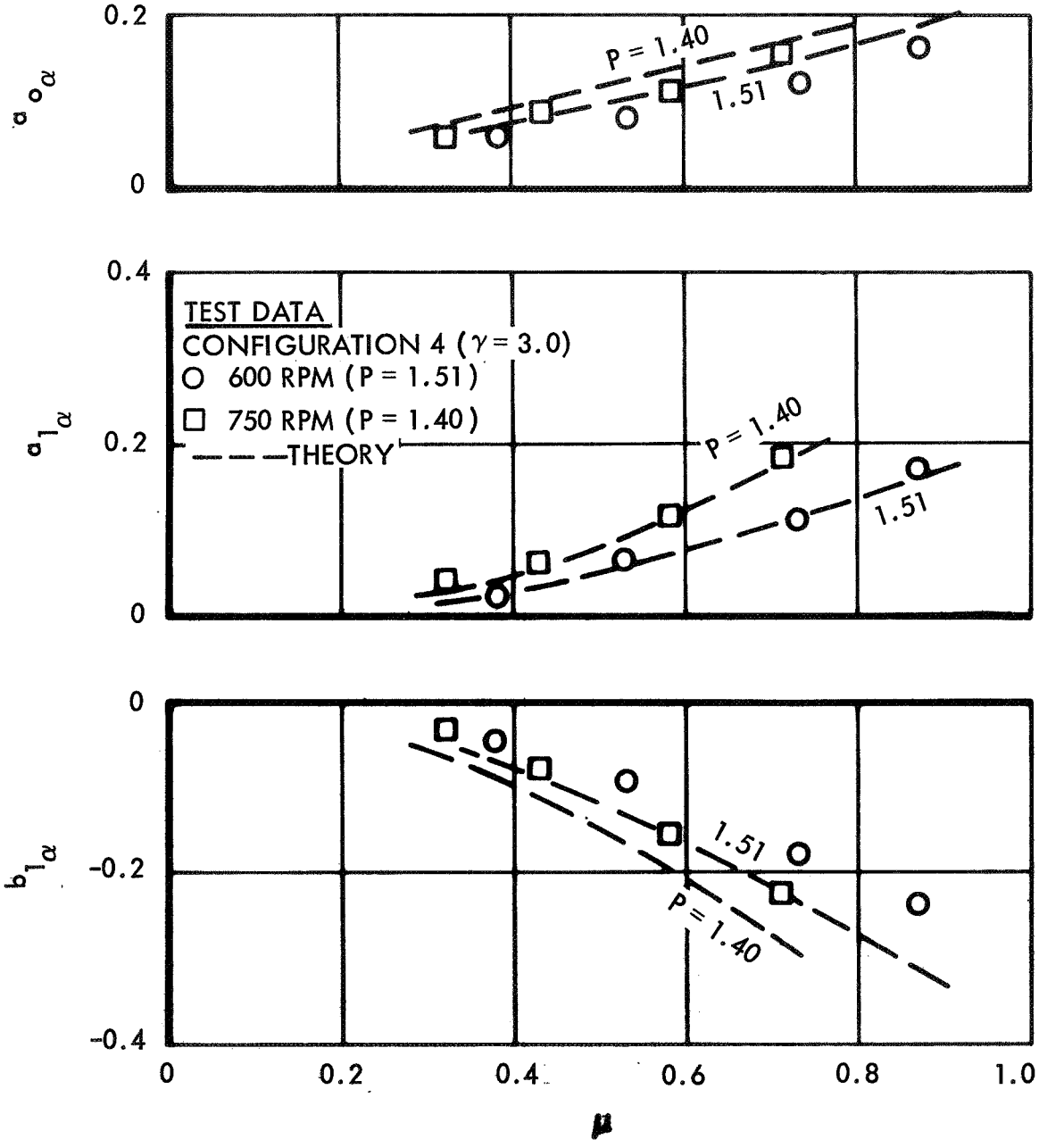

Figure 60. Comparison of Theoretical and Experimental Rotor Response Derivatives with Respect to Rotor Shaft Angle of Attack, Configuration 4

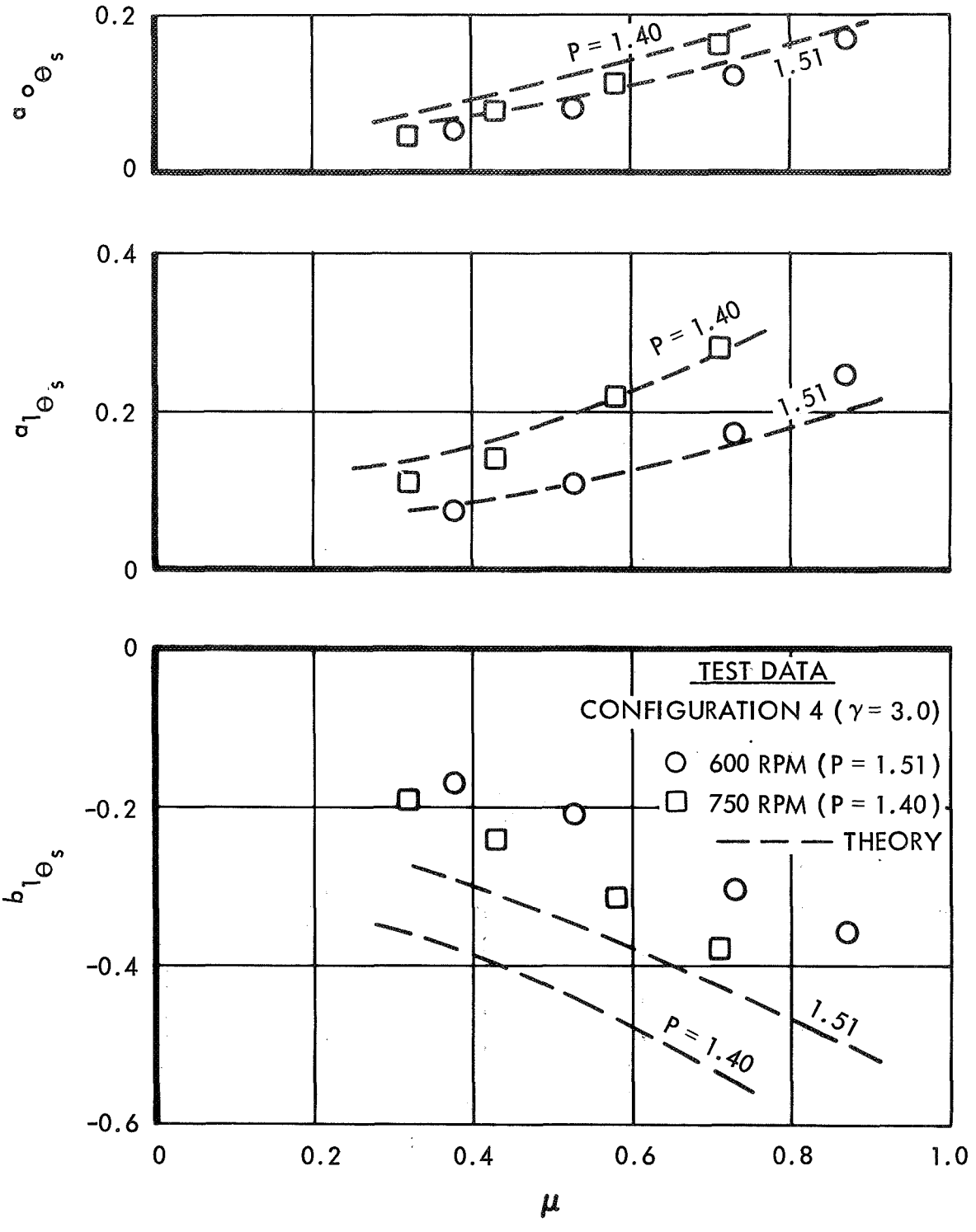

Figure 61. Comparison of Theoretical and Experimental Rotor Response Derivatives with Respect to Longitudinal Cyclic Pitch, Configuration 4

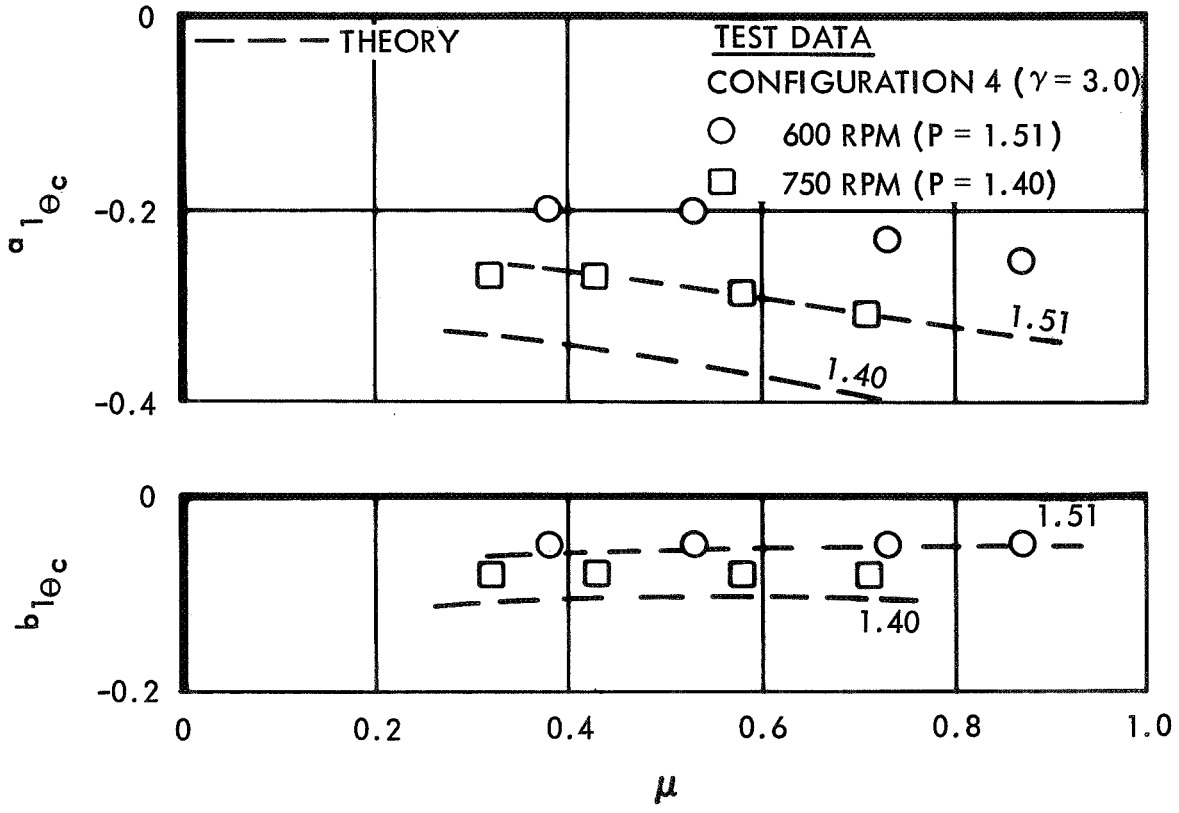

Figure 62. Comparison of Theoretical and Experimental Rotor Response Derivatives with Respect to Lateral Cyclic Pitch, Configuration 4

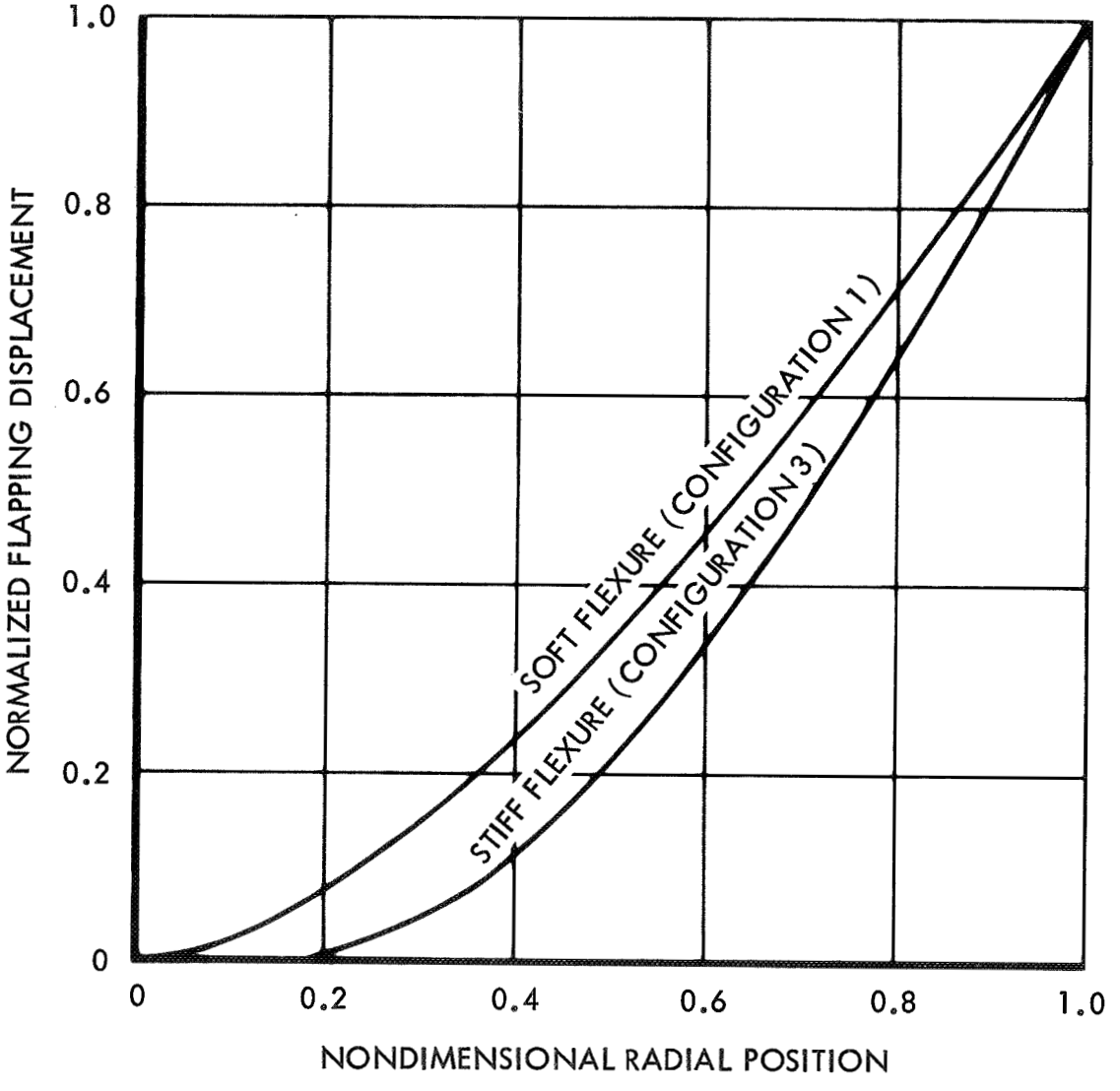

Figure 63. Effect of Flexure Stiffness on First Flap Bending Mode Shape

that within the advance ratio range of interest the torsional degree of freedom had a negligible effect on the results. This can be attributed to the high torsional stiffness of the blade. Succeeding calculations were made considering only the flapping degree of freedom. Since a single degree of freedom greatly simplifies the discussion of the method without compromising its generality, blade torsion will not be included in the following discussion.

The equation of motion for blade flapping is derived in Appendix A. Since stability is to be considered, only the homogeneous equation is of interest.

$$\frac{2}{\gamma}\ddot{\beta} + \Omega C(\psi)\dot{\beta} + \Omega^2\left[\frac{2}{\gamma}P^2 + K(\psi)\right]\beta = 0 \qquad (11)$$

It is convenient to simplify eq 11 slightly by eliminating the parameter Ω. This may be accomplished by considering derivatives with respect to ψ (i.e., $\psi = \Omega t$) rather than time. With

$$\frac{d\beta}{dt} = \frac{d\beta}{d\psi}\frac{d\psi}{dt} = \frac{\Omega d\beta}{d\psi} \qquad (12)$$

and

$$\frac{d^2\beta}{dt^2} = \frac{d}{dt}\left(\frac{d\beta}{d\psi}\frac{d\psi}{dt}\right)\frac{d\psi}{dt} = \frac{\Omega^2 d^2\beta}{d\psi^2} \qquad (13)$$

eq 11 may be rewritten as (after multiplying by $\frac{\gamma}{2}$)

$$\beta'' + \frac{\gamma}{2}C(\psi)\beta' + \left[P^2 + \frac{\gamma}{2}K(\psi)\right]\beta = 0 \qquad (14)$$

where

$$' = \frac{d}{d\psi}$$

Eq 14 must be expressed in canonical form. Let

$$X_1 = \beta \qquad (15)$$

$$X_2 = \beta' \qquad (16)$$

Then

$$X_1' = X_2 \qquad (17)$$

and eq 14 and eq 17 can be collected in matrix form.

$$\begin{Bmatrix} X_1' \\ X_2' \end{Bmatrix} = \begin{bmatrix} 0 & 1 \\ -P^2 - \frac{\gamma}{2} K(\psi) & -\frac{\gamma}{2} C(\psi) \end{bmatrix} \begin{Bmatrix} X_1 \\ X_2 \end{Bmatrix} \qquad (18)$$

The solution to eq 18 at any ψ can be expressed in terms of the state transition matrix $\underline{\phi}(\psi,\tau)$ and initial values of the state variables $\underline{X}(\tau)$.

$$X(\psi) = \underline{\phi}\ (\psi,\tau)X(\tau) \qquad (19)$$

The bar under a symbol indicates a matrix. $\underline{\phi}$ is a square matrix whose i^{th} column contains the solution to eq 18 (after one period of the coefficients) with the initial condition

$$X_j(0) = \begin{cases} 1 & i = j \\ 0 & i \neq j \end{cases} \qquad (20)$$

The stability of the linear system, eq 18, is reflected by the eigenvalues, λ_ϕ, of the state transition matrix $\underline{\phi}$. The eigenvalues are expressed in familiar terms by

$$\text{Damping Constant} = \frac{1}{T} \text{Re}(\ln\lambda_\phi) \qquad (21)$$

$$\text{Frequency} = \frac{1}{T} \text{Im}(\ln\lambda_\phi) \qquad (22)$$

where T is the period of the coefficients $C(\psi)$ and $K(\psi)$.

The theoretical stability of configurations 1 and 2 are shown in Figure 64 and Figure 65. The root loci are plotted over a range of advance ratios for values of P corresponding to the tested rotor speeds. Both the frequency and damping are nondimensional. The curves indicate that the rotor flapping motion will become unstable if the advance ratio is sufficiently high. The frequency of the unstable motion is always at an integer multiple of one-half the rotor rotational frequency.

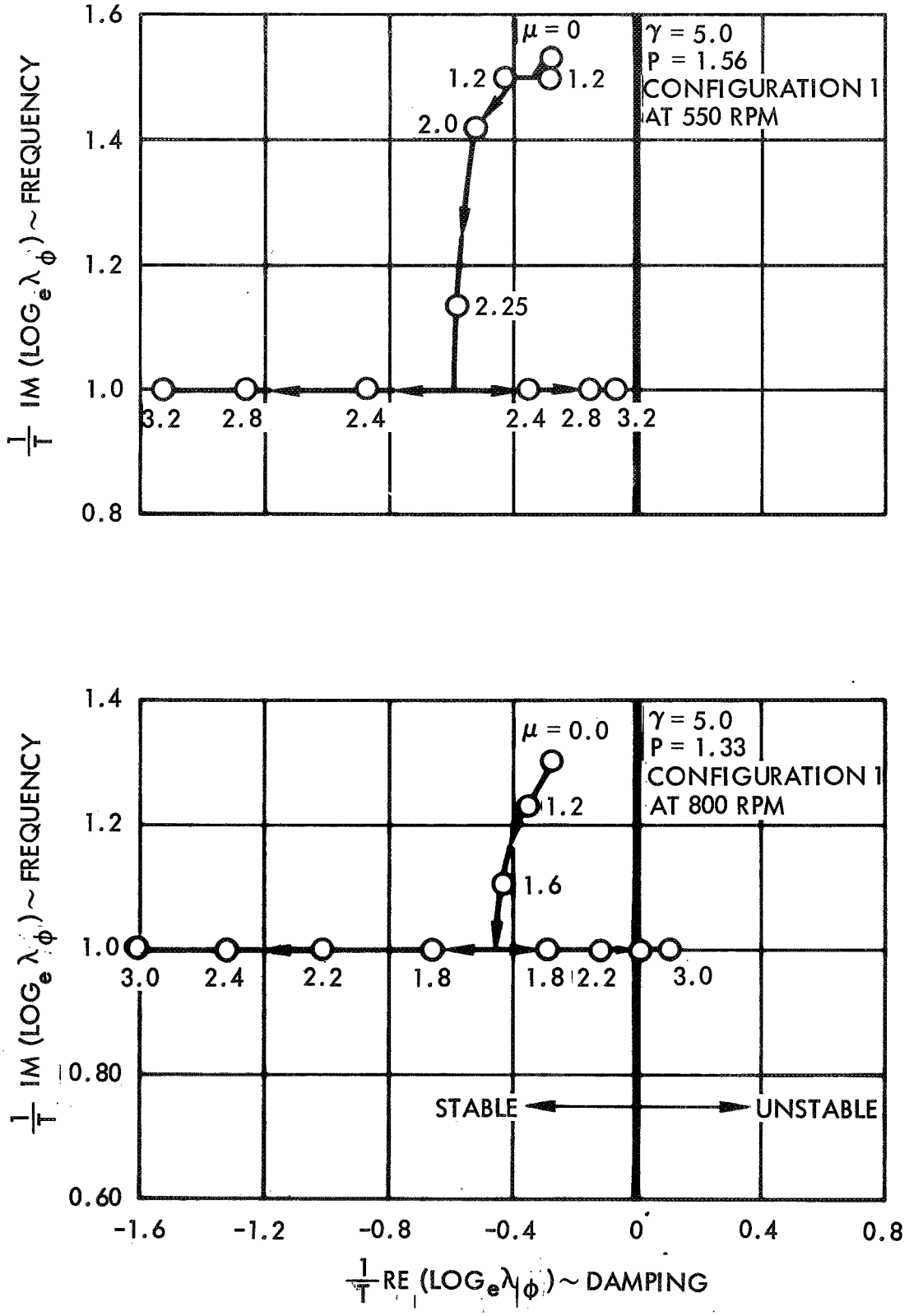

Figure 64. Theoretical Flapping Stability by Floquet Theory

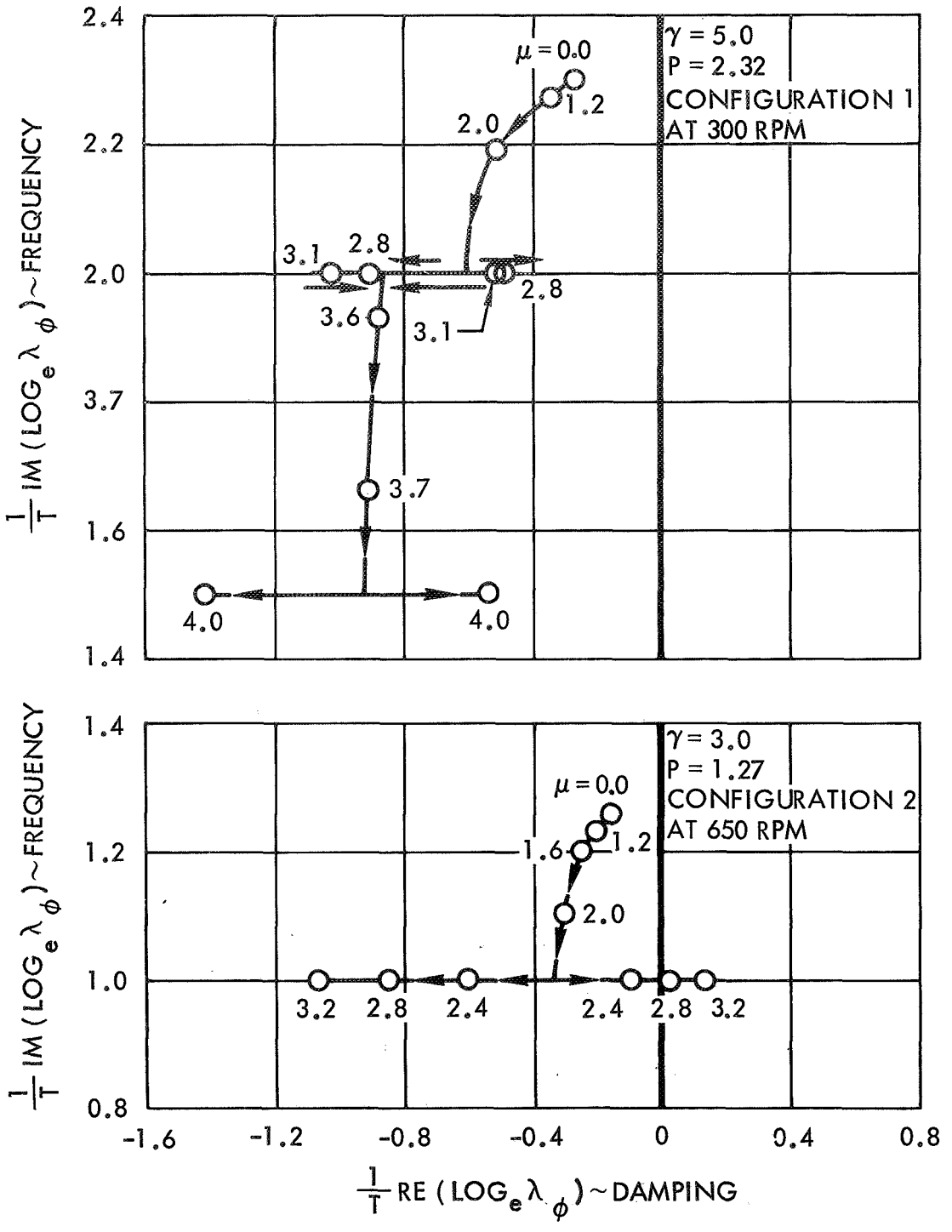

Figure 65. Theoretical Flapping Stability by Floquet Theory

The theoretical stability analysis tacitly agrees with the test results. That is, the analysis indicates that within the tested advance ratio ranges indications of an approaching instability should not be visible. In fact, the analysis shows the damping of the flapping motion increasing with forward speed, implying greater flapping stability.

SECTION 8

CONCLUDING REMARKS

The first phase of the Lockheed/AARL High Advance Ratio Research Program has provided an excellent experimental foundation for the study of the dynamic characteristics of hingeless rotors. Steady state response characteristics have been obtained for an array of rotors, each defined by a discreet combination of Lock number and flapping frequency. The data cover advance ratios ranging from 0 to 1.75. The stability of several rotor configurations has also been examined for advance ratios as high as $\mu = 2.15$. No instabilities or indications of approaching instabilities were observed.

The acquisition of good test data has facilitated the evaluation of a relatively simple mathematical model. Generally the model predicts steady rotor response satisfactorily when the first flap bending mode shape of the blade is reasonably represented by a rigid blade which flaps about the center of rotation. The indication is that the mathematical model may be improved if blade flapping is represented by a first bending mode shape. The theoretical stability of the model tacitly agrees with the test data to the extent that within the tested advance ratio range, indications of an instability are not predicted.

During the second phase of the program the model will be equipped with a moment feedback control system which automatically compensates external one-per-rev rotor disturbances. A soft flexure configuration without the tip weight will be tested. The system will be analyzed theoretically using the rotor flapping model in Appendix A coupled with appropriate control system equations. Test data will include steady state response characteristics and frequency response of the closed loop rotor and control system. The frequency response of the isolated rotor will also be obtained. These data will be compared with theoretical predictions. The experimental frequency response of the isolated rotor can be used to evaluate any feedback control system which may be of interest.

SECTION 9

REFERENCES

1. G.J. Sissingh, "Dynamics of Rotors Operating at High Advance Ratios," Journal of the American Helicopter Society, 13(3) 56-63 (July 1968).

2. G.J. Sissingh, W.A. Kuczynski, "Investigations on the Effect of Blade Torsion on the Dynamics of the Flapping Motion," Journal of the American Helicopter Society, 15(2) 2-9 (April 1970).

3. E.S. Cruz, N.B. Gorenberg, A.W. Kerr, "A Flight Envelope Expansion Study for the XH-51A Compound Helicopter," USAAVLABS Technical Report 69-79 (October 1969).

4. W.F. Paul, "A Self-Excited Rotor Blade Oscillation at High Subsonic Mach Numbers," Journal of the American Helicopter Society, 14(1) 38-48 (January 1969).

5. D.A. Peters, K.H. Hohenemser, "Application of the Floquet Transition Matrix to Problems of Lifting Rotor Stability," presented at the 26th Annual Forum of the American Helicopter Society, Washington, D.C., (June 1970).

6. DeRusso, Roy, Close, State Variables for Engineers John Wiley & Sons, Inc., New York (June 1967).

APPENDIX A

OUTLINE AND DISCUSSION OF THEORY

The mathematical model used to generate the theoretical rotor response characteristics which were compared with test data in Section 7 is described in this Appendix. The various aerodynamic functions involved are derived as are the equations of motion for blade flapping and torsion. The theory covers the advance ratio range, $0 \leq \mu < \infty$. The development is identical with those of References 1 and 2. It is repeated here for the convenience of the reader. Comprehensive discussions of the ramifications of the theory are contained in the original publications.

DESCRIPTION OF MATHEMATICAL MODEL

The rotor blades are assumed to be rigid in bending, elastic in torsion and connected to an inelastic control system. They flap about a centrally arranged flapping hinge with spring restraint. The spring rate of the hypothetical restraint is selected such that the rigid blade flapping frequency coincides with that of the first flap-bending mode of the elastic blade being represented. A torsional restraint is chosen in a similar manner with the spring rate based upon the 1st torsion mode frequency. The two degrees of freedom considered are the flapping angle β and the torsional deflection of the blade tip, δ. The radial distribution of blade torsion is expressed as ϕ where $\phi = \phi(x)$ is a normalized mode shape for torsion. For simplicity, the numerical calculations are based on $\phi = x$, i.e., a linear torsional deflection has been assumed.

The equation of motion for blade torsion postulates that the blades are balanced chordwise. This means that the cg and elastic axis coincide with the 25% chord line. The airfoil section extends from the center of rotation to the blade tip. The investigations are based on classical rotor theory, i.e., blade stall, Mach number effects and deviations from a uniform induced velocity field are ignored. With the exception of the damping of blade feathering and torsion steady-state aerodynamic theory is used.

FLOW REGIONS AND BASIC LIFT EQUATIONS

During its rotation a blade operating at advance ratios greater than B(B ≃ 0.97) encounters three different flow regions (Figure 66). They are:

Region	Azimuth Range	Type of Flow
1	$0 \leq \psi \leq \pi$	Normal
2	$\pi < \psi \leq \pi + \varepsilon$	Mixed
	$2\pi - \varepsilon \leq \psi < 2\pi$	
3	$\pi + \varepsilon < \psi < 2\pi - \varepsilon$	Reversed

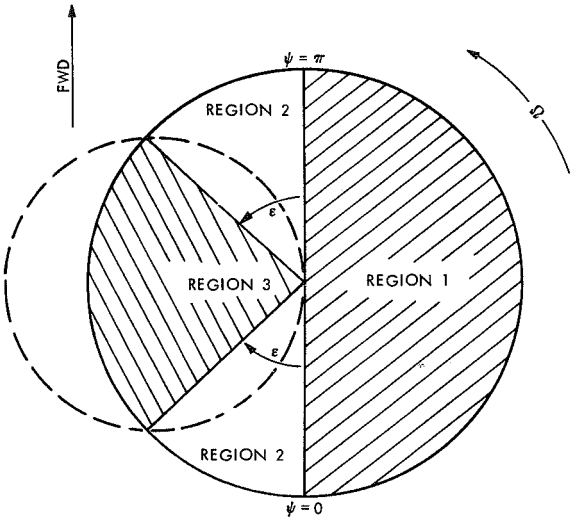

Figure 66. Flow Regions Encountered by Blade

In normal flow the air approaches the blade element from the leading edge and in reversed flow from the trailing edge of the blade. In the case of mixed flow, region 2, the blade elements from x = 0 to x = $-\mu\sin\psi$ operate in reversed flow and those from x = $-\mu\sin\psi$ to x = B operate in normal flow. The angle ε which defines the azimuthal expanse of region 2 is given by the equation

$$\sin\varepsilon = B/\mu \qquad (A1)$$

From Figure 66 it can be seen that region 3 exists if $\mu > B$. For advance ratios less than B, region 2 covers the whole retreating half of the rotor disc, i.e., it extends from $\psi = \pi$ to $\psi = 2\pi$.

From classical rotor theory, the following assumptions are made for the lift coefficient C_L of a blade element.

normal flow $$C_L = a \left(\frac{U_P}{U_T} + \Theta + \Delta\Theta\right) \tag{A2}$$

reversed flow $$C_L = -a \left(\frac{U_P}{U_T} + \Theta + \Delta\Theta\right) \tag{A3}$$

In these equations the nondimensional velocity components U_P, U_T and the pitch setting Θ of a blade element are defined as:

$$U_P = \lambda - \mu\,\beta\cos\psi - x\dot{\beta}/\Omega \tag{A4}$$

$$U_T = x + \mu\sin\psi \tag{A5}$$

$$\Theta = \Theta_o + x\,\Theta_t + \Theta_s \sin\psi + \Theta_c \cos\psi \tag{A6}$$

$\Delta\Theta = \phi\delta$ represents the pitch of a blade element due to torsion

BLADE FLAPPING

The equation of motion for blade flapping is expressed as

$$\frac{1}{2} R^4\,\Omega^2\,\rho ac\,m - I_1\,\ddot{\beta} - I_1\,P^2\,\Omega^2\,\beta = 0 \tag{A7}$$

where $$m = \int U_T^{\,2}\, x \left(\frac{U_P}{U_T} + \Theta + \Delta\Theta\right) dx \tag{A8}$$

is the nondimensional aerodynamic flapping moment. Substituting $\phi\,\delta$ for $\Delta\Theta$ and eqs A4, A5, A6 into eq A8 leads to

$$\begin{aligned} m = {} & \lambda\int U_T\, x\, dx + \Theta_o\int U_T^{\,2}\, x\, dx + \Theta_t\int U_T^{\,2}\, x^2\, dx + \delta\int \phi\, U_T^{\,2}\, x\, dx \\ & + \Theta_s\int U_T^{\,2}\, x \sin\psi\, dx + \Theta_c \int U_T^{\,2}\, x \cos\psi\, dx \\ & - \beta\int U_T\, x\, \mu\cos\psi\, dx - (\dot{\beta}/\Omega)\int U_T\, x^2\, dx \end{aligned} \tag{A9}$$

With regard to the sign and boundaries of these integrals the following rules apply:

Region 1 $$m_1 = +\int_o^B \qquad \text{(A10)}$$

Region 2 $$m_2 = +\int_{-\mu\sin\psi}^{B} - \int_o^{-\mu\sin\psi} = m_1 - 2\int_o^{-\mu\sin\psi} \qquad \text{(A11)}$$

Region 3 $$m_3 = -\int_o^B = -m_1 \qquad \text{(A12)}$$

For convenience the aerodynamic flapping moment m (eq A9) is rewritten as

$$m(\psi) = \sum f(\psi) + \delta m_\delta(\psi) - \beta K(\psi) - (\dot{\beta}/\Omega) C(\psi) \qquad \text{(A13)}$$

where the term

$$\sum f(\psi) = \lambda m_\lambda + \theta_o m_{\theta_o} + \theta_t m_{\theta_t} + \theta_s m_{\theta_s} + \theta_c m_{\theta_c} \qquad \text{(A14)}$$

summarizes the forcing functions due to inflow, blade twist, collective and cyclic pitch.

The second term of eq A13 accounts for the effect of blade torsion. For the mode shape $\phi = x$, m_δ is identical with m_{θ_t}. The quantities $K(\psi)$ and $C(\psi)$ in eq A13 represent aerodynamic spring and damping moments. All aerodynamic functions involved change periodically with the azimuth angle. They have been calculated and are given in Table 6. The subscripts 1, 2 refer to the flow regions. Since the equations for region 3 are the negative of those for region 1 (eq A12), they have not been listed separately.

Dividing m (ψ) as defined by eq A13 by $R^4 cap/2$ leads to the flapping equation of motion.

$$\frac{2}{\gamma}\ddot{\beta} + \Omega\dot{\beta}\,C(\psi) + \Omega^2\beta\left[\frac{2}{\gamma}P^2 + K(\psi)\right] = \Omega^2\left\{\delta m_{\theta_t}(\psi) + \sum f(\psi)\right\} \qquad \text{(A15)}$$

Numerical calculations indicate that at high values of μ a change in rotor angle of attack and the resulting change in rotor thrust have a minor

TABLE 6. CHARACTERISTIC FUNCTIONS FOR BLADE FLAPPING

K	$K_1 = \frac{1}{3} B^3 \mu \cos \psi + \frac{1}{4} B^2 \mu^2 \sin 2\psi$ $K_2 = K_1 + \mu^4 \left(- \frac{1}{12} \sin 2\psi + \frac{1}{24} \sin 4\psi \right)$
C	$C_1 = \frac{1}{4} B^4 + \frac{1}{3} B^3 \mu \sin \psi$ $C_2 = C_1 + \mu^4 \left(\frac{1}{16} - \frac{1}{12} \cos 2\psi + \frac{1}{48} \cos 4\psi \right)$
m_λ	$m_1 = \frac{1}{3} B^3 + \frac{1}{2} B^2 \mu \sin\psi$ $m_2 = m_1 + \mu^3 \left(- \frac{1}{4} \sin\psi + \frac{1}{12} \sin 3\psi \right)$
m_{θ_o}	$m_1 = \left(\frac{1}{4} B^4 + \frac{1}{4} B^2 \mu^2 \right) + \frac{2}{3} B^3 \mu \sin \psi - \frac{1}{4} B^2 \mu^2 \cos 2\psi$ $m_2 = m_1 + \mu^4 \left(- \frac{1}{16} + \frac{1}{12} \cos 2\psi - \frac{1}{48} \cos 4\psi \right)$
m_{θ_t}	$m_1 = \left(\frac{1}{5} B^5 + \frac{1}{6} B^3 \mu^2 \right) + \frac{1}{2} B^4 \mu \sin \psi - \frac{1}{6} B^3 \mu^2 \cos 2\psi$ $m_2 = m_1 + \mu^5 \left(\frac{1}{24} \sin \psi - \frac{1}{48} \sin 3\psi + \frac{1}{240} \sin 5\psi \right)$
m_{θ_s}	$m_1 = \frac{1}{3} B^3 \mu + \left(\frac{1}{4} B^4 + \frac{3}{8} B^2 \mu^2 \right) \sin\psi - \frac{1}{3} B^3 \mu \cos 2\psi - \frac{1}{8} B^2 \mu^2 \sin 3\psi$ $m_2 = m_1 + \mu^4 \left(- \frac{5}{48} \sin \psi + \frac{5}{96} \sin 3\psi - \frac{1}{96} \sin 5\psi \right)$
m_{θ_c}	$m_1 = \left(\frac{1}{4} B^4 + \frac{1}{8} B^2 \mu^2 \right) \cos \psi + \frac{1}{3} B^3 \mu \sin 2\psi - \frac{1}{8} B^2 \mu^2 \cos 3\psi$ $m_2 = m_1 + \mu^4 \left(- \frac{1}{48} \cos \psi + \frac{1}{32} \cos 3\psi - \frac{1}{96} \cos 5\psi \right)$

effect on the mean induced flow. In this case the forcing function representing a change in rotor angle of attack can be expressed as

$$m_\alpha = \mu m_\lambda \tag{A16}$$

where λm_λ is the nondimensional excitation due to a change in the inflow ratio λ.

E_q A15 represents a Hill-type equation of motion with periodic coefficients which depend upon the advance ratio. Of special interest are the spring and damper characteristics. They will be discussed briefly According to eg A15 there are two spring rates involved, a constant and a periodic term. The constant term, $\frac{2}{\gamma} P^2$, summarizes the spring effect of the centrifugal forces and of the hypothetical spring. The periodic term, $K(\psi)$, is of aerodynamic origin. Its variation with the azimuth angle is shown in Figure 67.

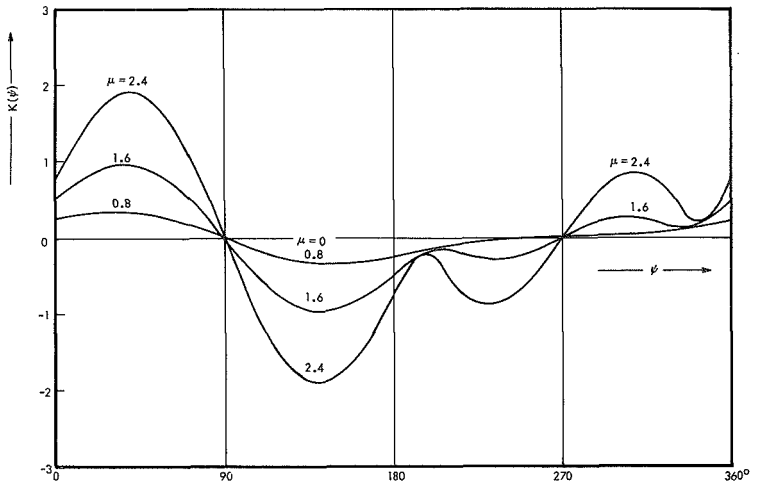

Figure 67. Effect of Advance Ratio on Aerodynamic Spring Rate

As can be seen, for $\mu > o$ the aerodynamic forces have a negative spring effect in the azimuth range $\frac{1}{2}\pi < \psi < \frac{3}{2}\pi$, i.e., at the front half of the rotor disc. The amplitude of the periodic variation increases greatly with increasing advance ratio. The minimum instantaneous aerodynamic spring occurs at $\psi \sim 140^{o}$.

Depending upon the magnitude of $\frac{2}{\gamma} P^2$ and the advance ratio, the blade may or may not encounter azimuth regions with a resulting negative spring rate. According to eq A15 the transient spring rate subsides to zero if

$$\left[\frac{2}{\gamma} P^2 + K(\psi)\right]_{\psi = 140^{o}} = 0 \qquad \text{(A17)}$$

or if $$\frac{P^2}{\gamma} = -\left(\frac{1}{6} B^3 \mu \cos 140^{o} + \frac{1}{8} B^2 \mu^2 \sin 280^{o}\right) \qquad \text{(A18)}$$

The (P^2/γ) value given by eq A18 has been calculated and is shown in Figure 68 as a function of the advance ratio. The curve which is based on B = 0.97 reveals, for instance, that for a blade with

$$P = 1.15$$
$$\gamma = 6$$
$$\frac{P^2}{\gamma} = 0.22 \qquad \text{(A19)}$$

negative transient spring effects come into the picture at advance ratios $\mu > 0.96$. Analyses indicate that the negative spring rates encountered by the blade at higher advance ratios are one of the main sources for the flapping instabilities that may occur.

With regard to the damping coefficient $C(\psi)$ of eq A15 the following statements can be made. (Figure 69). For $\mu = 0$, $C(\psi)$ is constant. The periodic content increases with increasing advance ratio. It should be noted, however, that $C(\psi)$ always remains positive. This means the blade flapping motion is always damped although, at times, the damping may subside to nearly zero.

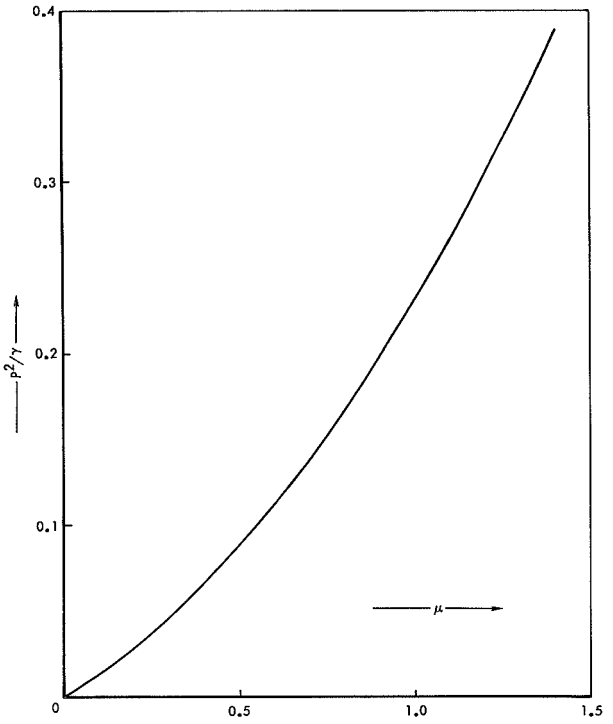

Figure 68. Boundary for Transient Negative Spring Effects (Flapping)

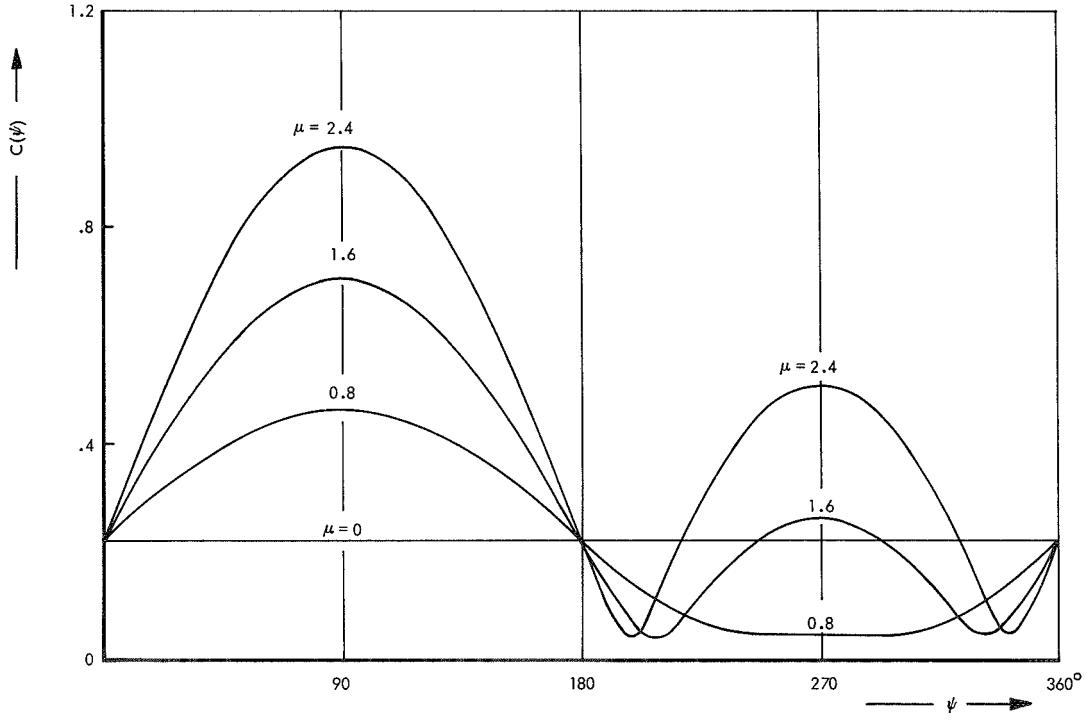

Figure 69. Effect of Advance Ratio on Damping Coefficient

To show the typical variation of a forcing function with the advance ratic the flapping excitation due to a change in rotor shaft angle of attack, m_α (ψ) has been plotted in Figure 70. Both the constant and periodic content increase with increasing advance ratio. Due to the periodic variation of the spring rate, $K(\psi)$, the blade responds to a constant excitation with a periodic response for $\mu>0$.

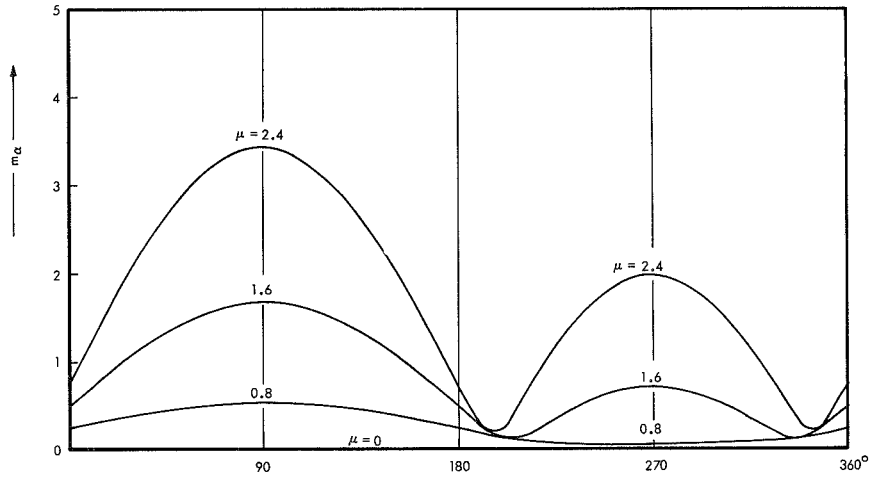

Figure 70. Excitation Due to Rotor Angle of Attack

BLADE TORSION

AERODYNAMIC DAMPING

Normal Flow

According to classical unsteady aerodynamic theory a feathering velocity

$$\Delta \dot{\theta} = \phi \dot{\delta} \tag{A20}$$

results in two lift components; one acts at the 25-percent, and the other at the 75-percent, chord line. The former has no damping effects and can be disregarded. The latter amounts to

$$L_{0.75} = \frac{1}{8} R^2 c^2 a \rho \Omega \dot{\delta} \int U_T \phi dx \tag{A21}$$

and generates a feathering moment

$$M_f = -\frac{1}{16} R^2 c^3 a\rho C_\delta \Omega\dot{\delta} \qquad (A22)$$

The quantity C_δ in eq A22 is a damping coefficient defined as

$$C_\delta = \int U_T \phi dx \qquad (A23)$$

which is applicable to the flow regions 1 and 2_n. Subscripts n and r refer respectively to the normal and reversed flow portions of the mixed flow region.

Reversed Flow

In reversed flow the blade feathers about the 75-percent chord line, measured from the trailing edge of the blade. Classical aerodynamic theory states that the lift generated acts at the location of the feathering axis, which means that no damping moments occur. As a result of this the torsional motion of the blade is aerodynamically damped in regions 1, 2 and has zero damping in region 3.

Since flow region 3 comes into the picture only if $\mu > B$, it follows that for $\mu < B$ the feathering motion is always damped. However, for $\mu > B$ the blade experiences azimuth ranges with zero damping.

AERODYNAMIC SPRING EFFECT

It has been assumed that the elastic axis coincides with the 25-percent chord line. Consequently, aerodynamic feathering moments due to torsion can only occur in the reversed flow regions 2_r and 3. In these regions a torsional deflection $\Delta\theta = \phi\delta$ results in a lift

$$L_r = -\frac{1}{2} R^3 ca'\rho \Omega^2 \delta \int U_T^2 \phi dx \qquad (A24)$$

and generates a feathering moment

$$M_f = -\kappa c L_r \qquad (A25)$$

$$= -\frac{1}{2} R^3 c^2 \kappa a'\rho K_\delta \Omega^2 \delta$$

The quantity

$$K_\delta = -\int U_T^2 \, \phi dx \tag{A26}$$

denotes a nondimensional aerodynamic spring rate applicable to the flow regions 2_r and 3. As the integrand in eq A26 is positive, the aerodynamic forces act as a negative spring. This means a torsional deflection of the blade results in a moment which tends to increase the deflection.

The problem is aggravated by the fact that at the time a blade element experiences a negative spring effect, the damping is zero. It must therefore be expected that at high advance ratios and low torsional frequencies the blade torsion has a deteriorating effect on rotor stability.

In order to illustrate the periodic variation of the aerodynamic spring and damper rates of blade torsion, the quantities $\bar{K}_\delta$ and $\bar{C}_\delta$ have been plotted versus the azimuth angle for the advance ratios 0.8, 1.6 and 2.4 in Figures 71 and 72. The bar over K_δ and C_δ indicates a torsion mode shape $\phi = x$ has been assumed.

EXCITATION BY LIFT OF REVERSED FLOW REGION

At advance ratios greater than zero the retreating blade operates either partially (region 2) or completely (region 3) in reversed flow. The lift produced under these conditions acts approximately at the 75-percent chord line and excites the torsional degree of freedom. In order to investigate these excitations, the appropriate lift functions are derived.

Let

$$\ell_r(\psi) = \frac{\text{lift due to reversed flow}}{R^3\Omega^2 ca'\rho/2} \tag{A27}$$

be a nondimensional coefficient characterizing the lift of the reversed flow region. It is convenient to break $\ell_r(\psi)$ down into its components and to write

$$\ell_r(\psi) = \beta\ell_{r_\beta} + (\dot{\beta}/\Omega)\,\ell_{r_{\dot{\beta}}} + \lambda\ell_{r_\lambda} + \theta_o\ell_{r_{\theta_o}} + \theta_t\ell_{r_{\theta_t}} + \theta_s\ell_{r_{\theta_s}} + \theta_c\ell_{r_{\theta_c}} \tag{A28}$$

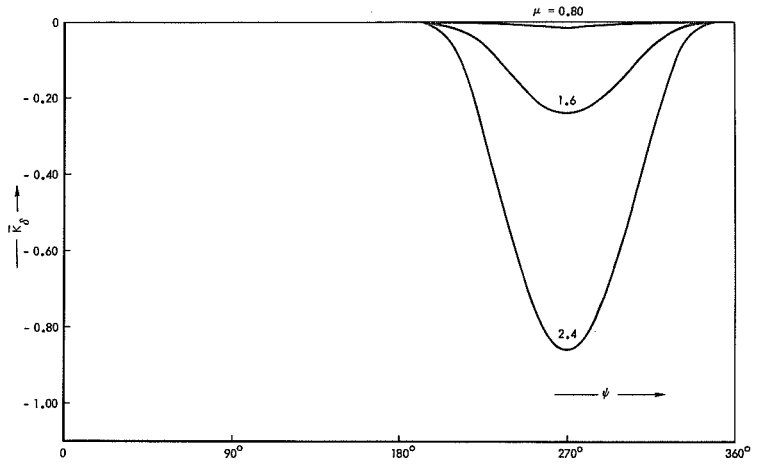

Figure 71. Aerodynamic Spring Effect of Blade Torsion

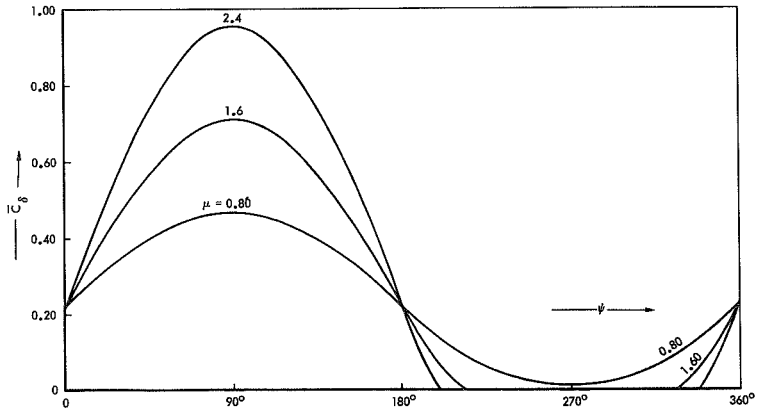

Figure 72. Aerodynamic Damping of Blade Torsion

It can be shown that

$$\left.\begin{aligned}
\ell_{r_\beta} &= \mu \int U_T \cos\psi dx \\
\ell_{r_{\dot\beta}} &= \int U_T x dx \\
\ell_{r_\lambda} &= - \int U_T dx \\
\ell_{r_{\theta_o}} &= - \int U_T^{\,2}\, dx \\
\ell_{r_{\theta_t}} &= - \int U_T^{\,2} x^2 dx \\
\ell_{r_{\theta_s}} &= - \int U_T^{\,2} \sin\psi dx \\
\ell_{r_{\theta_c}} &= - \int U_T^{\,2} \cos\psi dx
\end{aligned}\right\} \qquad \text{(A29)}$$

For these integrals the following limits apply

Flow region 2 : $x = 0$ to $x = -\mu\sin\psi$

Flow region 3 : $x = 0$ to $x = B$

For flow region 1, all functions are zero.

EQUATION OF MOTION OF BLADE TORSION

The equation of motion is derived from Lagrange's energy equation. Table 7 lists the kinetic energy, the potential energy of aerodynamic spring effects, the dissipation function and the generalized forces. The latter encompass all work done by inflow, flapping angle, flapping velocity, blade twist, and cyclic and collective pitch.

TABLE 7

ENERGY FUNCTIONS AND GENERALIZED FORCES OF BLADE TORSIONAL MOTION

Component		Applicable Flow Regions
Kinetic Energy	$T = \frac{1}{2}R \int_0^1 i_f \left(\dot{\theta} + \phi\dot{\delta}\right)^2 dx$	
Potential Energy of Aerodynamic Spring Effects	$V = -\frac{1}{4}R^3c^2\kappa a' \rho\Omega^2\delta^2 \int U_T^2\phi^2 dx$	2_r, 3
Dissipation Function	$D = \frac{1}{32}R^2c^3a\rho\Omega\dot{\delta}^2 \int U_T\phi^2 dx$	1, 2_n
Generalized Forces	$G = +\frac{1}{2}R^3c^2\kappa a' \rho\Omega^2 \int U_T^2\left(\frac{U_P}{U_T} + \theta\right)\phi dx$	2_r, 3
	$-\frac{1}{16}R^2c^3a\rho\Omega\dot{\theta} \int U_T\phi dx$	1, 2_n

If $f\Omega$ denotes the undamped natural frequency without consideration of the aerodynamic spring effects, the equation of motion for blade torsion is expressed as;

$$\begin{aligned} &\tfrac{1}{3}I_f\ddot{\delta} + \tfrac{1}{16}R^2c^3a\rho\,\bar{C}_\delta\,\Omega\dot{\delta} + \Omega^2\delta\,(\tfrac{1}{3}f^2I_f + \tfrac{1}{2}R^3c^2\kappa a'\rho\bar{K}_\delta) \\ &\qquad + \tfrac{1}{2}R^3c^2\kappa a'\rho\,(\Omega^2\beta\,\bar{\ell}_{r\beta} + \Omega\dot{\beta}\,\bar{\ell}_{r\dot{\beta}}) \\ &\qquad = -\tfrac{1}{2}I_f\ddot{\theta} - \tfrac{1}{16}R^2c^3a\rho\bar{C}_\theta\Omega\dot{\theta} - \tfrac{1}{2}R^3c^2\Omega^2\kappa a'\rho\Sigma\bar{\ell}_{re} \end{aligned} \qquad \text{(A30)}$$

where the last term on the right side summarizes the excitation by the lift due to inflow, blade twist, and cyclic and collective pitch, i.e.,

$$\Sigma\bar{\ell}_{re} = \lambda\bar{\ell}_{r\lambda} + \theta_o\,\bar{\ell}_{r\theta_o} + \theta_t\,\bar{\ell}_{r\theta_t} + \theta_s\,\bar{\ell}_{r\theta_s} + \theta_c\,\bar{\ell}_{r\theta_c} \qquad \text{(A31)}$$

$\bar{C}_\theta$ is the nondimensional aerodynamic damping of the feathering motion excluding torsion.

All barred quantities refer to the virtual work done by the mode shape ϕ investigated. They are periodic functions of the azimuth angle and, for the simplified case $\phi = x$, can be taken from Table 8.

Dividing eq 30 by γI_f leads to

$$\ddot{\delta}\frac{1}{3\gamma} + \Omega\dot{\delta}\,F\bar{C}_\delta + \Omega^2\delta\left(\frac{f^2}{3\gamma} + Q\,\bar{K}_\delta\right) + Q\left(\Omega^2\beta\;\bar{\ell}_{r\beta} + \Omega\dot{\beta}\bar{\ell}_{r\dot{\beta}}\right) + \ddot{\theta}\frac{1}{2\gamma} + \Omega\dot{\theta}\,F\bar{C}_\theta + Q\Omega^2\Sigma\,\bar{\ell}_{re} = 0 \tag{A32}$$

In this equation F and Q are nondimensional quantities which, similar to the blade Lock number, characterize the blade. They are defined as

$$F = \frac{I_l}{16I_f}\left(\frac{c}{R}\right)^2 \tag{A33}$$

$$Q = \frac{\kappa ca'I_l}{2RaI_f} \sim \frac{cI_l}{4RI_f} \tag{A34}$$

The above eq A32 and the flapping equation of motion, eq (A15) fully describe the dynamic characteristics of the blade motion.

TABLE 8

CHARACTERISTIC FUNCTIONS FOR BLADE TORSION ($\phi = x$)

Function	Region	
$\overline{K_\delta} = -\int U_T^2 \phi^2 dx$	2_r	$\mu^5 \left(\frac{1}{48}\sin\psi - \frac{1}{96}\sin 3\psi + \frac{1}{480}\sin 5\psi\right)$
	3	$-\left(\frac{1}{5}B^5 + \frac{1}{6}B^3\mu^2\right) - \frac{1}{2}B^4\mu \sin\psi + \frac{1}{6}B^3\mu^2 \cos 2\psi$
$\overline{C}_\delta = \int U_T \phi^2 dx$	1	$\frac{1}{4}B^4 + \frac{1}{3}B^3\mu \sin\psi$
	2_n	$\frac{1}{4}B^4 + \frac{1}{3}B^3\mu \sin\psi + \mu^4\left(\frac{1}{32} - \frac{1}{24}\cos 2\psi + \frac{1}{96}\cos 4\psi\right)$
$\overline{C}_\theta = \int U_T \phi dx$	1	$\frac{1}{3}B^3 + \frac{1}{2}B^2\mu \sin\psi$
	2_n	$\frac{1}{3}B^3 + \frac{1}{2}B^2\mu \sin\psi + \mu^3\left(-\frac{1}{8}\sin\psi + \frac{1}{24}\sin 3\psi\right)$
$\overline{\ell}_{r\beta} = \mu \int U_T \phi \cos\psi dx$	2_r	$\mu^4\left(\frac{1}{24}\sin 2\psi - \frac{1}{48}\sin 4\psi\right)$
	3	$\frac{1}{3}B^3\mu \cos\psi + \frac{1}{4}B^2\mu^2 \sin 2\psi$
$\overline{\ell}_{r\dot{\beta}} = \int U_T \phi x dx$	2_r	$\mu^4\left(-\frac{1}{32} + \frac{1}{24}\cos 2\psi - \frac{1}{96}\cos 4\psi\right)$
	3	$\frac{1}{4}B^4 + \frac{1}{3}B^3\mu \sin\psi$
$\overline{\ell}_{r\lambda} = -\int U_T \phi dx$	2_r	$\mu^3\left(-\frac{1}{8}\sin\psi + \frac{1}{24}\sin 3\psi\right)$
	3	$-\left(\frac{1}{3}B^3 + \frac{1}{2}B^2\mu \sin\psi\right)$
$\overline{\ell}_{r_{\theta_o}} = -\int U_T^2 \phi dx$	2_r	$\mu^4\left(-\frac{1}{32} + \frac{1}{24}\cos 2\psi - \frac{1}{96}\cos 4\psi\right)$
	3	$-\left(\frac{B}{4}^4 + \frac{B}{4}^2\mu^2\right) - \frac{2}{3}B^3\mu \sin\psi + \frac{1}{4}B^2\mu^2 \cos 2\psi$
$\overline{\ell}_{r_{\theta_t}} = -\int U_T^2 \phi dx$	2_r	$\mu^5\left(\frac{1}{48}\sin\psi - \frac{1}{96}\sin 3\psi + \frac{1}{480}\sin 5\psi\right)$
	3	$-\left(\frac{B}{5}^5 + \frac{B}{6}^3\mu^2\right) - \frac{B}{2}^4\mu \sin\psi + \frac{B}{6}^3\mu^2 \cos 2\psi$
$\overline{\ell}_{r_{\theta_s}} = -\int U_T^2 \phi \sin\psi dx$	2_r	$\mu^4\left(-\frac{5}{96}\sin\psi + \frac{5}{192}\sin 3\psi - \frac{1}{192}\sin 5\psi\right)$
	3	$-\frac{B}{3}^3\mu - \left(\frac{B}{4}^4 + \frac{3}{8}B^2\mu^2\right)\sin\psi + \frac{B}{3}^3\mu \cos 2\psi + \frac{1}{8}B^2\mu^2 \sin 3\psi$
$\overline{\ell}_{r_{\theta_c}} = -\int U_T^2 \phi \cos\psi dx$	2_r	$\mu^4\left(-\frac{1}{96}\cos_\psi + \frac{1}{64}\cos 3\psi - \frac{1}{192}\cos 5\psi\right)$
	3	$-\left(\frac{B}{4}^4 + \frac{B}{8}^2\mu^2\right)\cos\psi - \frac{B}{3}^3\mu \sin 2\psi + \frac{1}{8}B^2\mu^2 \cos 3\psi$

TRANSIENT NEGATIVE TORSIONAL SPRING RATES

The minimum aerodynamic spring rate for torsion occurs at $\psi = 270^\circ$ and the overall spring rate of the equation of motion is zero if (eq A32)

$$\left[\frac{f^2}{3\gamma} + Q\,\bar{K}_\delta\right]_{\psi = 270^\circ} = 0 \qquad \text{(A35)}$$

Since Table 8 lists two functions for $\bar{K}_\delta$, a distinction must be made between advance ratios smaller and larger than B. It can easily be seen that zero overall spring rates are reached if the following conditions are fulfilled:

$\mu<B$

$$\frac{f^2}{Q\gamma} = -\mu^5\left(\frac{1}{16}\sin 270^\circ - \frac{1}{32}\sin 90^\circ + \frac{1}{160}\sin 270^\circ\right) \qquad \text{(A36)}$$

$\mu>B$

$$\frac{f^2}{Q\gamma} = 3\left[\left(\frac{1}{5}B^5 + \frac{1}{6}B^3\mu^2\right) + \frac{1}{2}B^4\mu\sin 270^\circ - \frac{1}{6}B^3\mu^2\cos 180^\circ\right] \qquad \text{(A37)}$$

The values given by eq A36, A37 are presented in Figure 73. For a typical blade with

$$f = 5$$
$$Q\gamma = 80$$
$$f^2/Q\gamma = 0.31$$

it follows that transient negative spring effects for torsion show up at advance ratios $\mu > 1.28$. This does not necessarily mean that the blade motion becomes dynamically unstable at this point. The studies of Reference 2 show that the blade motion is stable at advance ratios beyond the onset of a transient negative torsional spring.

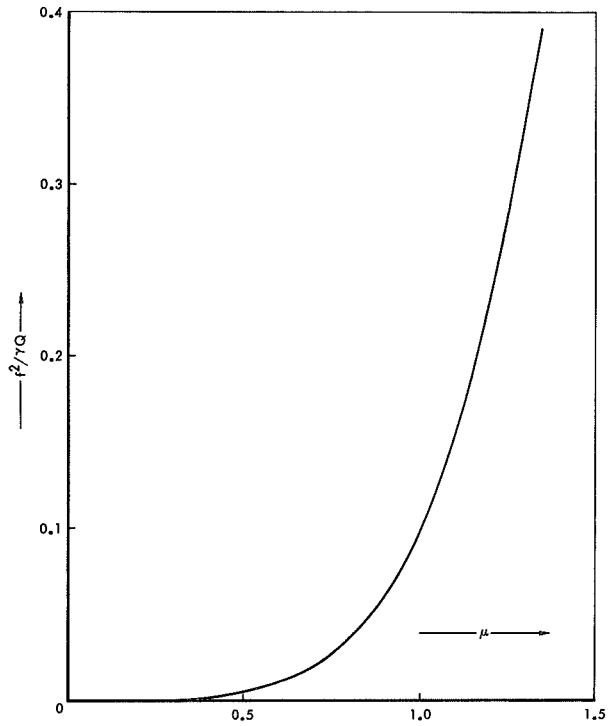

Figure 73. Boundary for Transient Negative Spring Effects (Torsion)

APPENDIX B

PLOTTED STEADY-STATE ROTOR RESPONSE TEST DATA

All of the rotor moment and lift data which were obtained during the wind tunnel tests are plotted in this appendix. These data were used to generate the summary derivative curves presented in the main body of the report (e.g., Figures 20, 21, 22, 24 and 25). The rotor moments were formed by resolving rotating blade flapping moments into stationary coordinates. Lift was measured by a six component strain gage balance which was an integral part of the model support strut.

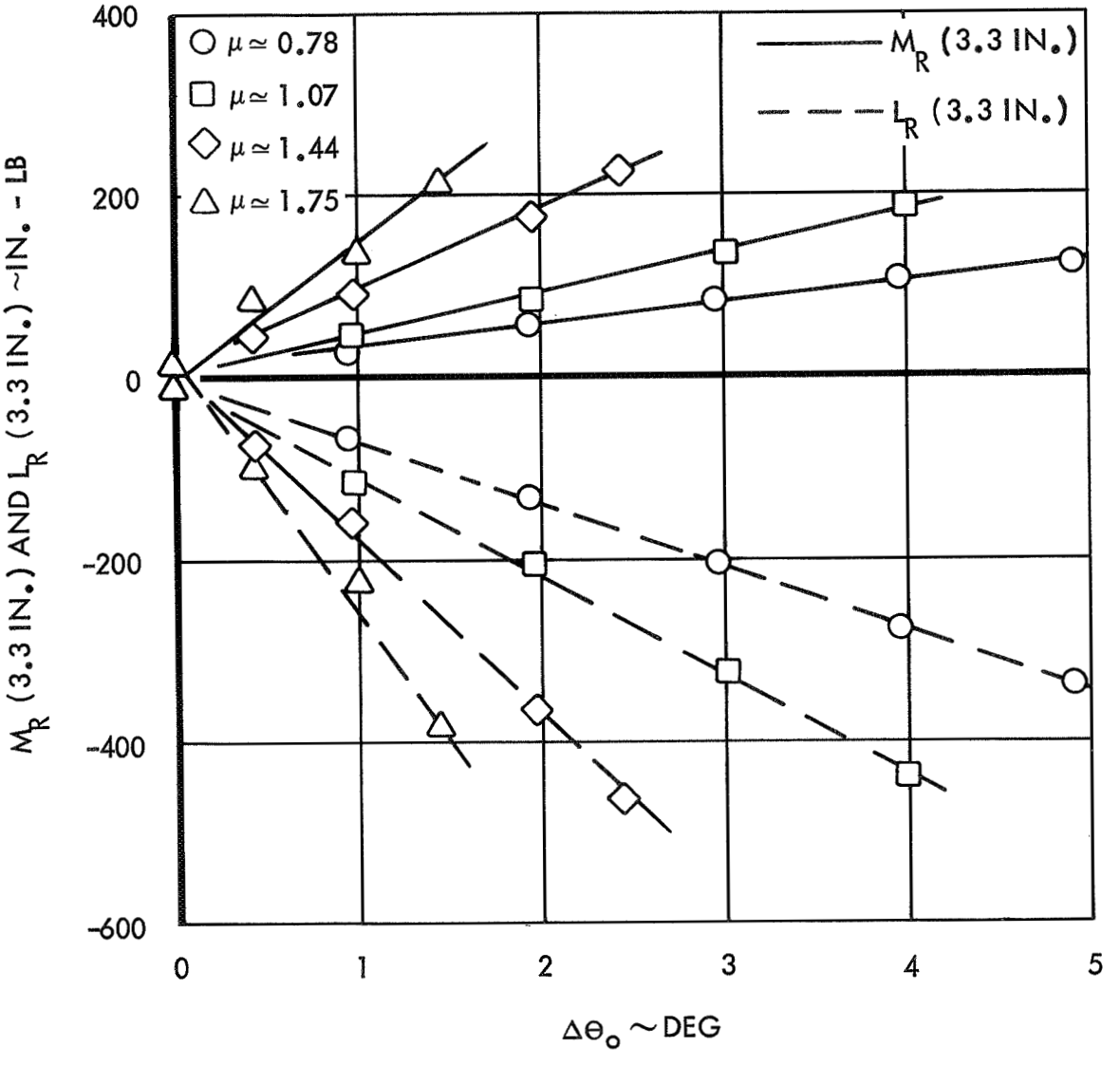

Figure 74. Rotor Pitch and Roll Response to Collective Pitch, Configuration 1, 300 RPM (γ=5.0, P=2.32)

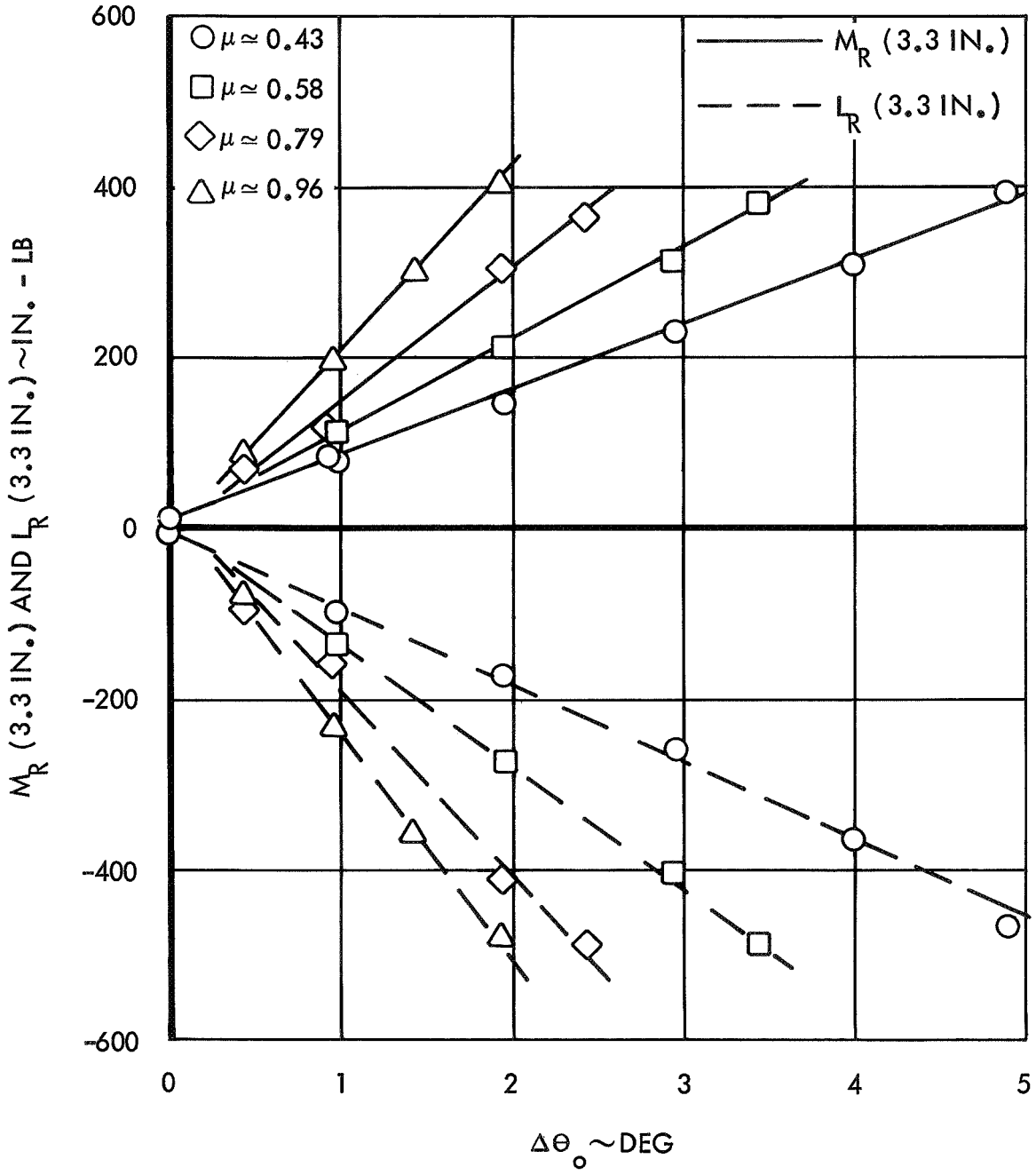

Figure 75. Rotor Pitch and Roll Response to Collective Pitch, Configuration 1, 550 RPM (γ=5.0, P=1.56)

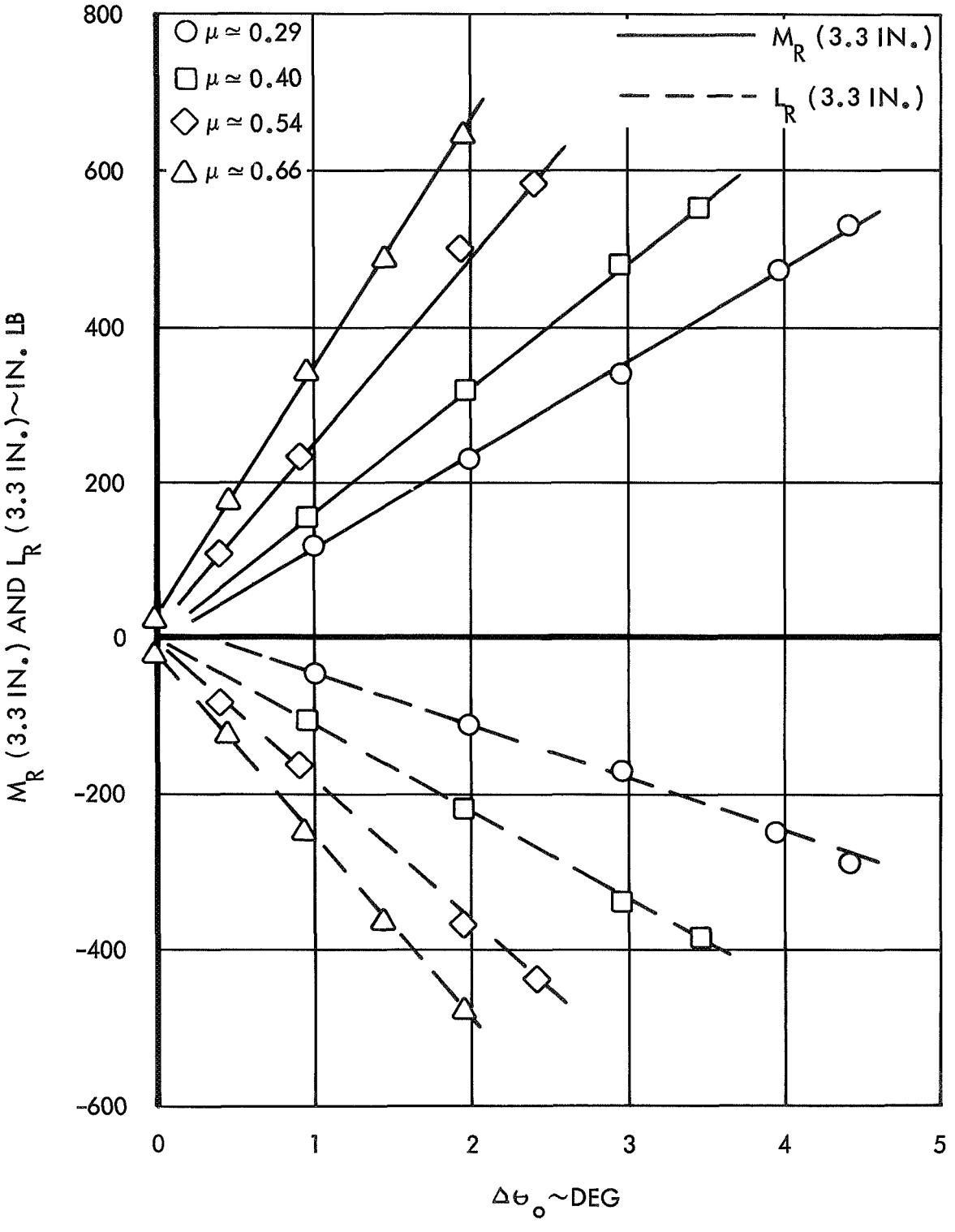

Figure 76. Rotor Pitch and Roll Response to Collective Pitch, Configuration 1, 800 RPM (γ=5.0, P=1.33)

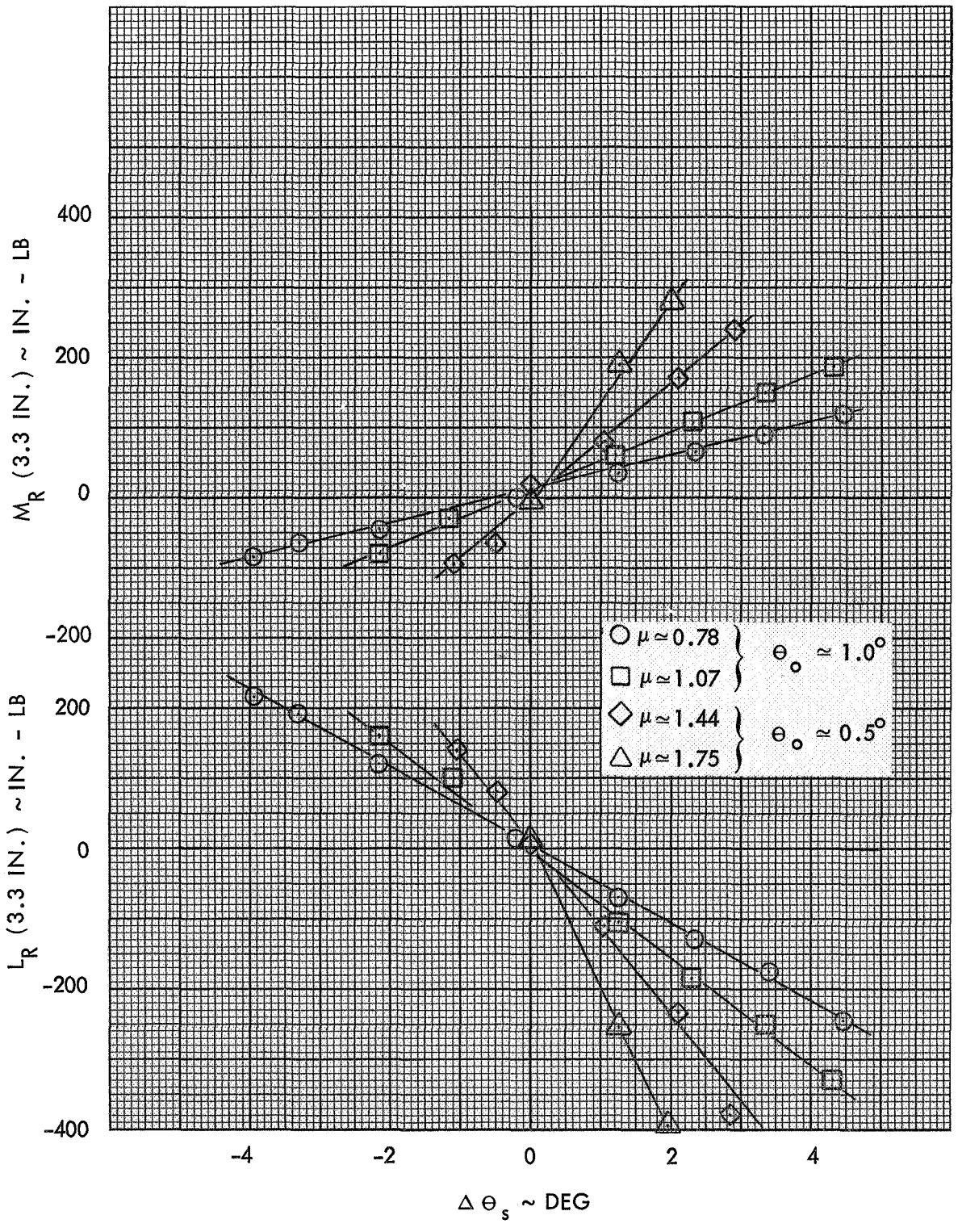

Figure 77. Rotor Pitch and Roll Response to Longitudinal Cyclic Pitch, Configuration 1, 300 RPM (γ=5.0, P=2.32)

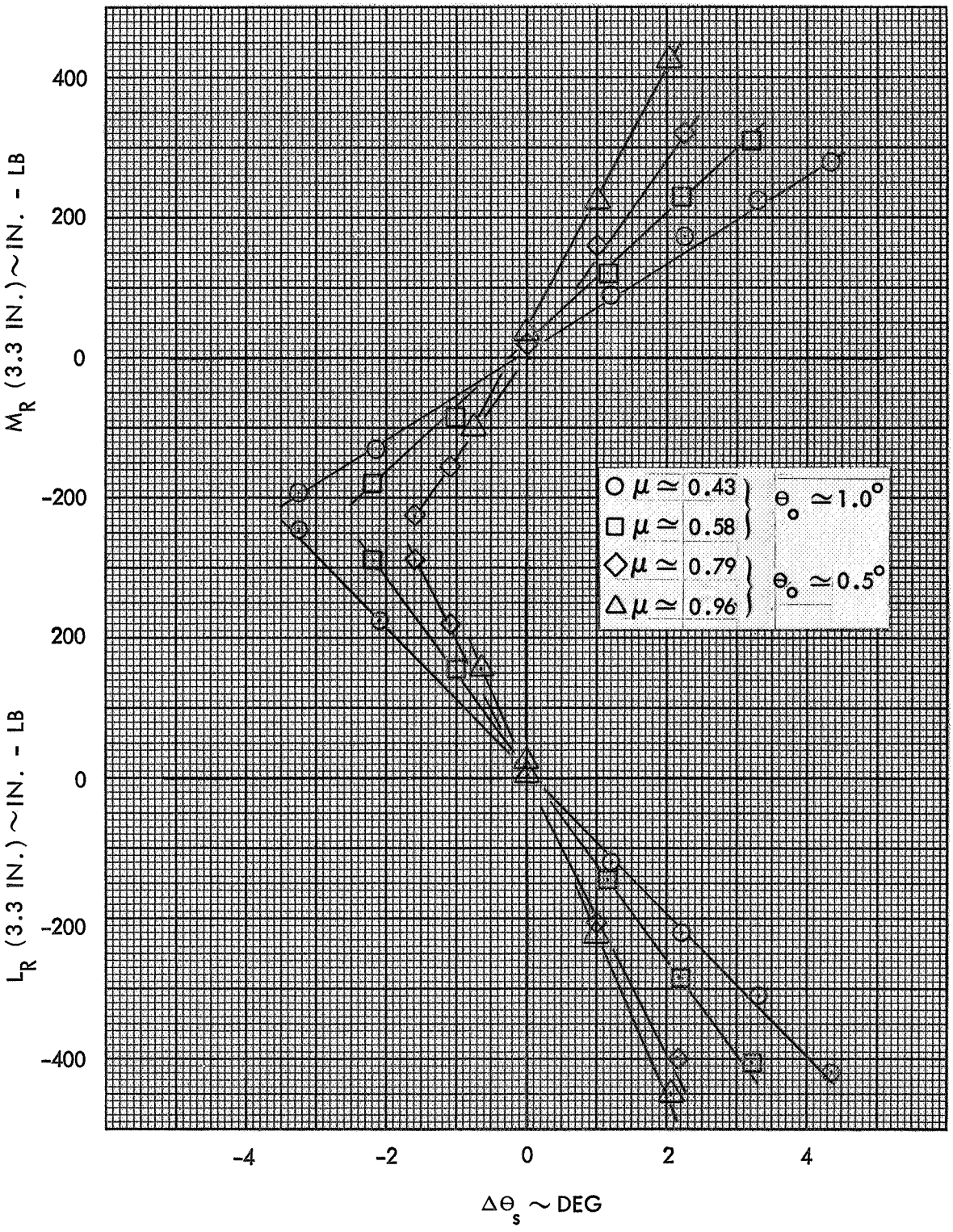

Figure 78. Rotor Pitch and Roll Response to Longitudinal Cyclic Pitch, Configuration 1, 550 RPM (γ=5.0,P=1.56)

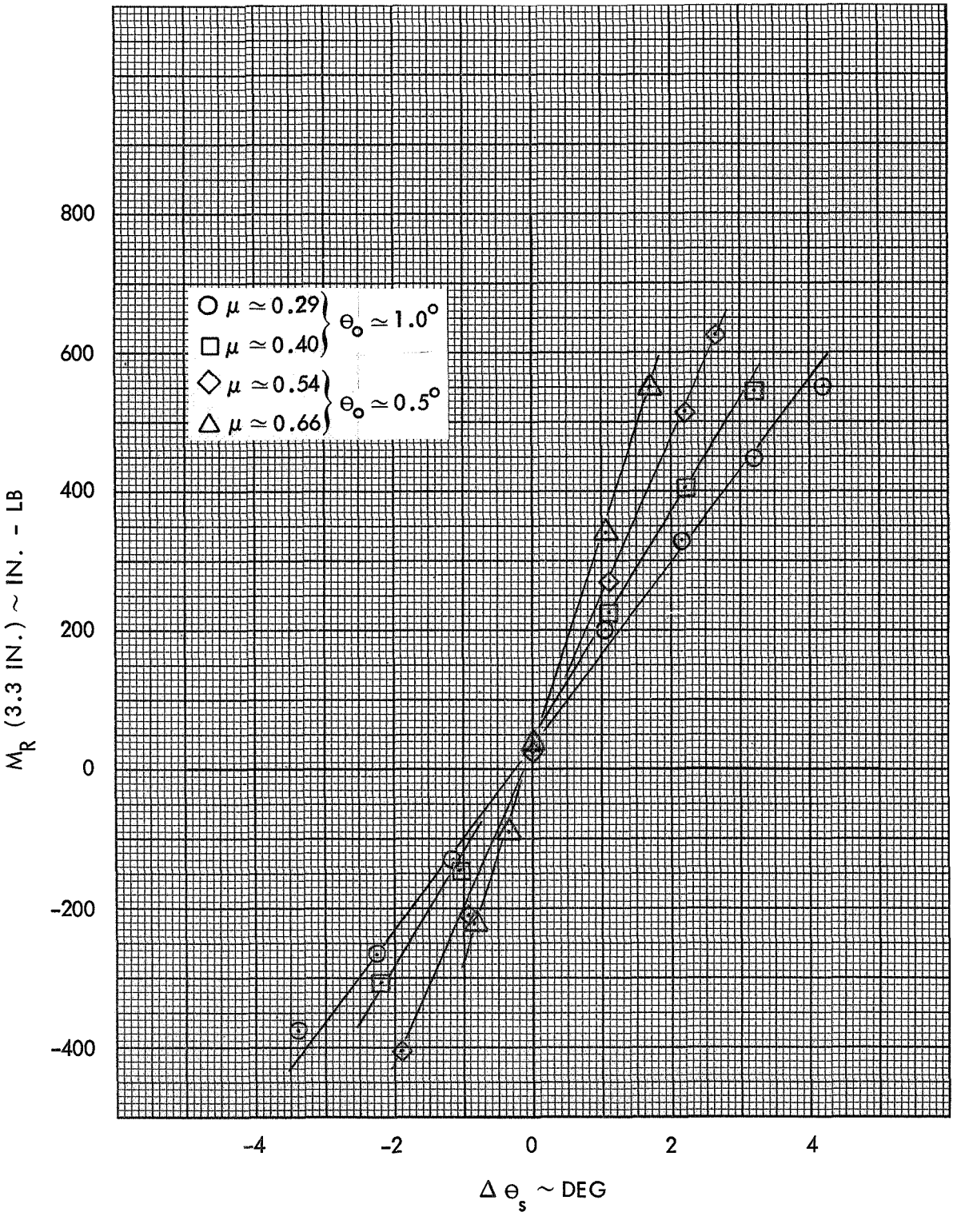

Figure 79. Rotor Pitch Response to Longitudinal Cyclic Pitch, Configuration 1, 800 RPM (γ=5.0, P=1.33)

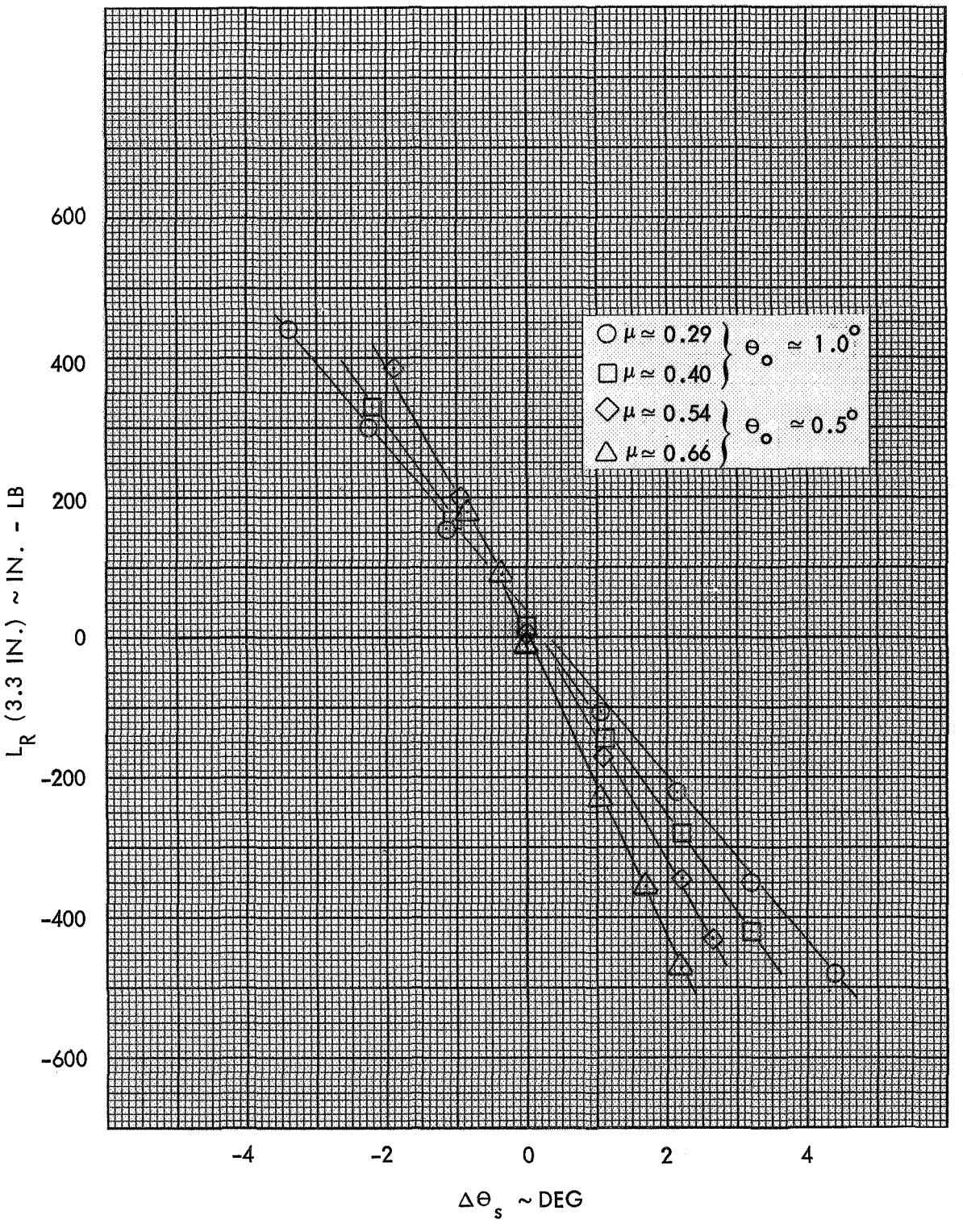

Figure 80. Rotor Roll Response to Longitudinal Cyclic Pitch, Configuration 1, 800 RPM(γ=5.0, P=1.33)

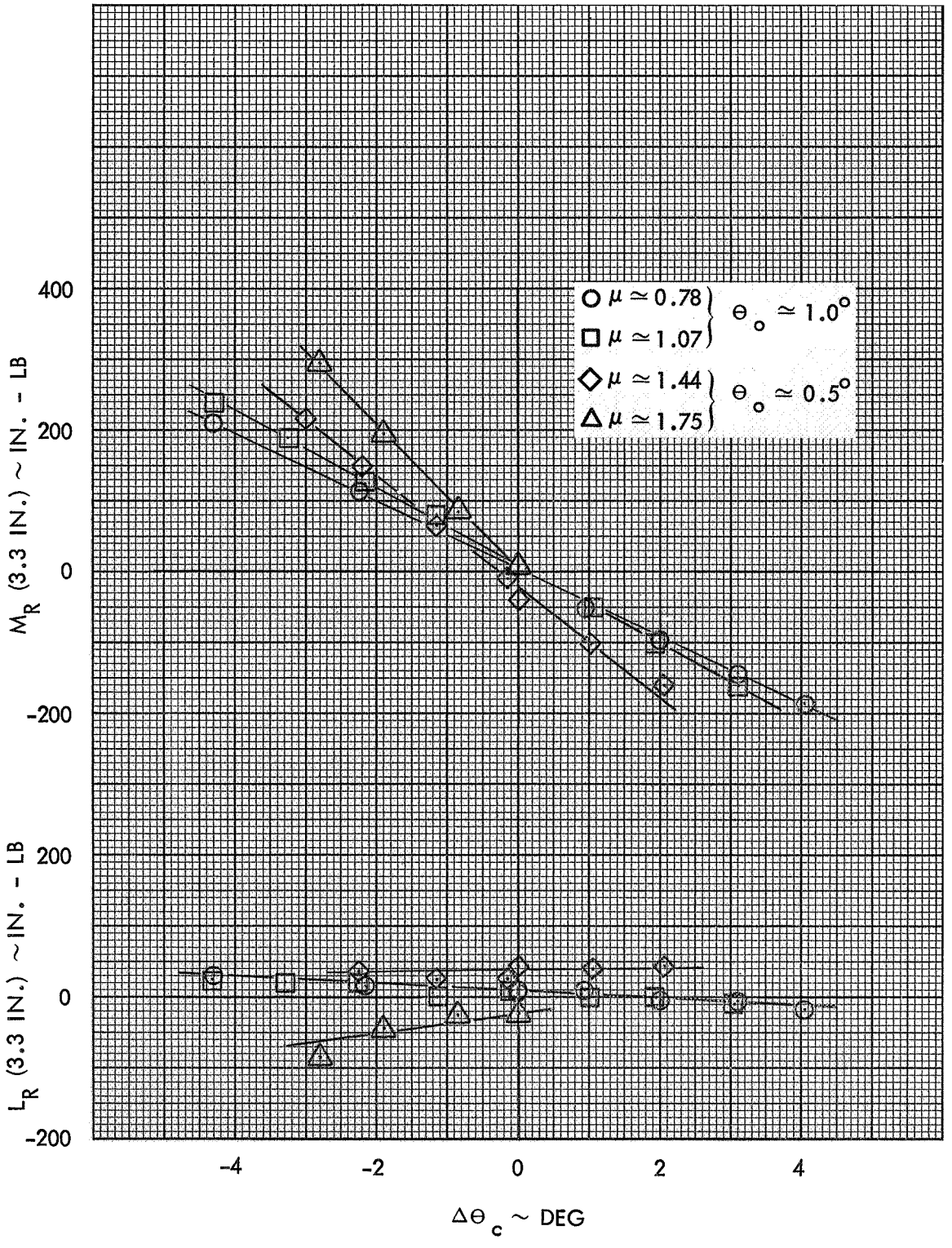

Figure 81. Rotor Pitch and Roll Response to Lateral Cyclic Pitch, Configuration 1, 300 RPM (γ=5.0, P=2.32)

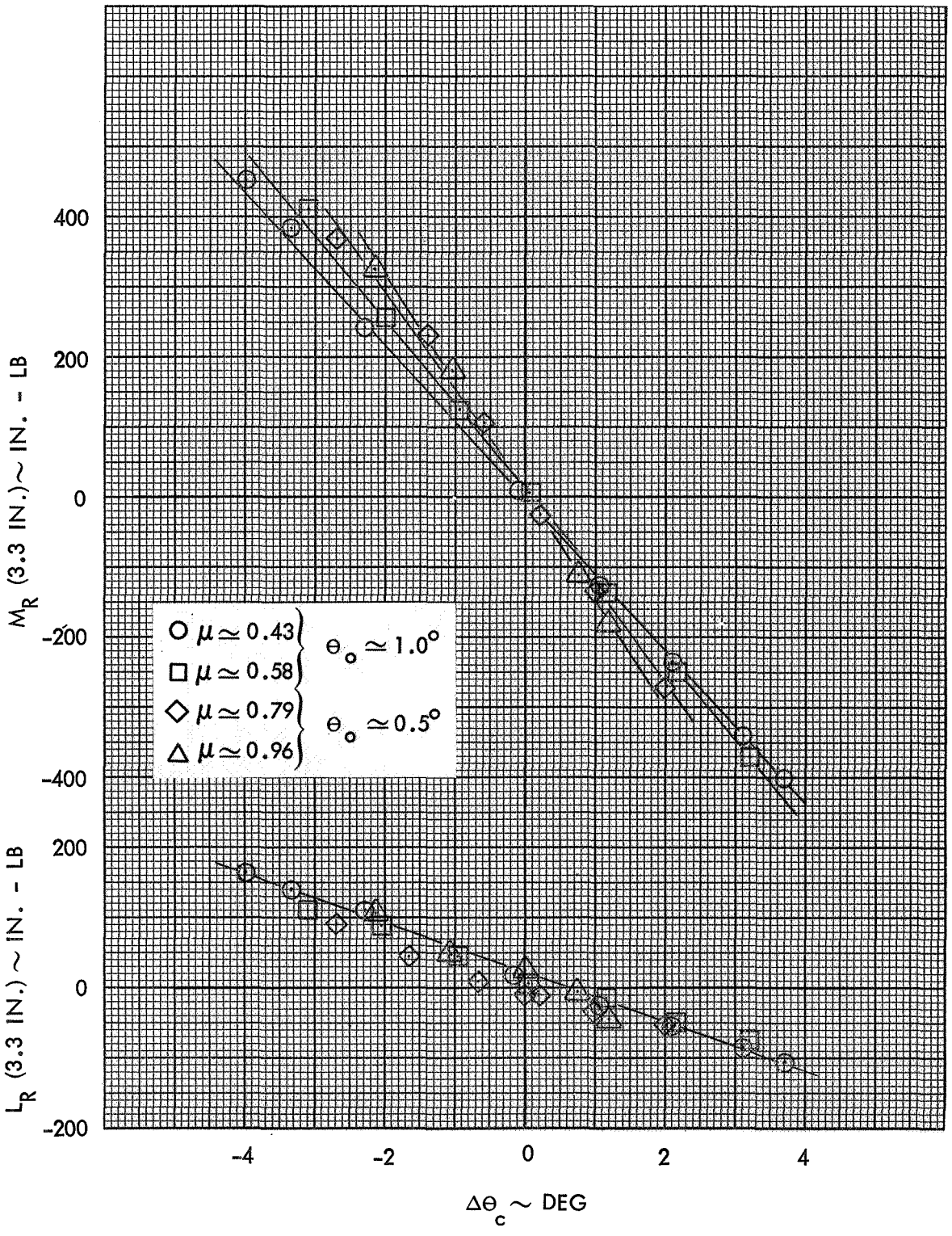

Figure 82. Rotor Pitch and Roll Response to Lateral Cyclic Pitch, Configuration 1, 550 RPM (γ=5.0, P=1.56)

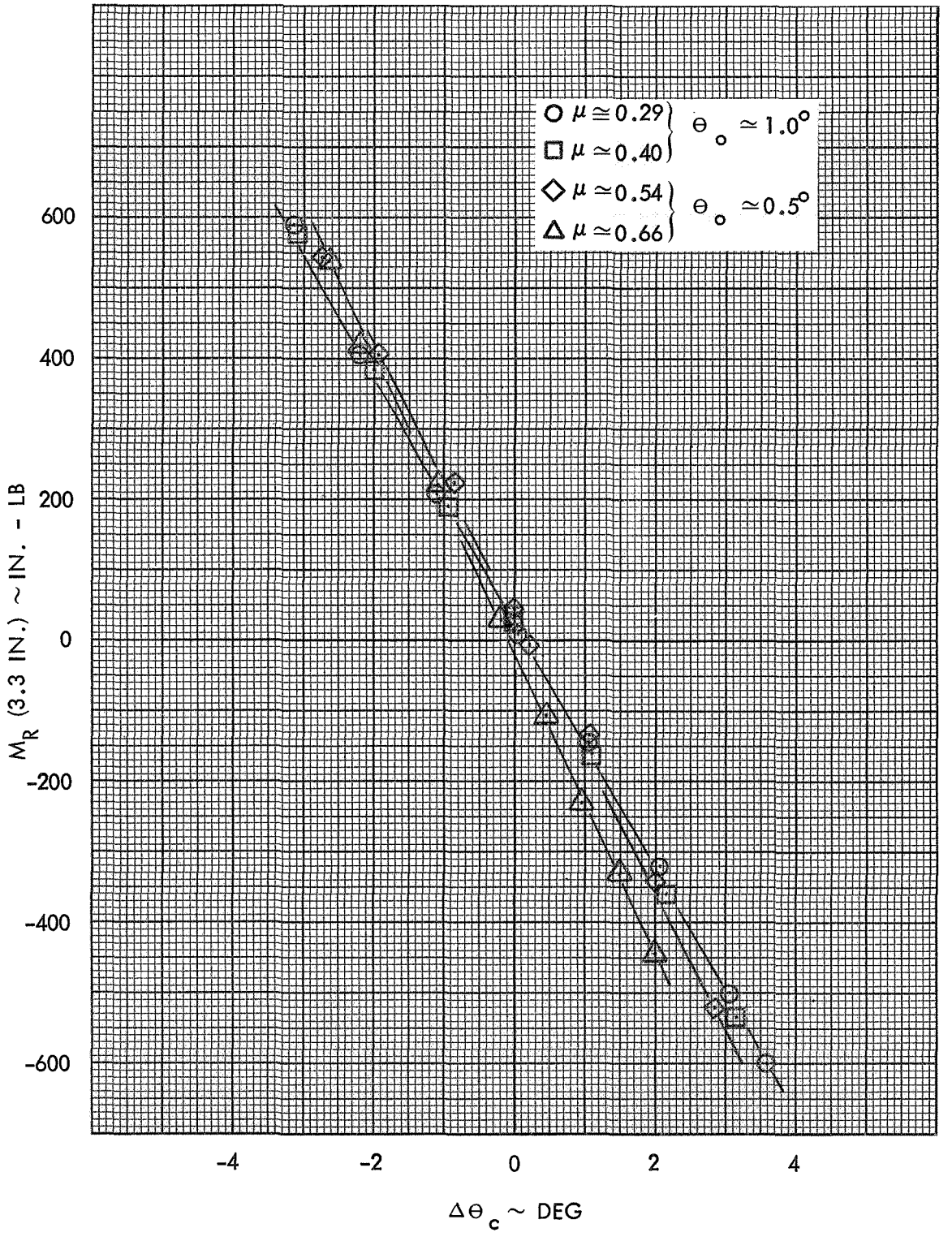

Figure 83. Rotor Pitch Response to Lateral Cyclic Pitch, Configuration 1, 800 RPM (γ=5.0, P=1.33)

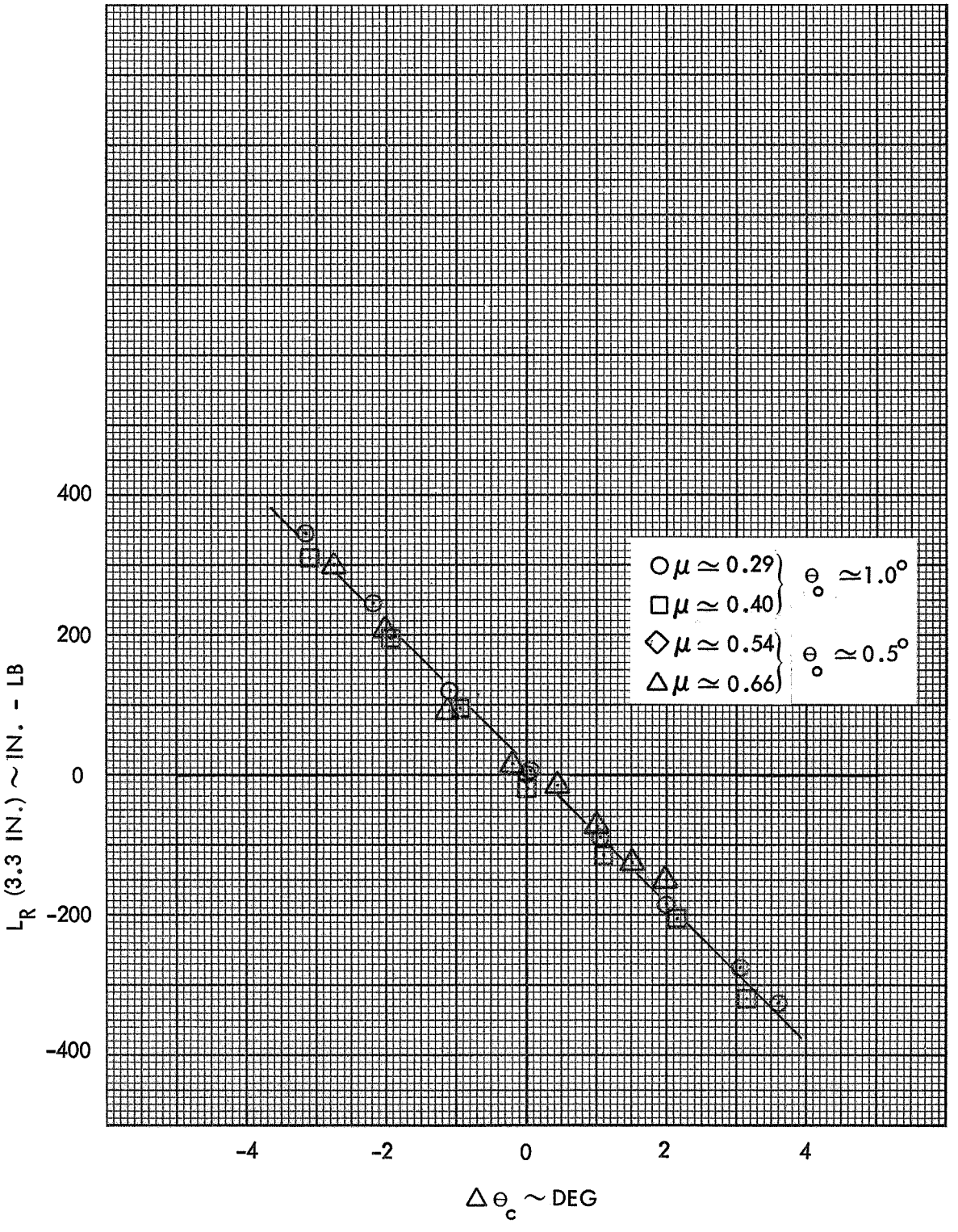

Figure 84. Rotor Roll Response to Lateral Cyclic Pitch, Configuration 1, 800 RPM (γ=5.0, P=1.33)

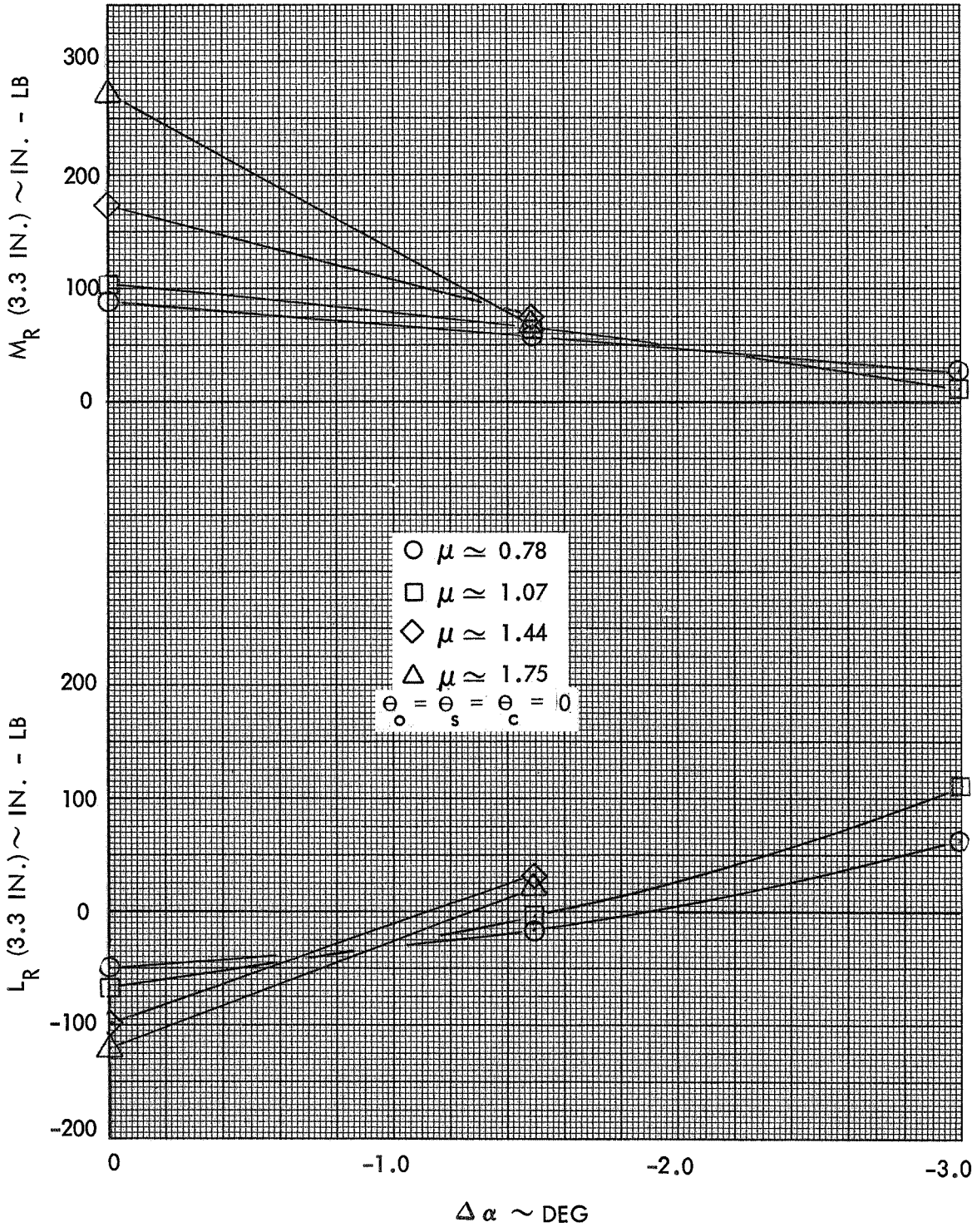

Figure 85. Rotor Pitch and Roll Response to a Rotor Shaft Angle of Attack Increment, Configuration 1, 300 RPM (γ=5.0, P=2.32)

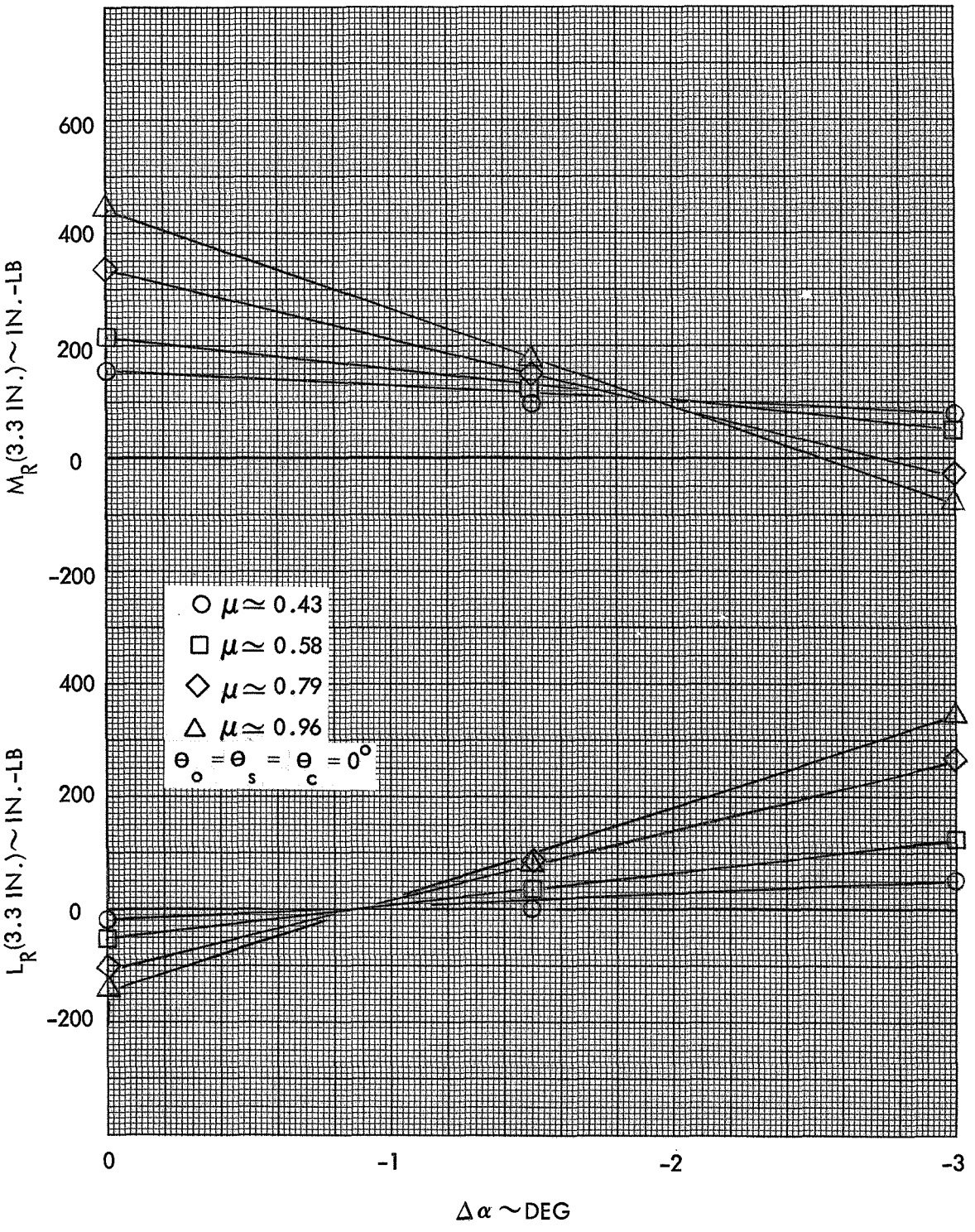

Figure 86. Rotor Pitch and Roll Response to a Rotor Shaft Angle of Attack Increment, Configuration 1, 550 RPM (γ=5.0, P=1.56)

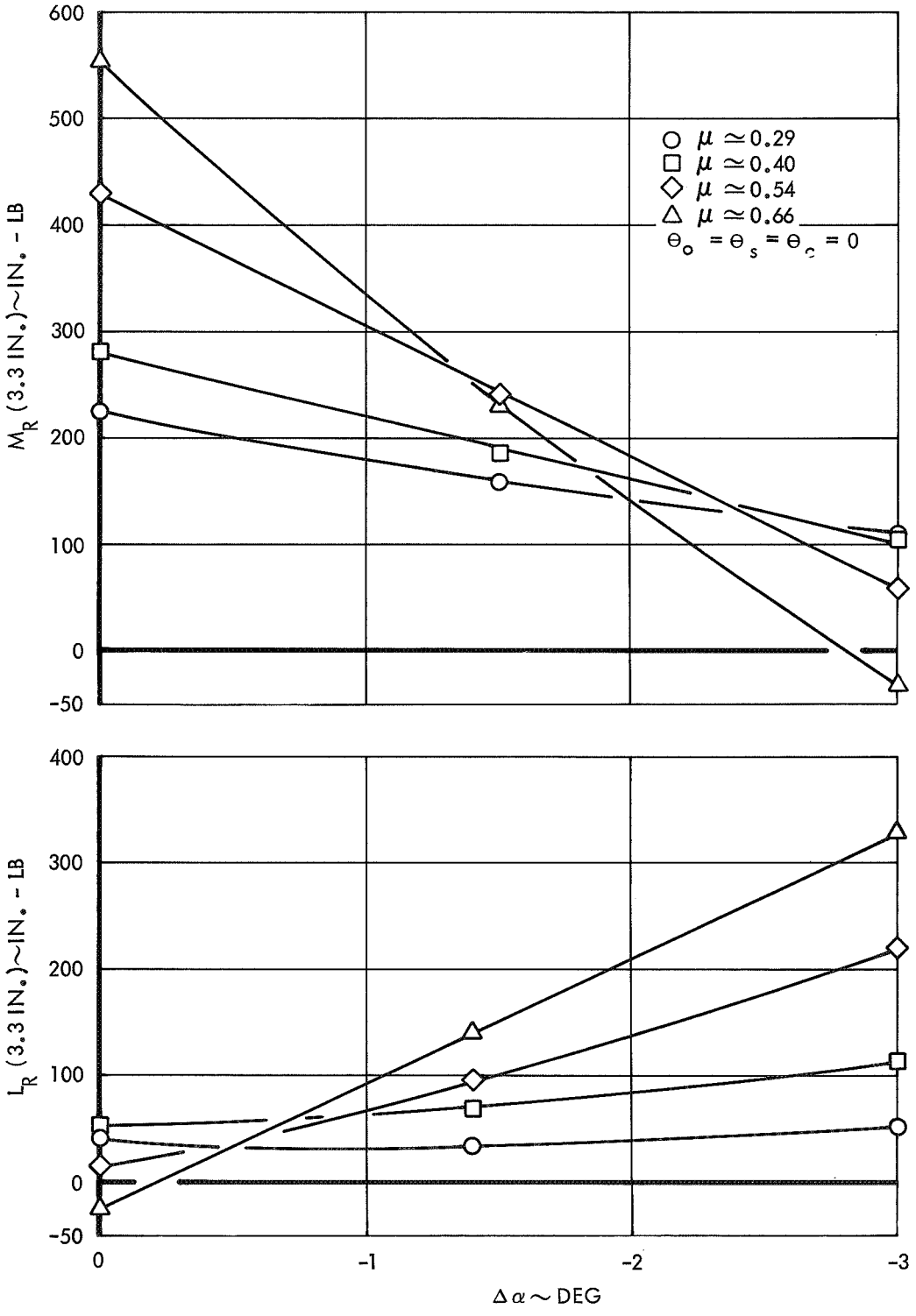

Figure 87. Rotor Pitch and Roll Response to a Rotor Shaft Angle of Attack Increment, Configuration 1, 800 RPM (γ=5.0, P=1.33)

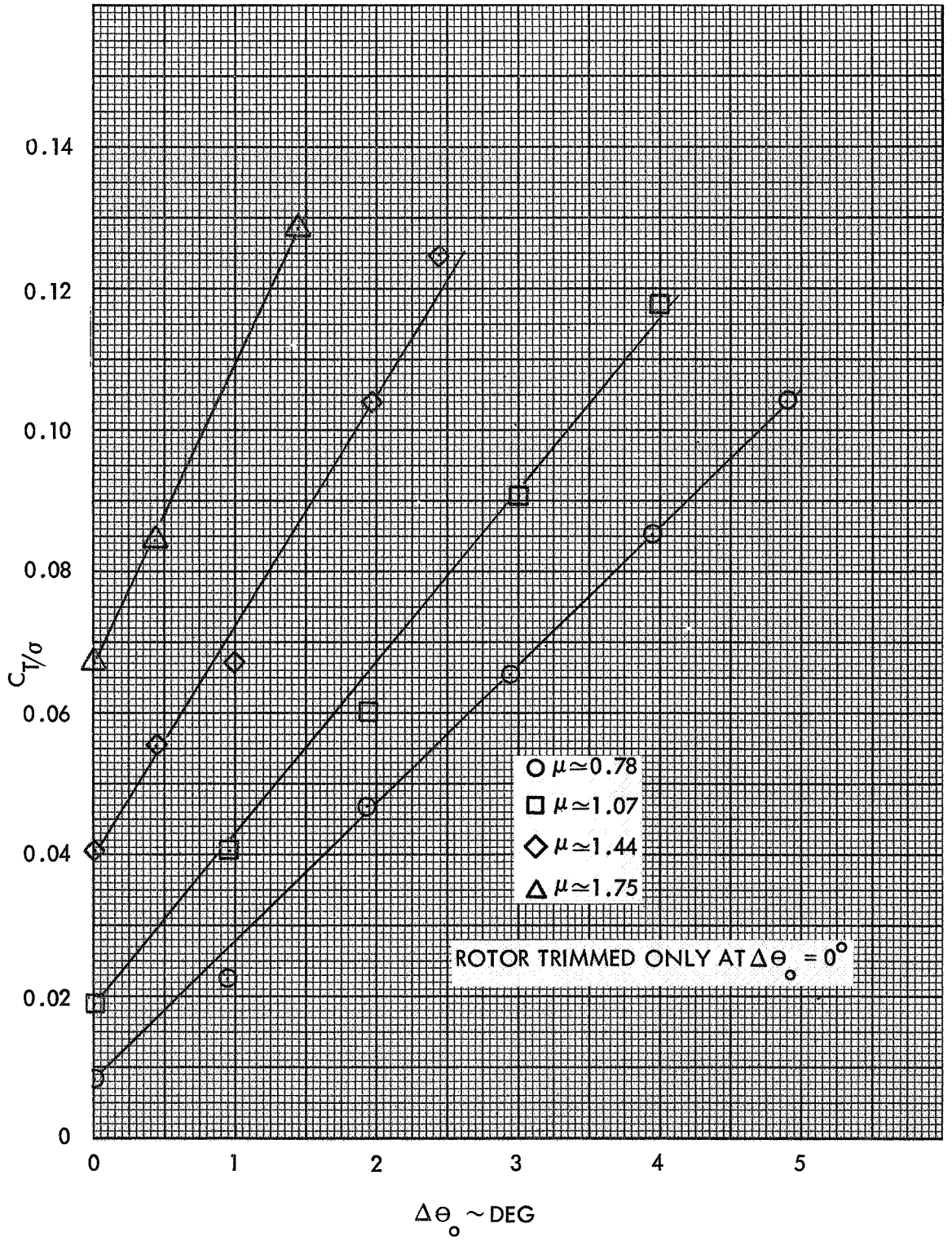

Figure 88. Rotor Lift versus Collective Pitch, Configuration 1, 300 RPM (γ=5.0, P=2.32)

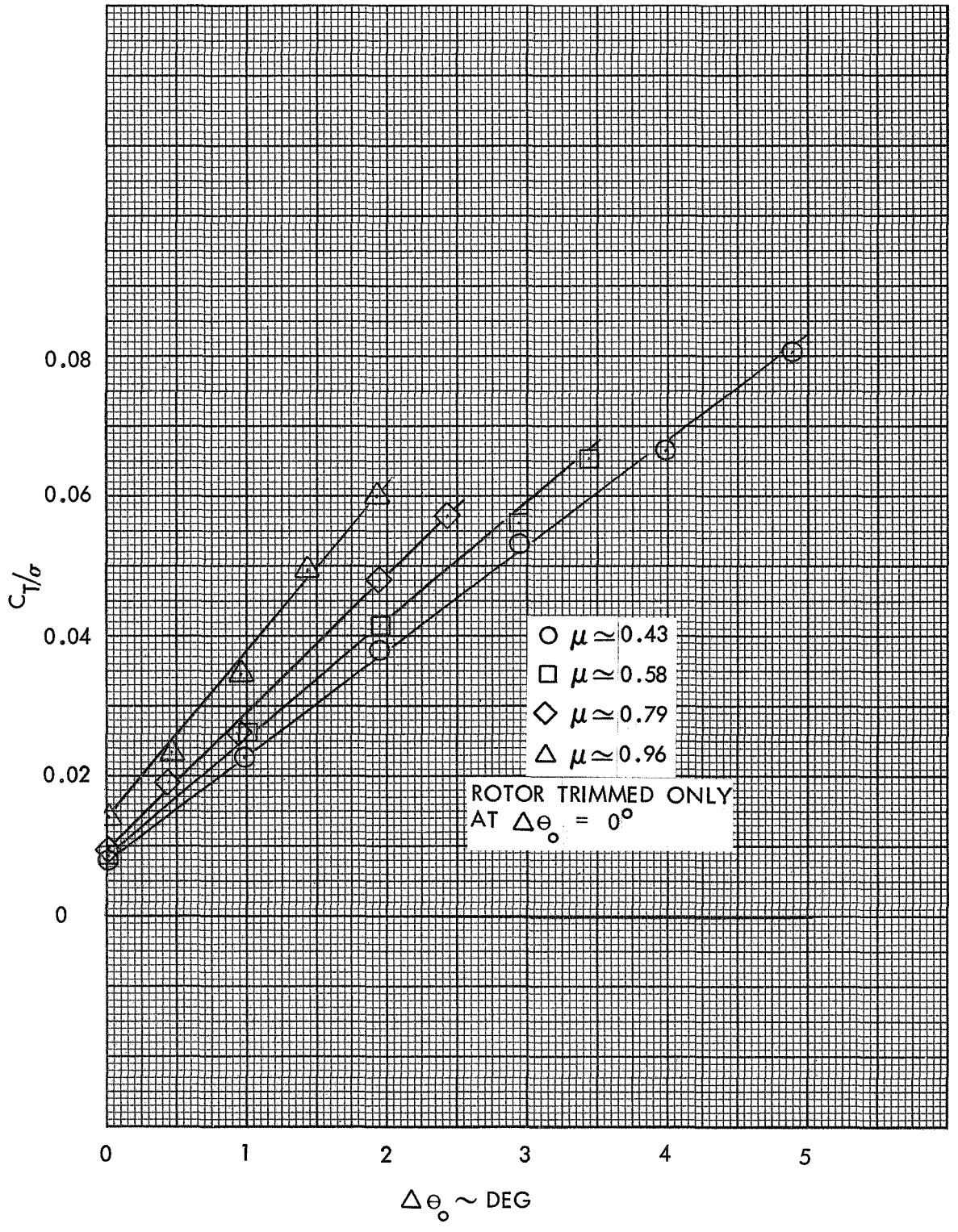

Figure 89. Rotor Lift versus Collective Pitch, Configuration 1, 550 RPM (γ=5.0, P=1.56)

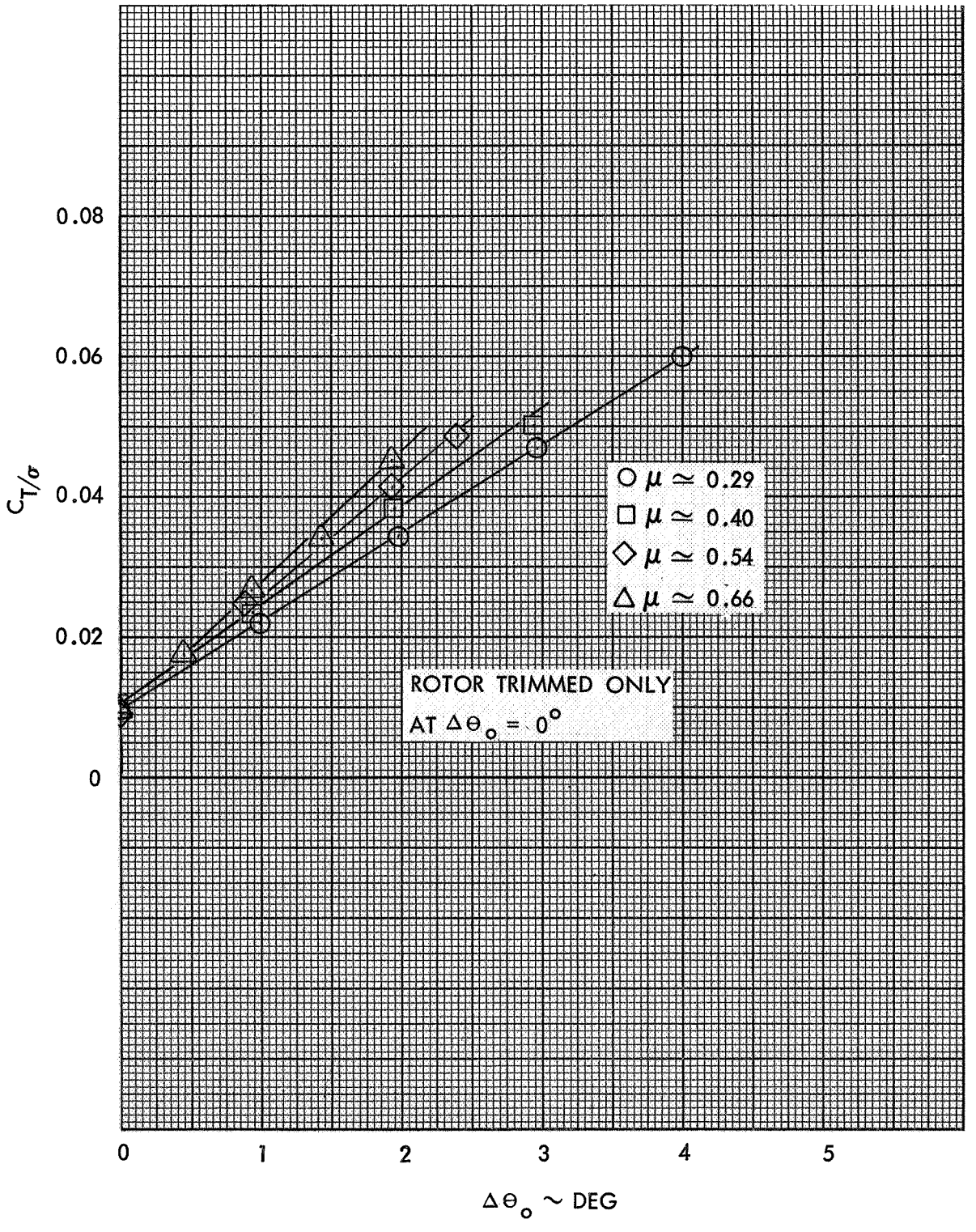

Figure 90. Rotor Lift versus Collective Pitch, Configuration 1, 800 RPM (γ=5.0, P=1.33)

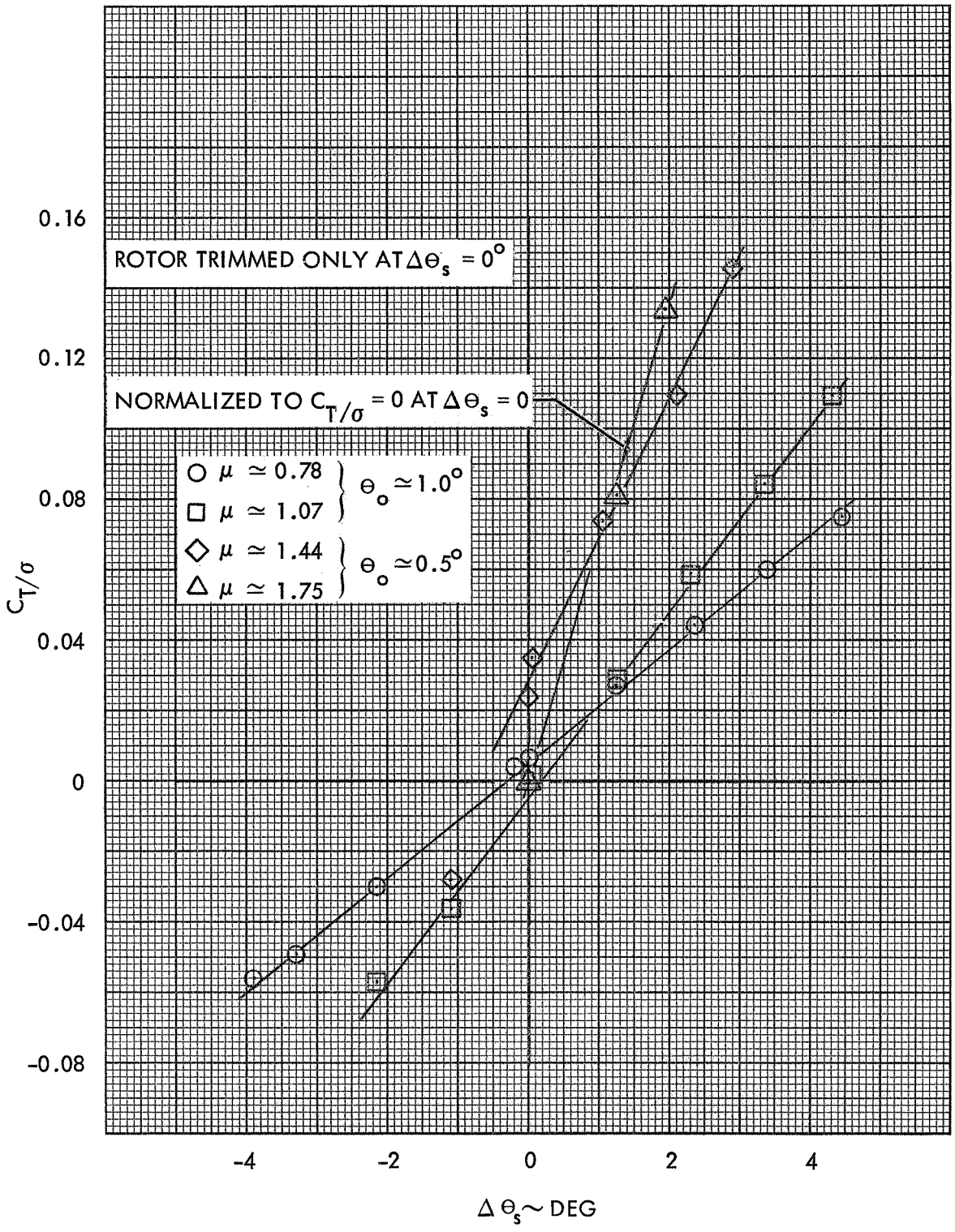

Figure 91. Rotor Lift versus Longitudinal Cyclic Pitch, Configuration 1, 300 RPM (γ=5.0, P=2.32)

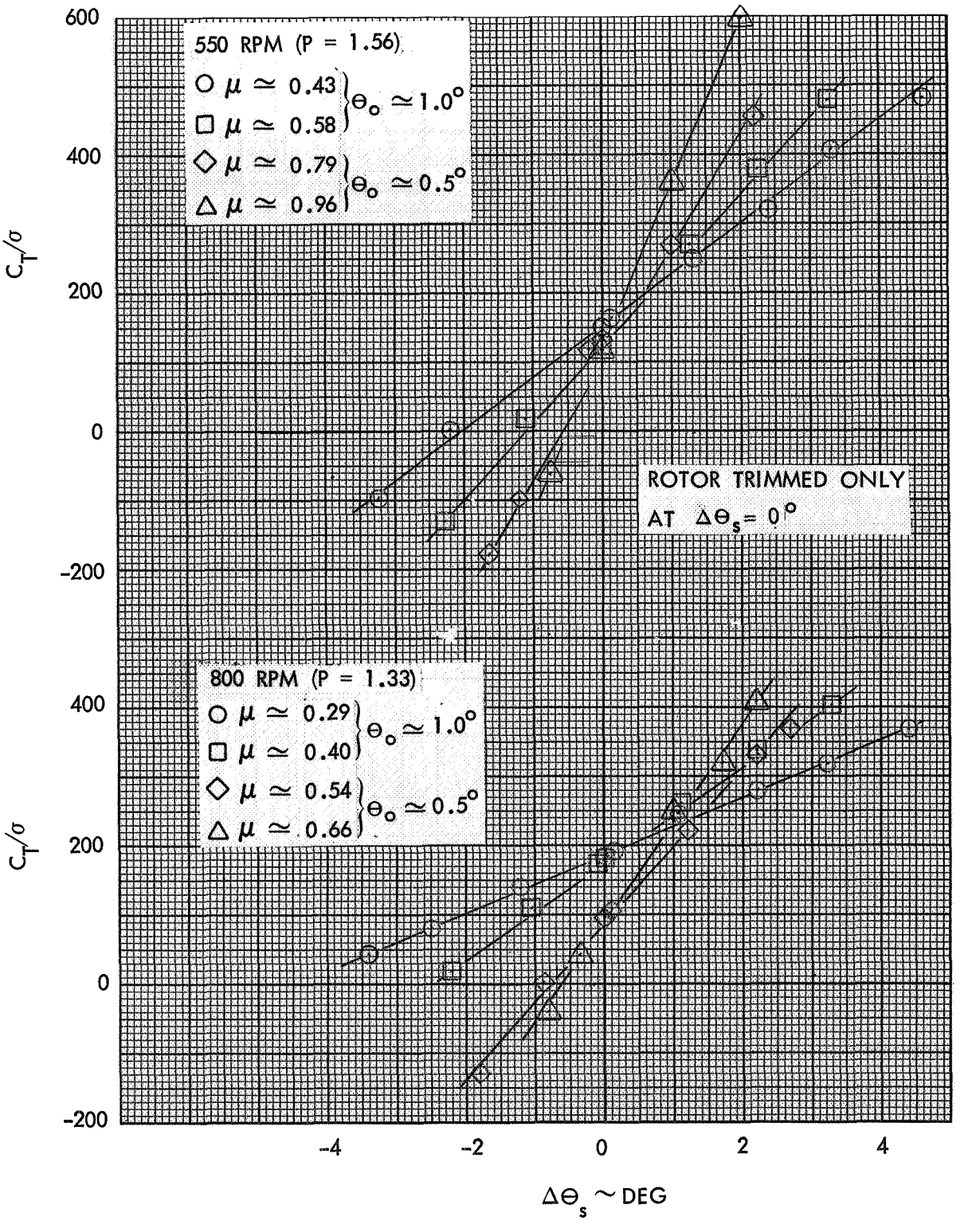

Figure 92. Rotor Lift versus Longitudinal Cyclic Pitch, Configuration 1, 550 RPM and 800 RPM (γ=5.0)

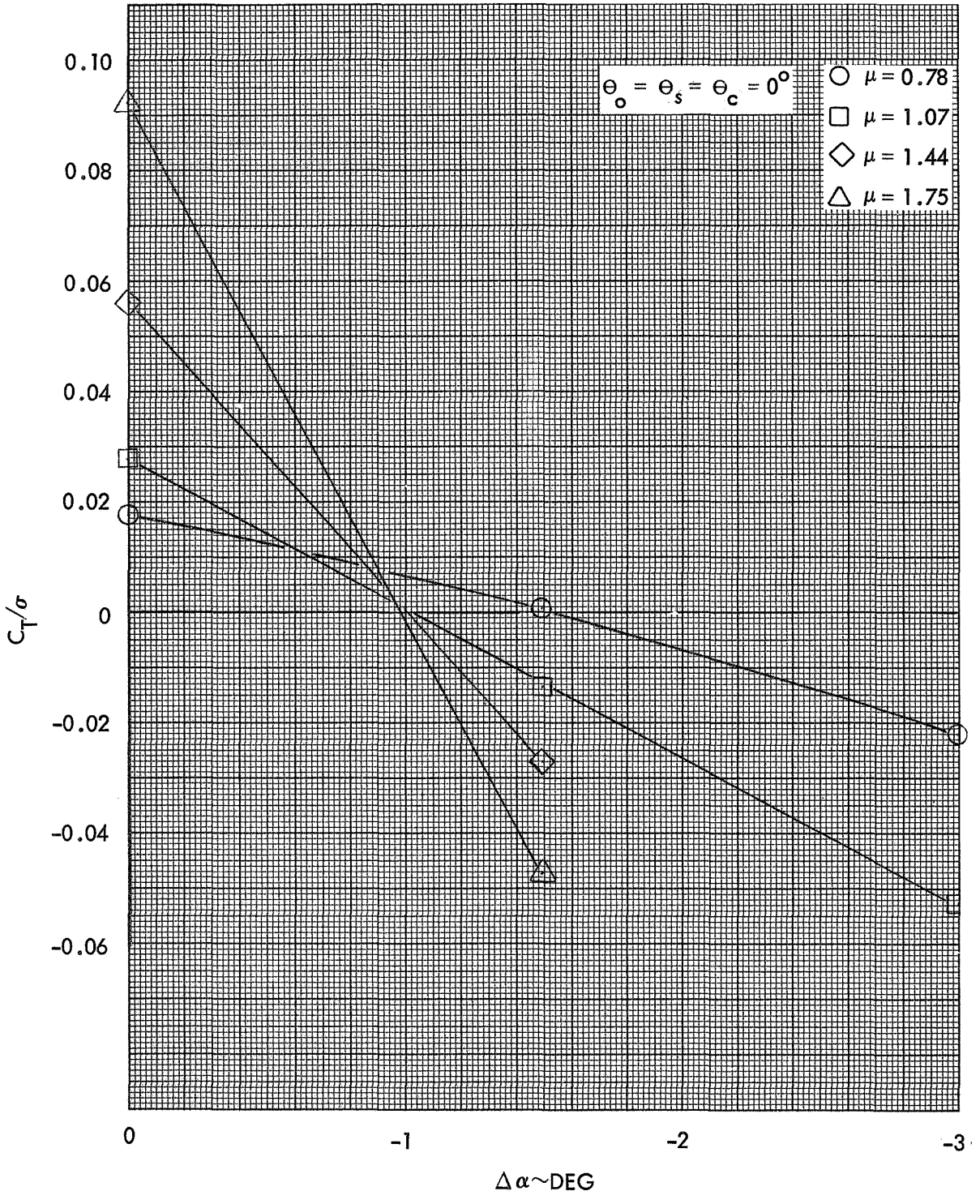

Figure 93. Rotor Lift versus Rotor Shaft Angle of Attack, Configuration 1, 300 RPM (γ=5.0, P=2.32)

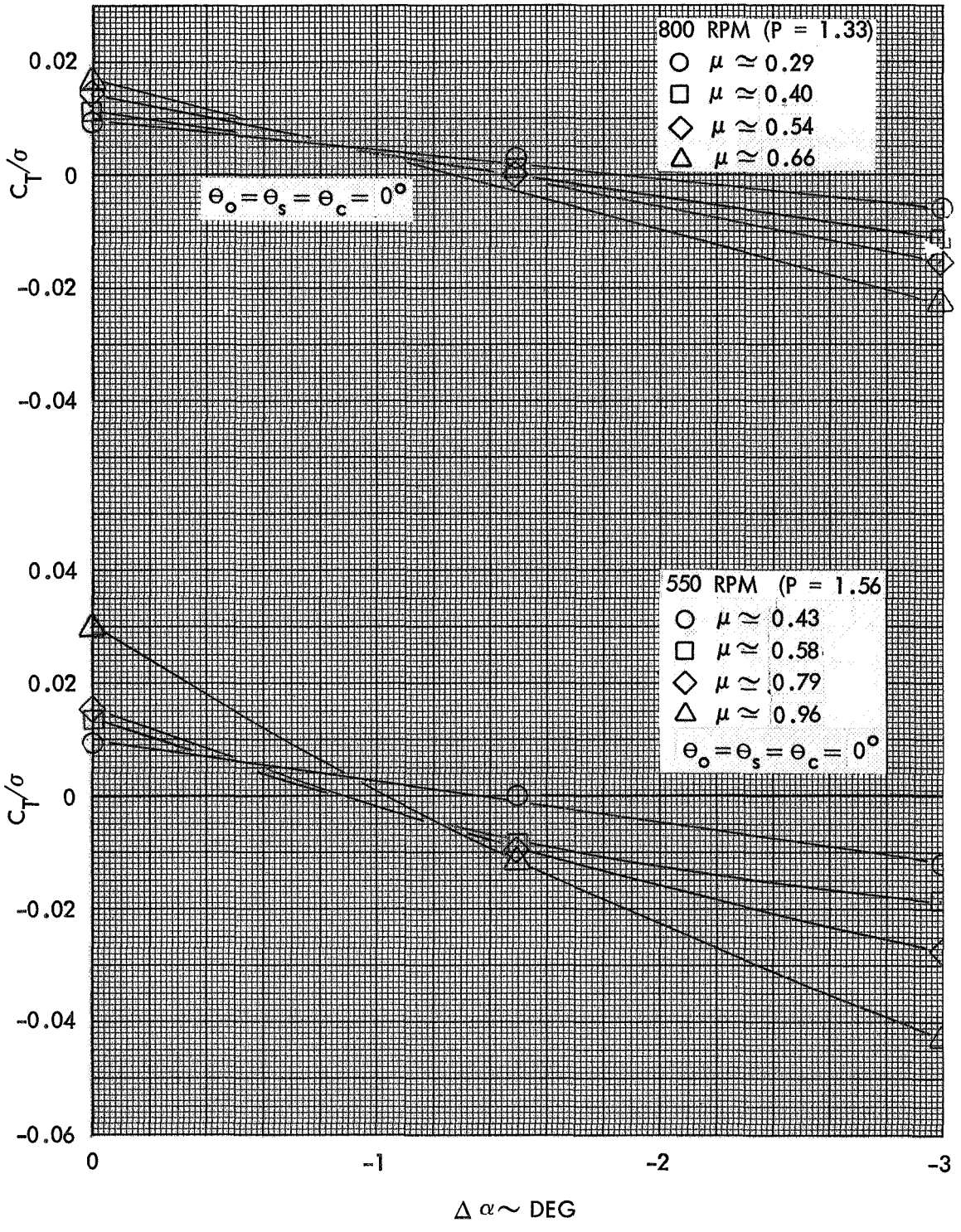

Figure 94. Rotor Lift versus Rotor Shaft Angle of Attack, Configuration 1, 550 RPM and 800 RPM (γ=5.0)

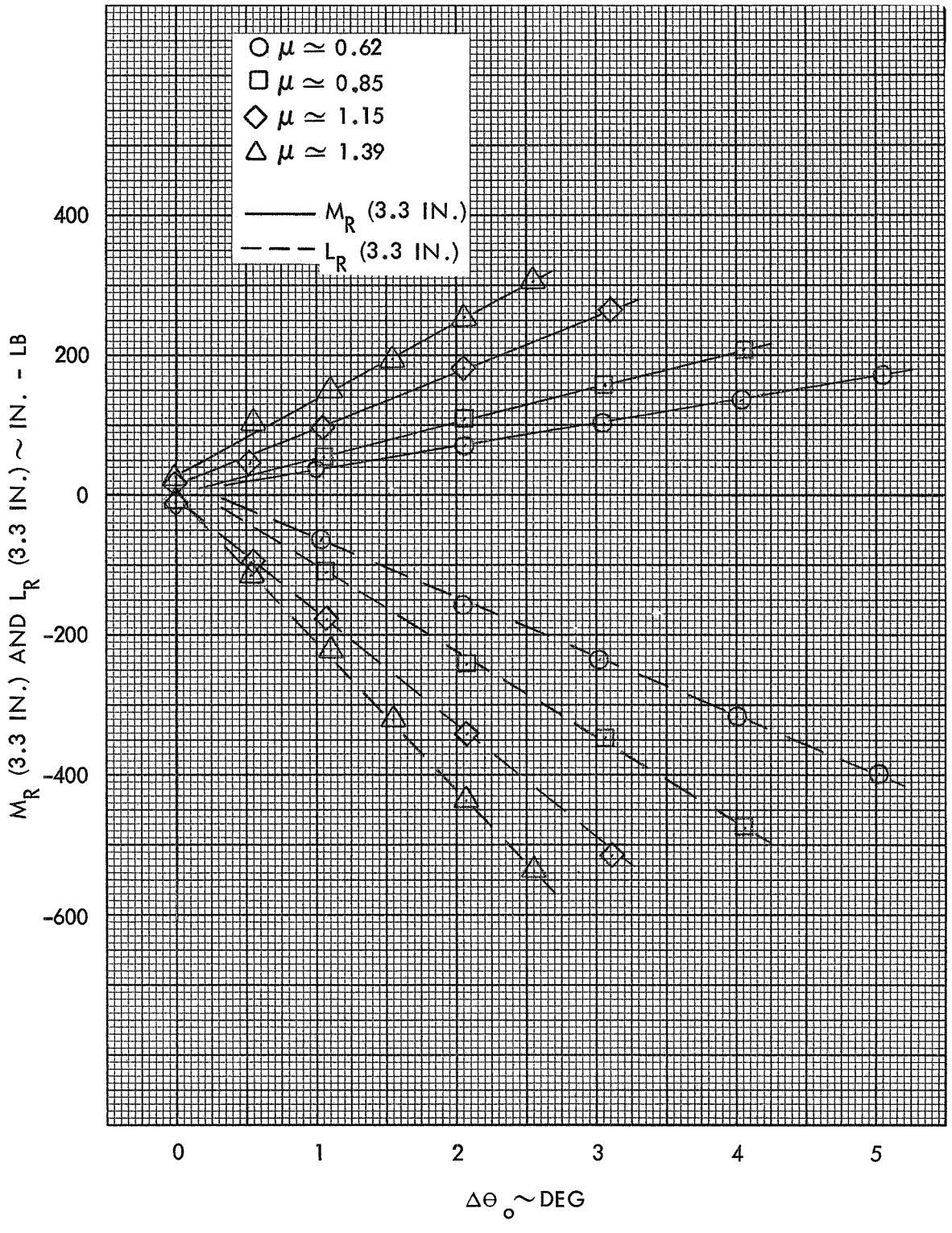

Figure 95. Rotor Pitch and Roll Response to Collective Pitch, Configuration 2, 375 RPM (γ=3.0, P=1.59)

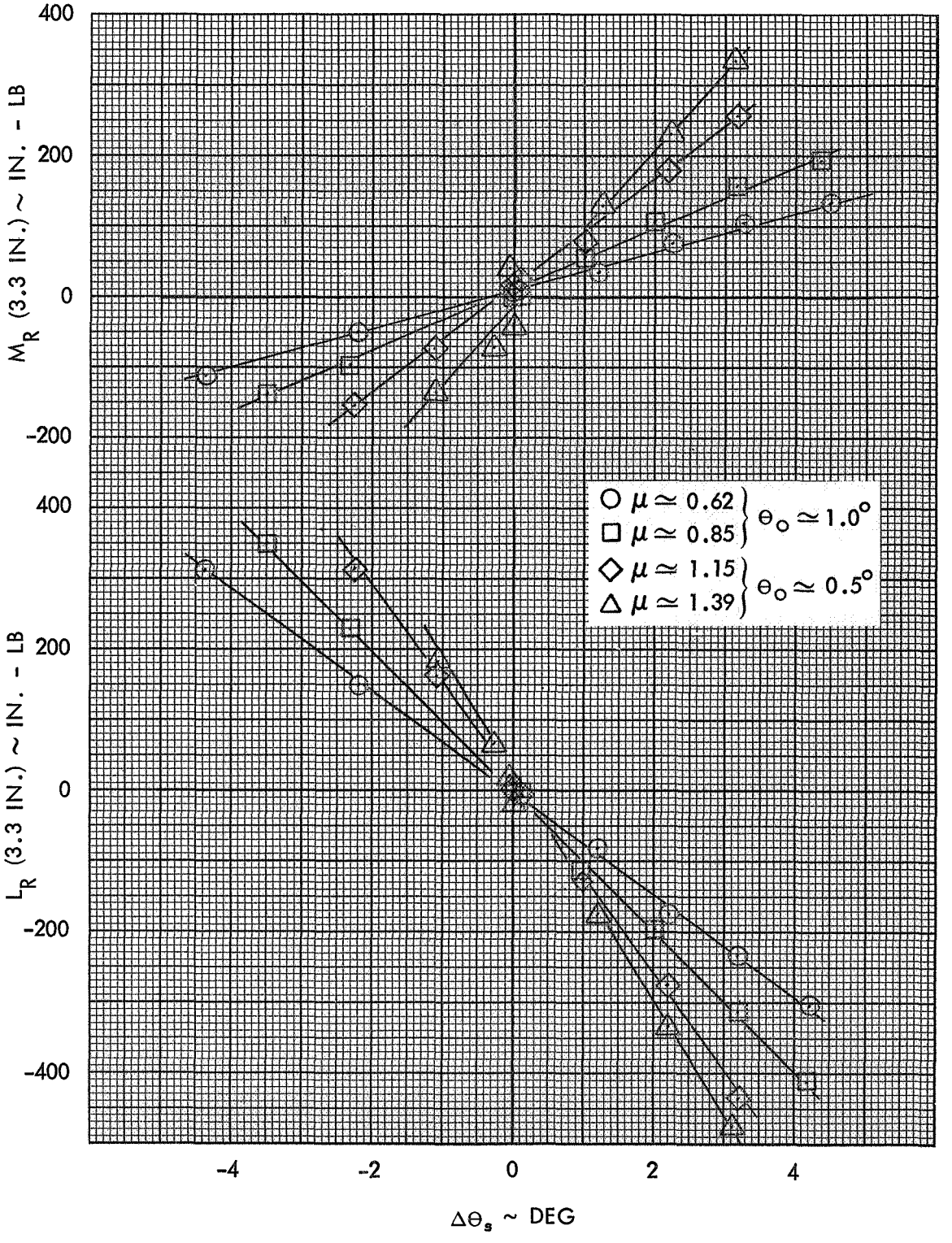

Figure 96. Rotor Pitch and Roll Response to Longitudinal Cyclic Pitch, Configuration 2, 375 RPM (γ=3.0, P=1.59)

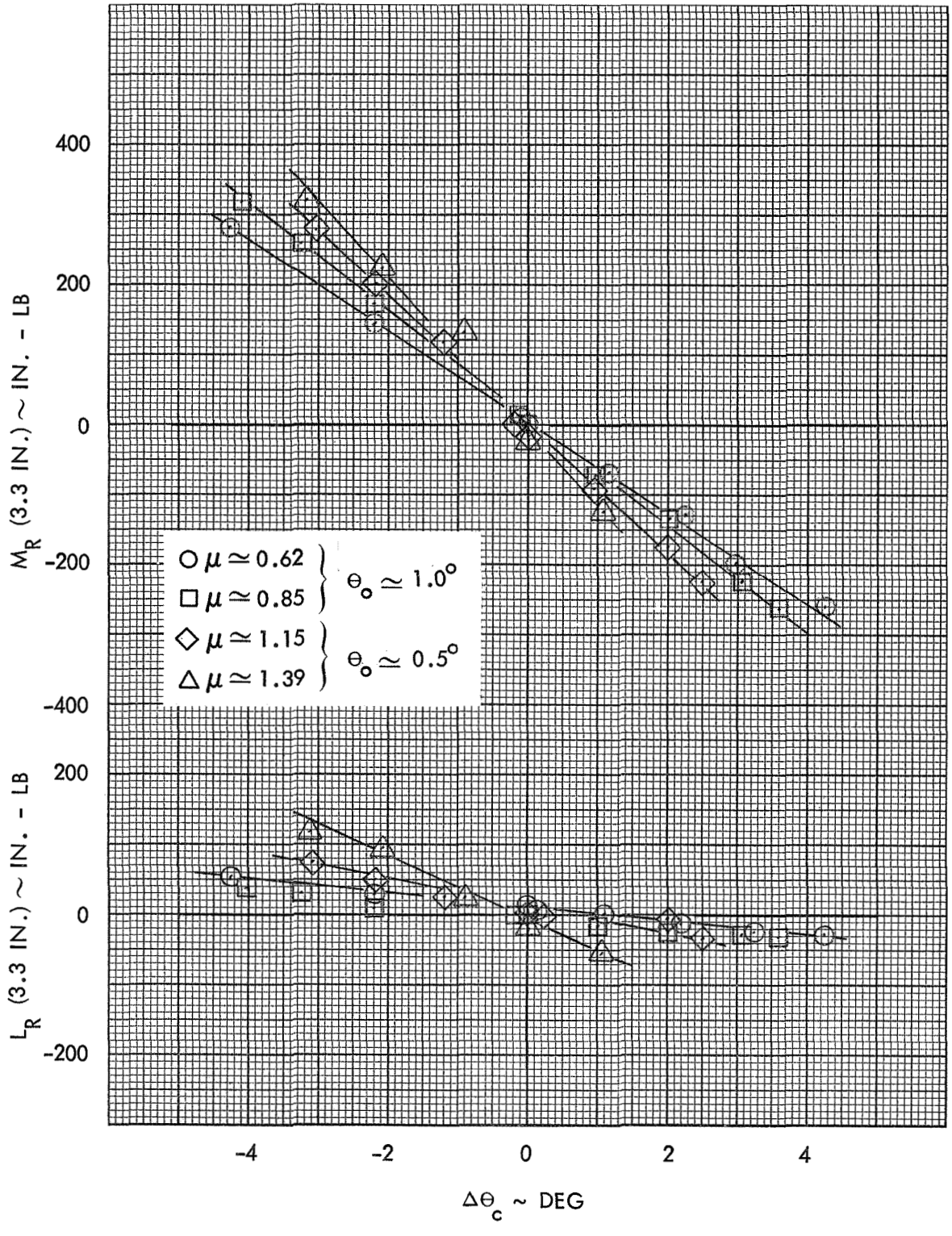

Figure 97. Rotor Pitch and Roll Response to Lateral Cyclic Pitch, Configuration 2, 375 RPM (γ=3.0, P=1.59)

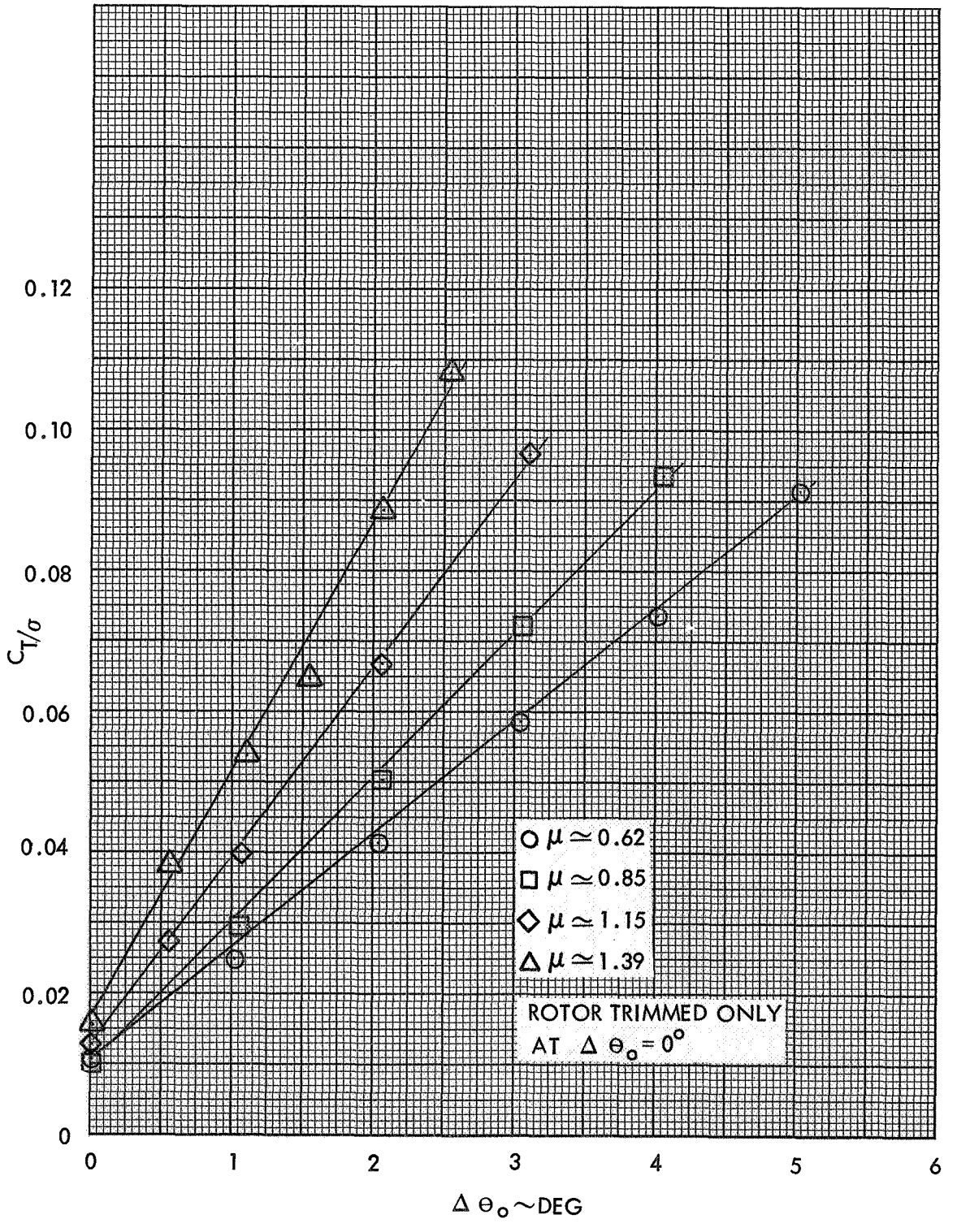

Figure 98. Rotor Lift versus Collective Pitch, Configuration 2, 375 RPM (γ=3.0, P=1.59)

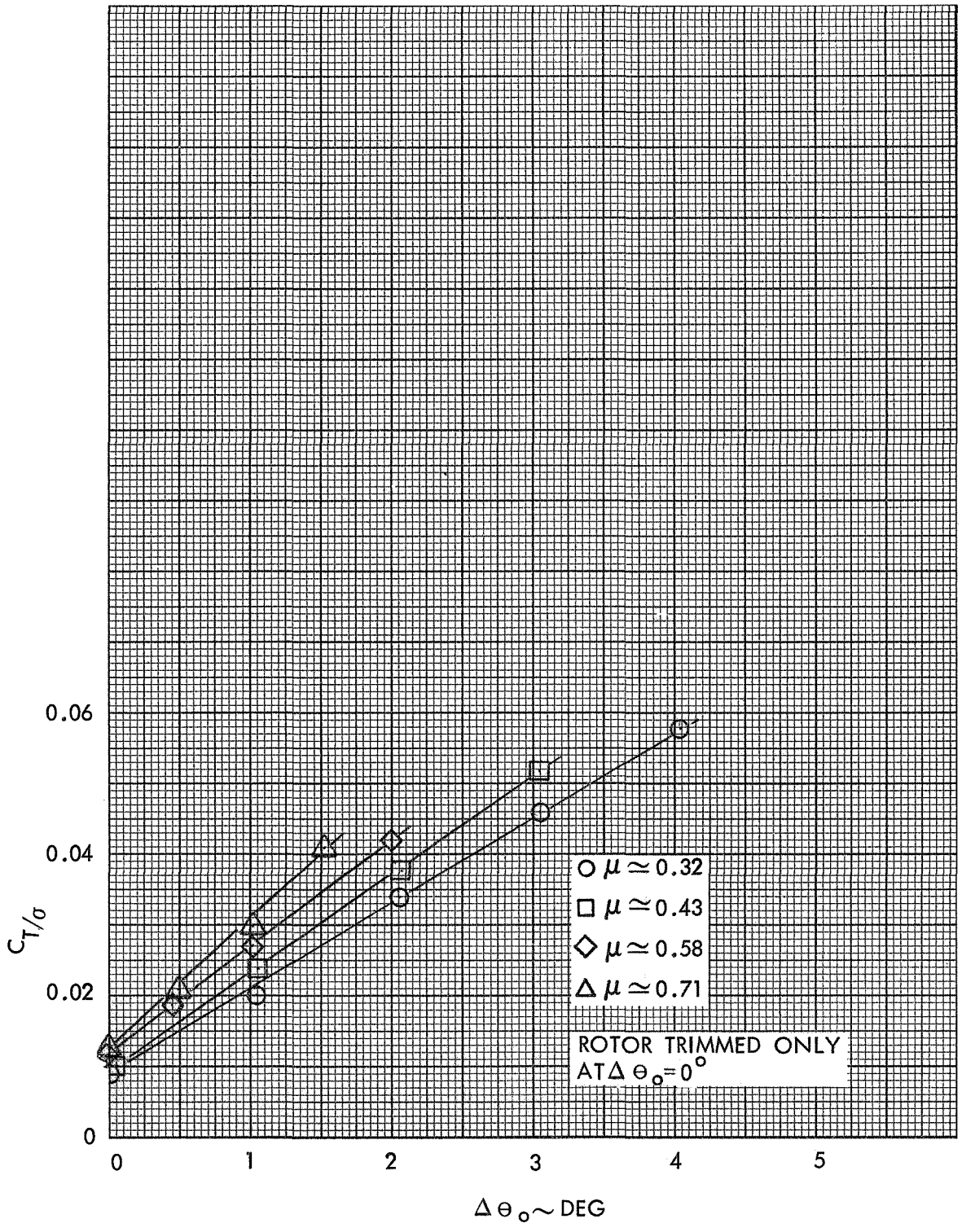

Figure 99. Rotor Lift versus Collective Pitch, Configuration 2, 750 RPM (γ=3.0, P=1.21)

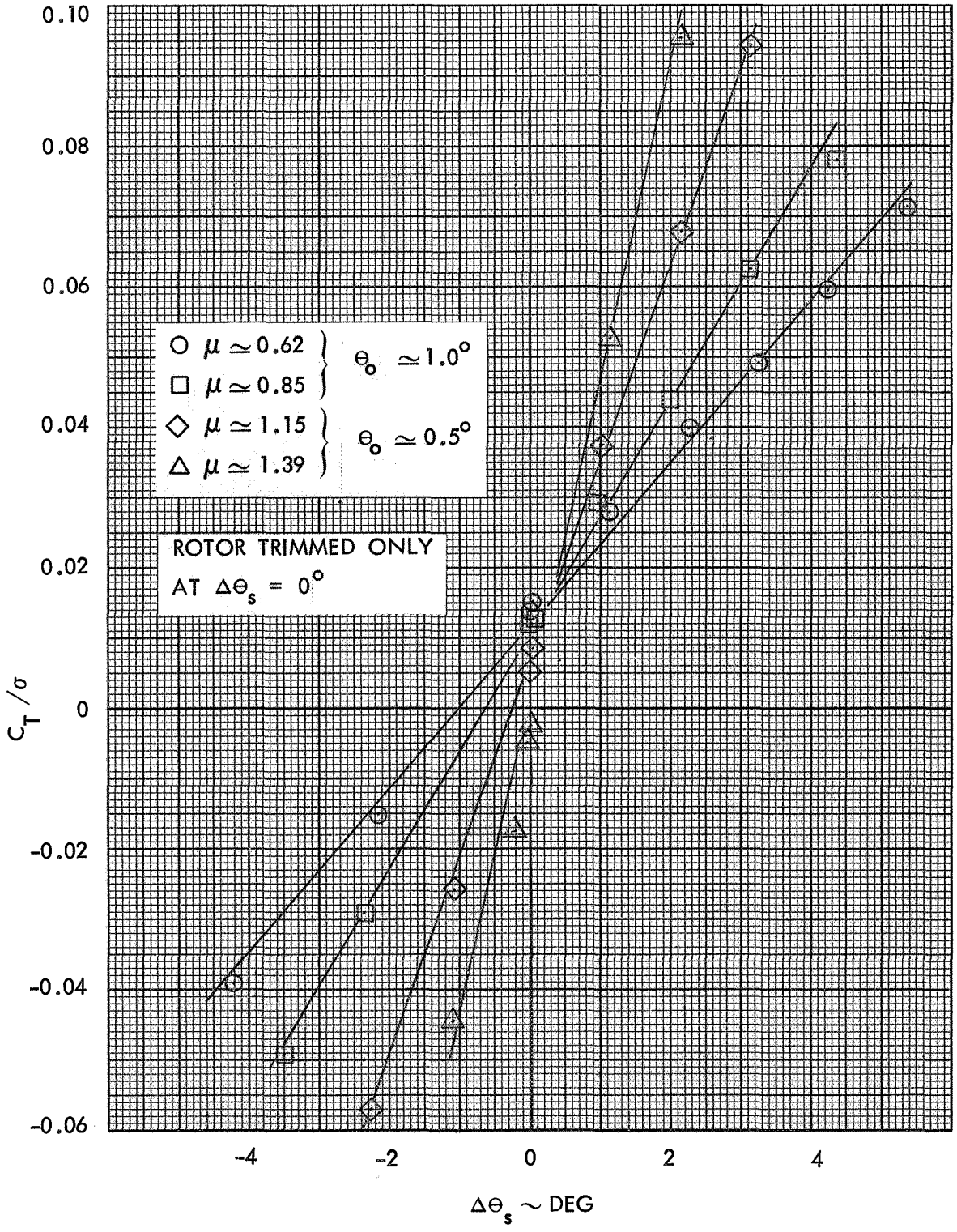

Figure 100. Rotor Lift versus Longitudinal Cyclic Pitch, Configuration 2, 375 RPM (γ=3.0, P=1.59)

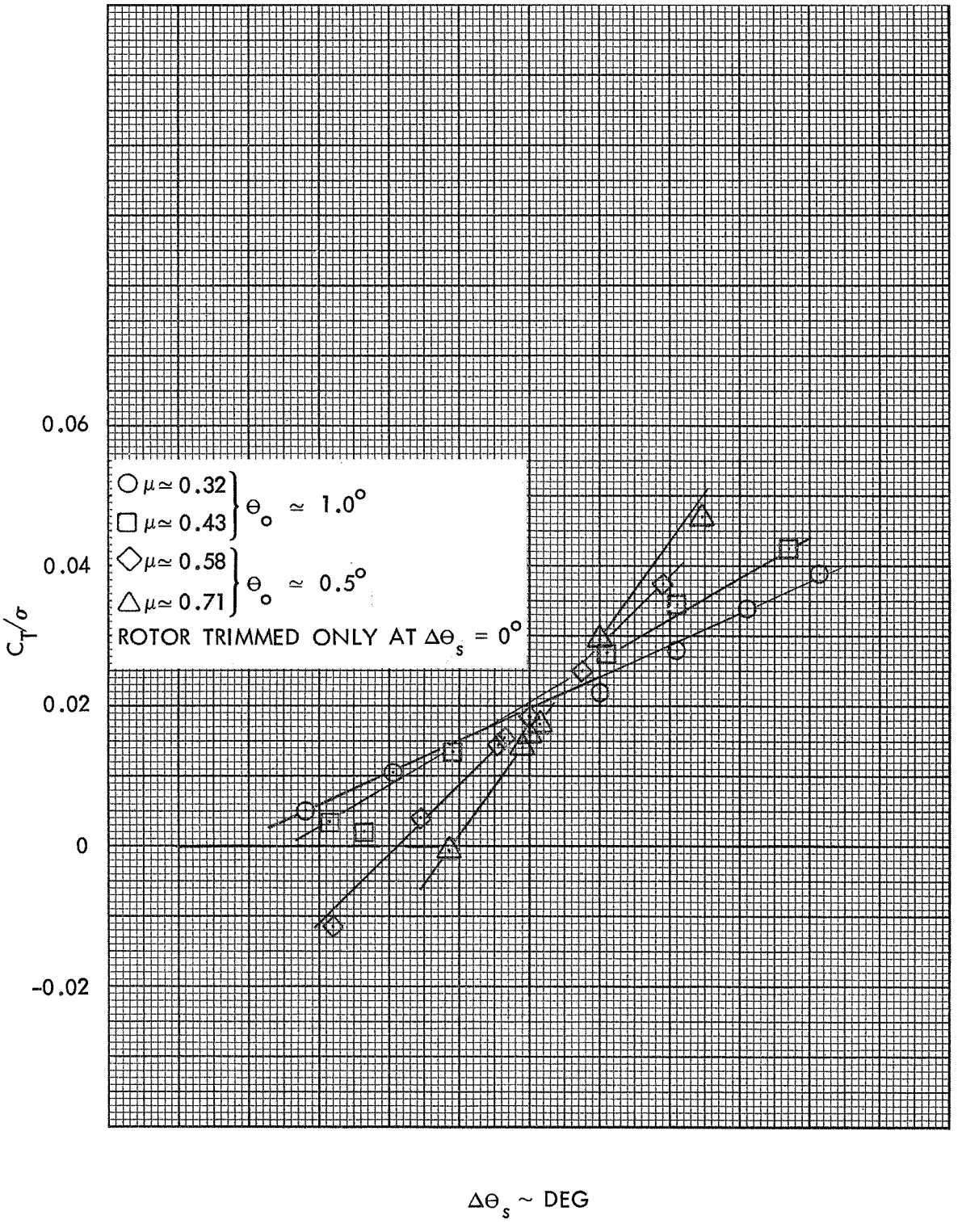

Figure 101. Rotor Lift versus Longitudinal Cyclic Pitch, Configuration 2, 750 RPM (γ=3.0, P=1.21)

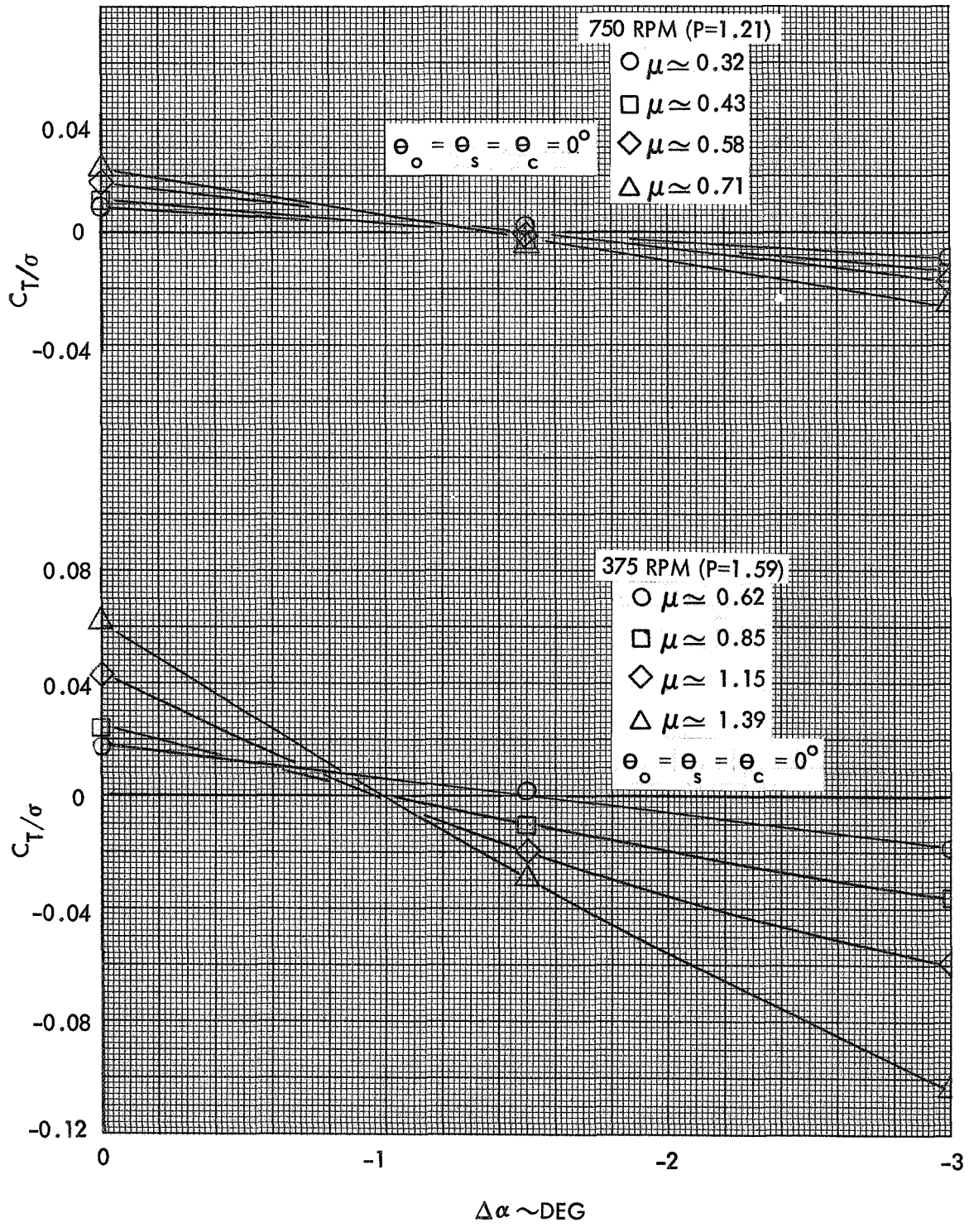

Figure 102. Rotor Lift versus Rotor Shaft Angle of Attack, Configuration 2, 375 RPM and 750 RPM

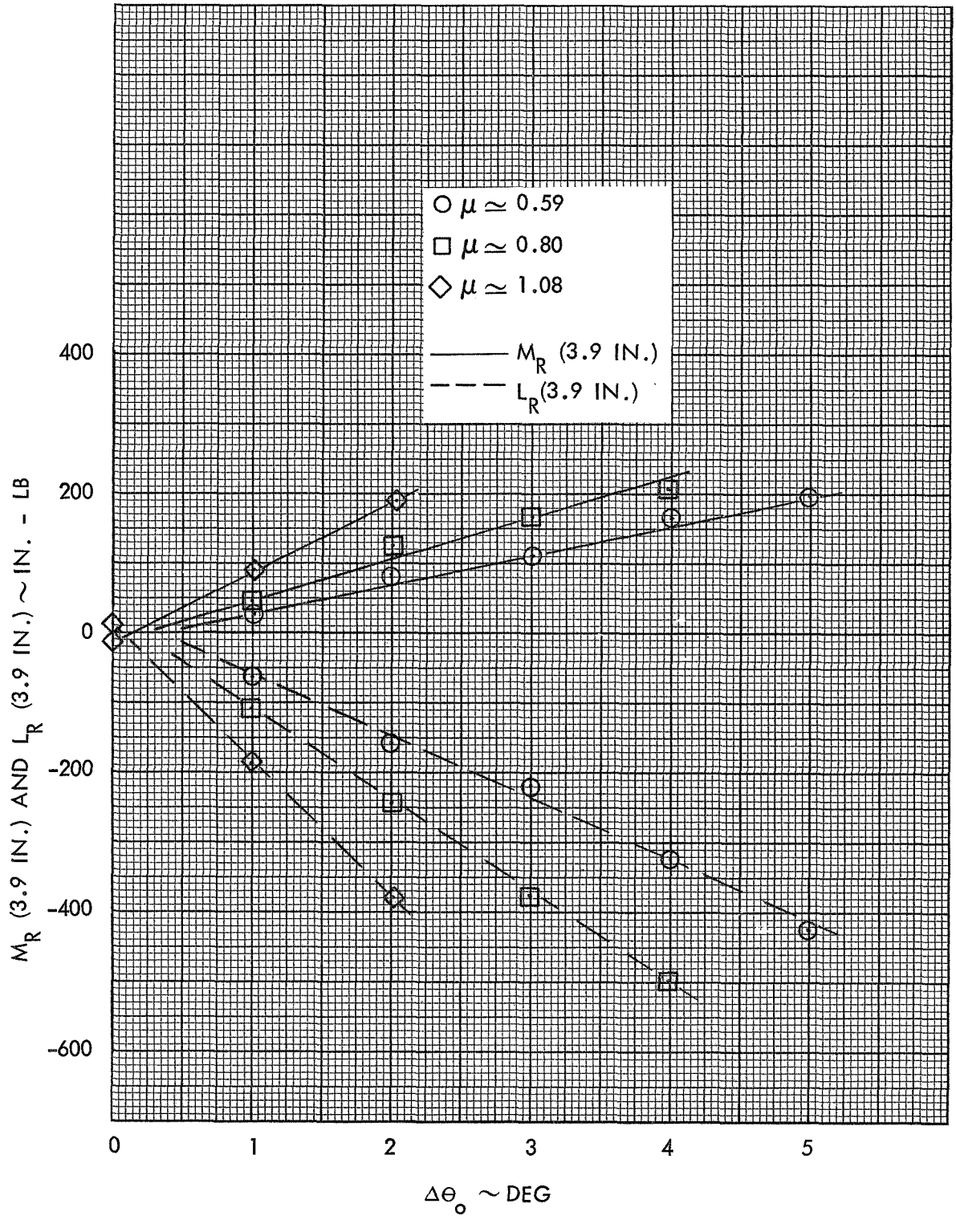

Figure 103. Rotor Pitch and Roll Response to Collective Pitch, Configuration 3, 400 RPM (γ=5.0, P=2.32)

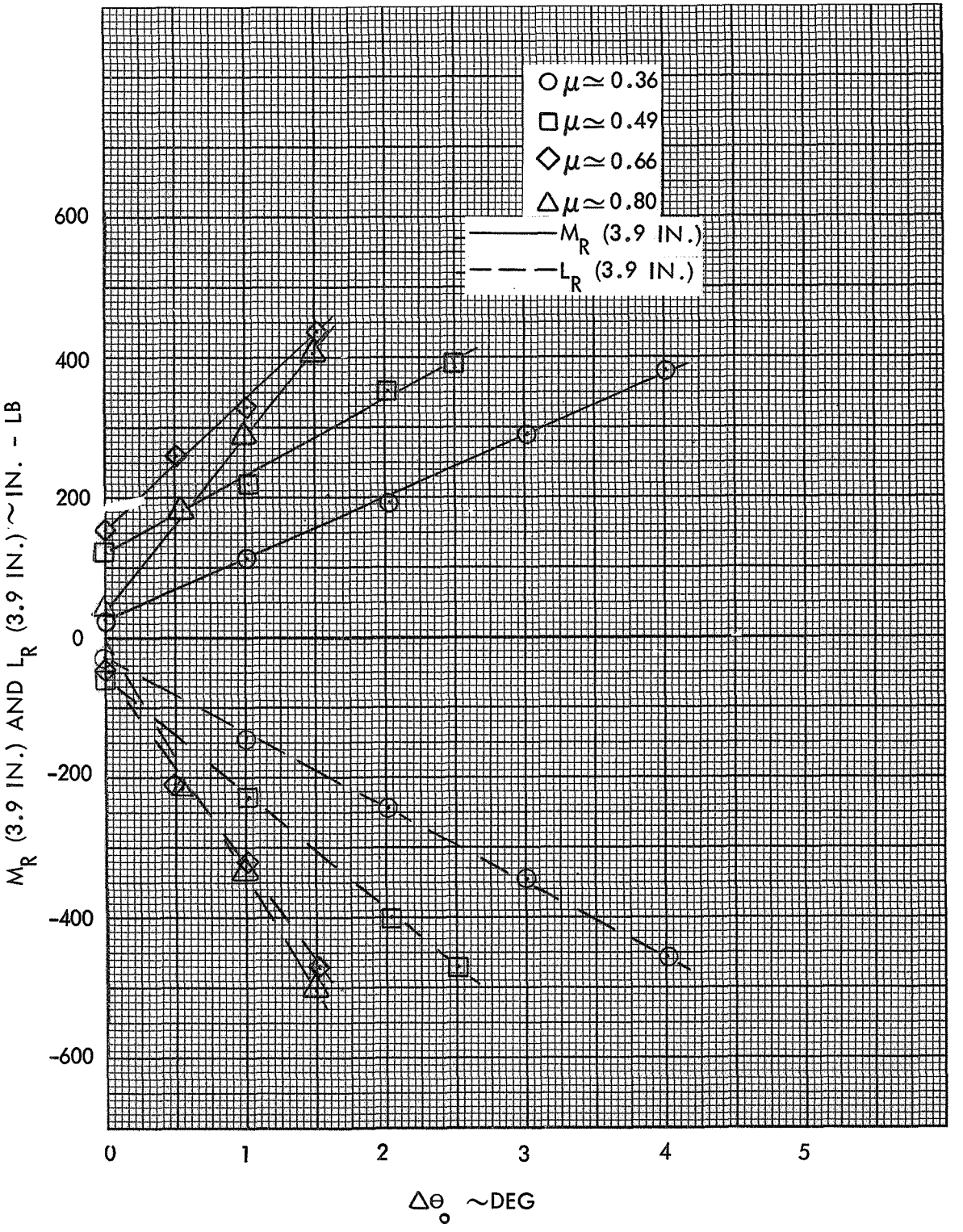

Figure 104. Rotor Pitch and Roll Response to Collective Pitch, Configuration 3, 650 RPM (γ=5.0, P=1.73)

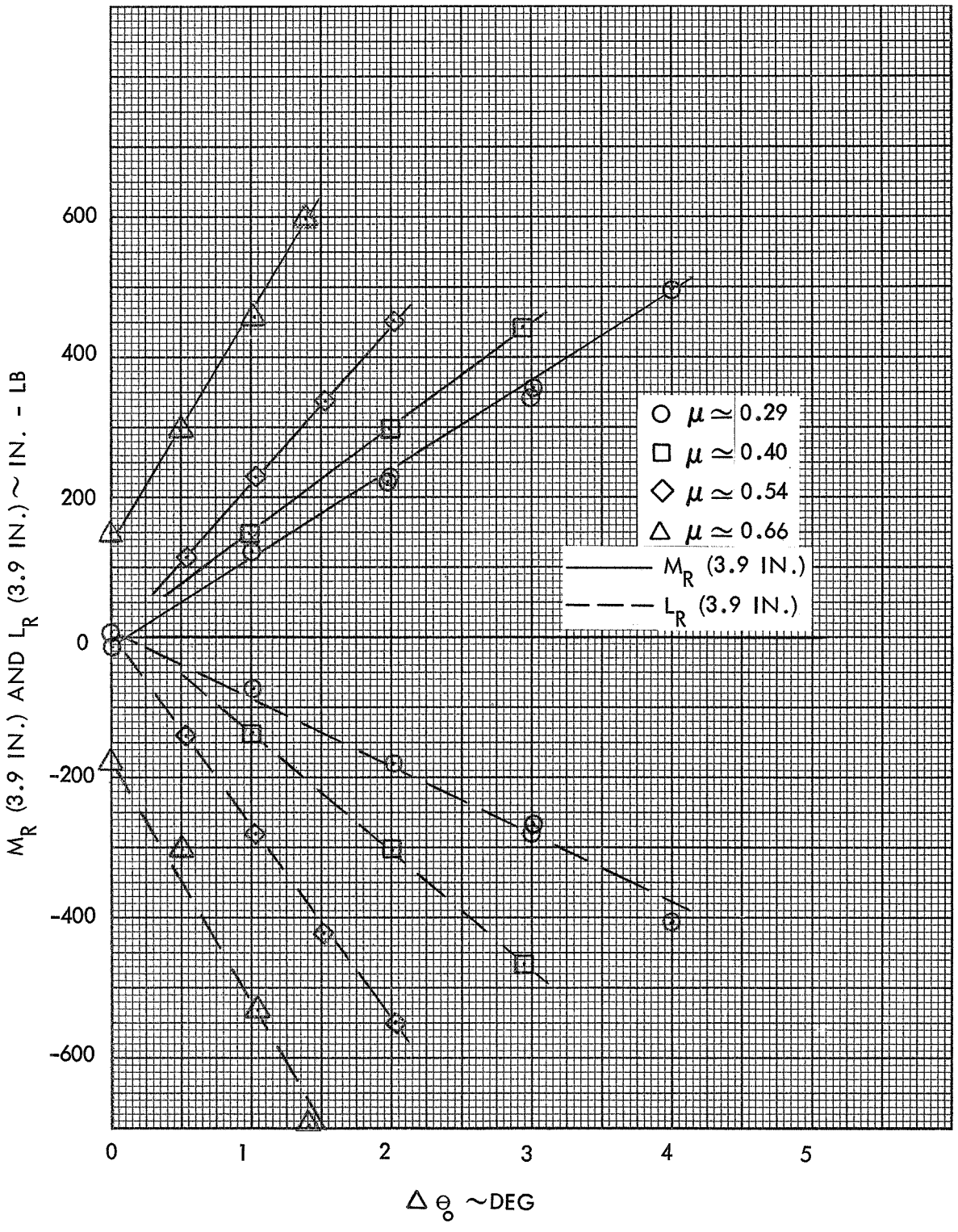

Figure 105. Rotor Pitch and Roll Response to Collective Pitch, Configuration 3, 800 RPM (γ=5.0, P=1.55)

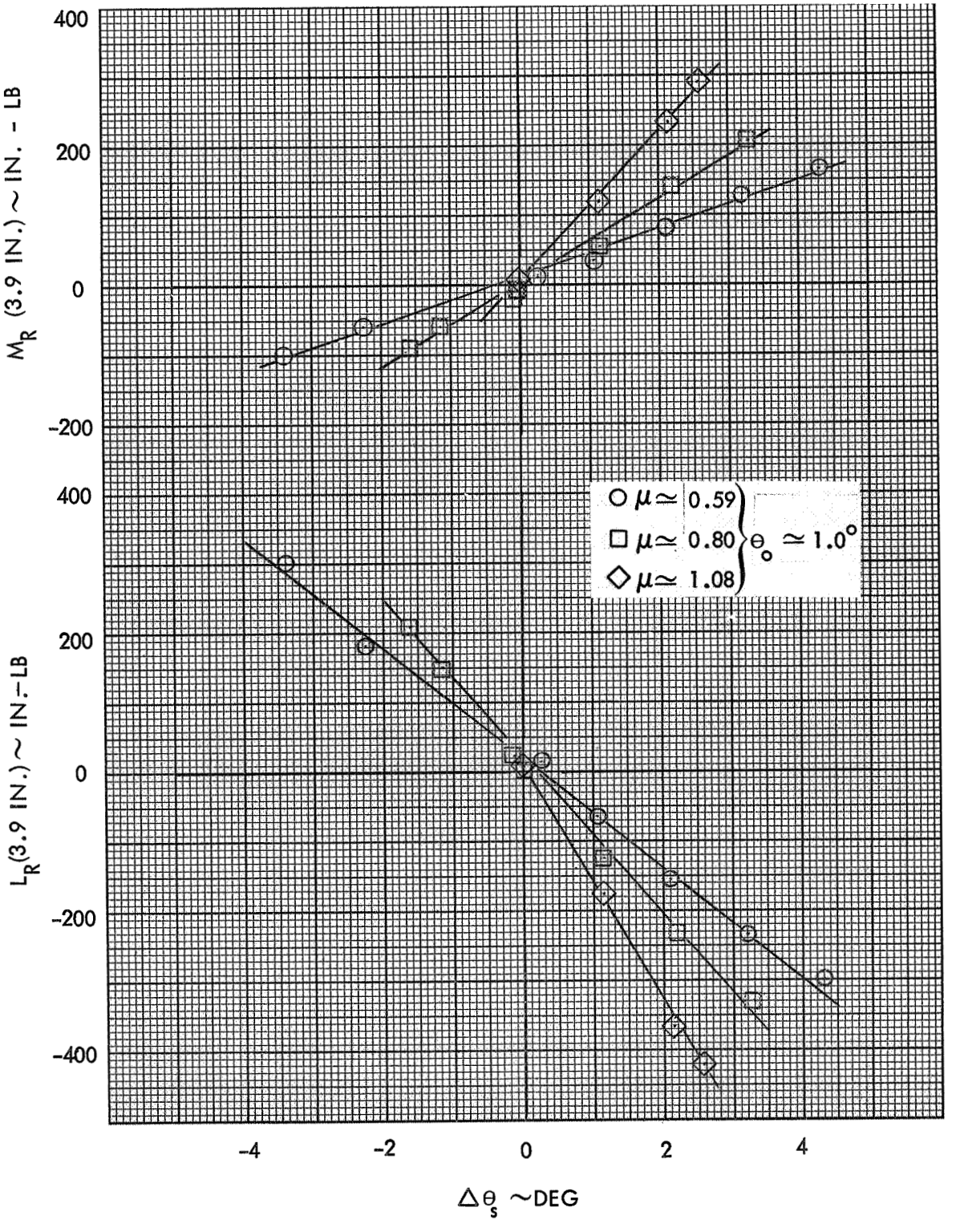

Figure 106. Rotor Pitch and Roll Response to Longitudinal Cyclic Pitch, Configuration 3, 400 RPM (γ=5.0, P=2.32)

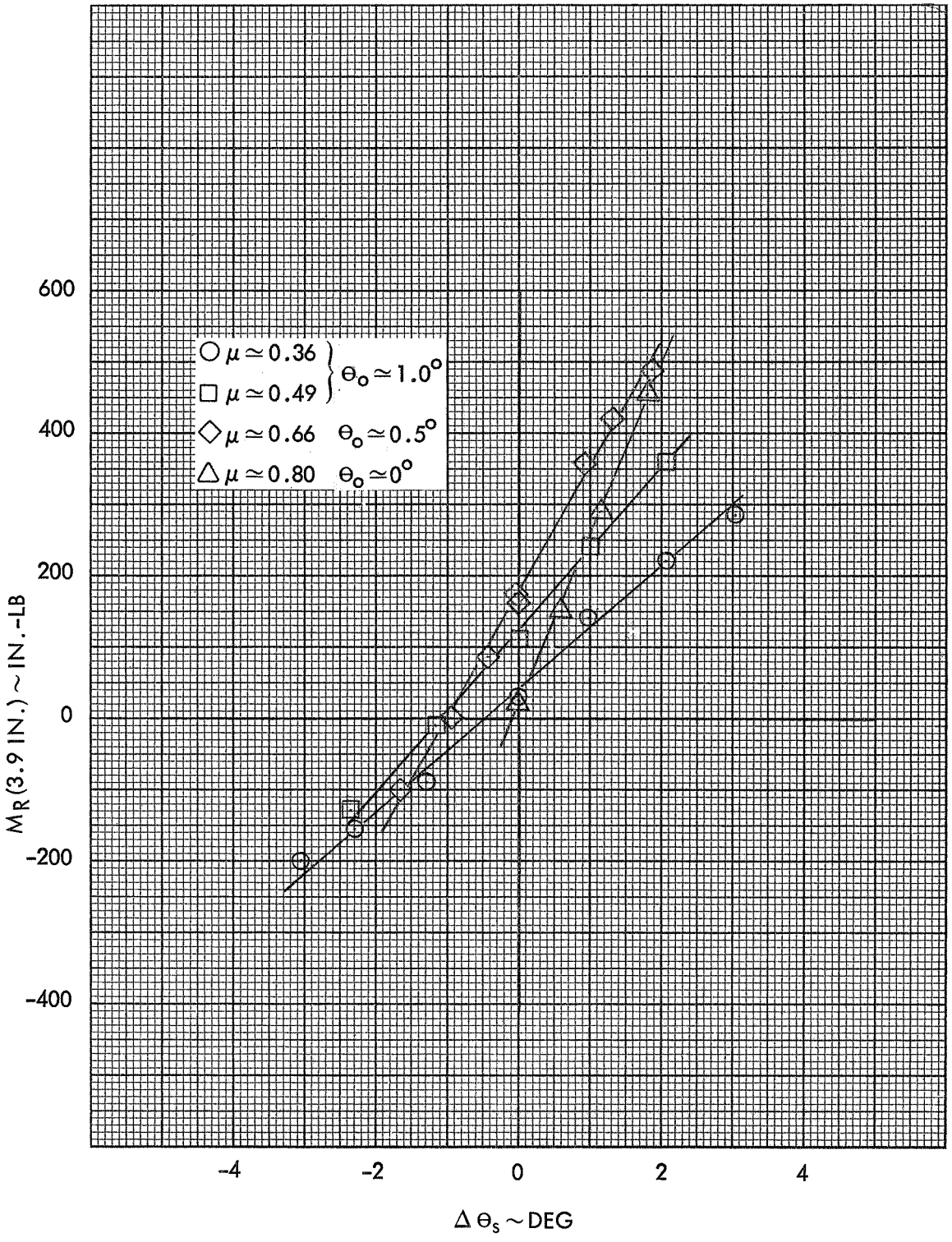

Figure 107. Rotor Pitch Response to Longitudinal Cyclic Pitch, Configuration 3, 650 RPM (γ=5.0, P=1.73)

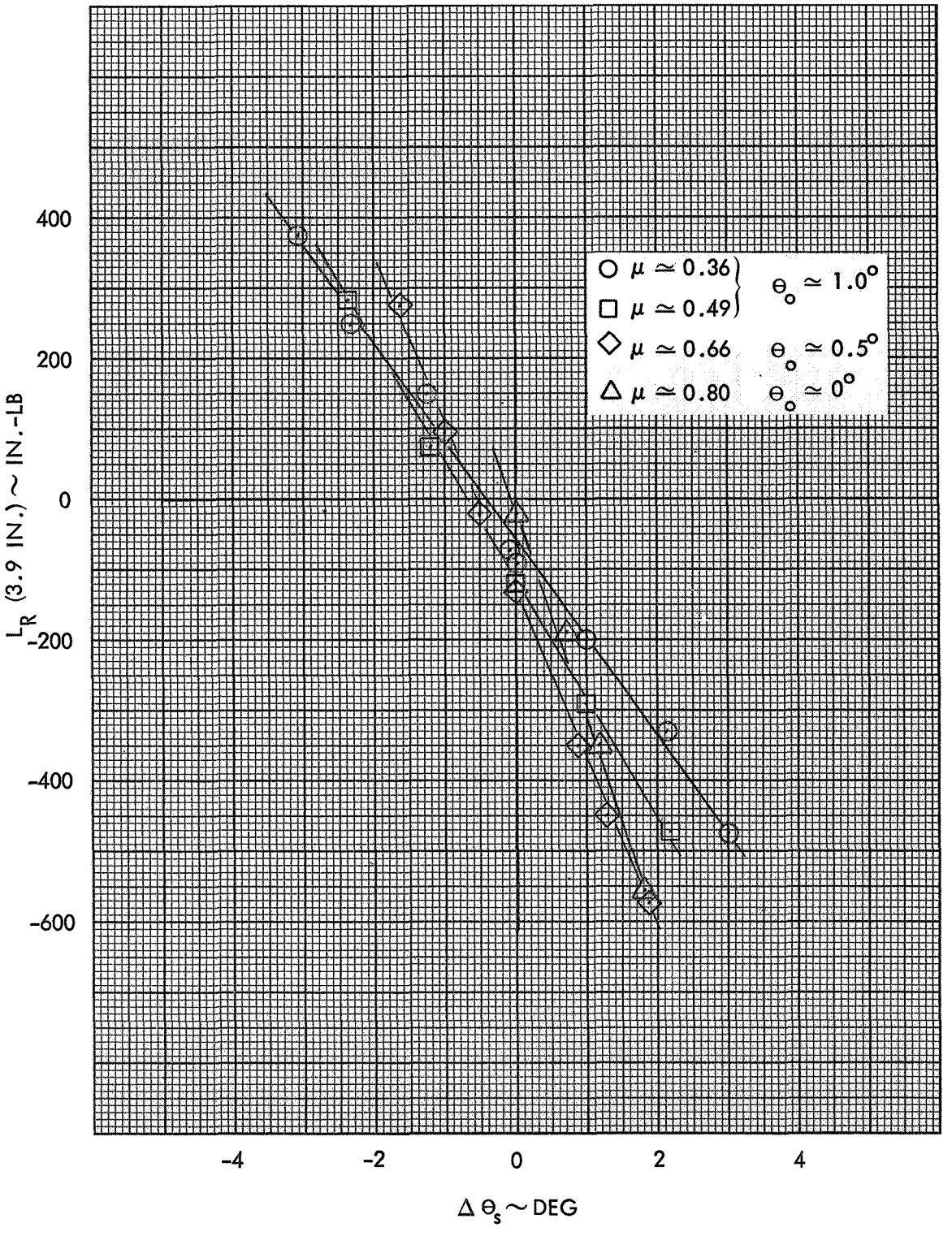

Figure 108. Rotor Roll Response to Longitudinal Cyclic Pitch, Configuration 3, 650 RPM (γ=5.0, P=1.73)

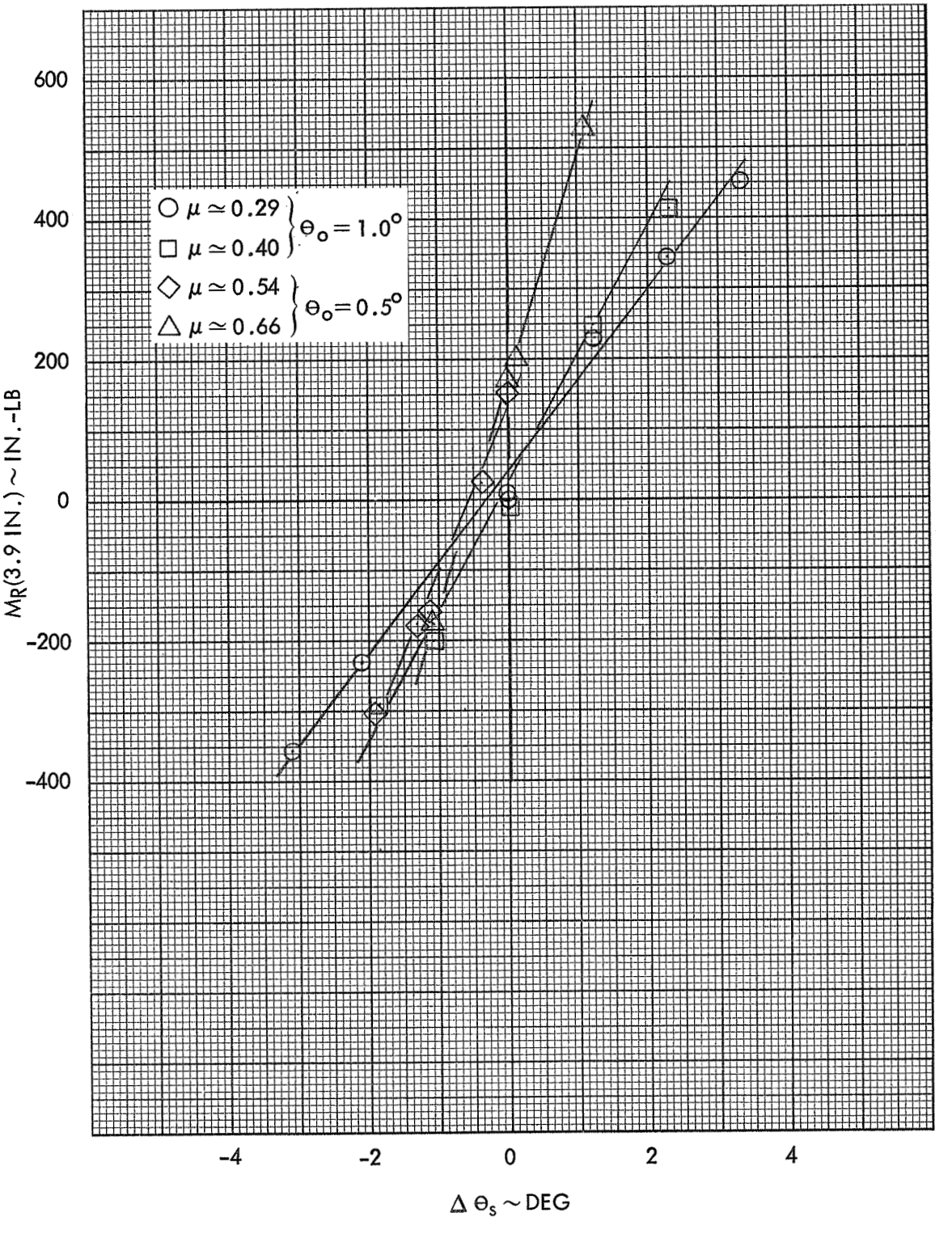

Figure 109. Rotor Pitch Response to Longitudinal Cyclic Pitch, Configuration 3, 800 RPM (γ=5.0, P=1.55)

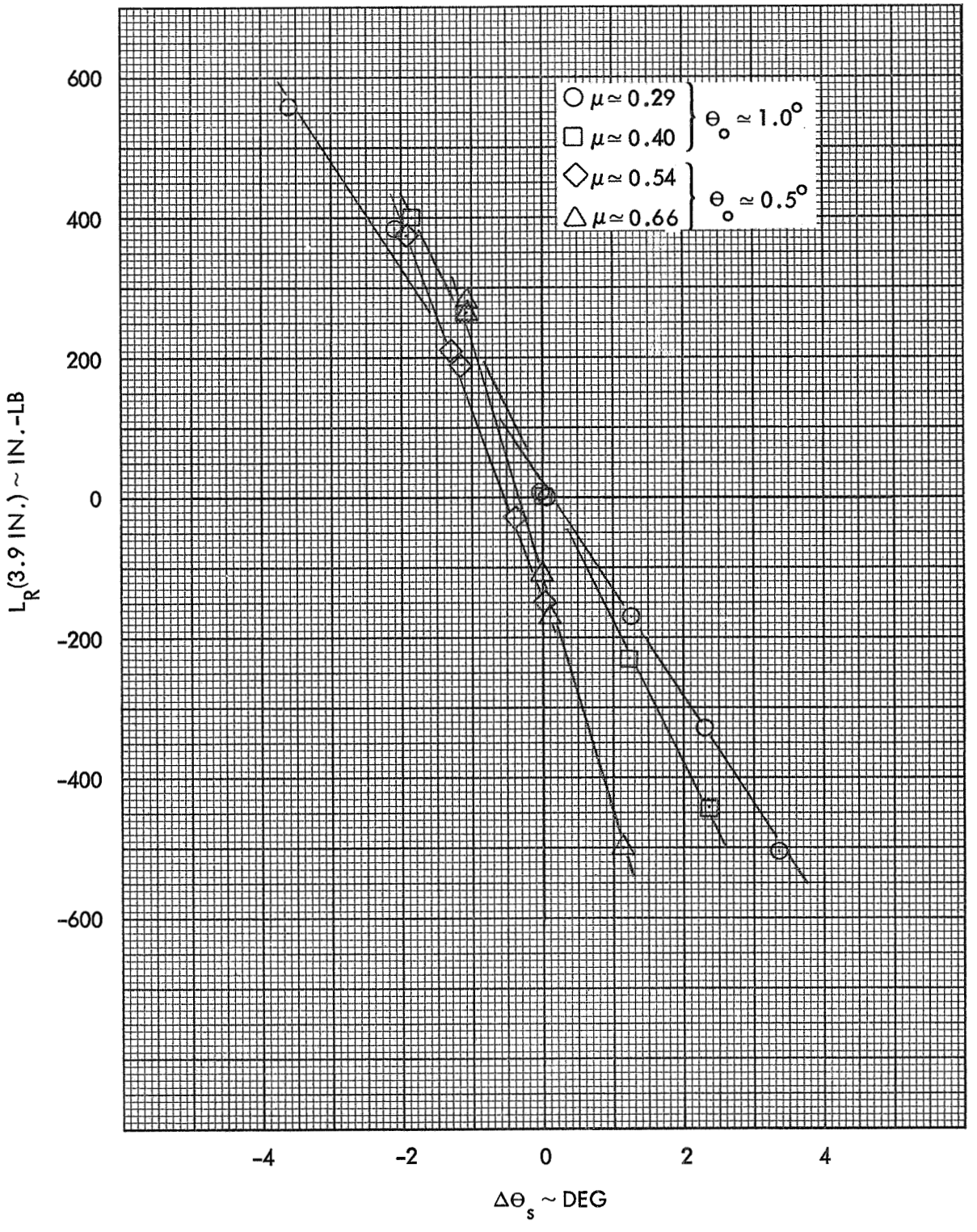

Figure 110. Rotor Roll Response to Longitudinal Cyclic Pitch, Configuration 3, 800 RPM (γ=5.0, P=1.55)

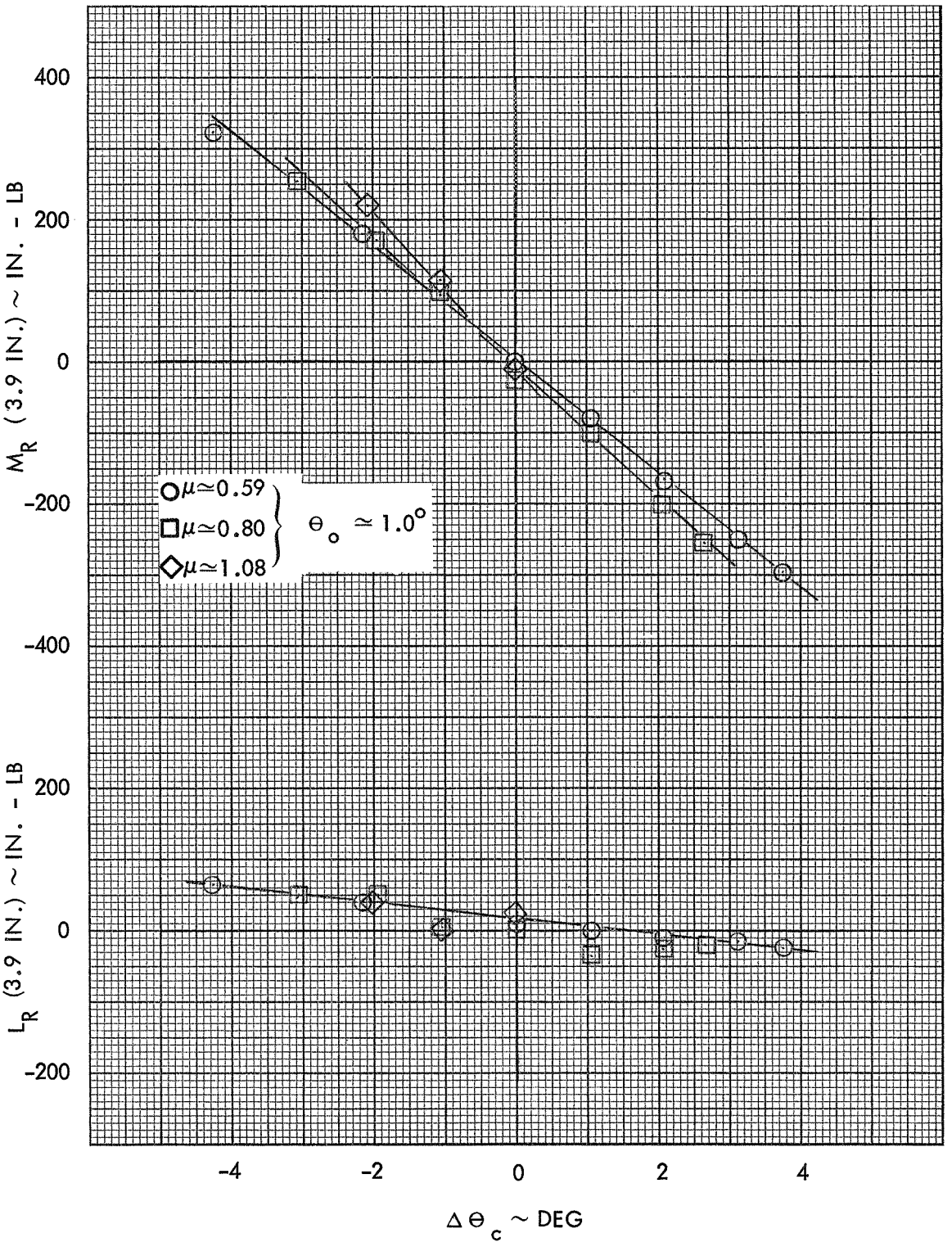

Figure 111. Rotor Pitch and Roll Response to Lateral Cyclic Pitch, Configuration 3, 400 RPM (γ=5.0, P=2.32)

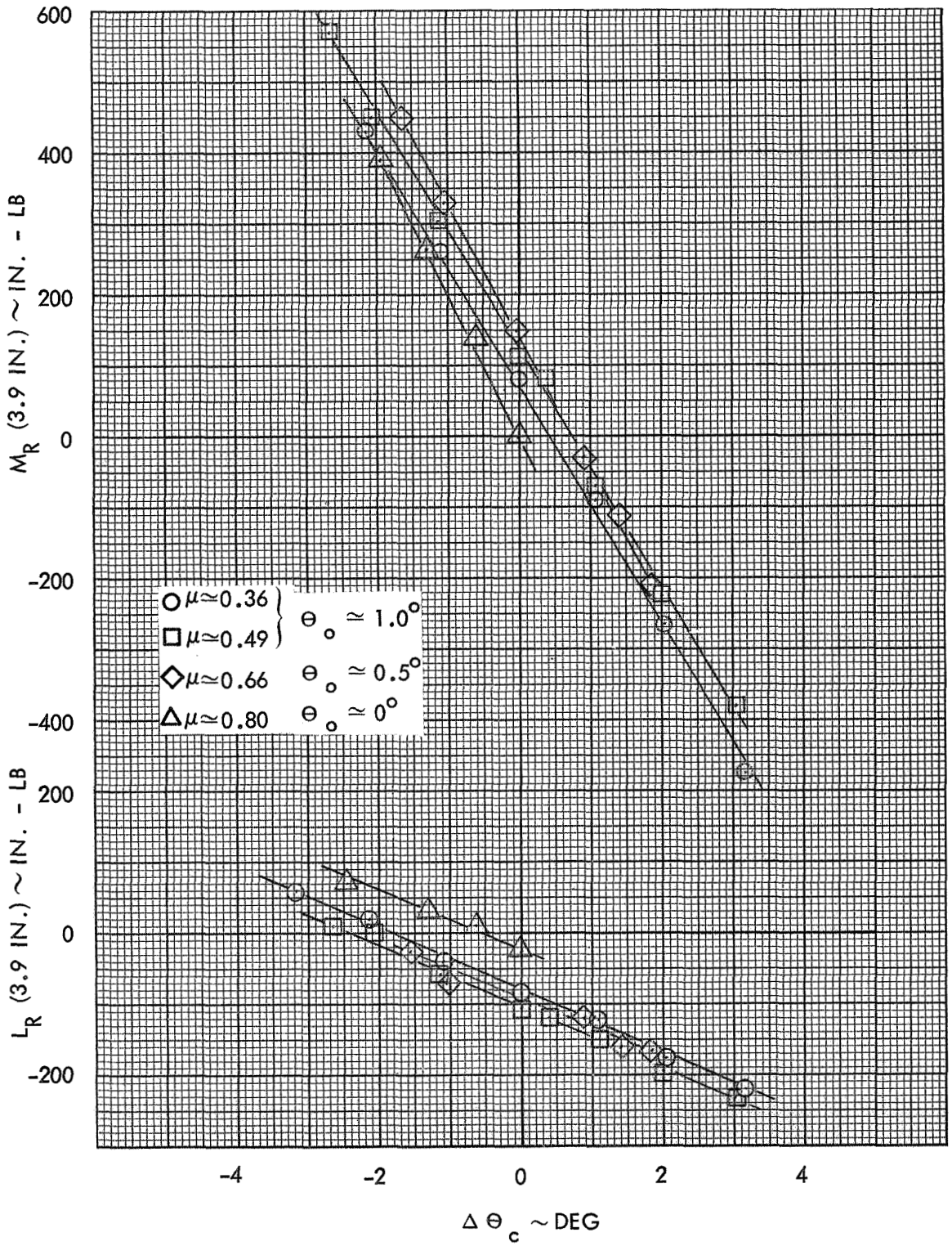

Figure 112. Rotor Pitch and Roll Response to Lateral Cyclic Pitch, Configuration 3, 650 RPM (γ=5.0, P=1.73)

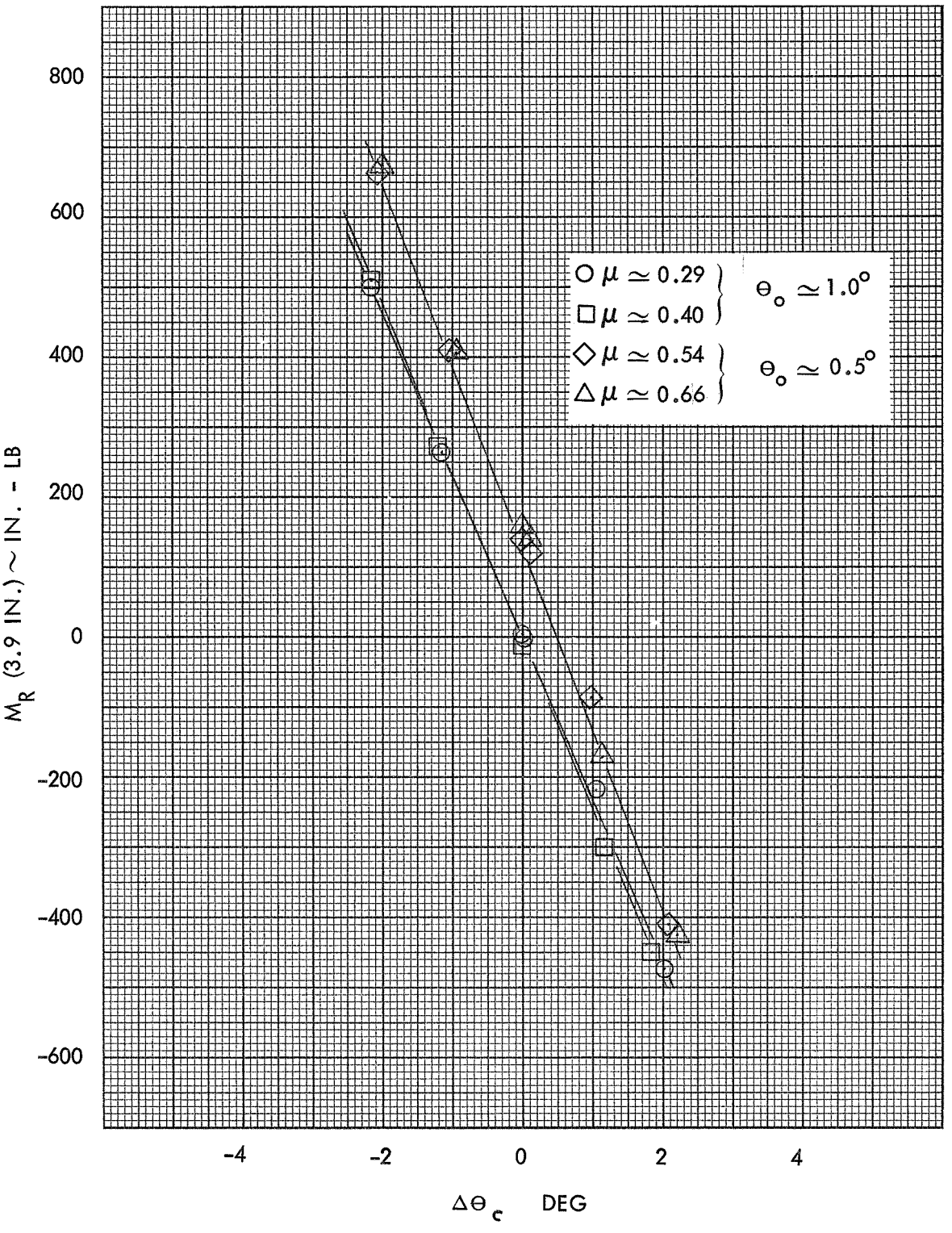

Figure 113. Rotor Pitch Response to Lateral Cyclic Pitch, Configuration 3, 800 RPM (γ=5.0, P=1.55)

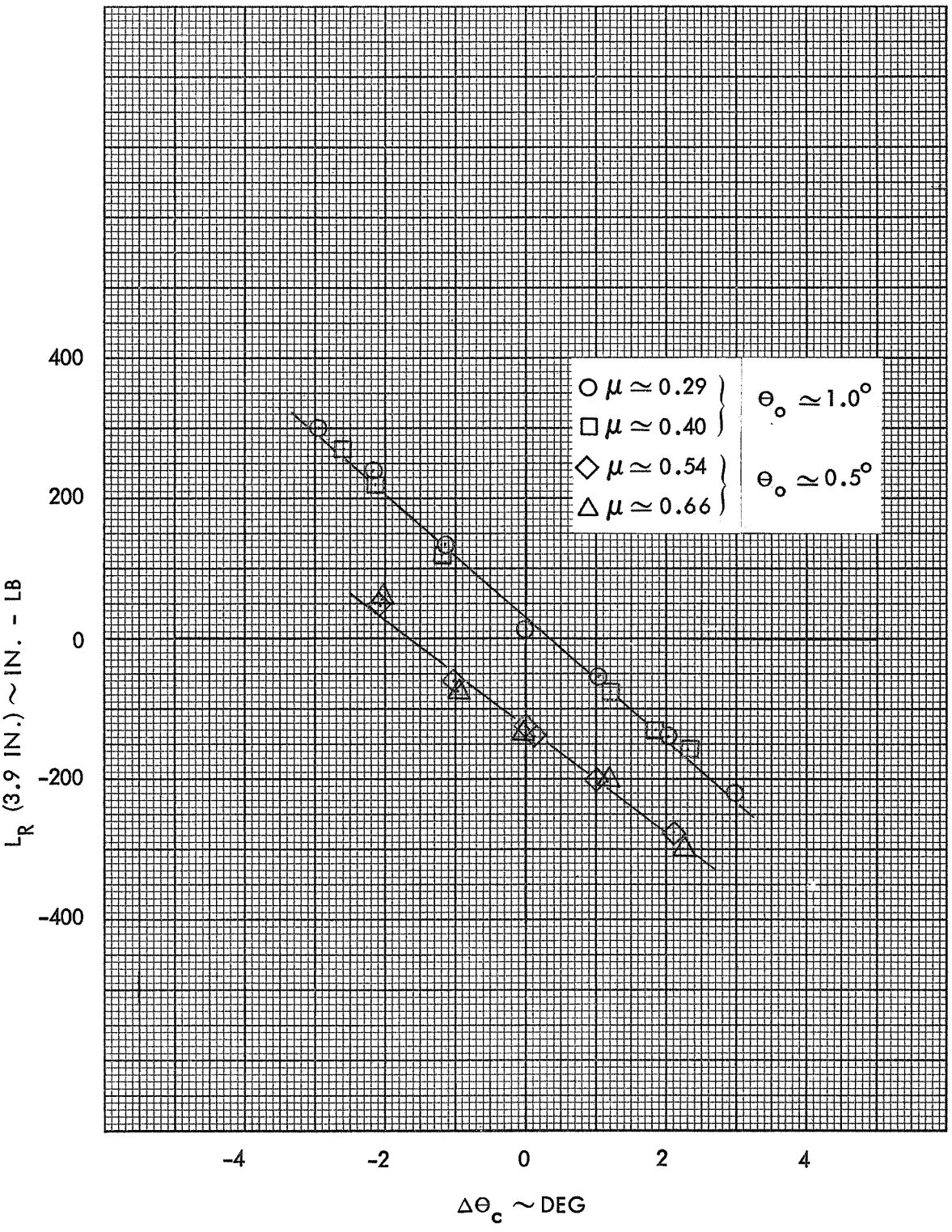

Figure 114. Rotor Roll Response to Lateral Cyclic Pitch, Configuration 3, 800 RPM (γ=5.0, P=1.55)

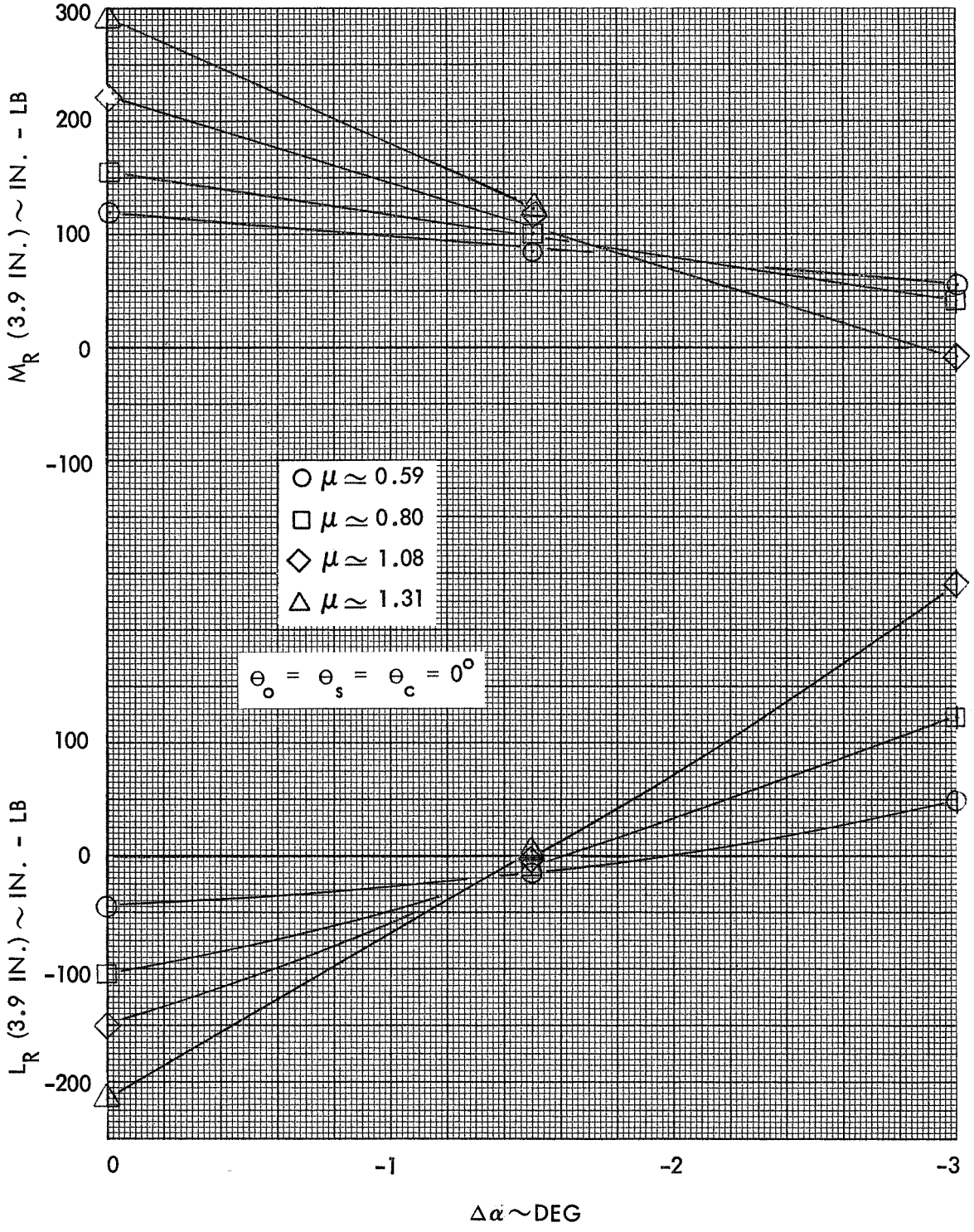

Figure 115. Rotor Pitch and Roll Response to a Rotor Shaft Angle of Attack Increment, Configuration 3, 400 RPM (γ=5.C , P=2.32)

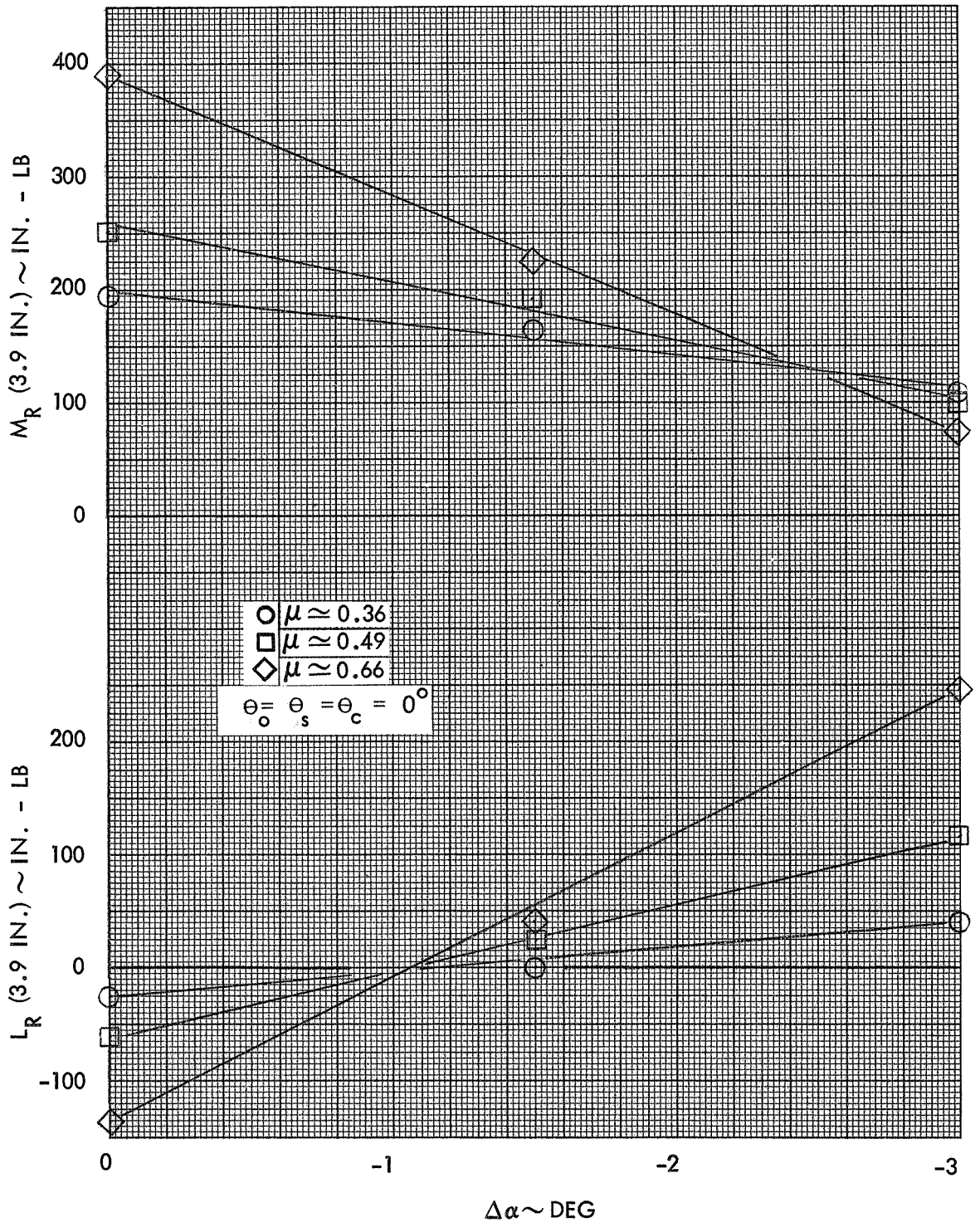

Figure 116. Rotor Pitch and Roll Response to a Rotor Shaft Angle of Attack Increment, Configuration 3, 650 RPM (γ=5.0, P=1.73)

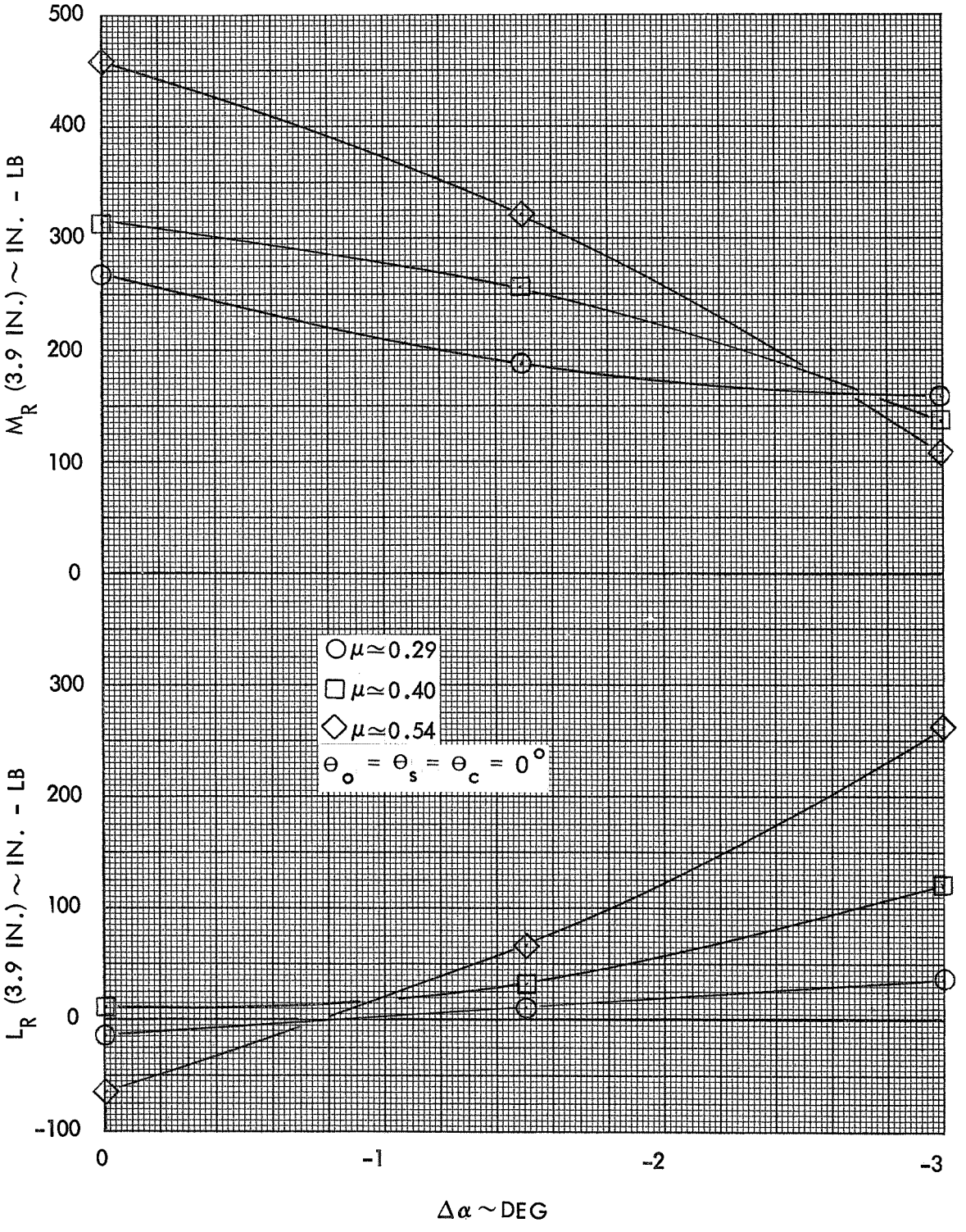

Figure 117. Rotor Pitch and Roll Response to a Rotor Shaft Angle of Attack Increment, Configuration 3, 800 RPM, (γ=5.0, P=1.55)

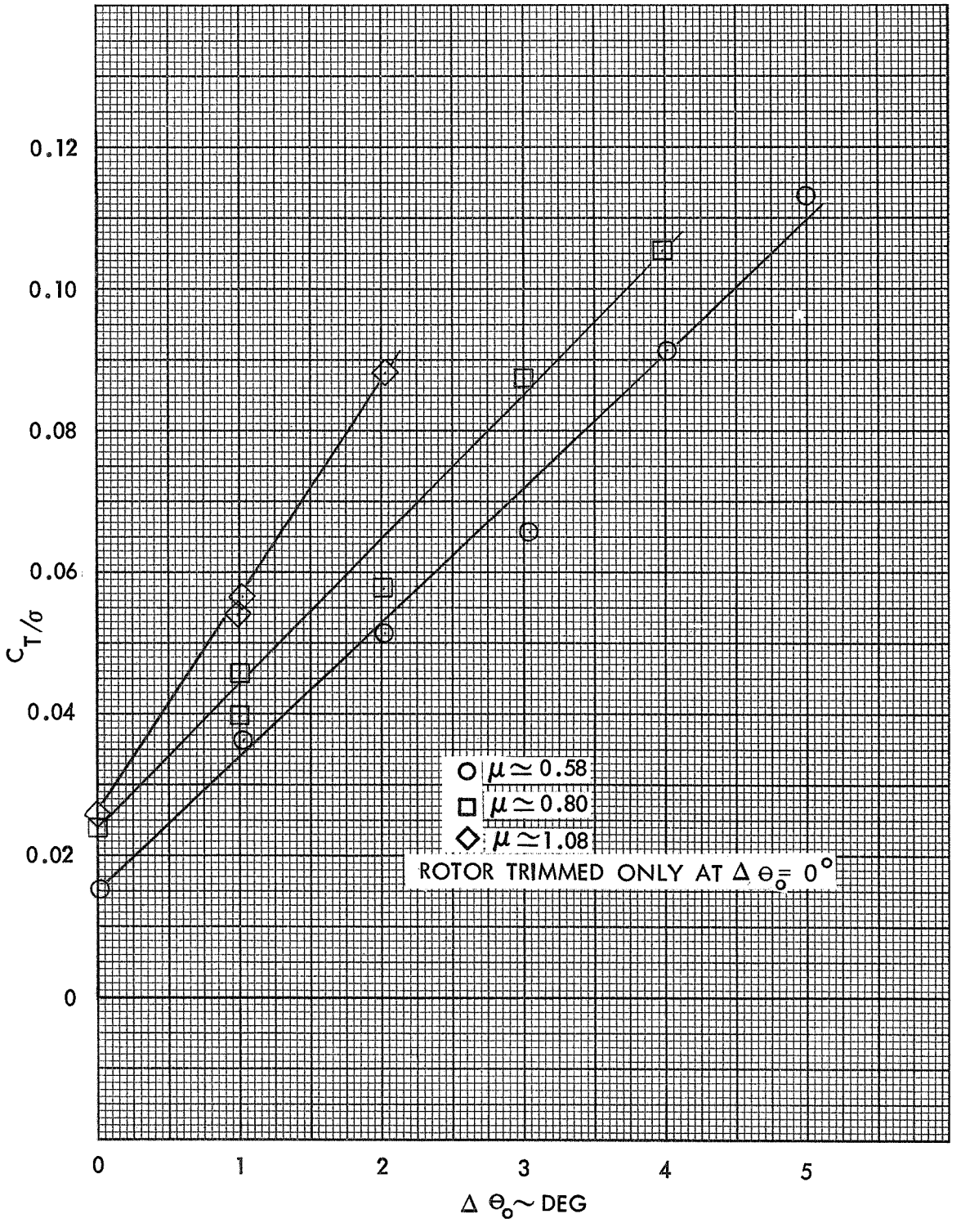

Figure 118. Rotor Lift versus Collective Pitch, Configuration 3, 400 RPM (γ=5.0, P=2.32)

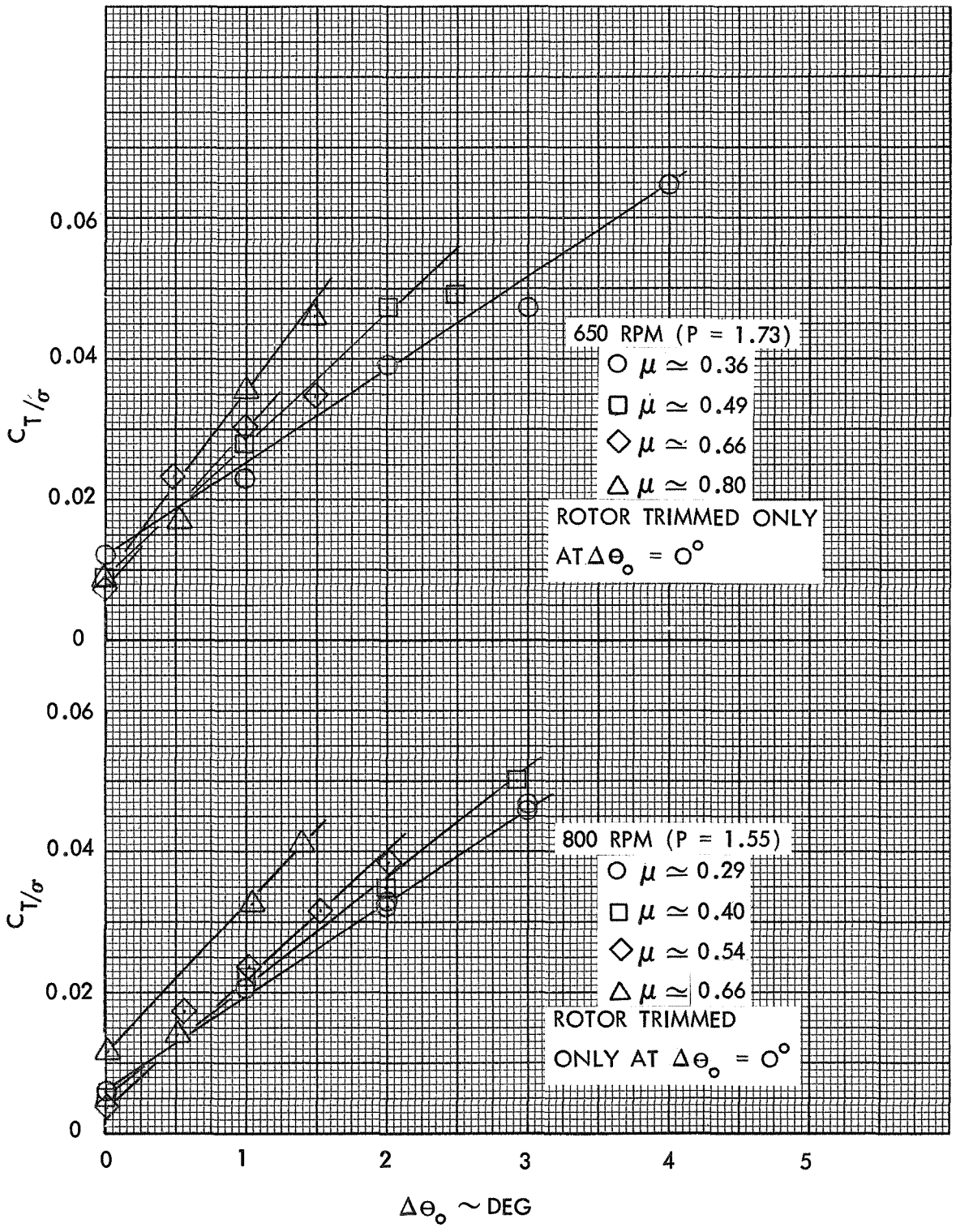

Figure 119. Rotor Lift versus Collective Pitch, Configuration 3, 650 RPM and 800 RPM

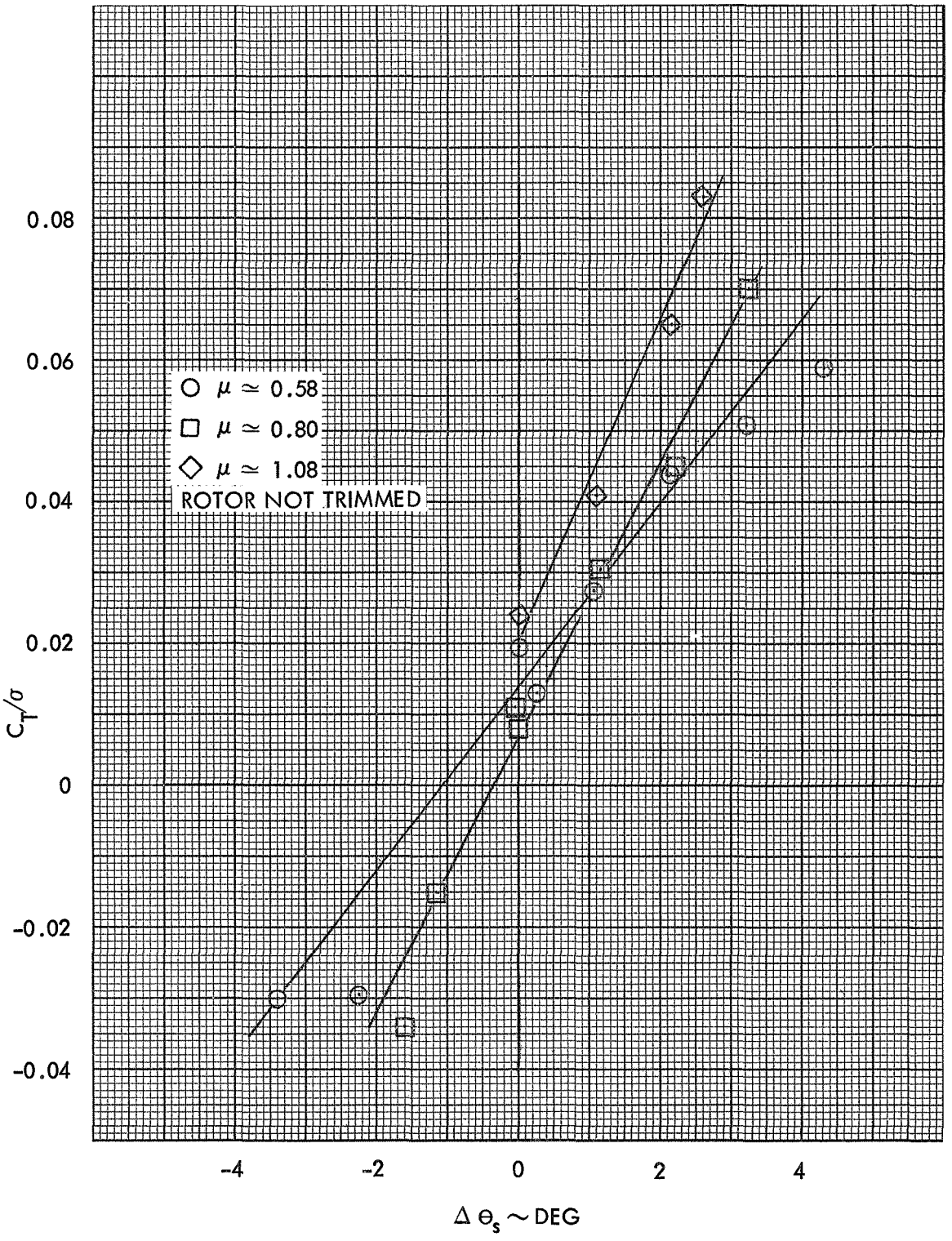

Figure 120. Rotor Lift versus Longitudinal Cyclic Pitch, Configuration 3, 400 RPM (γ=5.0, P=2.32)

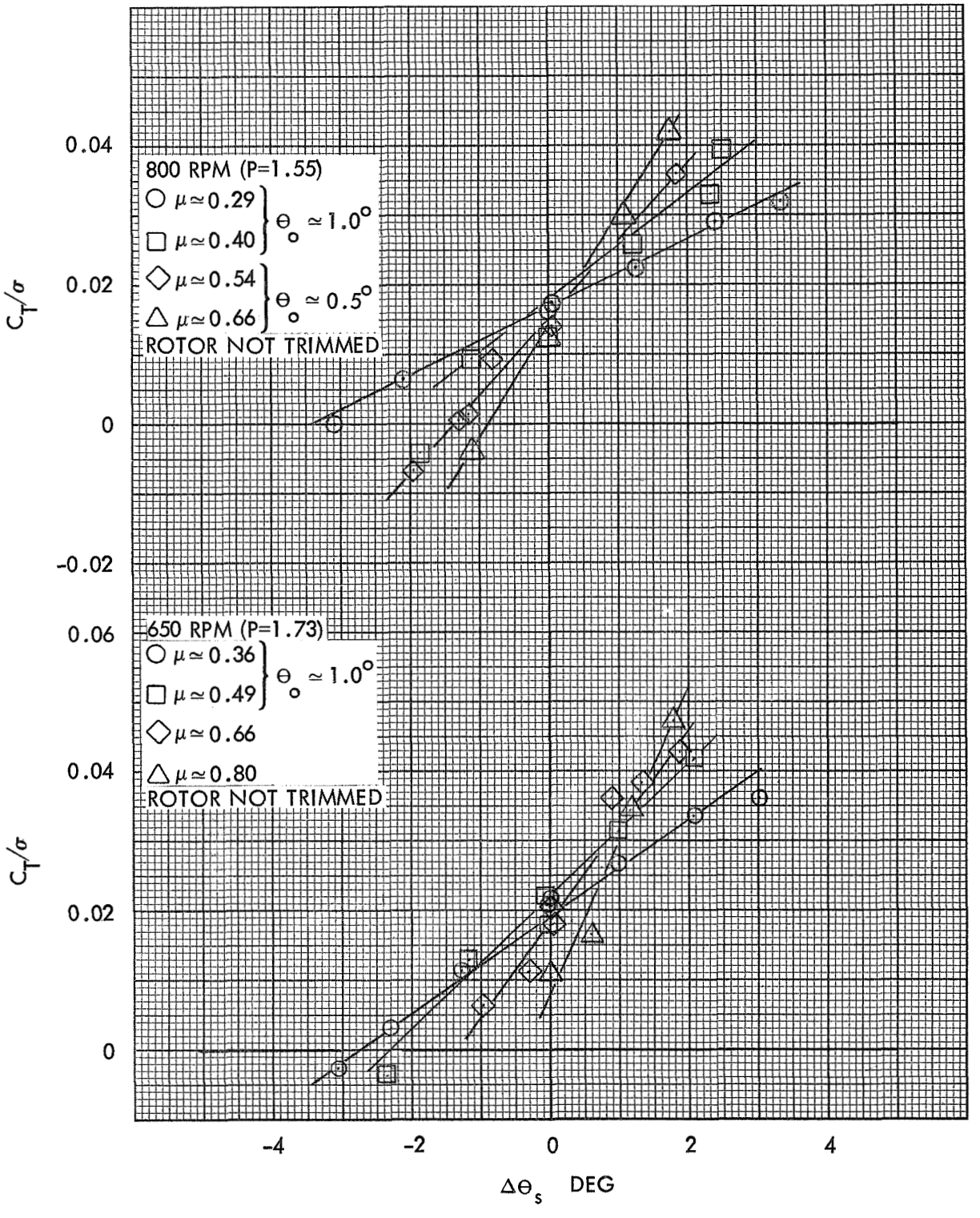

Figure 121. Rotor Lift versus Longitudinal Cyclic Pitch, Configuration 3, 650 RPM and 800 RPM

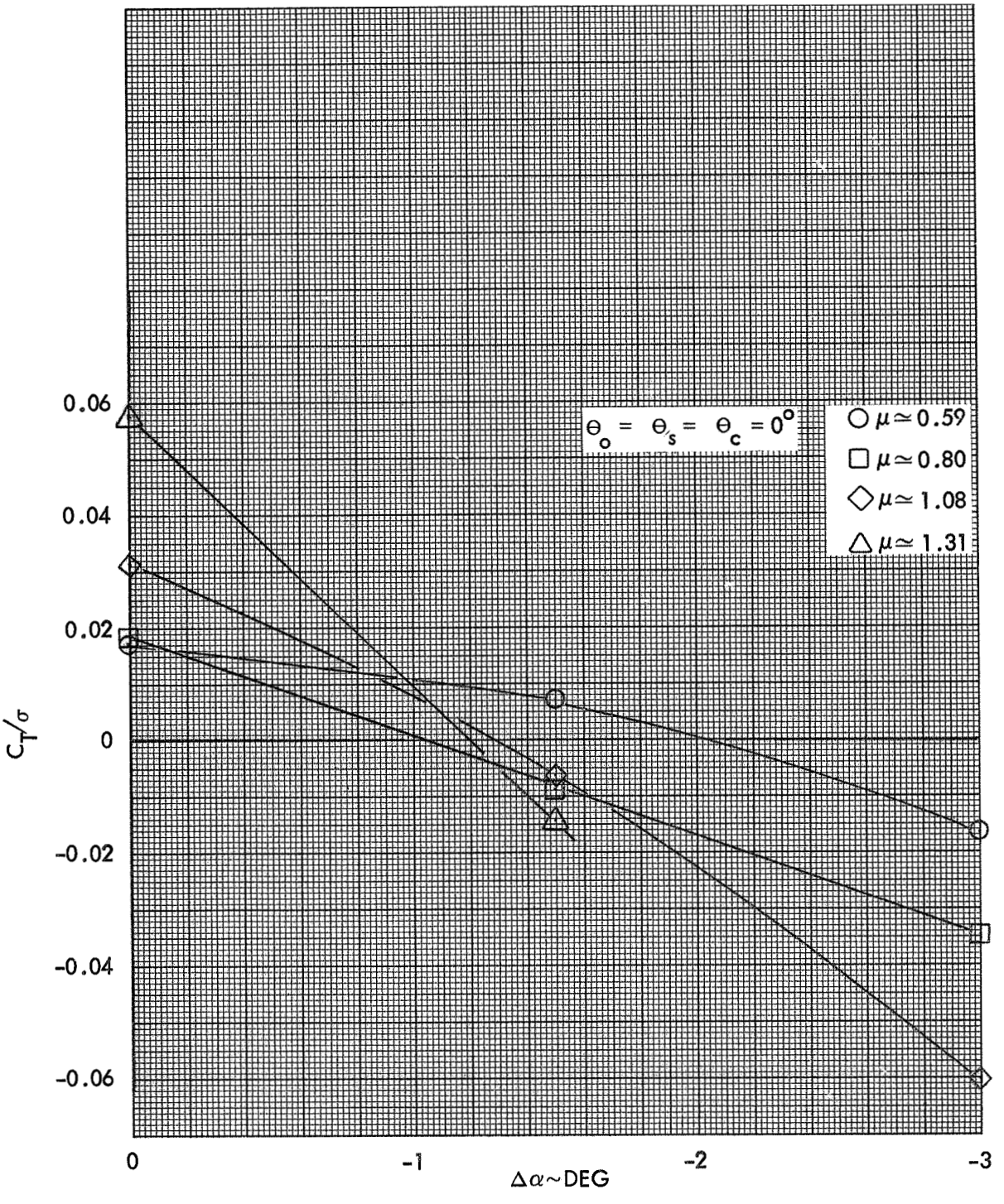

Figure 122. Rotor Lift versus Rotor Shaft Angle of Attack, Configuration 3, 400 RPM (γ=5.0, P=2.32)

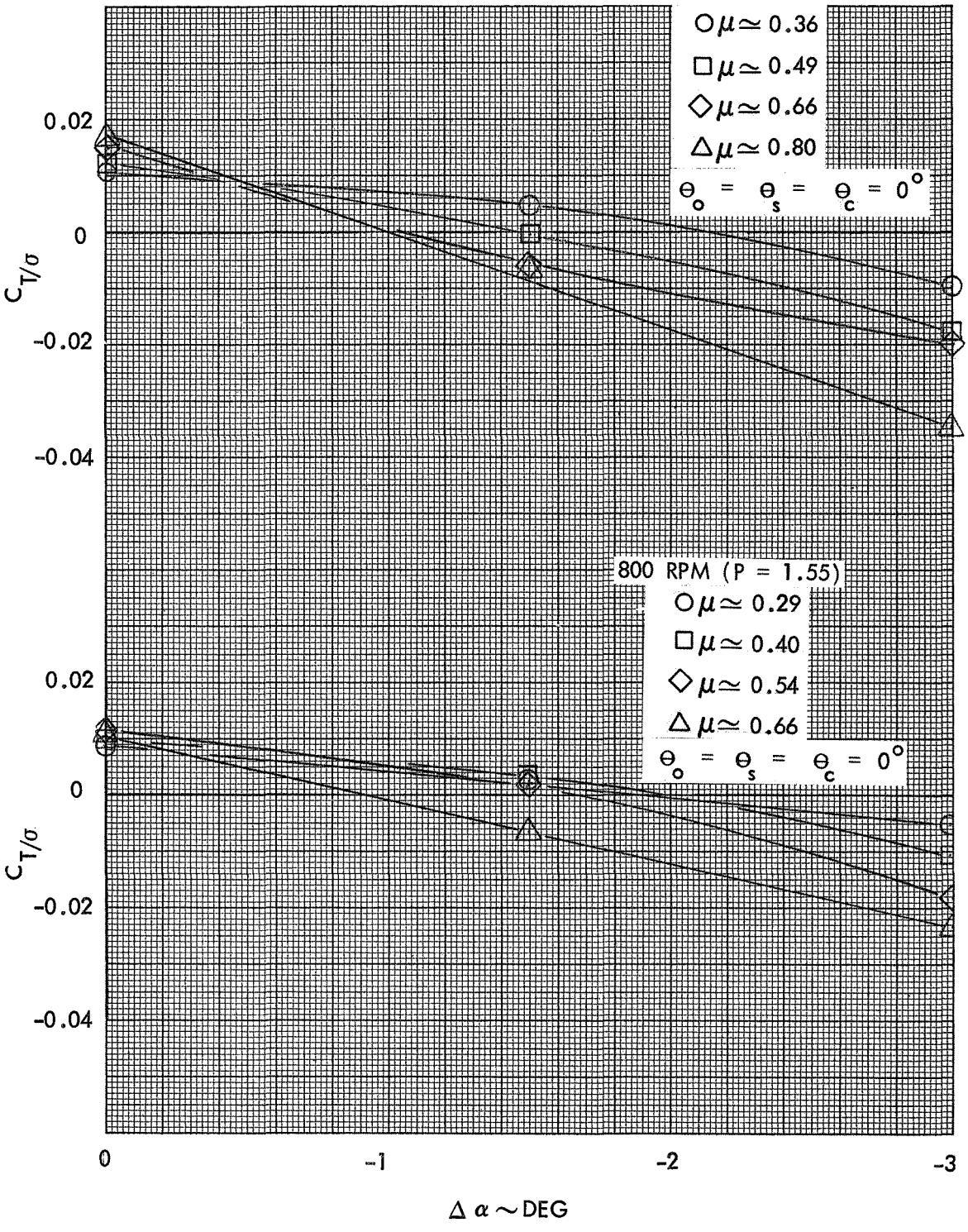

Figure 123. Rotor Lift versus Rotor Shaft Angle of Attack, Configuration 3, 650 RPM and 800 RPM

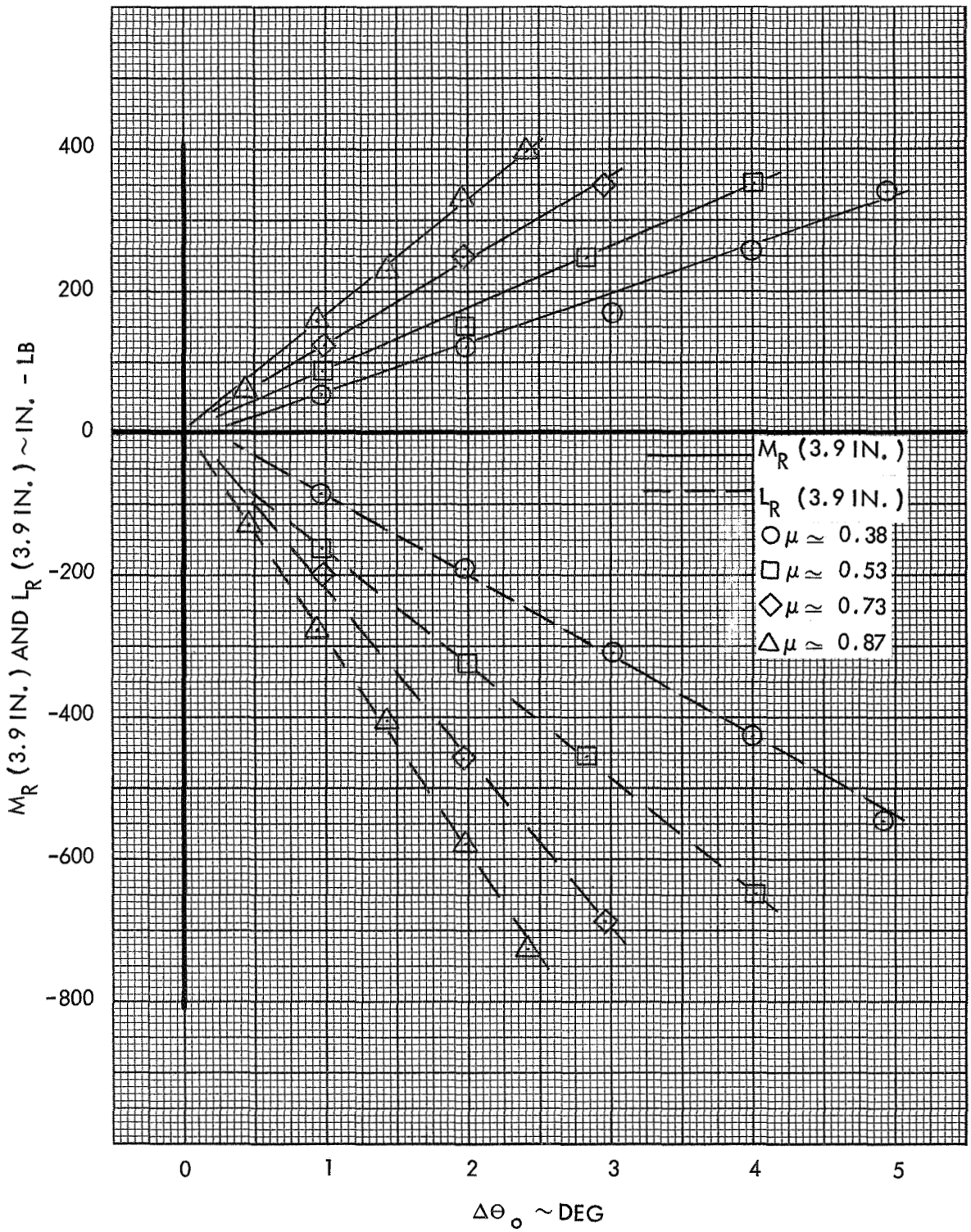

Figure 124. Rotor Pitch and Roll Response to Collective Pitch, Configuration 4, 600 RPM (γ=3.0, P=1.51)

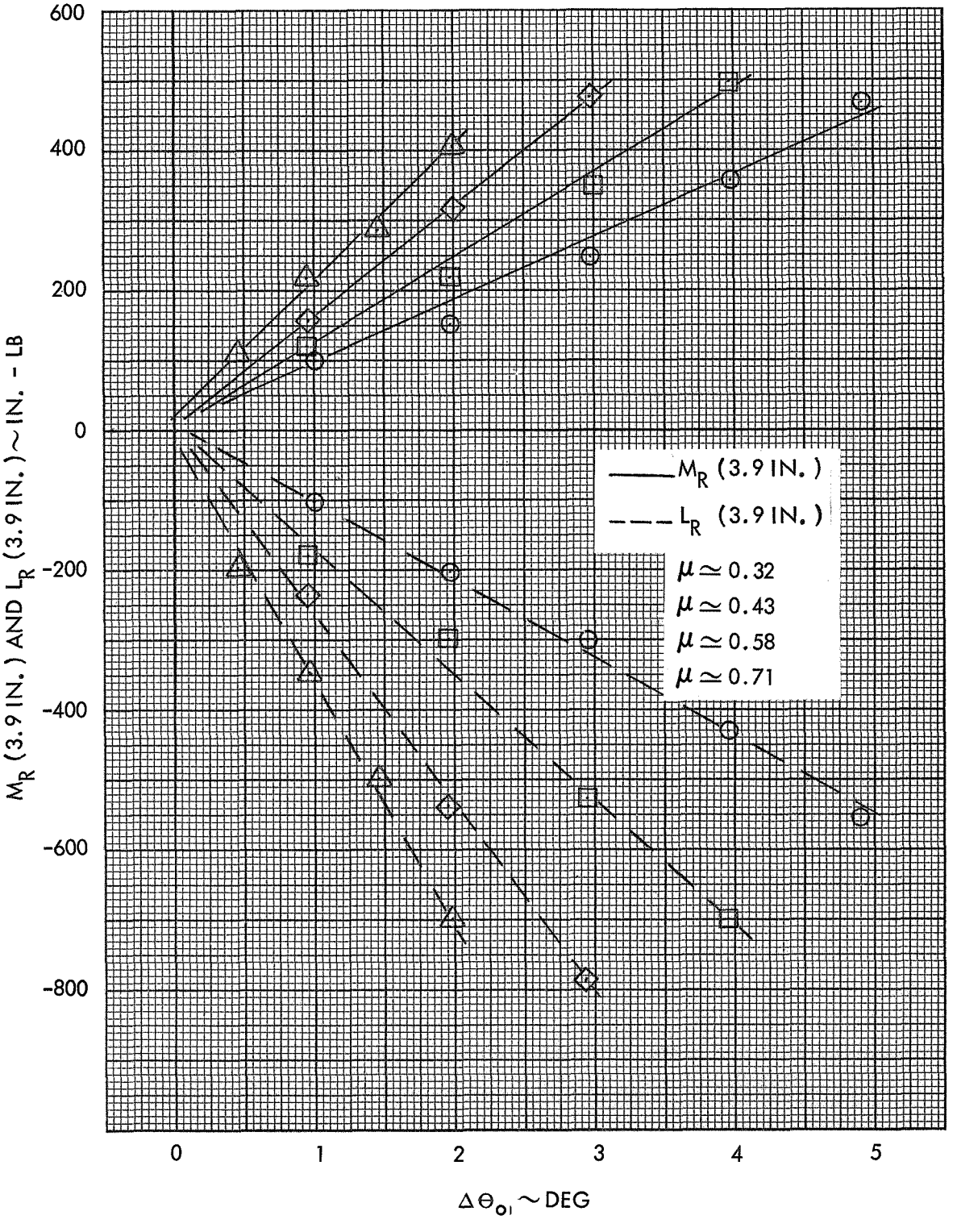

Figure 125. Rotor Pitch and Roll Response to Collective Pitch, Configuration 4, 750 RPM (γ=3.0, P=1.40)

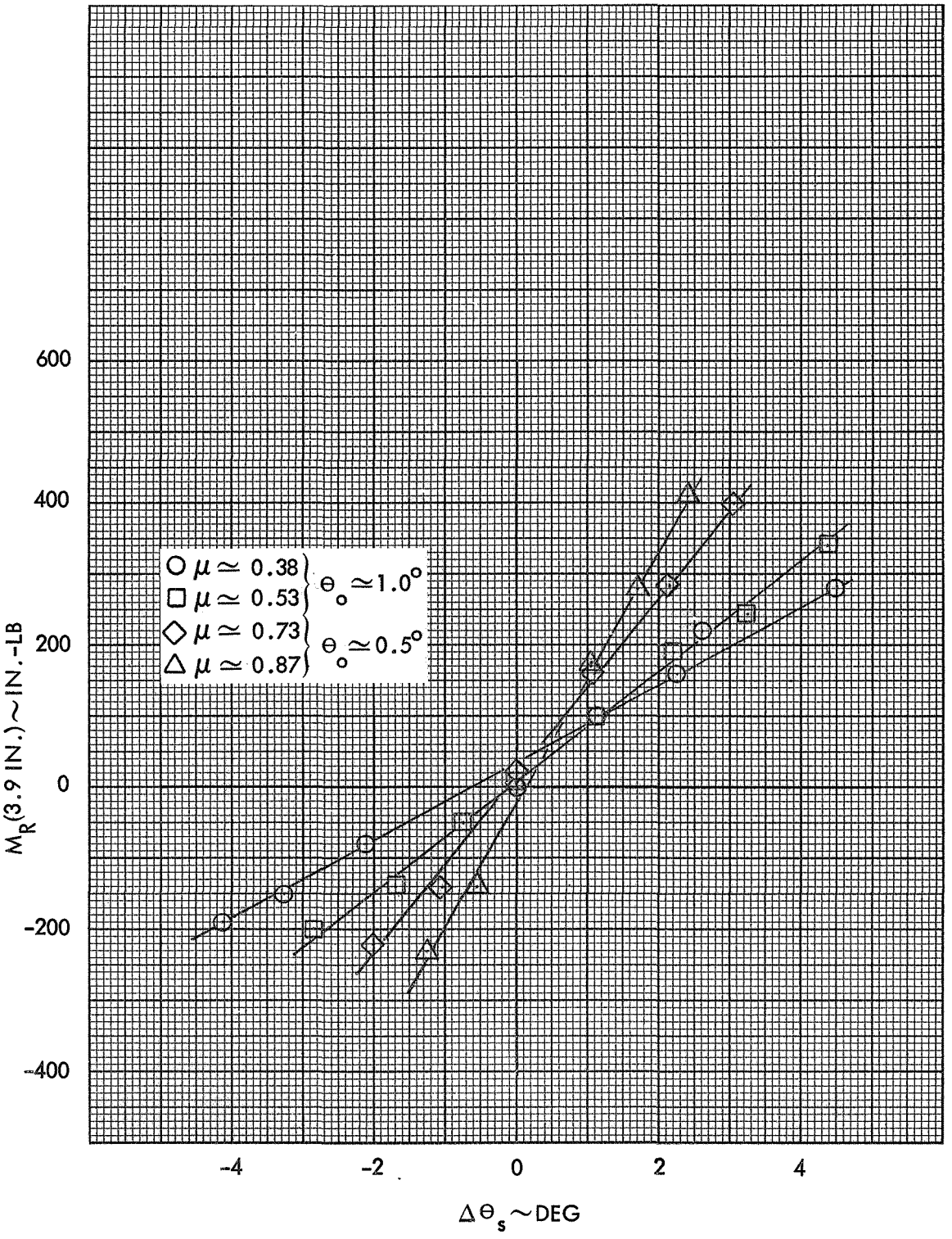

Figure 126. Rotor Pitch Response to Longitudinal Cyclic Pitch, Configuration 4, 600 RPM (γ=3.0, P=1.51)

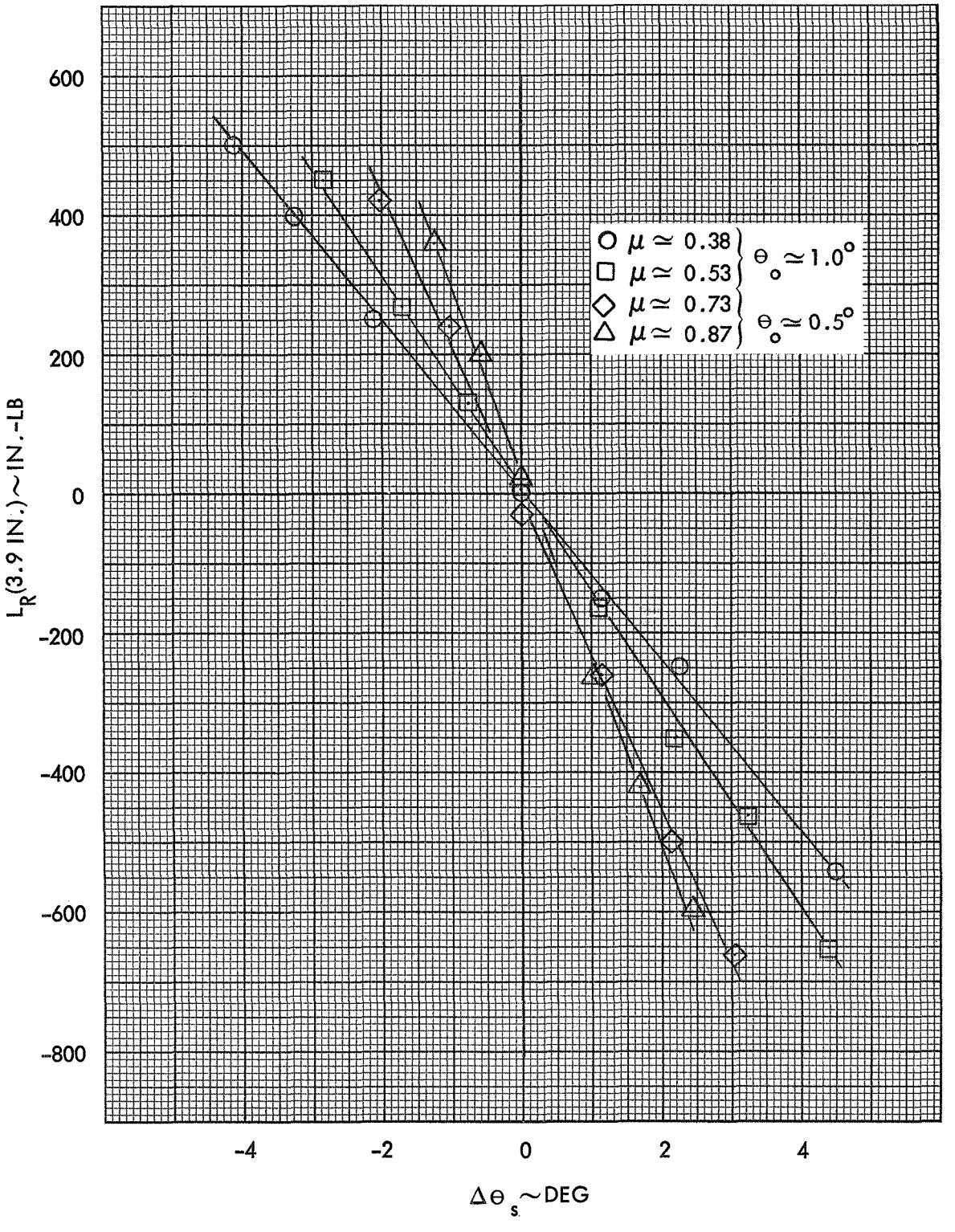

Figure 127. Rotor Roll Response to Longitudinal Cyclic Pitch, Configuration 4, 600 RPM (γ=3.0, P=1.51)

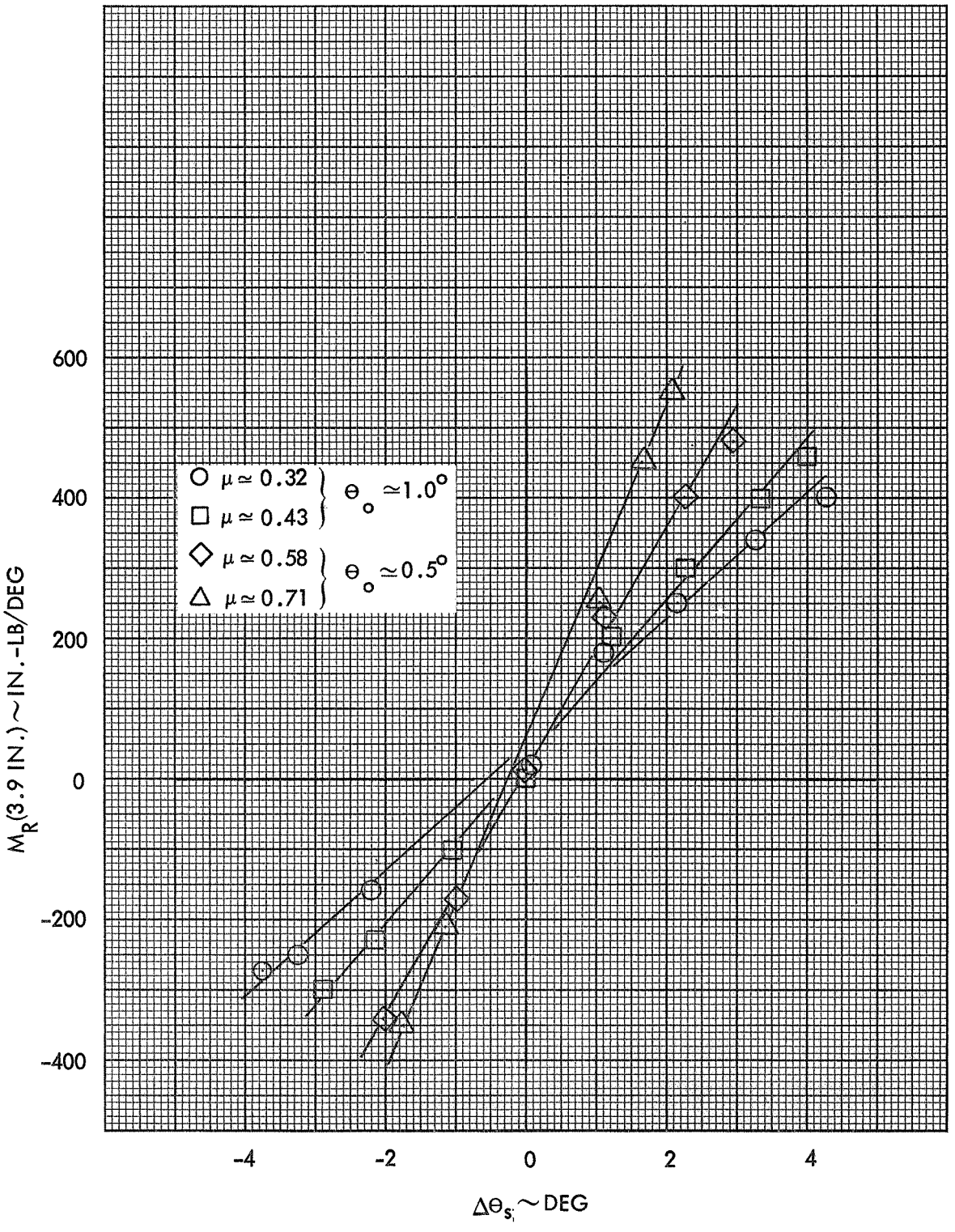

Figure 128. Rotor Roll Response to Longitudinal Cyclic Pitch, Configuration 4, 750 RPM (γ=3.0, P=1.40)

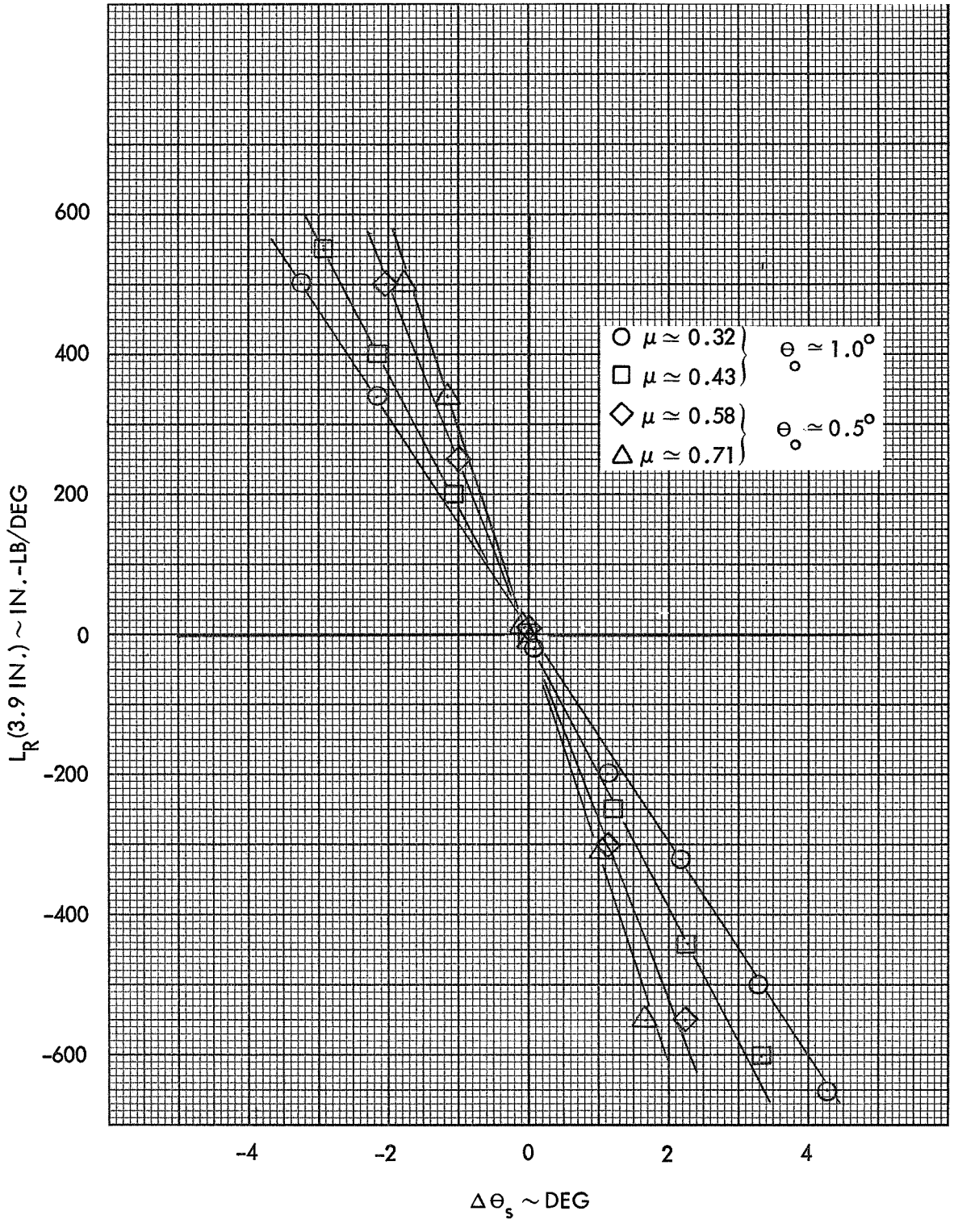

Figure 129. Rotor Roll Response to Longitudinal Cyclic Pitch, Configuration 4, 750 RPM (γ=3.0, P=1.40)

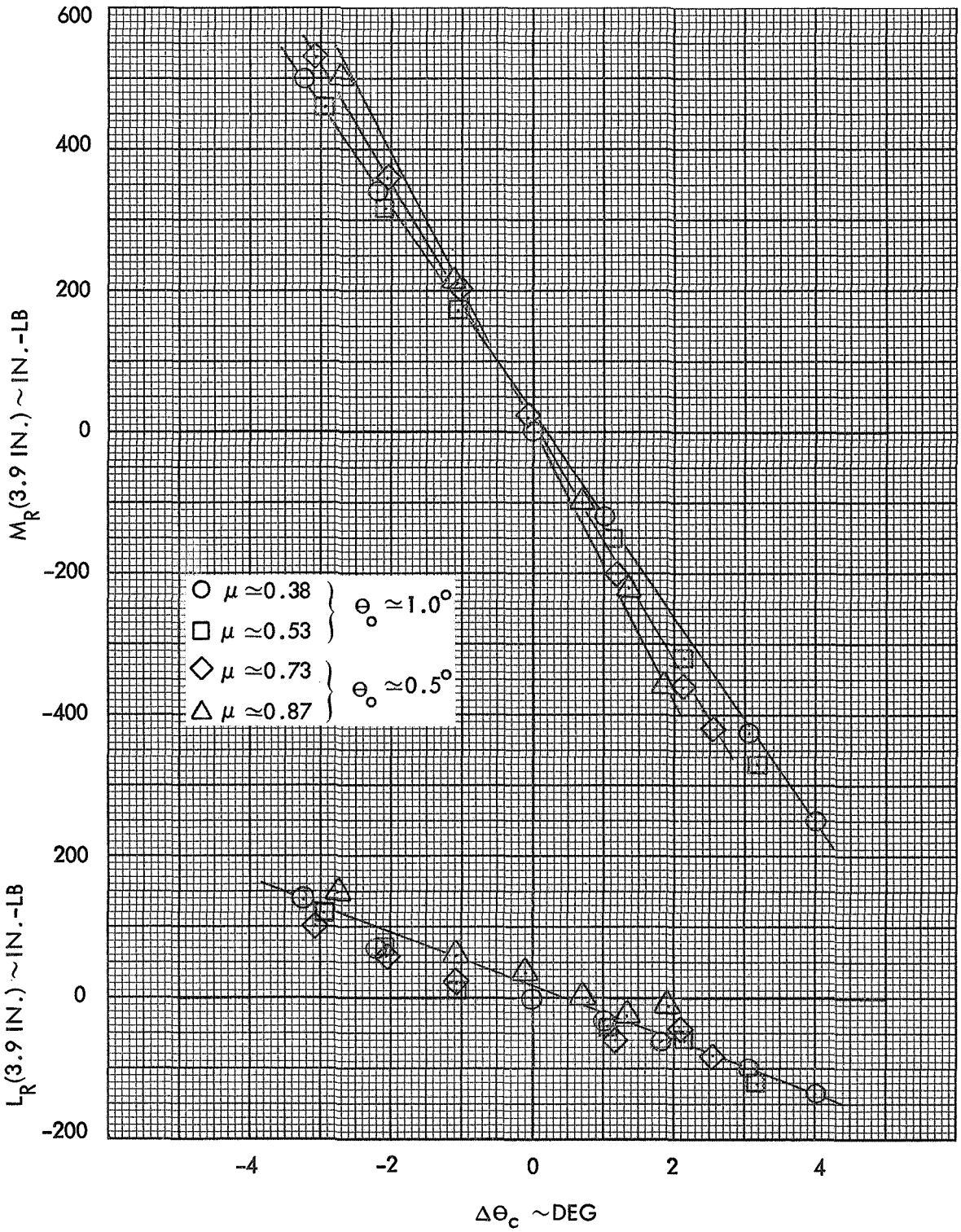

Figure 130. Rotor Pitch and Roll Response to Lateral Cyclic Pitch, Configuration 4, 600 RPM (γ=3.0, P=1.51)

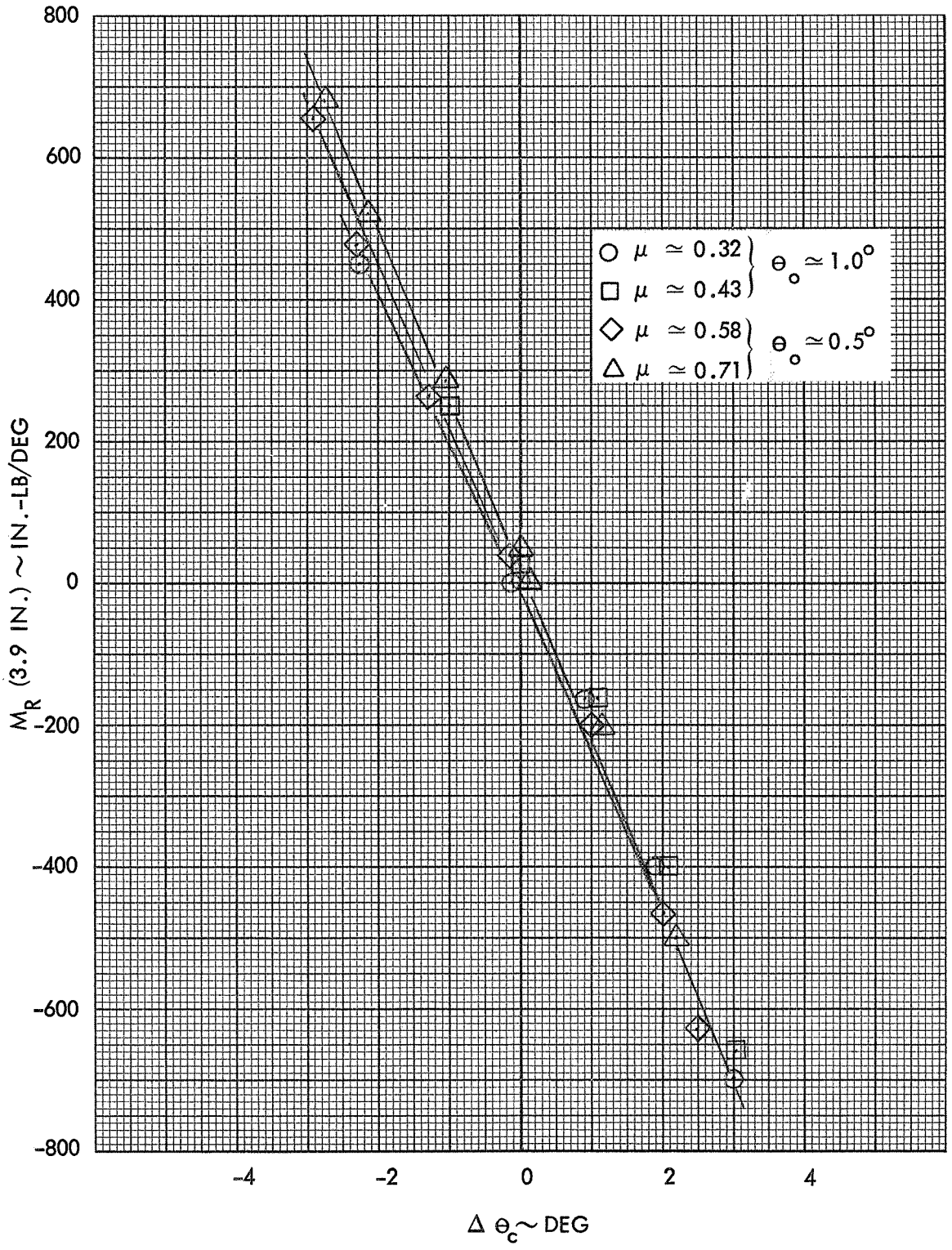

Figure 131. Rotor Pitch Response to Lateral Cyclic Pitch, Configuration 4, 750 RPM (γ=3.0, P=1.40)

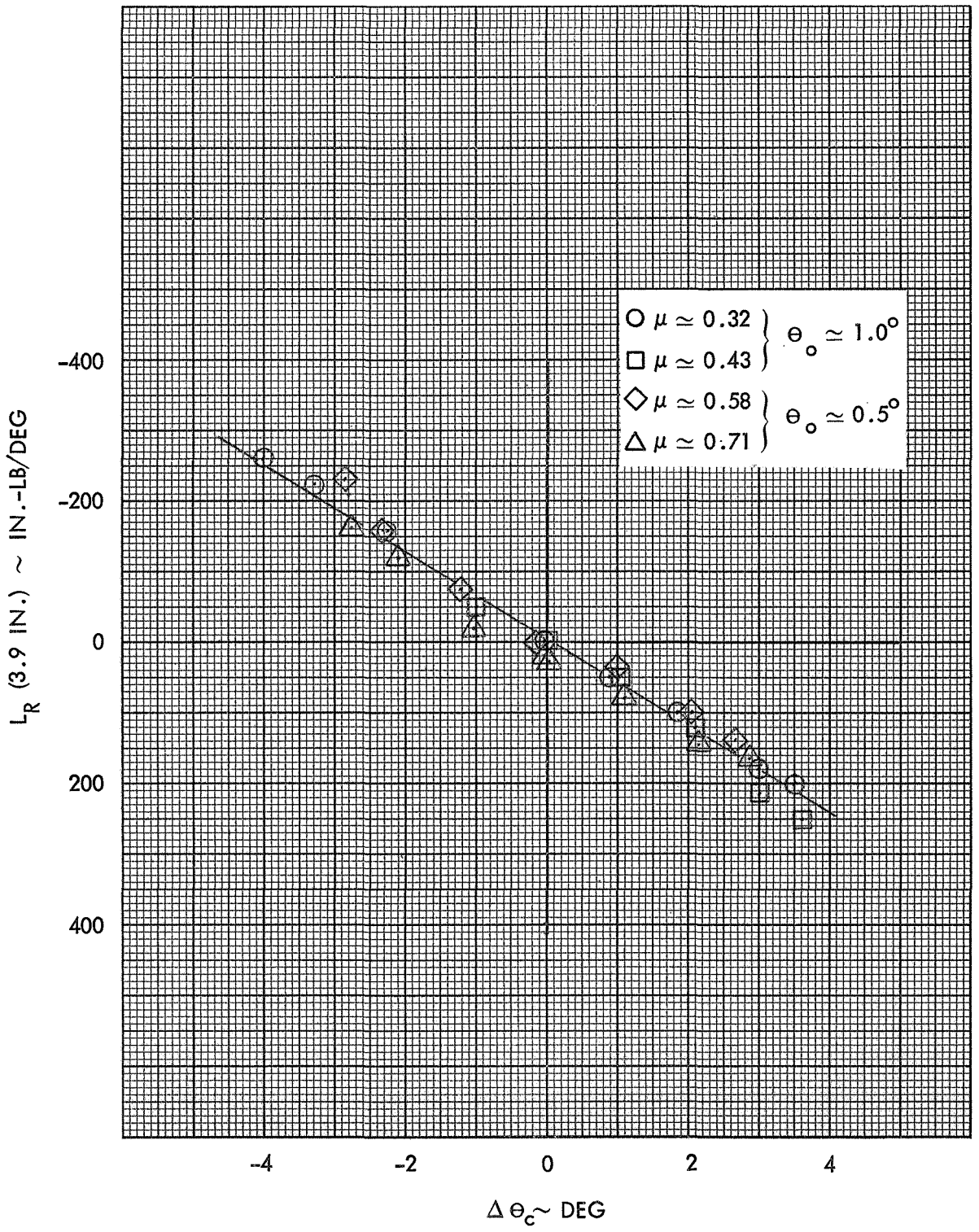

Figure 132. Rotor Roll Response to Lateral Cyclic Pitch, Configuration 4, 750 RPM (γ=3.0, P=1.40)

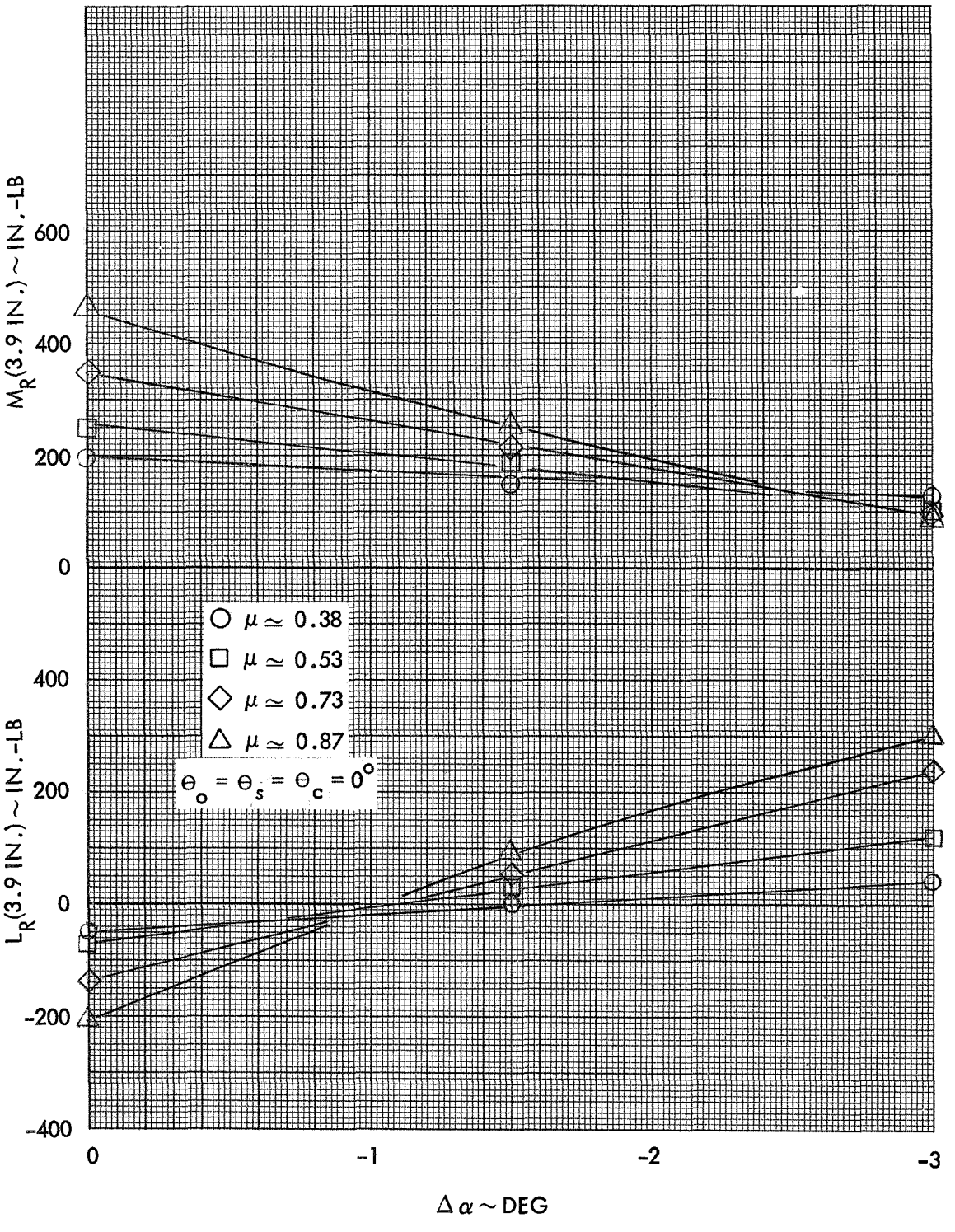

Figure 133. Rotor Pitch and Roll Response to a Rotor Shaft Angle of Attack Increment, Configuration 4, 600 RPM (γ=3.0, P=1.51)

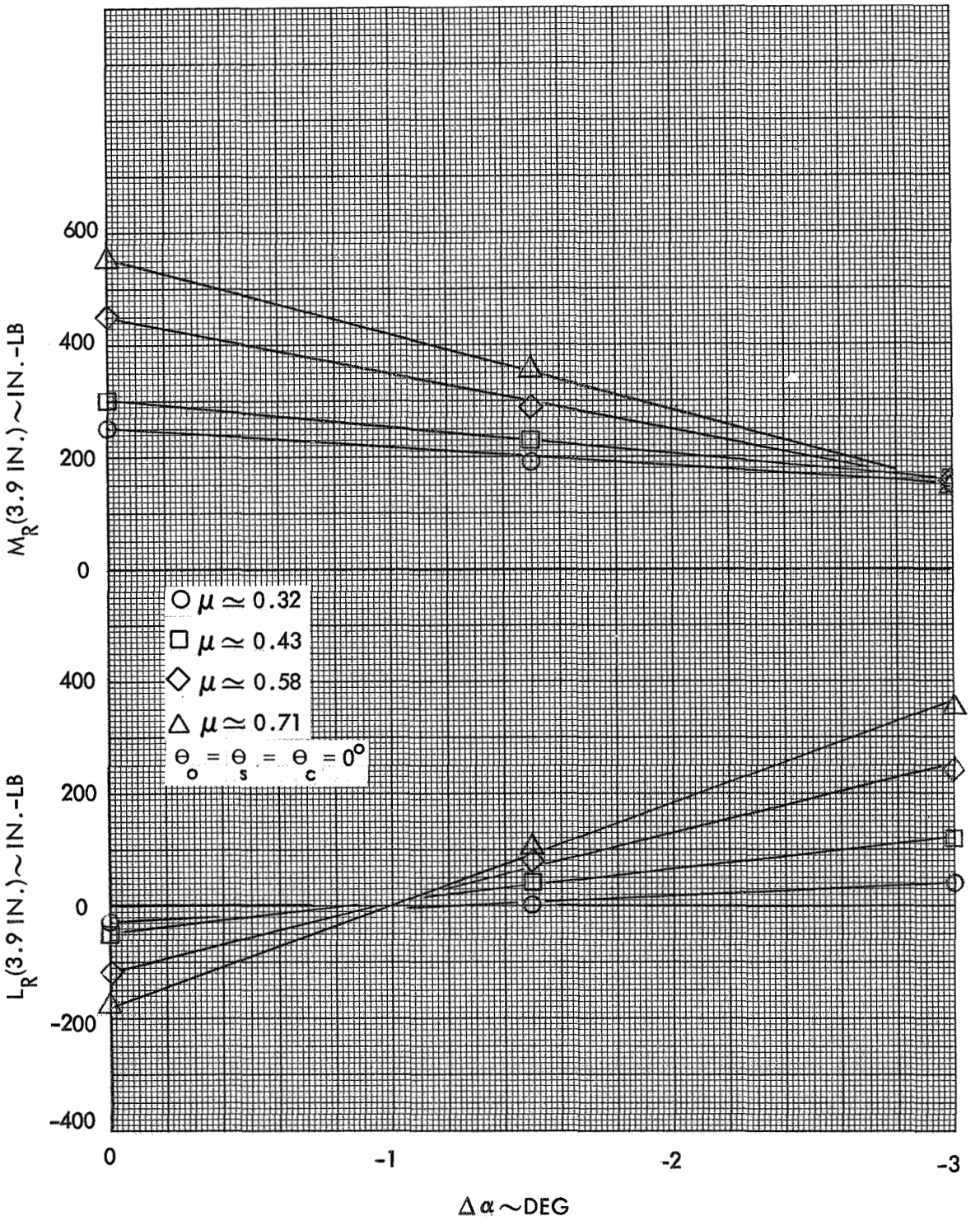

Figure 134. Rotor Pitch and Roll Response to a Rotor Shaft Angle of Attack Increment, Configuration 4, 750 RPM (γ=3.0, P=1.40)

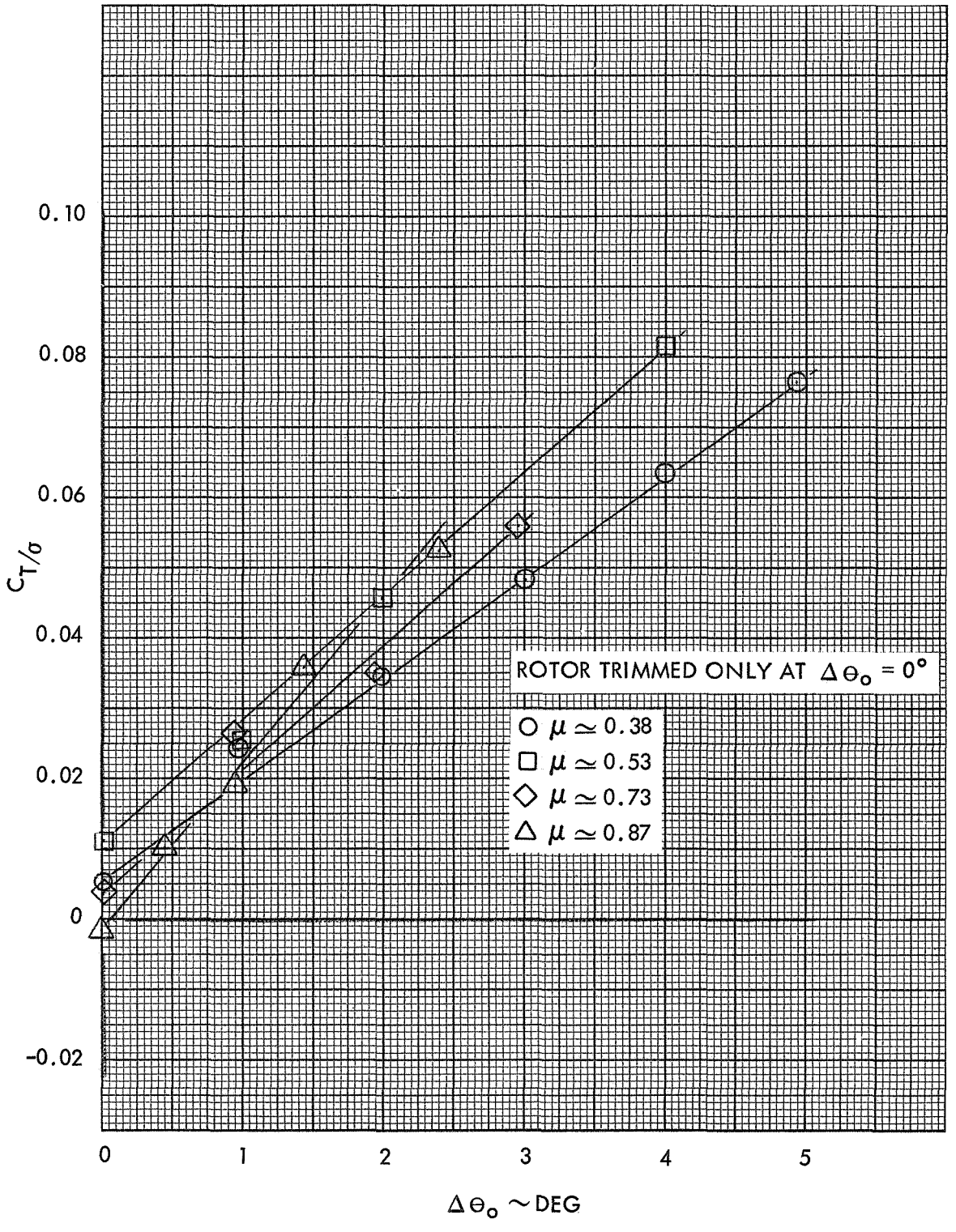

Figure 135. Rotor Lift versus Collective Pitch, Configuration 4, 600 RPM (γ=3.0, P=1.51)

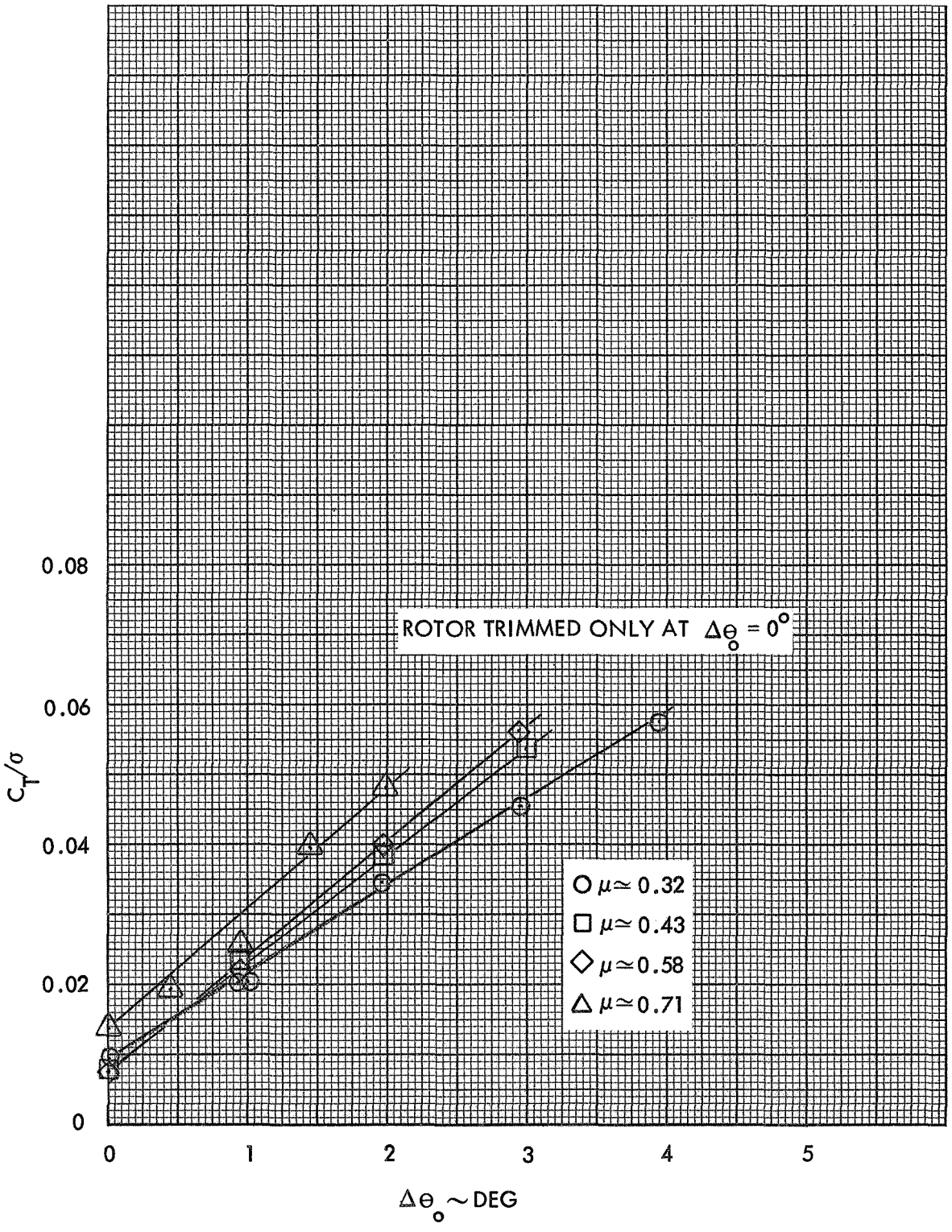

Figure 136. Rotor Lift versus Collective Pitch, Configuration 4, 750 RPM (γ=3.0, P=1.40)

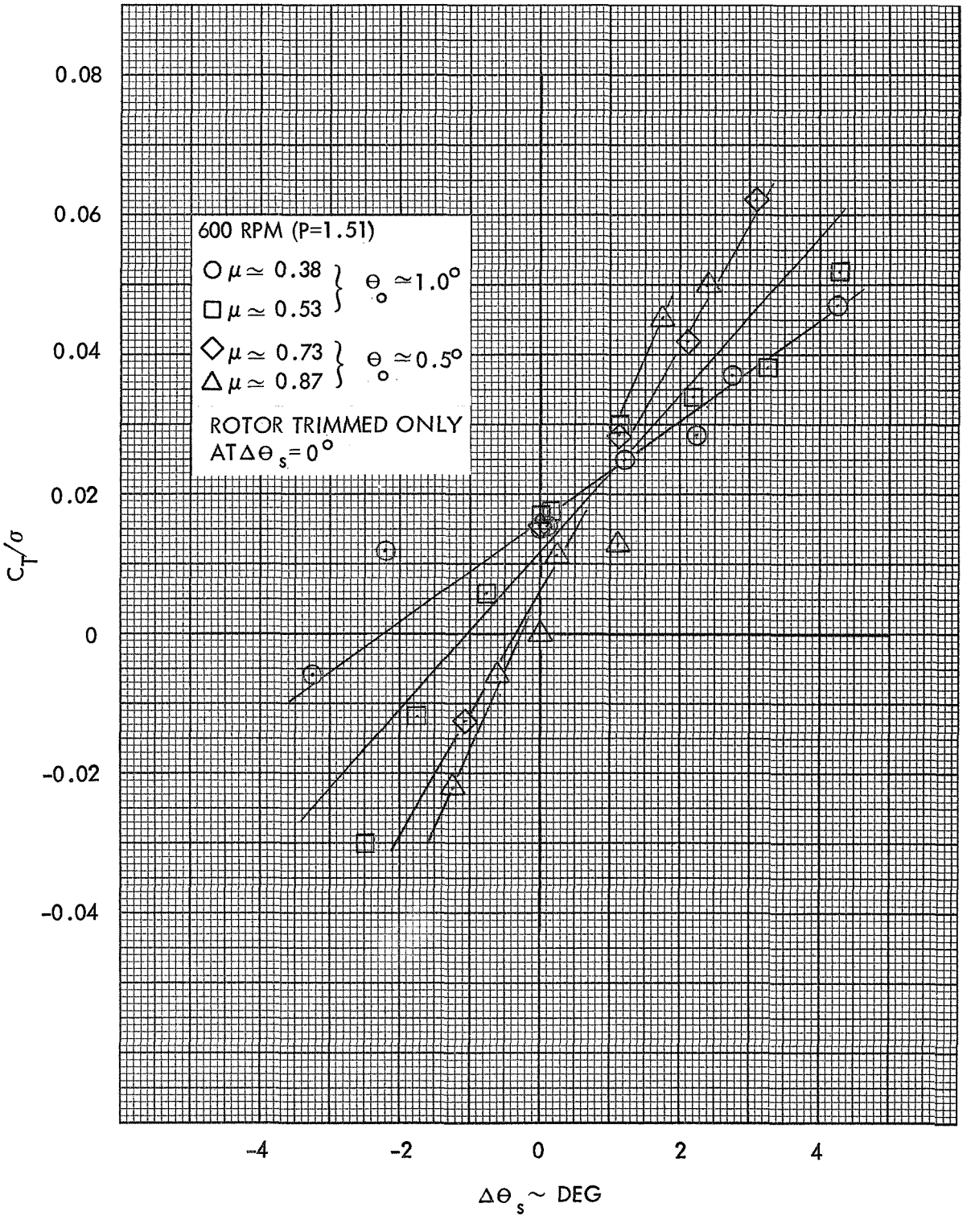

Figure 137. Rotor Lift versus Longitudinal Cyclic Pitch, Configuration 4, 600 RPM (γ=3.0)

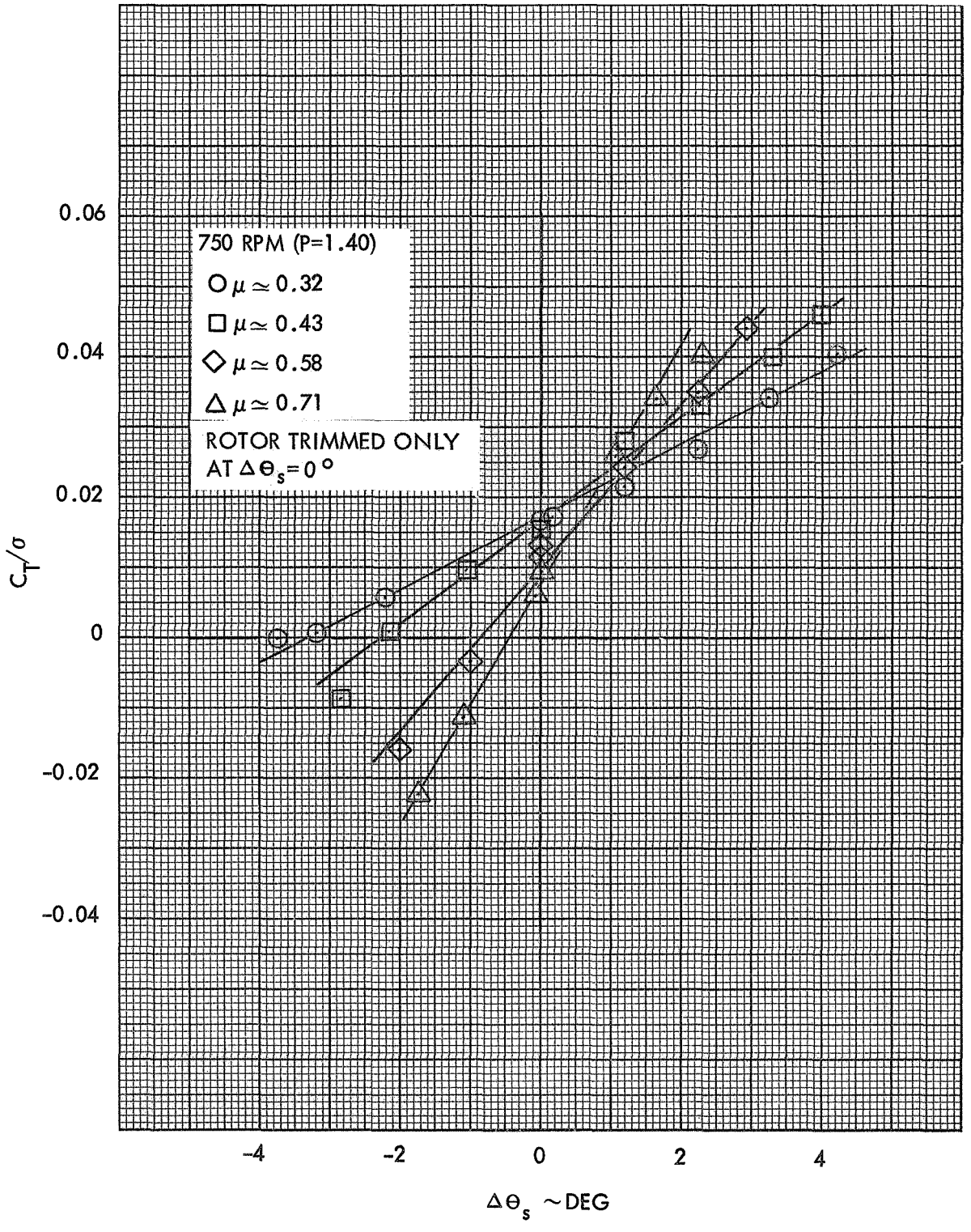

Figure 138. Rotor Lift versus Longitudinal Cyclic Pitch, Configuration 4, 750 RPM (γ=3.0)

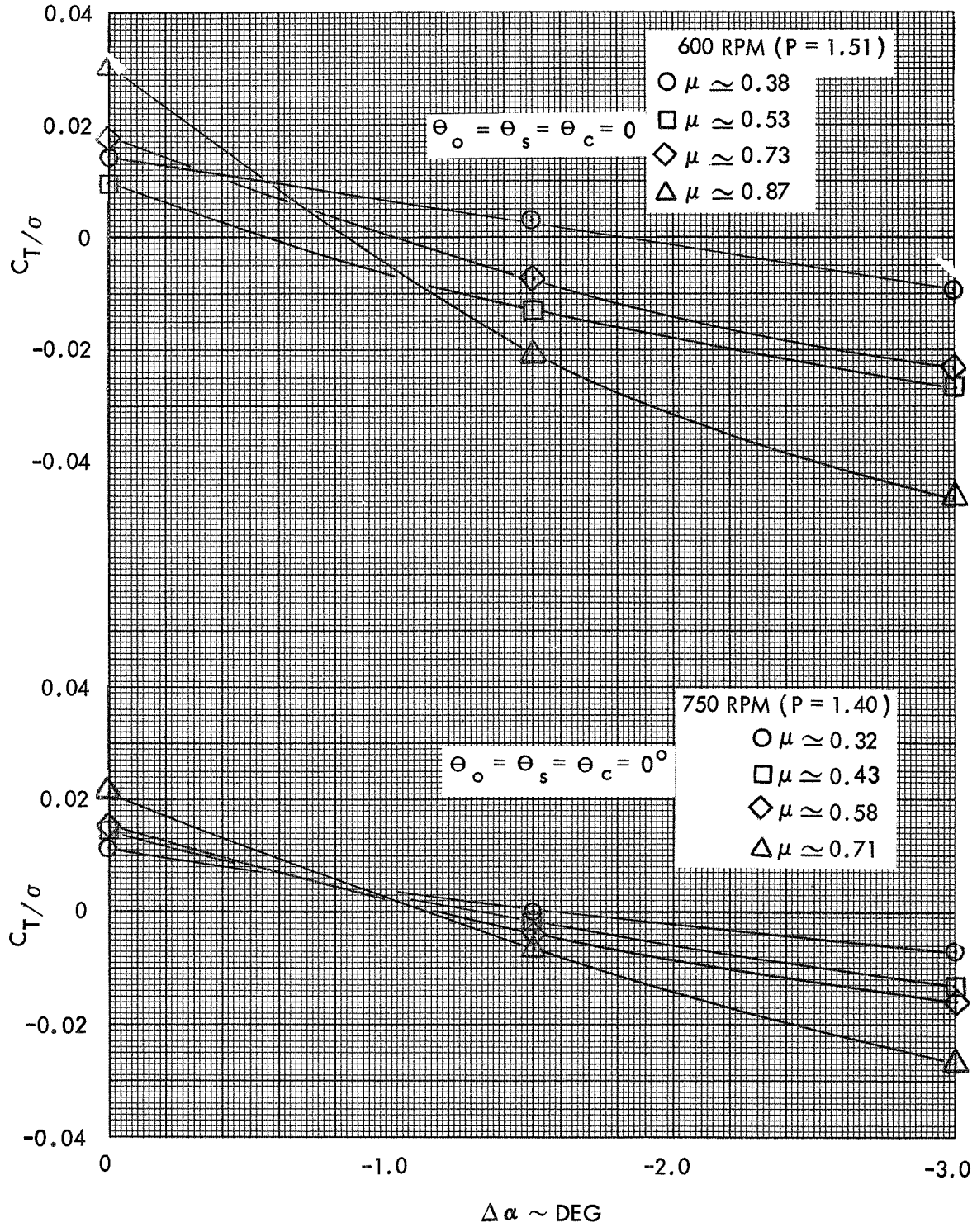

Figure 139. Rotor Lift versus Rotor Shaft Angle of Attack, Configuration 4, 600 RPM and 750 RPM (γ=3.0)

APPENDIX C

PLOTTED STEADY ROTATING BLADE MOMENT TEST DATA

The constant component of the rotating flapping moment of a single blade was determined numerically from a Fourier analysis of digitized analog data. These steady blade moments for all the test conditions are plotted herein. They are used to form summary derivative plots (e.g., Figure 26) in Section 6 and are further reduced to yield blade coning derivatives in Section 7.

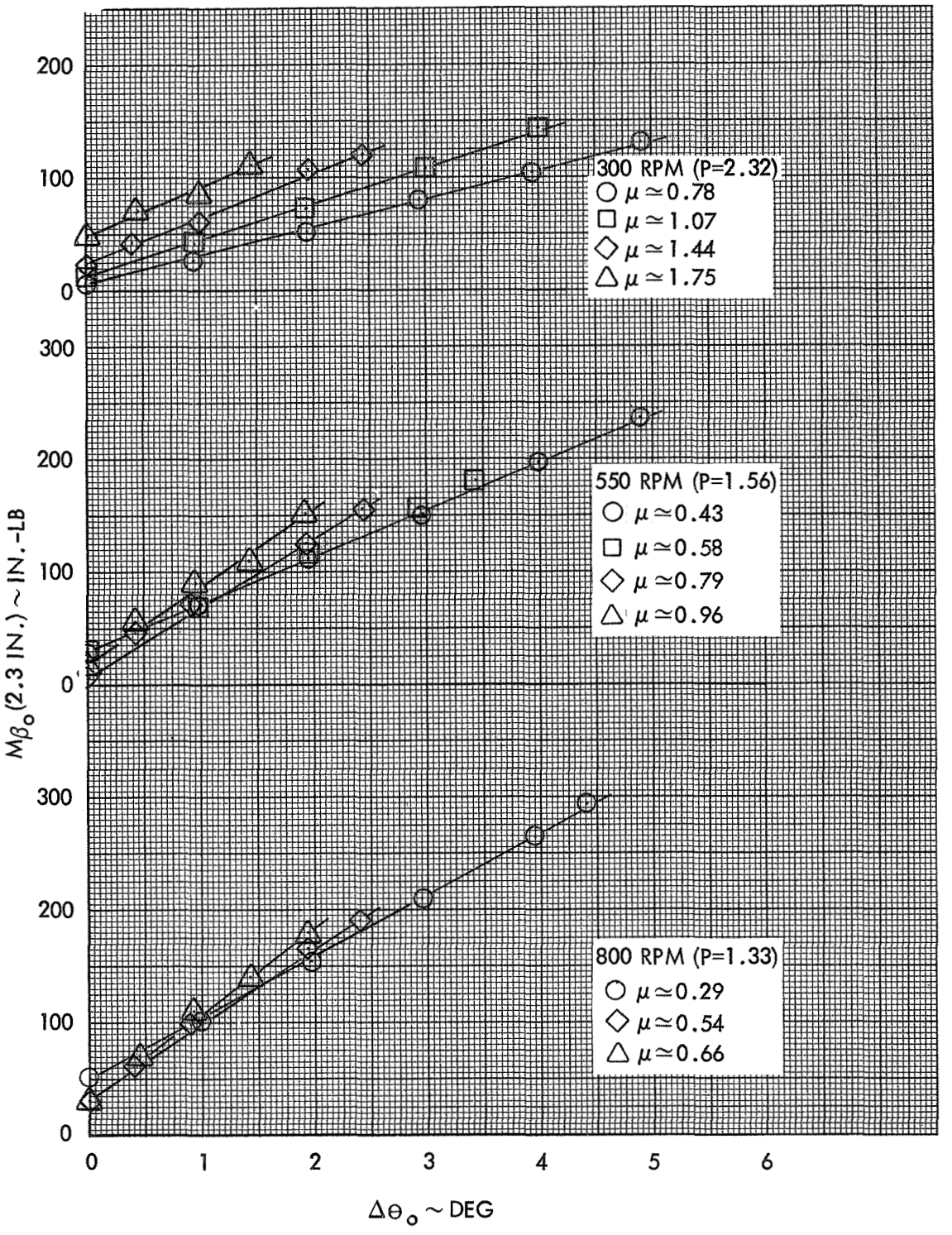

Figure 140. Steady Rotating Blade Flapping Response to Collective Pitch, Configuration 1 (γ=5.0)

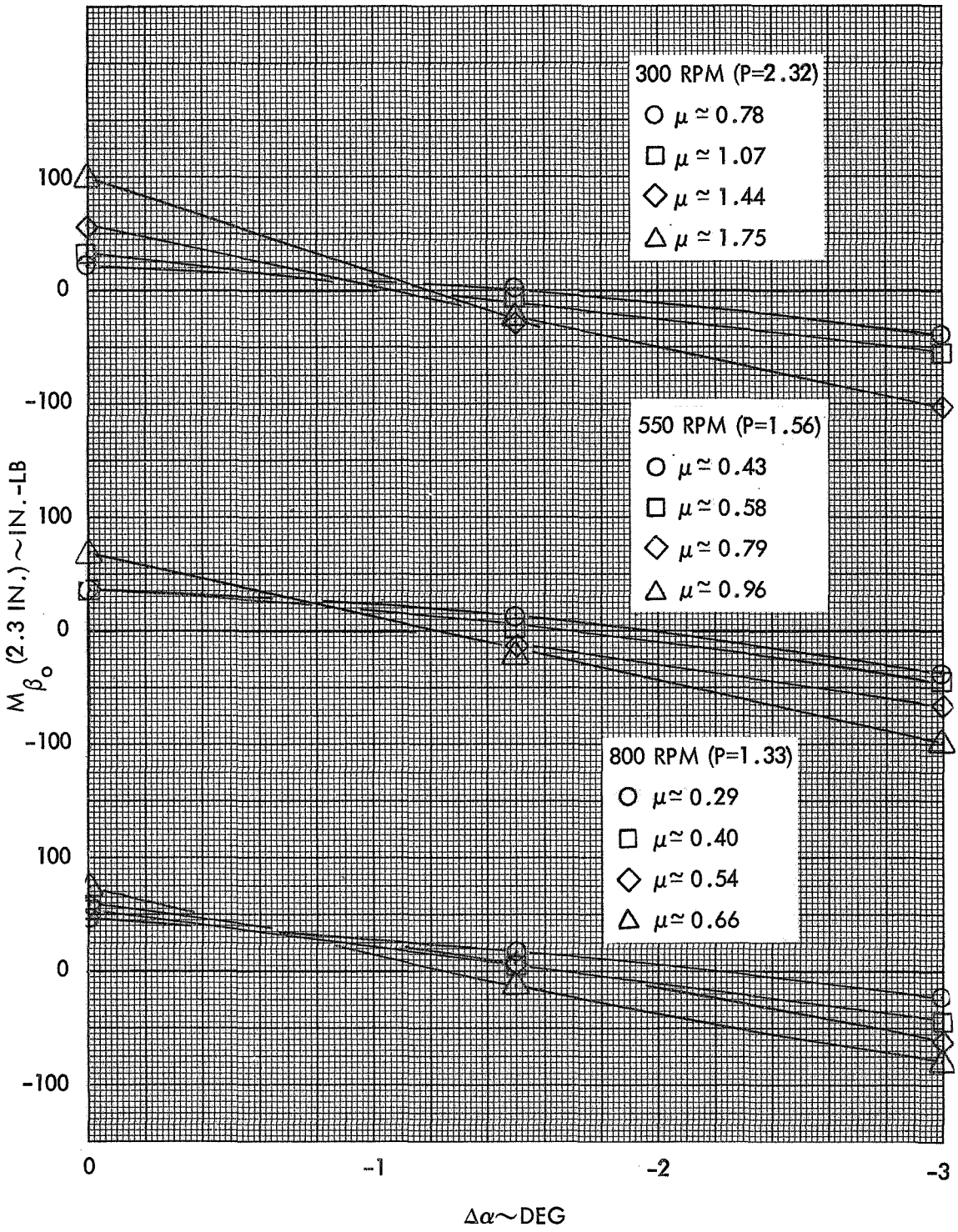

Figure 141. Steady Rotating Blade Flapping Response to Rotor Shaft Angle of Attack, Configuration 1 (γ=5.0)

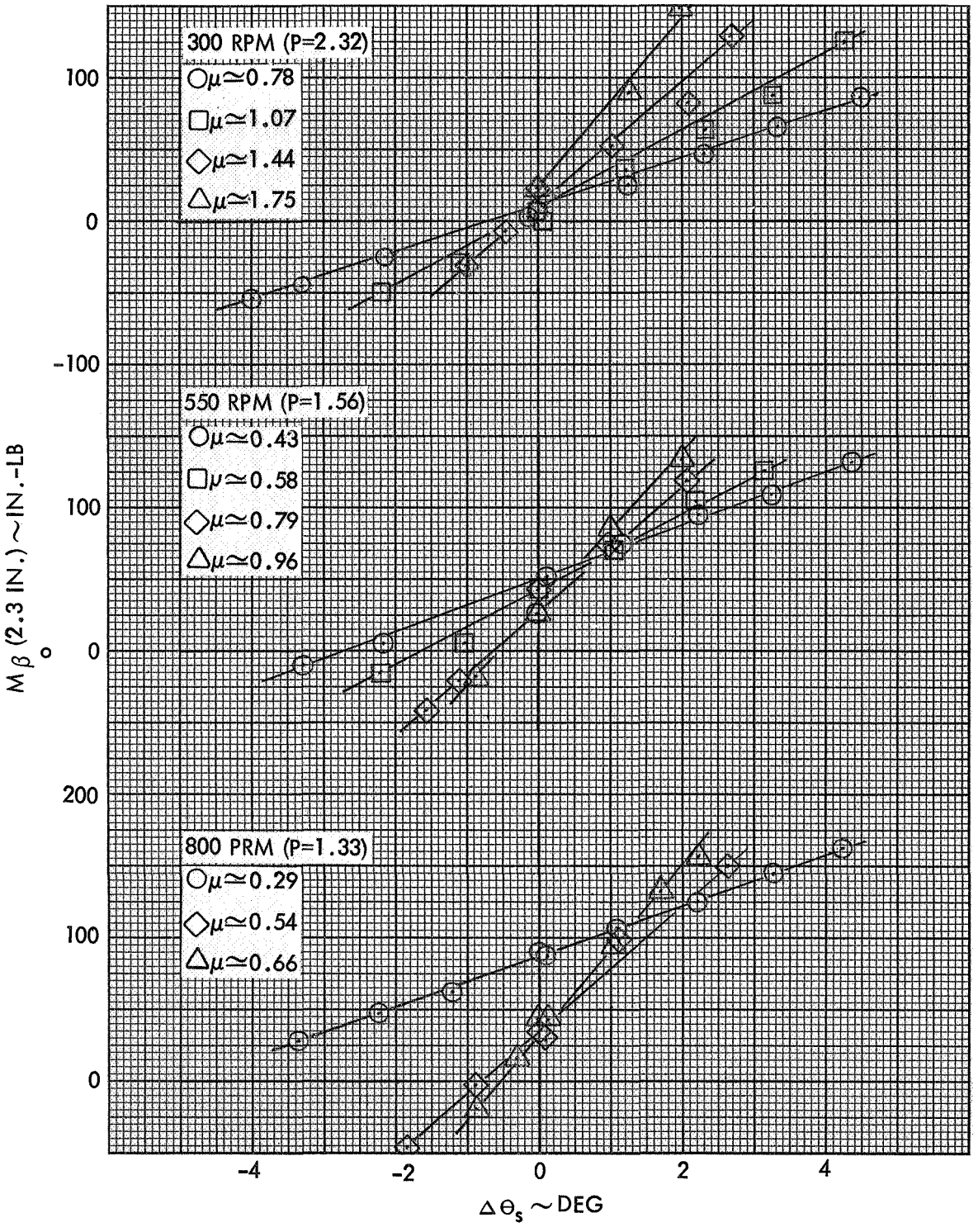

Figure 142. Steady Rotating Blade Flapping Response to Longitudinal Cyclic Pitch, Configuration 1 (γ=5.0)

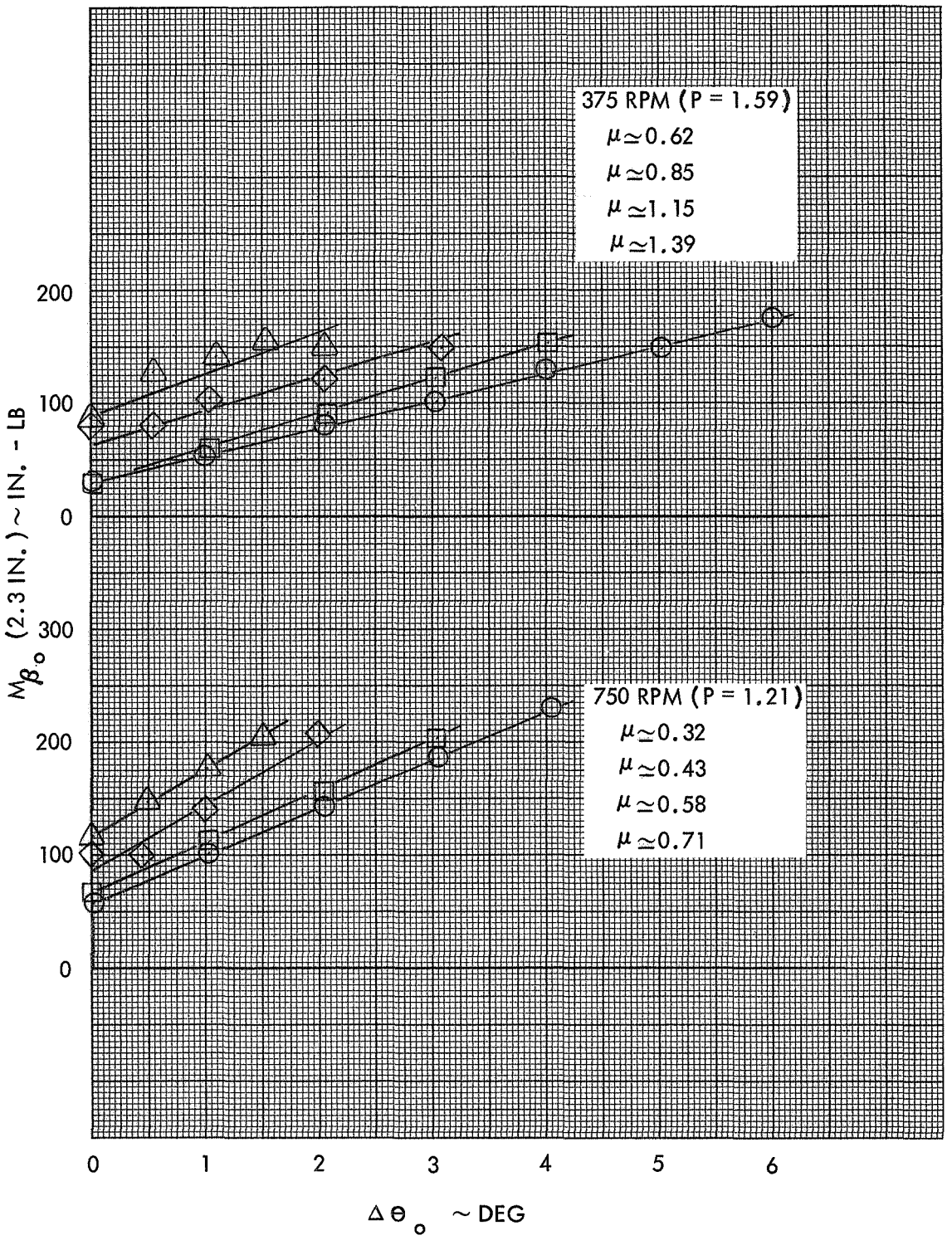

Figure 143. Steady Rotating Blade Flapping Response to Collective Pitch, Configuration 2 (γ=3.0)

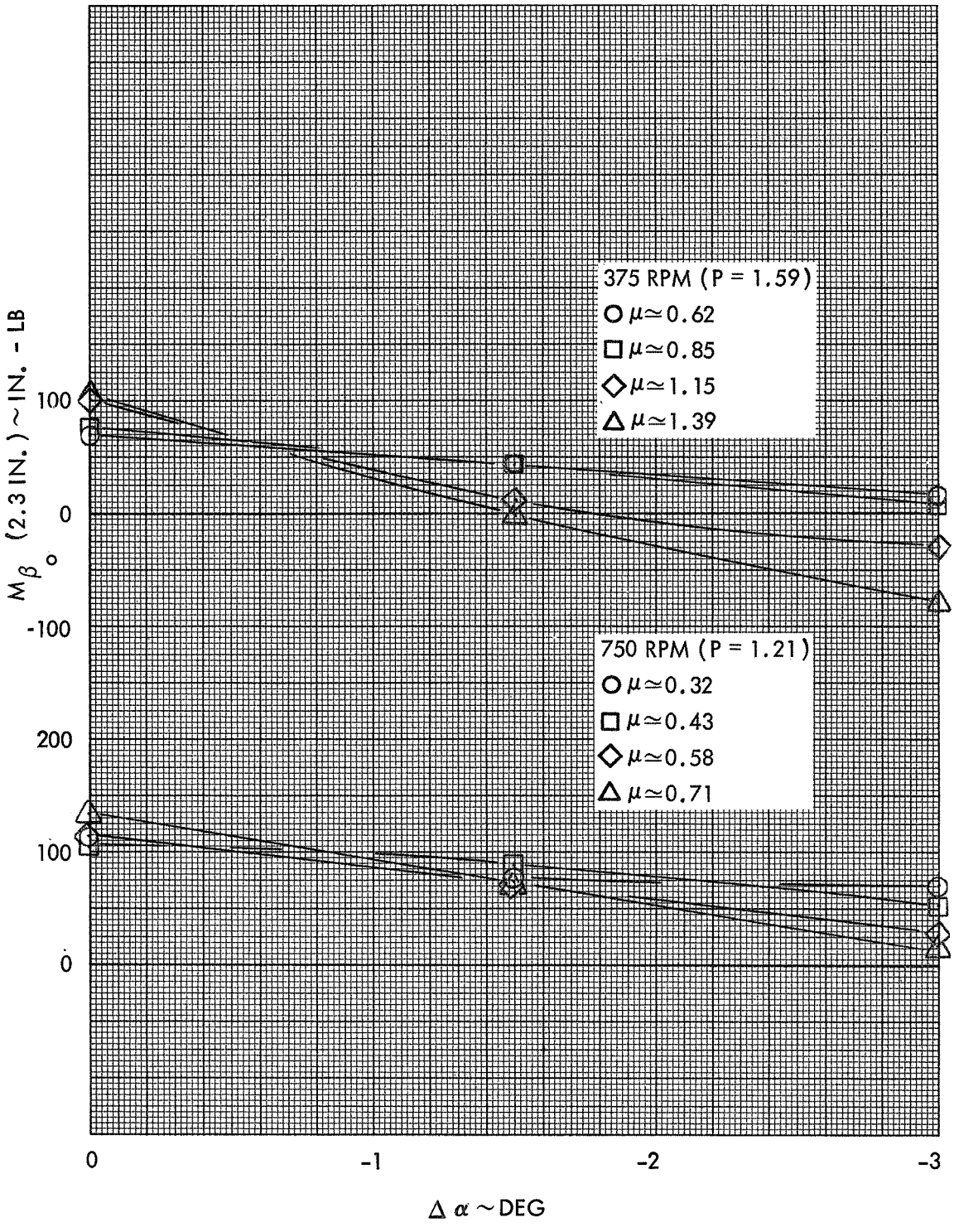

Figure 144. Steady Rotating Blade Flapping Response to Rotor Shaft Angle of Attack, Configuration 2 (γ=3.0)

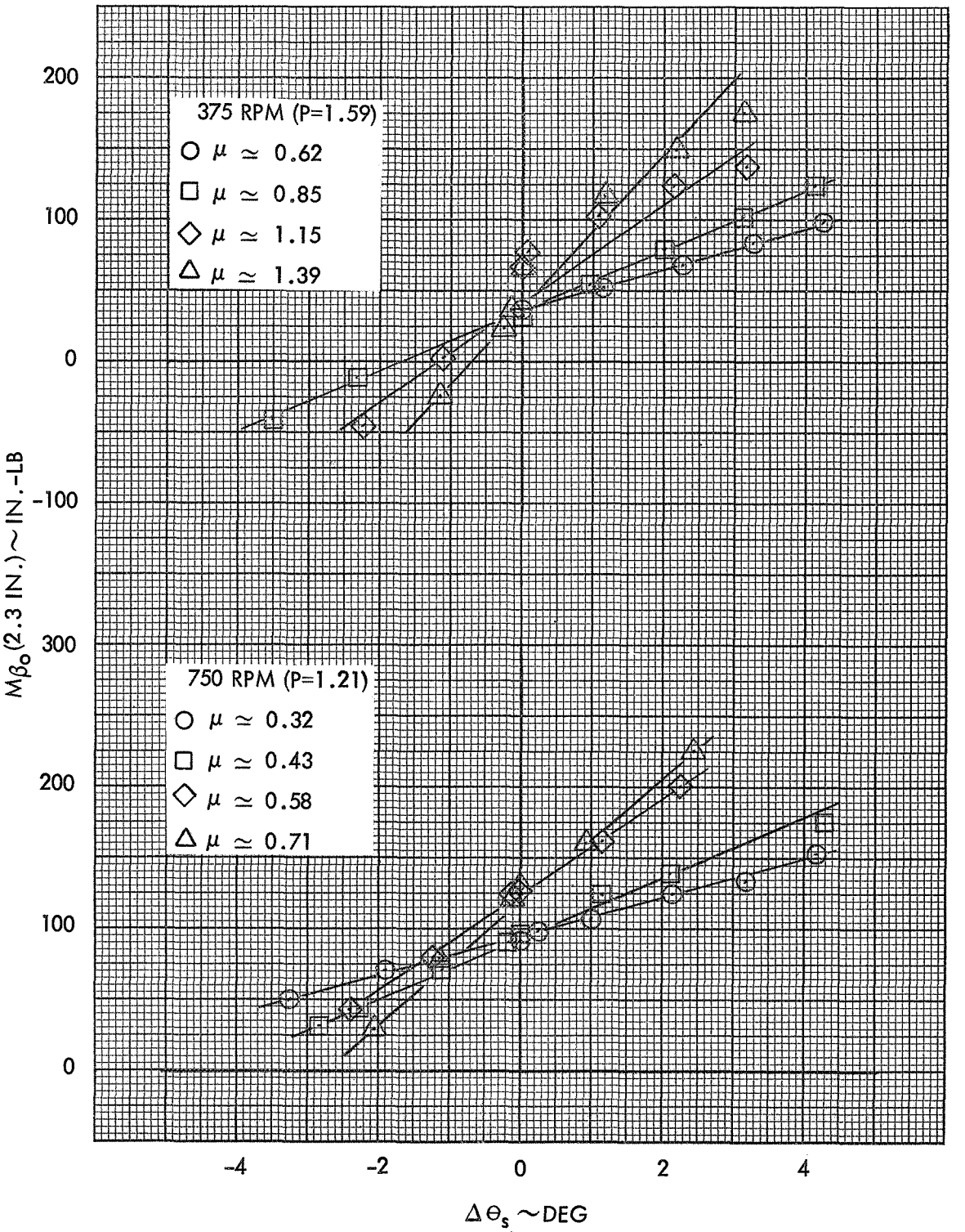

Figure 145. Steady Rotating Blade Flapping Response to Longitudinal Cyclic Pitch, Configuration 2 (γ=3.0)

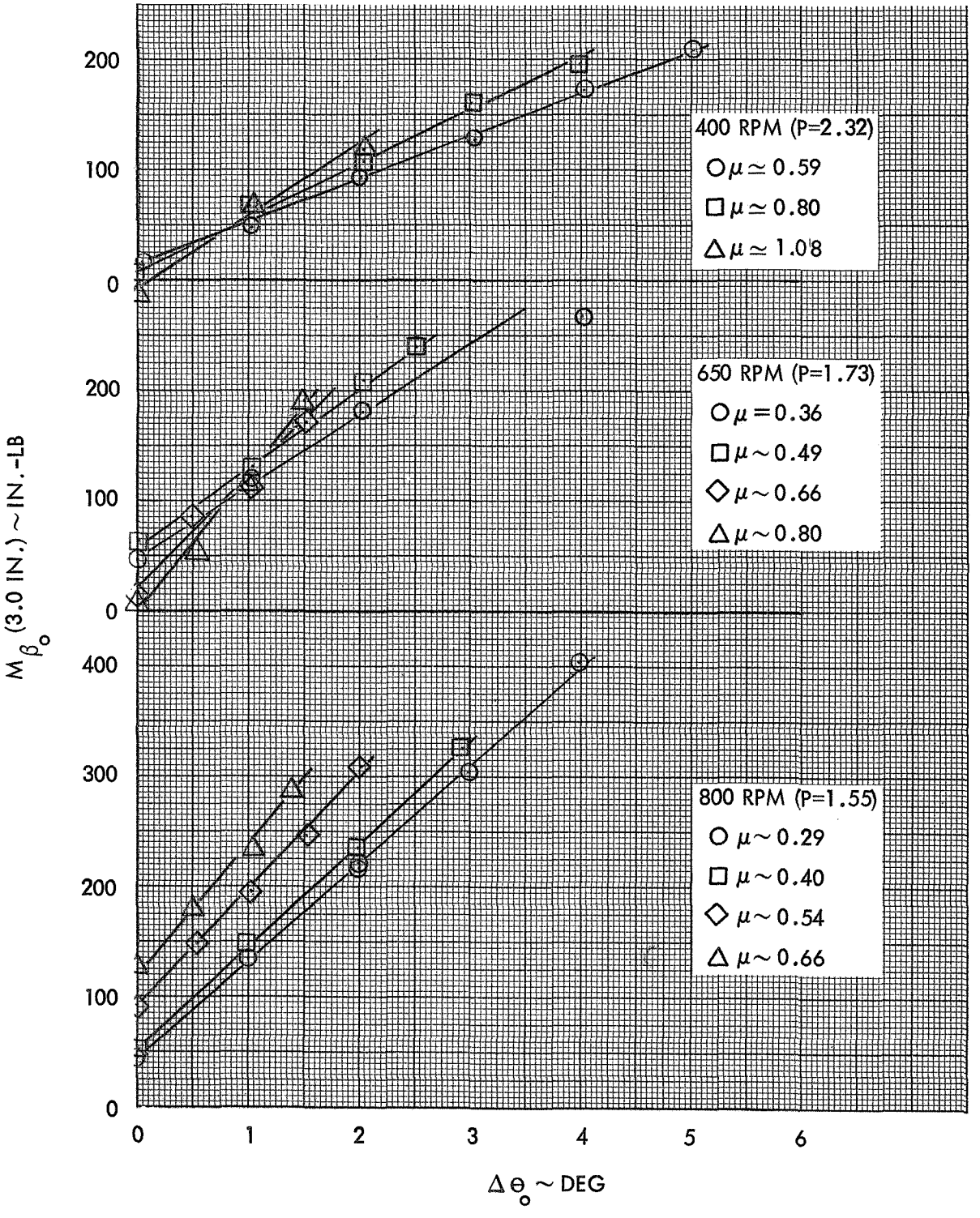

Figure 146. Steady Rotating Blade Flapping Response to Collective Pitch, Configuration 3 (γ=5.0)

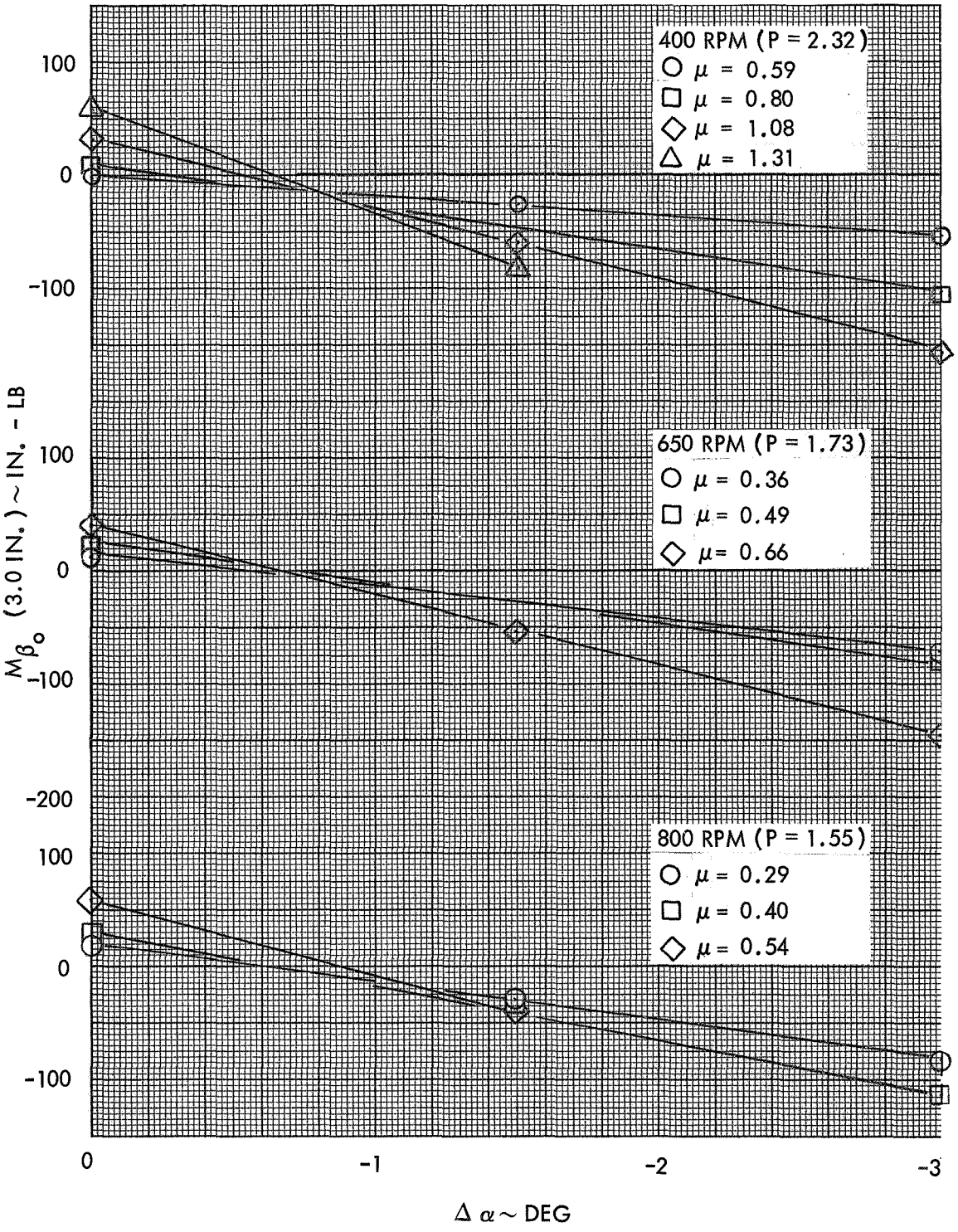

Figure 147. Steady Rotating Blade Flapping Response to Rotor Shaft Angle of Attack, Configuration 3 (γ=5.0)

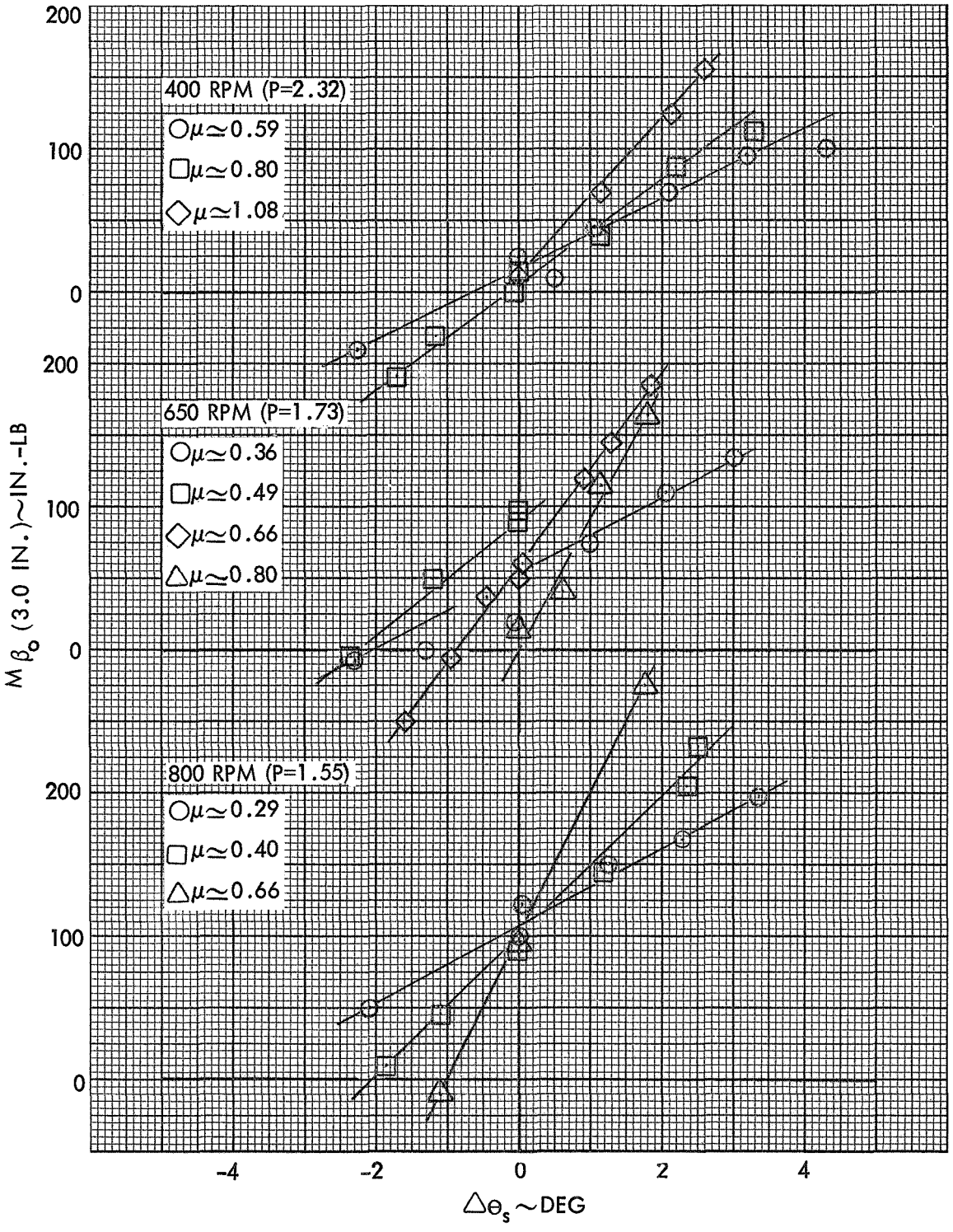

Figure 148. Steady Rotating Blade Flapping Response to Longitudinal Cyclic Pitch, Configuration 3 (γ=5.0)

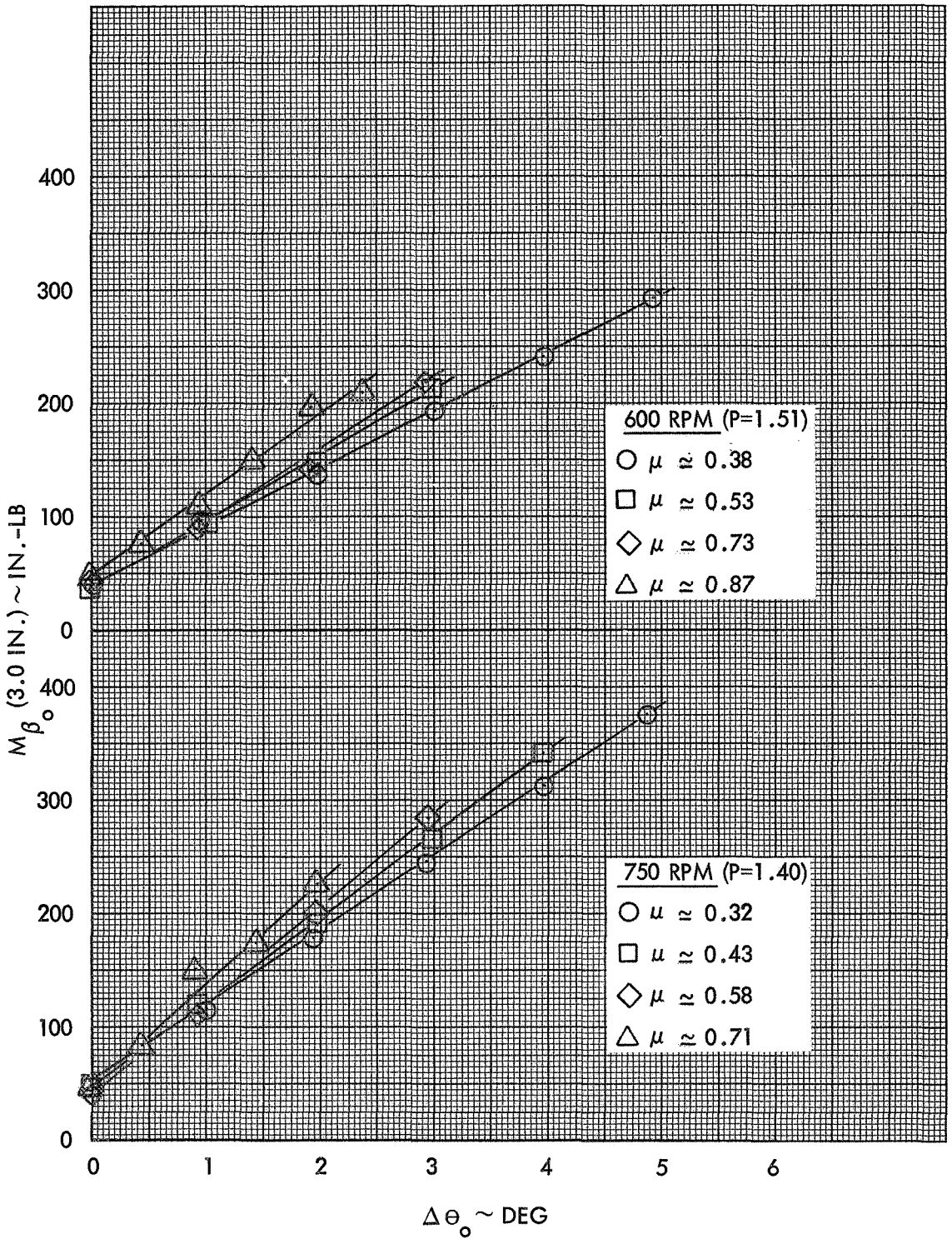

Figure 149. Steady Rotating Blade Flapping Response to Collective Pitch, Configuration 4 (γ=3.0)

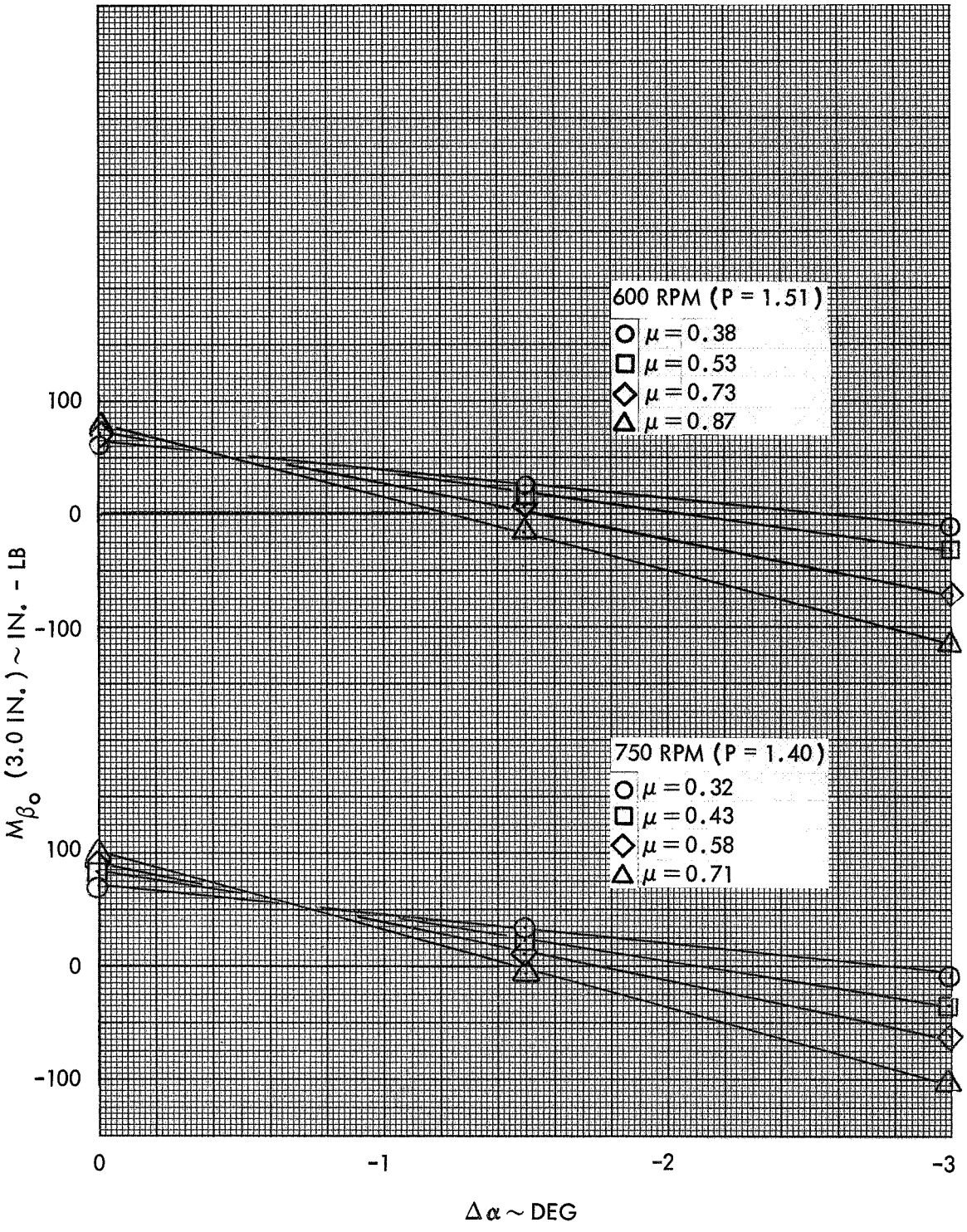

Figure 150. Steady Rotating Blade Flapping Response to Rotor Shaft Angle of Attack, Configuration 4 (γ=3.0)

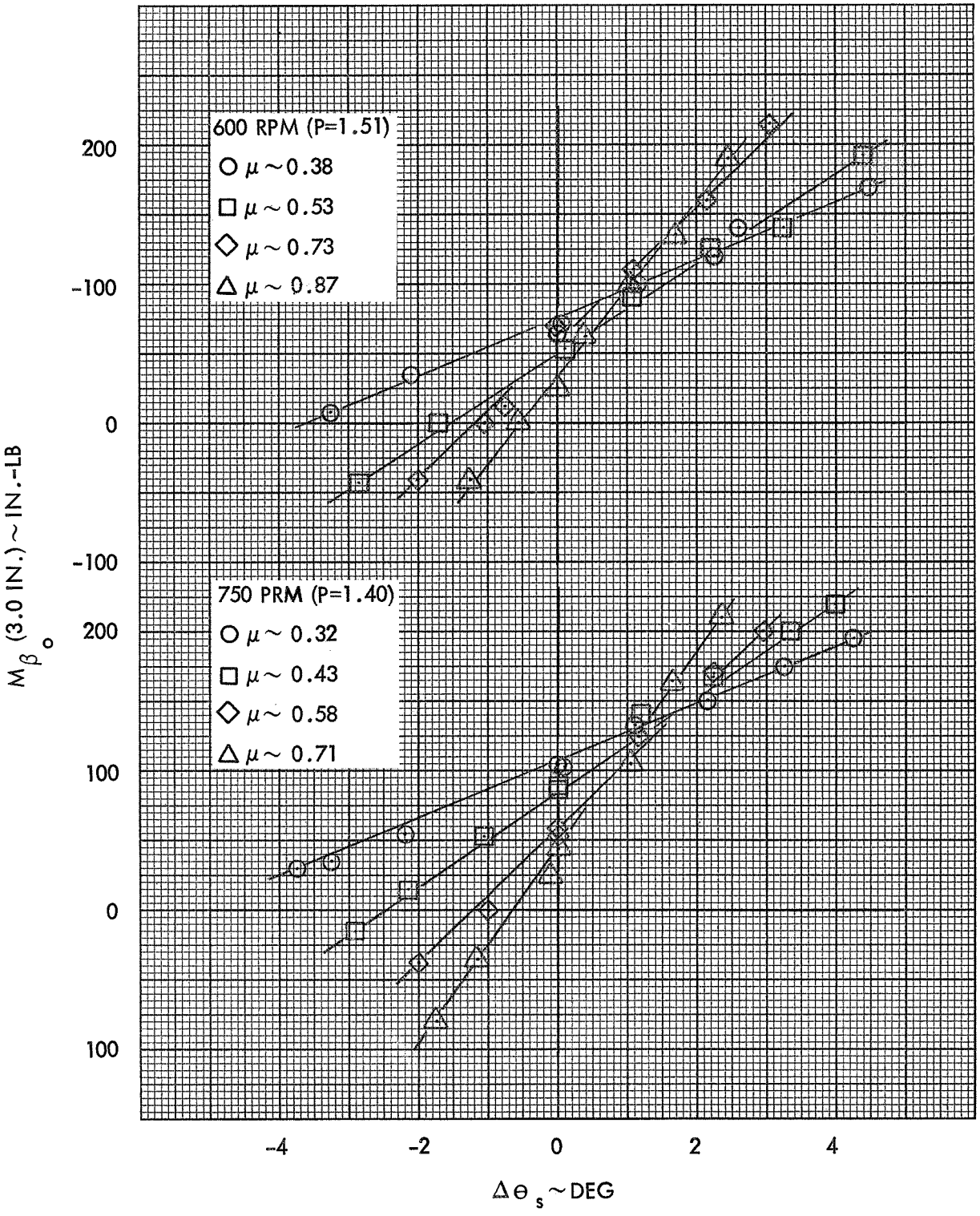

Figure 151. Steady Rotating Blade Flapping Response to Longitudinal Cyclic Pitch, Configuration 4 (γ=3.0)